Charged colloids and proteins: Structure, diffusion, and rheology.

Inaugural-Dissertation

zur Erlangung des Doktorgrades
der Mathematisch-Naturwissenschaftlichen Fakultät
der Heinrich-Heine-Universität Düsseldorf

vorgelegt von

Marco Heinen
aus Hürth

Düsseldorf, September 2011

aus dem Institute of Complex Systems (ICS-3),
Forschungszentrum Jülich GmbH

Gedruckt mit der Genehmigung der
Mathematisch-Naturwissenschaftlichen Fakultät der
Heinrich-Heine-Universität Düsseldorf

Referent:	Prof. Dr. Gerhard Nägele
Koreferent:	Prof. Dr. Hartmut Löwen

Tag der mündlichen Prüfung: 09.11.2011

This thesis is partially based on the following papers:

- M. Heinen, P. Holmqvist, A. J. Banchio, and G. Nägele, "Short-time diffusion of charge-stabilized colloidal particles: generic features", *J. Appl. Cryst.* **43**, 970-980 (2010).
- M. Heinen, P. Holmqvist, A. J. Banchio, and G. Nägele, "Pair structure of the hard-sphere Yukawa fluid: An improved analytic method versus simulations, Rogers-Young scheme, and experiment", *J. Chem. Phys.* **134**, 044532 (2011) ibid. *J. Chem. Phys.* **134**, 129901 (2011).
- M. Heinen, A. J. Banchio, and G. Nägele, "Short-time rheology and diffusion in suspensions of Yukawa-type colloidal particles", *J. Chem. Phys.* **135**, 154504 (2011).
- M. Heinen, F. Zanini, F. Roosen-Runge, D. Fedunová, F. Zhang, M. Hennig, T. Seydel, R. Schweins, M. Sztucki, M. Antalík, F. Schreiber, and G. Nägele, "Viscosity and diffusion: Crowding and salt effects in protein solutions", *accepted for publication in Soft Matter*, DOI:10.1039/C1SM06242E (preprint: arXiv:1109.3101v1 [cond-mat.soft]).
- D. Kleshchanok, M. Heinen, G. Nägele, and P. Holmqvist, "Dynamics of charged gibbsite platelets in the isotropic phase", *accepted for publication in Soft Matter*, DOI:10.1039/C1SM06735D (preprint: arXiv:1109.3293v1 [cond-mat.soft]).
- M. Heinen, P. Holmqvist, A. J. Banchio, and G. Nägele, "Short- and long-time dynamics of charged colloidal particles", *in preparation*.
- F. Westermeier, G. Grübel, W. Roseker, B. Fischer, G. Nägele, and M. Heinen, "Structure and short-time dynamics of concentrated charged colloidal systems", *in preparation*.

Other publications by the author of this thesis are:

- M. Heinen and H.-J. Kull, "Radiation boundary conditions for the numerical solution of the three-dimensional time-dependent Schrödinger equation with a localized interaction", *Phys. Rev. E* **79**, 056709 (2009).
- M. Heinen and H.-J. Kull, "Numerical Calculation of Strong-Field Laser-Atom Interaction: An Approach with Perfect Reflection-Free Radiation Boundary Conditions", *Laser Physics* **20**, 581-590 (2010).

Zusammenfassung

Die hier vorgestellte Arbeit befasst sich mit der theoretischen Beschreibung der Mikrostruktur, Diffusionseigenschaften, und rheologischen Eigenschaften geladener Brownscher Teilchen. Wir haben diverse analytisch-theoretische Methoden zur Berechnung statischer und dynamischer Größen entwickelt, getestet, und angewendet. Die Methoden zeichnen sich aus durch Genauigkeit, universelle Anwendbarkeit, und numerische Effizienz. Eine Vielzahl von Gleichgewichtsgrößen und Eigenschaften der Kurzzeit- und Langzeitdynamik sind im Rahmen dieser Arbeit berechnet worden. Die berechneten Größen umfassen den statischen Strukturfaktor, translative Diffusionskoeffizienten für kollektive Diffusion und Selbstdiffusion, die hydrodynamische Funktion, sowie die Hochfrequenzviskosität und die statische Scherviskosität.

In enger Zusammenarbeit mit experimentellen Arbeitsgruppen in Jülich, Tübingen, Utrecht (Niederlande) und Košice (Slowakei) wurden Suspensionen von geladenen synthetischen Silicakugeln, leicht asphärischen Rinderalbumin Proteinen, und dünnen Gibbsit-Plättchen untersucht. (Dynamische) Licht- und Röntgenstreudaten, und Viskositätsdaten dieser drei Systeme wurden bis in die Nähe des Übergangs zwischen der flüßigen und festen oder flüßigkristallinen Phase mit hoher Genauigkeit analytisch berechnet. Hierdurch ist eine genaue Charakterisierung der suspendierten Partikel gelungen. In Zusammenarbeit mit Prof. Banchio (Uni. Córdoba, Argentinien) haben wir unsere analytischen Methoden zur Berechnung der Gleichgewichts-Paarkorrelationen und der Kurzzeitdynamik in umfassenden Parameterstudien anhand von Computersimulationen validiert.

Als Grundlage unserer analytischen Verfahren dient ein Modell monodisperser geladener Kugeln in einer strukturlosen Flüssigkeit, die über ein abgeschirmtes Coulomb-Potential wechselwirken. Die Reichweite der elektrostatischen Abstoßung hängt vom Salzgehalt der Suspension ab, sodass bei niedriger Salzkonzentration bereits stark verdünnte Systeme ausgeprägte Paarkorrelationen aufweisen. Einen wichtigen Teil dieser Arbeit bildet eine neu entwickelte, analytische Integralgleichungsmethode, bezeichnet als „Modified Penetrating Background corrected Rescaled Mean Spherical Approximation“. Diese Methode erlaubt eine schnelle und genaue Berechnung statischer Paarkorrelationen. Die so berechneten Paarkorrelationsfunktionen dienen als Eingabegrößen für verschiedene analytische Methoden

zur Berechnung der Diffusionseigenschaften und der Scherviskosität ladungsstabilisierter kolloidaler Suspensionen und Proteinlösungen.

Eine besondere Herausforderung bei der Berechnung dynamischer Größen ist die notwendige Berücksichtigung der langreichweitigen und nichtsuperponierenden hydrodynamischen Wechselwirkungen. Hierzu haben wir Verbesserungen an der approximativen $\delta\gamma$ Methode von Beenakker und Mazur zur Berechnung der hydrodynamischen Vielteilchen-Wechselwirkungen entwickelt. Durch die eingeführten Modifikationen erweitert sich die Anwendbarkeit der $\delta\gamma$ Methode von ungeladenen auf ladungsstabilisierte Kolloide. Eine Alternative zur (modifizierten) $\delta\gamma$ Methode bildet die Näherung der paarweise additiven hydrodynamischen Wechselwirkungen (PA Methode). Unter Verwendung präziser analytischer Lösungen des hydrodynamischen Zweikörper-Mobilitätsproblems sind die Ergebnisse der PA Methode exakt für verdünnte Systeme. Die PA Methode eignet sich daher besonders zur Anwendung auf Suspensionen niedriger Salzkonzentration, mit stark unterdrückter Annäherung der geladenen Teilchen und der damit einhergehenden hydrodynamischen Dreikörper-Wechselwirkungen.

Zusammen mit den in dieser Arbeit diskutierten experimentellen Daten und Computersimulationen erlauben unsere theoretischen Methoden insbesondere Tests der Anwendbarkeit diverser generalisierter Stokes-Einstein (GSE) Relationen zwischen Diffusionsgrößen und Viskosität in konzentrierten Dispersionen. Die (näherungsweise) Gültigkeit einer GSE Relation ist nicht allein in theoretischer Hinsicht interessant. Vielfach ist man interessiert an Suspension deren Menge für mechanisch-rheologische Experimente nicht ausreicht, wie beispielsweise Lösungen aufwendig isolierter, biologisch relevanter Makromoleküle. Für solche Systeme erlaubt eine gültige GSE Relation die indirekte Bestimmung rheologischer Eigenschaften aus dynamischen Streuexperimenten. Unsere Tests zeigen jedoch, dass selbst diejenigen GSE Relationen, welche für neutrale Kolloide näherungsweise erfüllt sind, im Fall geladener Kolloide stark verletzt sind.

Summary

This thesis comprises a theoretical description of the microstructure, diffusion and rheological properties of dispersions of charged Brownian particles. We have developed, and thoroughly tested, various analytical theoretical methods to calculate static and dynamic properties, and have applied them to various experimental systems. The common features of these analytic methods are their high levels of accuracy, versatility, and numeric efficiency. We have calculated a large variety of equilibrium and short-time dynamic properties and also some long-time properties, including static structure factors, translational collective and self-diffusion coefficients, hydrodynamic functions, and static and high-frequency shear viscosities.

Suspensions of synthetic silica spheres, moderately aspheric bovine serum albumin proteins, and thin gibbsite platelets have been examined in collaboration with experimental groups in Jülich, Tübingen, Utrecht (Netherlands) and Košice (Slovakia). (Dynamic) Light- and X-ray scattering data, and shear viscosities for these systems have been calculated for concentrations up to the liquid-solid or liquid-liquid crystal phase transition point, allowing for a detailed characterization of the suspended particles. In comprehensive parameter studies, we have validated our analytic methods of calculating equilibrium pair-correlations and (short-time) dynamics against numerous computer simulation results. The computer simulations were conducted by Prof. Banchio (Uni. Córdoba, Argentina), in the course of an extended collaboration.

A model of monodisperse, charged Brownian spheres, suspended in a structureless fluid, and interacting via a screened Coulomb potential, serves as the basis of our analytic schemes. The salt content of the suspension affects the range of electrostatic repulsion, which can cause pronounced pair correlations in low-salinity systems at very low colloid concentrations. An important advancement of this thesis is the development of a new analytic integral equation scheme, named Modified Penetrating Background corrected Rescaled Mean Spherical Approximation, which allows for fast and accurate calculation of static pair correlations. The pair correlation functions computed by this method serve as input for various analytic methods of calculating diffusion properties, and static and high-frequency shear viscosities of charge-stabilized suspensions.

A severe complication in computing dynamic properties arises from the necessary inclusion of long-ranged, non-pairwise additive hydrodynamic interactions. To this end, we provide cor-

rections for the approximate $\delta\gamma$ scheme by Beenakker and Mazur, a method accounting for hydrodynamic many-body interactions in an approximate way. Our corrections extend the $\delta\gamma$ scheme in its range of applicability from neutral to charge-stabilized colloidal suspensions. As an alternative to the (modified) $\delta\gamma$ scheme, we have analyzed the approximation of pairwise additive hydrodynamic interactions (PA scheme). Employing precise analytic solutions of the hydrodynamic two-body mobility problem, the PA scheme gives results for short-time dynamic properties which are exact for hydrodynamically dilute systems. Hence, the PA scheme applies especially well to low-salinity suspensions of charged particles, where near-contact configurations and the accompanying hydrodynamic three-body interactions are strongly suppressed. To calculate the static viscosity and the long-time self-diffusion coefficient, we have used simplified mode-coupling theory expressions with the inclusion of far-field hydrodynamic contributions.

In conjunction with the experimental and computer simulation data provided by our collaborators, our theoretical methods have allowed us to test the validity of various generalized Stokes-Einstein (GSE) relations between diffusion properties and the static and high-frequency viscosities in dense media. The (approximate) validity of a GSE relation is of interest not only from a theoretical point of view, but has also experimental applications. Colloidal suspensions containing laboriously isolated biomolecules for instance, are often only available in amounts that are too small for mechanical rheological experiments. In these cases, a valid GSE relation can be used to deduce rheological properties indirectly from dynamic scattering experiments. However, our numerous tests on suspensions of charged colloids have revealed manifest violations of all considered GSE relations, including the ones which are approximately valid for neutral colloid suspensions.

CONTENTS

CHAPTER

ONE

Introduction

A widespread diversity of colloidal fluids is ubiquitously present in our every day life. Dairy products, pharmaceuticals, and hygienic and cosmetic agents constitute only a part of the most prominent examples encountered on a regular basis. In industrial applications, large amounts of colloid suspensions are processed in paints, inks, glues, petroleum emulsions, liquid crystals, and other systems. In addition, nearly all bodily fluids have to be considered as complex colloid suspensions. This includes blood and the highly crowded and confined cytoplasm inside the cell, to name only two examples.

The knowledge gained from studying colloidal suspensions is helpful in optimizing industrial and medical procedures, and in understanding biological materials and organisms. For many decades, fundamental physics research has been pushed forward by studying a large variety of colloids that can be synthesized with a virtually unlimited range of particle sizes, compositions, and interactions. Colloidal particles occur in many aggregated states, including highly dilute complex plasmas or dilute suspensions with a colloidal gas-like phase, colloidal fluids, glasses, gels, and crystals. Compared with molecular fluids, where the structure and the dynamic processes are observed on sub-nanometer and sub-nanosecond scales, colloidal features are exposed on much coarser spatial and temporal scales. This allows for studying colloidal systems in great detail by comparatively inexpensive experiments, and for gaining a deeper understanding of phase transitions as well as equilibrium and non-equilibrium phenomena such as diffusion and rheology.

Colloids are defined as solid or fluid particles of sizes ranging from a few nanometers to a few micrometers, suspended in a fluid or gaseous solvent in which they exhibit erratic Brownian motion driven by the thermal bombardment of small solvent molecules [1, 2]. The colloidal size range is bound from below by the requirement that a colloid should be orders of magnitude larger than the solvent molecules. This allows to separate the solvent and colloidal length- and time-scales, and to treat the colloids as an individual phase in a continuous solvent background. The colloidal size range is bound from above by the requirement that the

particle kinetic energy, which is of the order of k_BT, suffices to cause noticeable Brownian motion. Moreover, colloidal particles should be small enough for thermal motion to prevent pronounced sedimentation, driven under gravity by a density mismatch between colloid and solvent.

In the work presented in this thesis, we restrict our studies to solid colloidal particles suspended in a fluid solvent such as water or different types of organic low-molecular weight solvents. The smallest particles studied are globular bovine serum albumin (BSA) proteins, which have a mean linear extension of approximately 7 nm, whereas the largest particles studied are synthetic silica spheres with a mean diameter of 272 nm. As a third experimental system, we have investigated thin gibbsite platelets with a mean disk diameter of 88 nm. Each of the studied systems has been investigated in its fluid phase, in thermodynamic equilibrium. The colloidal volume fractions probed range from the very dilute regime up to the fluid-crystal or fluid-liquid crsytal (for gibbsite) phase transition point.

A common feature of all the systems studied is the dissociation of charged microionic surface groups from the particles into the solvent. The colloidal particles thereby attain charges of equal sign, giving rise to electrostatic repulsion. In the theoretical model applied here, the electrostatic repulsion of non-overlapping particles is described as an exponentially screened Coulomb potential of Derjaguin-Landau-Verwey-Overbeek type [3]. The screening length of the electric repulsion depends on the ionic strength. By adding salt, the total pair-potential can be continuously varied from long-ranged repulsion to a short-ranged hard-core potential describing uncharged, hard spheres.

A suspension of uncharged, monodisperse hard spheres in thermodynamic equilibrium is entirely described by a single control parameter, namely the colloidal volume fraction [4]. For this reason, hard spheres constitute the most simple and most extensively studied model system in theoretical [5–8] and experimental [9, 10] colloid science, and in computer simulation studies that date back to the pioneering simulation work in the 1950's [11–13]. In contrast, the characterization of colloidal fluids with hard-sphere plus screened Coulomb interactions requires at least two independent parameters, namely the coupling and screening constants of the electrostatic pair-potential. If the electrostatic interaction is weak enough to render direct hard-core contact configurations likely, the volume fraction enters as a third independent parameter. The three-dimensional parameter space makes comprehensive parameter studies of charged colloidal suspensions, as presented in this thesis, an elaborate task.

To sample a representative part of parameter space, analytical tools are required that combine high accuracy with fast evaluation. In this work, we have constructed and validated a hierarchy of (partially novel) interrelated analytic schemes. In the first step, the equilibrium pair-correlation functions are computed from the given pair-potential by a newly developed, analytical integral equation scheme [14, 15]. In the second step, the pair-structure functions are used as the only required input for different kinds of analytic schemes that allow for the calculation of diffusion properties and the suspension shear viscosity [16–20].

In computing dynamic properties, a particularly severe difficulty arises from the necessity

of including the indirect hydrodynamic interactions (HIs) that couple the particle motions via the intervening viscous fluid motion [21, 22]. In the systems studied here, HIs are the longest-ranged interactions, decaying asymptotically as the inverse center-to-center distance between two particles. In combination with the non-pairwise additive character of HIs revealed in denser systems, this makes an exact analytic treatment of HIs at larger volume fractions infeasible. A nearly exact account of many-body HIs is only possible in numerically expensive computer simulations [23–26]. In search for fast, analytic methods, one has to resort to an approximate treatment of the HIs. Two such analytic methods, namely the approximation of pairwise additive HIs (PA scheme), and a modified new version of the so-called $\delta\gamma$-expansion method by Beenakker and Mazur [17, 27–29], are discussed in detail in the present work and applied to analyze experimental systems.

It is demonstrated that our modifications of the $\delta\gamma$ scheme extend its applicability from uncharged hard-sphere systems to charged particles with long-ranged electric repulsion. For both kinds of systems, the modified $\delta\gamma$ scheme makes predictions in good agreement with experiments and computer simulations, up to concentrations where the fluid-crystal phase transition in spherical-particle systems takes place.

Both the PA and $\delta\gamma$ schemes are restricted in their application to the colloidal short-time regime, where particles diffuse only distances small compared to their size. For the computation of long-time dynamic properties, such as the static low-shear rate limiting viscosity and the long-time self-diffusion coefficient, we use a simplified mode-coupling theory which includes far-field HIs, and applies approximately to suspensions of moderately correlated spherical particles.

The experiments on the three studied systems, conducted by our experimental collaborators, include static and dynamic light scattering, small angle X-ray scattering, and rheological experiments. The experimentally obtained data contain information on single-particle properties, static pair-correlation functions, and short- and long-time dynamical suspension properties. In comparing the experimental data to predictions by our analytic models, we have succeeded in characterizing the suspended silica spheres, BSA proteins and gibbsite platelets. Most notably, reaching quantitative accuracy in most cases, we have been able to determine particle sizes, and the concentration- and salinity-dependent effective particle charges. In our theoretical treatment of the aspherical BSA proteins and gibbsite platelets, we demonstrate that analytical simplifying effective sphere models with isotropic pair-interactions are useful in explaining the behavior of the measured static and dynamic properties for extended concentration and salinity ranges.

The calculated, simulated, and experimentally measured quantities comprise the particle form factor $P(q)$, static structure factor $S(q)$, mean scattered intensity $I(q)$, radial distribution function $g(r)$, high-frequency viscosity η_∞ and steady-shear viscosity η, rotational diffusion coefficient d_r, and the hydrodynamic function $H(q)$. The hydrodynamic function includes the translational self-diffusion coefficient d_s, the collective diffusion coefficient d_c, and the cage-diffusion coefficient d_{cge} as special cases. Using our analytic methods, we have studied the

behavior of these static and dynamic properties, and their dependence on concentration, salt content, effective charge, and particle size and shape. We have explained all observed trends in terms of intuitive physical pictures involving concepts such as hydrodynamic shielding and concentration-scaling in low-salinity systems.

Comprehensive comparisons with Monte Carlo and accelerated Stokesian Dynamics simulations conducted by our collaborator, Prof. Adolfo J. Banchio (National University of Córdoba, Argentina), have enabled us to assess the accuracy of the analytic methods employed.

The discussed theoretical methods have been implemented into an integrated and user-friendly software package which is very useful both for experimental and theoretical applications.

We have applied our comprehensive experimental and computer simulation results, and our analytic theoretical schemes, to explore the validity ranges of several generalized Stokes-Einstein (GSE) relations between viscosity and diffusion properties in concentrated systems. In particular, we report the first comprehensive test of GSE relations proposed by Kholodenko and Douglas (KD-GSEs) [30]. Our tests cover the full fluid phase regime of charged and uncharged spheres. The KD-GSE relations combine the collective diffusion coefficient with the isothermal osmotic compressibility and the suspension viscosity, and are regularly used in biophysical and soft matter studies [31–34]. A valid GSE relation is interesting both from theoretical and experimental viewpoints, since it can be used to infer rheological properties indirectly from dynamic scattering experiments. This helps to characterize the rheological properties of suspensions that are available only in small amounts, rendering mechanical rheological measurements infeasible. Our tests show that the KD-GSE relations are fulfilled to decent accuracy by uncharged spheres only. Like several other GSE relations studied earlier, the KD-GSE relation is manifestly violated even in very dilute suspensions of charged particles under low-salinity conditions.

The outline of this thesis is as follows:

In Chapter 2, the considered physical systems are introduced, beginning with the one-component macroion fluid model of spheres with screened electrosteric repulsion, on which our theoretical calculations are based. The basic properties of the three experimentally studied systems are then summarized. The systems are: suspensions of silica spheres in a toluene-ethanol mixture; bovine serum albumin proteins in water; and gibbsite platelets in dimethyl sulfoxide. Brief descriptions of the instrumentation used by our experimental collaborators are included.

Chapter 3 presents the theory of equilibrium pair-structure of colloidal fluids. In particular, a detailed derivation of our newly developed Modified Penetrating Background corrected Rescaled Mean Spherical Approximation (MPB-RMSA) for calculating pair-structure functions is presented.

Various analytic schemes for the short- and long-time dynamic properties of colloidal fluids

are presented in Chapter 4, including our new improved version of the $\delta\gamma$-expansion method by Beenakker and Mazur.

Chapter 5 starts with a comprehensive test of the accuracy of the MPB-RMSA in comparison to computer simulation results and more elaborate Rogers-Young integral equation scheme calculations. The validation of the MPB-RMSA is followed by an extensive parameter study of the scaling behavior of pair-structure functions, for parameters representing the full fluid-phase regime of Yukawa-type colloidal particles. Our novel analytic scheme for calculating the static structure factor and radial distribution function is then applied to analyze the equilibrium microstructure of the three considered experimental systems.

In Chapter 6, our analytic schemes for short-time dynamic properties are first validated in comparison with a large body of Stokesian Dynamics computer simulation results. They are then applied to analyze the dynamics of the three experimental systems. Special emphasis is placed on testing several generalized Stokes-Einstein relations between viscosity and diffusion properties in concentrated media, using analytic theory, computer simulations, and experimental data.

Chapter 7 concludes the thesis and discusses future extensions of the presented work.

In Appendix A, analytic expressions for the static structure factor and the radial distribution function in mean spherical approximation (MSA) are given. A comprehensive description of the MPB-RMSA algorithm, based on the MSA expressions in Appendix A, is given in Appendix B. Appendix C lists the mobility expansion coefficients used in our implementation of the PA-scheme for short-time dynamic properties. In Appendix D, it is explained how the numeric coefficients of the $\delta\gamma$-scheme can be computed. A table of coefficients is given, which is sufficient for implementing the $\delta\gamma$-scheme in the form used in this thesis. Finally, in Appendix E, a brief introduction of the capabilities of our integrated software-package for calculation of structure and dynamics of colloidal suspensions is given.

CHAPTER

TWO

Physical Systems

2.1 Model system: One-component fluid of monodisperse macroions

Charge-stabilized systems of spherical Brownian particles form a particularly important class of soft matter systems, ubiquitously encountered in chemical industry, food science and biology [22, 35–42]. Moreover, Brownian spheres can serve as a reference system for more complex, non-spherical particles, by selecting an appropriate effective sphere radius. The range of particle sizes extends from large, micron-sized colloids [2, 39, 43] down to nanometer-sized micelles [44, 45], proteins [18, 41, 46], and DNA fragments [47].

Our calculations of the equilibrium microstructure, and short- and long-time dynamic properties of colloidal suspensions, are based on the one-component macroion fluid (OMF) model, which describes the colloidal particles as uniformly charged, monodisperse spheres with stick hydrodynamic boundary conditions, immersed in a structureless Newtonian fluid. In an overall neutral suspension, the Coulomb repulsion between colloidal spheres is screened by the diffuse part of an electric double layer consisting of microions, including the counterions released from the colloid surfaces, and additional ionic species originating, *e.g.*, from dissolved salt.

A well-established model for the pair-interaction potential of charged spherical colloids is the Derjaguin-Landau-Verwey-Overbeek (DLVO) potential [3],

$$u_{\mathrm{DLVO}}(x) = u_{\mathrm{vdW}}(x) + u_{\mathrm{HC}}(x) + u_{\mathrm{el}}(x), \tag{2.1}$$

consisting of the van der Waals attractive pair energy part,

$$\beta u_{\mathrm{vdW}}(x) = \begin{cases} 0, & x < 1+\Delta \\ \dfrac{-A_H}{12}\left[\dfrac{1}{x^2-1}+\dfrac{1}{x^2}+2\ln\left(1-\dfrac{1}{x^2}\right)\right], & x > 1+\Delta, \end{cases} \tag{2.2}$$

the hard-core potential,

$$u_{\mathrm{HC}}(x) = \begin{cases} \infty, & x < 1+\Delta \\ 0, & x > 1+\Delta, \end{cases} \tag{2.3}$$

that forbids the overlap of colloidal spheres, and the screened electrostatic repulsion part

$$\beta u_{\mathrm{el}}(x) = \begin{cases} 0, & x < 1 \\ \gamma \dfrac{e^{-kx}}{x}, & x > 1. \end{cases} \tag{2.4}$$

Here, $x = r/\sigma$ is the separation of the centers of colloids, measured in units of the diameter σ. All potentials are expressed in units of the thermal energy $k_B T = 1/\beta$, with absolute temperature T and Boltzmann's constant k_B. If the cutoff distance Δ were selected equal to zero, the van der Waals interaction potential with Hamaker constant $A_{\mathrm{H}} \sim 1$, and $-A_{\mathrm{H}}/[24(x-1)]$ for $x \approx 1$, would unphysically diverge at contact, leading to a divergence of the second virial coefficient $B_2(T)$. This artificial divergence arises from neglecting the Born repulsion between atoms or molecules experiencing electronic orbital overlap. By setting $\Delta \times \sigma \approx 10^{-10}$ m, which is of the order of the microion size, the Born repulsion is approximated by an infinite potential step.

The electrostatic interaction between two microion-dressed colloidal spheres is fully characterized by the coupling parameter $\gamma > 0$ and the screening parameter $k > 0$. The two dimensionless parameters are related to experimentally accessible quantities via

$$\gamma = \frac{L_{\mathrm{B}}}{\sigma}\left(\frac{e^{k/2}}{1+k/2}\right)^2 Z^2, \qquad \text{and} \tag{2.5a}$$

$$k^2 = \frac{L_{\mathrm{B}}/\sigma}{1-\phi}\left(24\phi|Z| + 8\pi n_s \sigma^3\right) = k_{\mathrm{c}}^2 + k_{\mathrm{s}}^2, \tag{2.5b}$$

where $L_{\mathrm{B}} = \beta e^2/\varepsilon$ is the solvent-characteristic Bjerrum length in Gaussian units, ε is the solvent dielectric constant, Z is the colloidal effective charge in units of the proton elementary charge e, n_{s} is the concentration of added monovalent coions originating from a $1-1$ electrolyte, and ϕ is the fraction of the suspension volume occupied by the spherical particles. The volume fraction is related to the number concentration, n, of colloids by $\phi = (\pi/6)n\sigma^3$. The

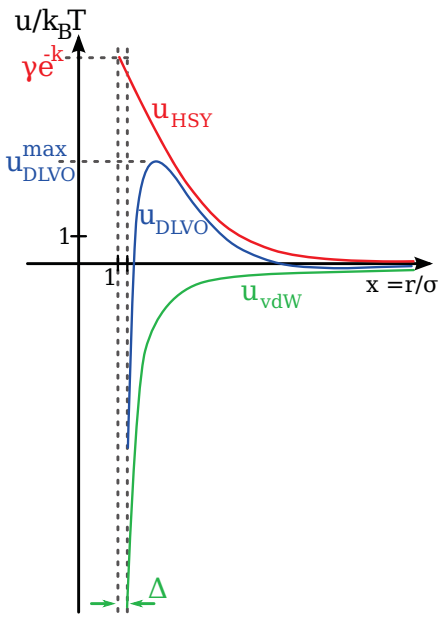

Fig. 2.1: *Sketch of the DLVO pair potential $u_{DLVO}(r)$ in Eq. (2.1), with the attractive van der Waals part $u_{vdW}(r)$ and repulsive part $u_{HSY}(r)$. For a system of high effective charge Z and low coion concentration n_s (high γ and low k), the HSY pair potential $u_{HSY}(r)$ in Eq. (2.6) is a good approximation of the full $u_{DLVO}(r)$. Figure is not to scale.*

factor $(1-\phi)^{-1}$ in (2.5b) corrects, in a non-dilute system, for the free volume accessible to the microions [48, 49].

Note that Eq. (2.5b) is the sum of two contributions: The first contribution, $k_c^2 = 24L_B\phi|Z|/[\sigma(1-\phi)]$, is due to monovalent counterions released from the colloid surfaces. The second contribution, $k_s^2 = 8\pi n_s L_B \sigma^2/(1-\phi)$, is due to all other monovalently assumed microions present in the solvent, denoted as salt ions for simplicity. The total charge of all salt ions is zero. Likewise, the total charge of the surface-released counterions equals the overall charge of the colloids, but differs in sign. In pH-neutral water, there is a lower bound of $n_s \geq 10^{-7}$ M, due to the self-dissociation of water molecules. Additional contributions to n_s arise from dissolved CO_2, added $1-1$ electrolyte such as NaCl, and counterions released from the surfaces of other charged macroionic species such as oligomers and impurities, which are not considered in the present one-component model.

For systems with sufficiently large coupling parameter γ, and sufficiently low screening parameter k, *i.e.* for a large effective charge and low salt concentration, the global maximum of the DLVO potential (the Coulomb barrier $u_{\mathrm{DLVO}}^{\mathrm{max}}$) is large compared to k_BT (c.f. Fig 2.1). In these systems, the particles virtually never overcome the Coulomb barrier and, therefore, the strongly attractive part of the DLVO potential at separations $x \approx 1+\Delta$ is not probed. Whenever $u_{\mathrm{DLVO}}^{\mathrm{max}}$ is substantially larger than k_BT, van der Waals attraction can be neglected,

and the DLVO potential is well approximated by its repulsive parts only, *i.e.*

$$\beta u_{\mathrm{DLVO}}(x) \approx \beta u_{\mathrm{HC}}(x) + \beta u_{\mathrm{el}}(x) = \beta u_{\mathrm{HSY}}(x) = \begin{cases} \infty, & x < 1 \\ \gamma \dfrac{e^{-kx}}{x}, & x > 1. \end{cases} \tag{2.6}$$

Systems described by the repulsive potential in Eq. (2.6) are denoted as hard-sphere Yukawa (HSY) systems. In (2.6) we can skip the cutoff Δ, since it is no longer necessary to remedy an unphysical divergence at contact. It is worthwhile to note in going from Eq. (2.1) to Eq. (2.6), that not only the near-contact part of the pair potential is simplified, but also the long-range asymptotic behavior is altered. At long distances, the DLVO potential is dominated by the van der Waals part proportional to $-x^{-6}$, which gives rise to a secondary minimum in the total DLVO potential [50]. On the other hand, the purely repulsive HSY potential decays exponentially according to $\exp(-kx)/x$ for all non-overlap distances. However, the qualitative change from long-range attraction to long-range repulsion is well justified for strongly charged particles at low salinity since the depth of the secondary DLVO minimum is small compared to k_BT.

Note that by using the HSY pair potential, or more generally the DLVO pair potential, all microions are treated as pointlike and isotropically smeared out on the scale of the colloidal particles. Furthermore, non-Coulombic microion-microion correlations are disregarded, which is not a valid assumption for non-monovalent counterions. Non-pairwise additive colloidal particle interactions, which may play a role at very low salinity, are also neglected. The HSY pair potential has been derived as the potential of mean force in the limit $\phi \to 0$, on basis of the linearized Poisson-Boltzmann theory [3], or likewise using the linear mean-spherical approximation applied to a highly asymmetric ionic mixture treated in the so-called Primitive Model [51–53], on assuming point-like microions and $L_BZ^2/\sigma \ll 1$. For more strongly charged macroions, the DLVO potential can still be used, but Z should be interpreted then as an effective macroion charge number smaller than the bare one, since it has to be corrected for the fraction of surface-condensed counterions. The effective macroion charge Z, in relation to the bare charge, can be estimated, *e.g.* using simplifying mean-field-type cell model [54, 55] or self-consistent jellium model calculations [47, 56, 57]. There are also non-mean field extensions allowing to describe macroion overcharging, and ion-pairing effects in multivalent electrolyte solutions [58]. Due to the approximative nature of all these calculations, different values for Z are obtained in general.

The model system of hard spheres with a Yukawa-type repulsive pair interaction is extensively used not only in colloid science. In a more general context, with differing definitions for γ, k, and σ, the HSY model is used as a reference system for complex plasmas [59], and for a large variety of atomic systems including plasmas, liquid metals [4, 60, 61], and alloys [62, 63]. Part of the present thesis is devoted to applying and testing integral equation schemes and computer simulation tools for computing the equilibrium pair-structure of the colloidal

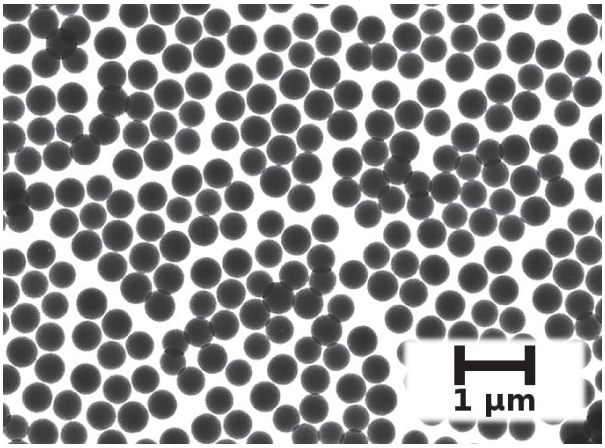

Fig. 2.2: *Transmission electron micrograph picture of silica spheres similar to the ones used in the present study. The spheres depicted here have a mean diameter of* $\sigma = 365$ *nm, and a polydispersity of* 6%*. The silica particles used in the static and dynamic light scattering experiments discussed in this thesis have a diameter* $\sigma = 272$ *nm at* 6% *polydispersity. Image printed with kind permission of Dr. Johan Buitenhuis, Research Centre Jülich.*

HSY fluid. These tools are applicable also to atomic HSY fluids and plasmas, since the equilibrium pair-structure is solely determined by the direct interaction potential. On the other hand, the dynamics of colloidal particles is entirely different from that of plasmas and atomic fluids. While the particles in the latter systems move essentially ballistically, colloidal spheres move in a viscous fluid of mass density similar to their own. In a suitable course-grained time resolution, the dynamics of colloids appears overdamped, and the particles exhibit erratic Brownian motion [21, 64].

2.2 Silica spheres

The static- and dynamic light scattering experiments on silica spheres in a toluene-ethanol mixture, and the characterization of the silica spheres by small angle X-ray scattering, have been performed by our collaborator Dr. Peter Holmqvist at Research Centre Jülich. The light scattering data presented in this thesis have been analyzed in our joint theoretical-experimental project.

Trimethoxysilylpropyl methacrylate (TPM)-coated silica spheres [65] dispersed in an index-matching organic solvent constitute a well-characterized realization of a HSY-like system of nearly monodisperse colloidal particles. Fig. 2.2 is a transmission electron micrograph (TEM) picture of a dried specimen of silica spheres similar to the ones discussed in this thesis. The TEM-determined average diameter of the spheres in Fig. 2.2 is $\sigma = 365$ nm with a relative

size-polydispersity (relative standard deviation) of 6%. A similar mean diameter of $\sigma = 272$ nm, and 6% polydispersity, has been determined for the silica spheres used in the present studies by fitting the form factor recorded in small angle X-ray scattering (SAXS) experiments to the average form factor of homogeneously scattering spheres.

The hydrophobic TPM surface groups on the silica particles allow for their dispersion in a 80:20 toluene-ethanol solvent mixture at $T = 20^o$ C with Bjerrum length $L_B = 8.64$ nm [43]. This organic solvent mixture allows for fine-tuning the salinity without having to worry about self-dissociation of solvent molecules and uncontrolled CO_2 adsorption, problems commonly encountered in aqueous suspensions. Moreover, the very similar refractive index of solvent and particles minimizes the influence of the residual van der Waals attraction. The silica spheres with $\sigma = 272$ nm attain a concentration-dependent negative surface charge in the range of $-250 \lesssim Z \lesssim -100$ by the dissociation of protons from the particle surfaces. For a residual salinity smaller than 10^{-6} M, the suspension solidifies at a volume fraction of $\phi_f \approx 0.16$.

Static light scattering (SLS) experiments were conducted using a light scattering set-up by the ALV-Laservertriebsgesellschaft (Langen, Germany), for a series of concentrations from $\phi = 0.057$ to 0.159. The samples have been carefully filtered, and it was checked that there is no noticeable multiple scattering. The scattering data are consequently quite reliable, and of remarkably little noise even in the small wavenumber regime.

2.3 Bovine serum albumin proteins

The static and dynamic light scattering experiments, the X-ray scattering experiments, and the rheometric measurements of aqueous solutions of bovine serum albumin have been conducted by the experimental co-authors of Ref. [18], from the University of Tübingen, the Slovak Academy of Sciences, the P. J. Šafárik University in Košice, Slovakia, the Institut Laue-Langevin, and from the European Synchrotron Radiation Facility in Grenoble, France. The data presented in this thesis have been jointly analyzed in our theoretical-experimental project.

A quantitative understanding of the dynamics in concentrated solutions of interacting proteins is of importance to the evaluation of cellular functions, and the improvement of drug delivery. Diffusion mechanisms such as collective and self-diffusion, and rheological properties such as the static and high-frequency shear viscosities, are strongly affected by the aqueous environment [66], and in particular by crowding effects due to a high concentration of macromolecules. The particles are coupled both by direct and solvent-mediated, hydrodynamic interactions (HIs) [67–69]. The latter type of indirect interaction, which is both long-ranged and of many-body nature, poses a particularly challenging task to the theoretical treatment of diffusion and rheological transport properties.

Here, we report on a combined experimental and theoretical study on collective diffusion,

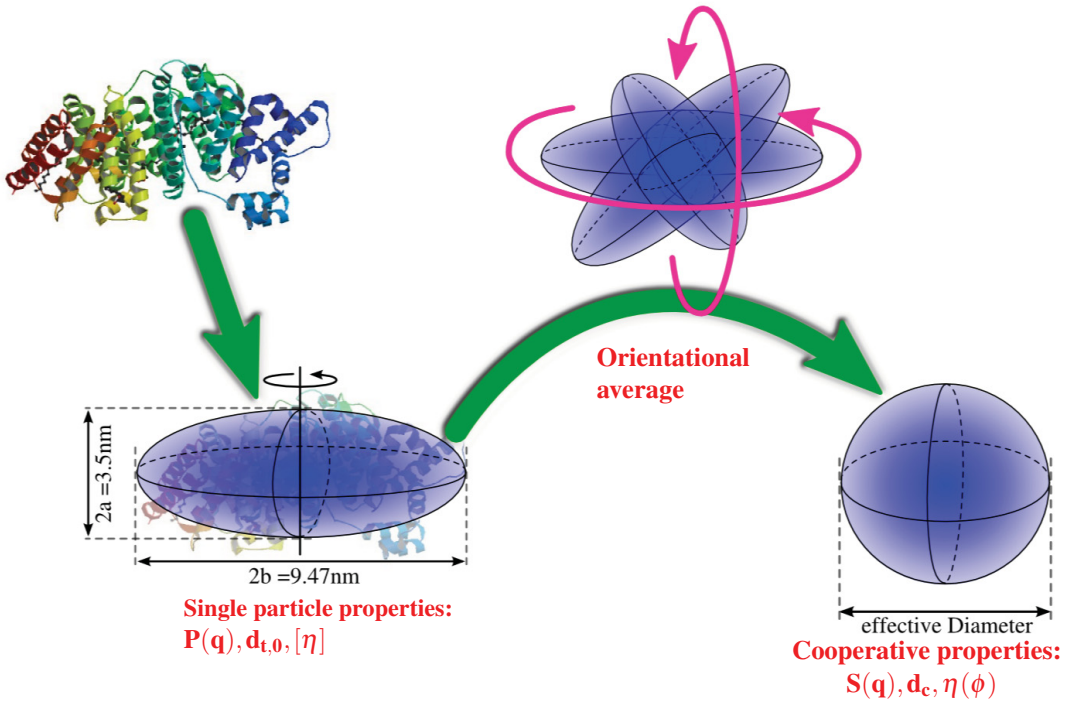

Fig. 2.3: *Illustration of the spheroid-Yukawa model for serum albumin proteins. Secondary structure image of human serum albumin protein (top, left) taken from entry 1E7I of the RCSB Protein Data Bank [70], as created by the authors of Ref. [71].*

low shear-rate static viscosity, and static and dynamic scattering functions of concentrated solutions of bovine serum albumin (BSA) proteins. The goal of our study is twofold. On the one hand, we explore how far a simple colloidal model in combination with state-of-the-art theoretical schemes can capture the microstructure and dynamics of proteins in solution. On the other hand, we investigate the concentration- and salt-dependence of collective diffusion and the static shear viscosity, and use our results to test the validity range of a generalized Stokes-Einstein (GSE) relation which combines the collective diffusion coefficient with the isothermal osmotic compressibility and the shear viscosity.

BSA is a globular protein which is readily soluble in water and stable over a wide range of salt and protein concentrations. Its stability and reproducibility make it well-suited as a model system of globular proteins. Proteins constitute identical solute units surpassing any synthetic colloid suspension in terms of monodispersity. In this respect, they are ideally suited to the application of analytical theoretical models used with good success for large colloids. However, the construction of a quantitatively accurate theoretical model for protein solutions is considerably obstructed not only by the potential presence of impurities and oligomers, but also by the complex internal conformation and surface of a protein. The folding state depends on various control parameters such as temperature, protein concentration, pH value, and salinity. The irregular protein surface implies an orientation-dependent protein interaction energy with repulsive and attractive parts, and furthermore complicates the description of hydroynamically influenced transport properties.

In a first step towards calculating dynamic properties of proteins, it is advisable to use a model of reduced complexity, with system parameters such as the pH-dependent particle charge determined from a consistent fit of theoretical expressions for the scattered intensity to the experimental static scattering functions. We use here a simple colloid model where the BSA interactions are described by the isotropic HSY pair-potential in Eq. (2.6). The effect of the non-spherical shape of BSA proteins is accounted for in the static intensity calculations within the so-called translational-orientational decoupling approximation, by describing the proteins as oblate spheroids interacting by a spherically symmetric effective pair potential. Fig. 2.3 illustrates the simplified model of BSA used in the present study. Note that the protein displayed in Fig. 2.3 is not BSA but human serum albumin (HSA), whose shape and size is expected to be similar to the one of BSA [72–74], and for which structural data from crystallographic and nuclear magnetic resonance spectroscopy studies are more readily available.

2.3.1 Sample preparation

BSA is a globular protein with a mean linear extension of about 7 nm. The considered aqueous solutions of BSA with no added salt, and with monovalent added salt such as NaCl, have a pH in between 5.5 and 7. Under these conditions, BSA is stable in solution, folded in its native state, and carrying a negative net charge in the range of roughly 8 to 20 elementary charge

units (see Section 5.4 for details) [75, 76]. BSA was purchased from Sigma (cat. A3059) as a lyophilized powder, certified globulin- and protease free.

The sample preparation for all experimental techniques started with the dissolution of protein powder in a solvent, and subsequent waiting until the solution was homogenized. The protein mass concentration, c_p , in the solution volume given by $V_{H_2O} + m_p \cdot \theta$, is determined by the BSA weight m_p via

$$c_p = \frac{m_p}{V_{H_2O} + m_p \cdot \theta} \quad , \tag{2.7}$$

where the specific protein volume $\theta = 0.74$ ml/g [77] determines the self-volume of proteins upon dissolution.

For small-angle X-ray scattering, deionized and degased water was used as solvent. The samples with concentrations higher than 15 mg/ml were prepared directly, while smaller concentrations were prepared from a stock solution of 18 mg/ml. The samples were filled into a plastic syringe and inserted into the capillary during the measurement.

For the viscosity measurements, the solutions were prepared similarly using as solvent both deionized water, and solutions of NaCl in deionized water. The NaCl molarity is calculated from the total solution volume, including the protein self-volume. All solutions used for the viscosity experiments were further degased by a water-jet air-pump.

For our light scattering experiments, stock solutions of BSA proteins in deionized water were mixed with solutions of NaCl in deionized water according to the required concentration. The NaCl molarity is calculated from the total water volume. Then, every sample was pressed with a plastic syringe through a hydrophilized nylon membrane filter with a pore size of 100 nm (Whatman Puradisc 13), and transferred into a cylindrical glass scattering cell. The cell was sealed immediately with a plastic cap.

The effect of the difference in NaCl concentrations between light scattering and viscosity samples, arising from the slightly differing sample preparation, is negligibly small.

2.3.2 Static and dynamic light scattering

Multi-angle DLS experiments were performed at various concentrations of protein and added salt, at a temperature of $T = 295$ K. In particular, the BSA mass concentration, c_p, was chosen between 0.1 to 150 mg/ml, and the concentration of added salt was 0 (no added salt), 5×10^{-3}, 0.15 and 0.5 M. Note that even in the zero added-salt case, the analysis of the scattering data discussed in Sec. 5.4 reveals a residual electrolyte concentration of a few mM, which scales roughly linearly with c_p (see Tab. 5.1). This suggests a few possible sources of the residual electrolyte ions. First, a possible source could be the surface-released counterions of charged BSA oligomers, not contained in our monodisperse model. Second, a salt contamination of the BSA stock, and third, the dissociation of acidic or alkaline surface groups off the BSA proteins cannot be excluded.

SLS experiments were performed on the same samples. We used a combined SLS/DLS

device from ALV (goniometer: CGS3, correlator: 7004/FAST), located at the Institut Laue Langevin in Grenoble, with a minimum correlation time of 3.125 ns as initial and shortest time. The HeNe laser was operating at wavelength $\lambda_0 = 632.8$ nm, with an output power of 22 mW. The accessible range for the scattering angle (wavenumber) was 30 - 150° (q = 0.007 - 0.026 nm^{-1}). Moreover, the DLS intensity autocorrelation function decays on a time scale much slower than the interaction time, $\tau_I \sim \sigma^2_{d_{t,0}}/(4d_{t,0}) \sim 0.3$ μs, of BSA, where $\sigma_{d_{t,0}}$ is an effective hydrodynamic diameter (see Sections 4.1 and 5.4.2 for a discussion of colloidal timescales and effective sphere diameters for BSA). Hence, DLS probes the long-time collective diffusion of BSA, in the $q \to 0$ limit.

The normalized intensity autocorrelation function (IACF) obtained from DLS,

$$g_2(q,t) = \frac{\langle I(\mathbf{q},0)I(\mathbf{q},t)\rangle}{\langle I(\mathbf{q})\rangle^2},$$

was fitted, according to the Siegert relation, by the double exponential decay function

$$g_2(q,t) - 1 = \left(\sum_{i=1,2} A_i \cdot \exp\left[-D_i q^2 t\right] \right)^2 + \mathrm{B}, \tag{2.8}$$

with decay constants D_1 and D_2, and amplitudes A_1 and A_2. The fit results were essentially the same with and without the background-correction constant B. At all probed angles, the two decay constants are widely separated ($D_1 \gg D_2$). The faster mode coefficient, D_1, is attributed to the (long-time) collective diffusion coefficient, d_c^L, of BSA monomers. The appearance of the slower mode characterized by D_2, can be attributed to the slow motion of the larger impurities and oligomers. After having checked that D_1 is overall q-independent within the experimental resolution, it was averaged with respect to its residual scattering angle fluctuations to gain better statistics. Data on D_2 are rather noisy in comparison to D_1, and show no clear dependence on q, c_p, and on the concentration of added salt.

2.3.3 Small-angle X-ray scattering

Aqueous solutions of BSA with mass concentrations in between 0.9 mg/ml and 270 mg/ml, and without added salt, were measured by SAXS, at the beam line ID02 of the European Synchrotron Radiation Facility (ESRF) in Grenoble, France. The standard configuration at a 2m sample-to-detector distance, and a photon energy of 16051 eV was used. Measurements were repeated several times in the flow mode and with short detection times to ensure the absence of radiation damage. The data from the CCD were processed with the standard routines available at the beam line for radially averaging the data and correcting for transmission. Repeated measurements were summed up, and the solvent scattering was measured independently and subtracted from the data. Additionally, two dilute samples (at $c_p = 1$ and 2 mg/ml), with 0.15 M of added NaCl, were measured for form factor fitting.

2.3.4 Static viscosity measurements

The viscosity data were measured at $T = 25^\circ$ C, for different concentrations of protein and added salt. The first dataset was obtained for solutions without added salt, while the second set describes systems with 0.15 M NaCl. All measurements were performed at a shear rate of 60 Hz $\ll 1/\tau_I$, using the suspended couette-type viscometer described in Ref. [78]. The important advantage of this instrument is the possibility to collect data without errors caused by the surface shear-viscosity. A test made for $c_p \approx 20$ mg/ml and 100 mg/ml, without salt and for 2M added NaCl, revealed no shear-rate dependence of the viscosity for shear rates between 50 and 95 Hz. The precision of the viscosity measurements is approximately 0.1%. In order to minimize systematic errors, every measurement was repeated three times, including separate sample preparations.

The viscometer directly measures the relative shear-viscosity of the solution against pure water (for technical details see Ref. [78]). For the aqueous BSA solutions without added salt discussed in this work, the relative viscosity was directly measured. For BSA solutions with added salt, this quantity was obtained as the ratio of the following two values: (a) the directly measured relative viscosity of the BSA solution with salt against water divided by (b) the directly measured relative viscosity of the salt solution (without BSA) against water.

2.4 Gibbsite platelets

The static- and dynamic light scattering experiments on gibbsite platelets in dimethyl sulfoxide (DMSO), and the characterization of the gibbsite particles' size and shape by TEM and atomic force microscopy (AFM) have been done by Dr. Dzina Kleshchanok from Utrecht University (The Netherlands), and Dr. Peter Holmqvist from Research Centre Jülich. The data presented in this thesis have been analyzed in our theoretical-experimental project.

Colloidal platelets are abundant in nature (*e.g.*, as clay minerals or red blood cells) and can be readily synthesized in the laboratory in form of mixed metal hydroxides, gibbsite, gold platelets, et cetera. The most prominent examples of colloidal platelets are various types of natural clays [79], which figure in sediment transport in rivers, and in the oceans and lakes, and which are responsible for dangerous landslides [80]. Clays are widely used as rheological modifiers for surface coatings, paints, and drilling fluids [81, 82].

The rheological applications of clays are based on their microstructural properties, originating from a highly anisotropic shape and a correspondingly anisotropic particle interaction. As a necessary step towards understanding the more complex behavior of concentrated clay platelet suspensions regarding rheology, sedimentation, and sediment transport, the fundamental dynamic properties in dilute isotropic solutions must be addressed.

So far, most studies on the dynamics of clay and colloidal platelet suspensions have been focused on the non-equilibrium ergodic to non-ergodic transition in dense systems [83–85],

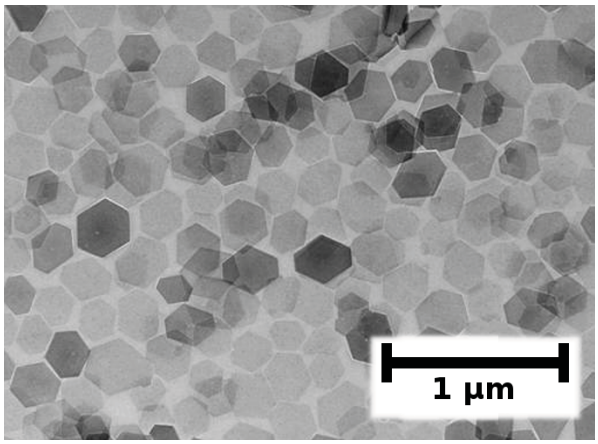

Fig. 2.4: *Transmission electron micrograph picture of gibbsite platelets similar to the ones used in the present study. Image printed with kind permission of Dr. Dzina Kleshchanok, Utrecht University (The Netherlands).*

and on the properties of the non-ergodic state [86, 87]. Only few theoretical and experimental investigations have been made so far on less concentrated, fluid-state isotropic suspensions of clays or colloidal platelets. For instance, both the translational and rotational diffusion coefficients of a single platelet were studied by simulation, and the resulting data for an extended range of aspect ratios were fitted to general polynomial expressions for cylinders by Ortega and García de la Torre [88]. The study in Ref. [88] allows to compare the single-platelet diffusion properties of non interacting platelets with the results of experimental diffusion measurements, but it includes no hint on how diffusion is affected by particle interactions.

The concentration dependence of sedimentation and diffusion coefficients of uncharged, sterically interacting platelets and clays has been explored in [89, 90] by dynamic light scattering and ultracentrifugation. For platelets, the earlier investigations in [89] were made in a rather dilute concentration regime where no effect of particle interactions on diffusion was detected. Moreover, explicit theoretical expressions have been derived for the time-dependent intensity autocorrelation function of noninteracting cylindrical particles such as platelets [21, 89, 91–93] which, in principle, can be used to determine the single-platelet rotational diffusion coefficient from standard dynamic light scattering or X-ray photon correlation spectroscopy (XPCS) measurements in non-interacting particle systems.

For rather dilute systems of uncharged polymer-grafted clay suspensions [90], normalized IACFs have been measured in vertical-vertical (VV) and vertical-horizontal (VH) scattering geometry [94]. Here, VV and VH indicate the orientations of two polarizers in the light scattering setup. The first polarizer is used to linearly polarize the incident beam before it gets scattered from the sample, and the second polarizer (referred to as the analyzer) is placed in the scattered beam. In VH geometry, also referred to as the depolarized dynamic light scattering (DDLS) setup, with the two polarizers crossed, only that part of the scattered light is

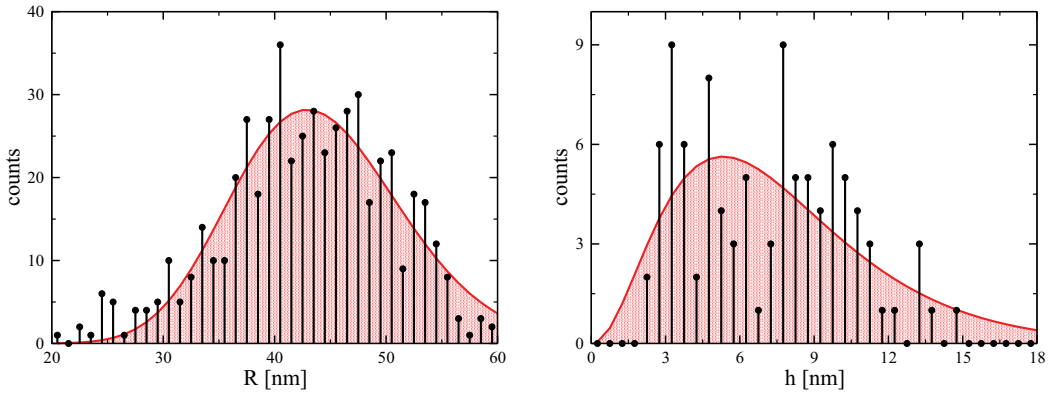

Fig. 2.5: *Size histograms for the radius R (left) and thickness h (right) of the gibbsite platelets used in the present study, determined from TEM and AFM pictures of the dried specimen, respectively. The red shaded areas are best fits by unimodal Schulz-Zimm distributions in Eq. (2.9), multiplied by constant prefactors. The fitted distributions have mean values* $\langle R \rangle = 44.2$ *nm and* $\langle h \rangle = 7.66$ *nm, and relative standard deviations of* $s_R = 17.3\%$ *and* $s_h = 55.3\%$.

detected that got depolarized in the scattering process. In VV geometry, only that part of light is detected that retains its polarization in the scattering process. If all scattered light conserves its inbound polarization, a VV scattering setup is equivalent to a vertical-unpolarized (VU) setup, where no analyzer is used.

In Ref. [90], a strong slowing of diffusive modes was found both in VH and in VV geometry. In VV geometry, only a single diffusive mode was detected, even though it was argued that a second, cooperative mode should be present due to the osmotic pressure of polymers grafted on the clay particles [90].

In the present study, we explore how the dynamics of charged colloidal gibbsite platelets suspended in DMSO and existing in their isotropic phase, is affected by particle interactions. Using SLS and (D)DLS, we study the effect of the platelet concentration on the measured translational and rotational self-diffusion coefficients, and on the collective diffusion coefficient. Moreover, the concentration- and shear-rate dependence of the static dispersion viscosity is determined experimentally. Our scattering and rheological experiments cover the full isotropic phase concentration-regime up to the isotropic-liquid crystal (I/LC) transition.

2.4.1 Size- and shape-characterization

The gibbsite radius- and thickness histograms depicted in Fig. 2.5 have been obtained from TEM and AFM pictures of the dried specimen, respectively. Both histograms have been fitted

by the unimodal Schulz-Zimm [95, 96] size distribution function

$$P_S(x,\langle x\rangle,t)=\left[\frac{t+1}{\langle x\rangle}\right]^{t+1}\frac{x^t}{\Gamma(t+1)}\exp\left[-\frac{t+1}{\langle x\rangle}x\right],\qquad(t>0),\tag{2.9}$$

multiplied by constant prefactors, as depicted in Fig. 2.5 by the red shaded areas. Analytic expressions are known for all moments of the Schulz-Zimm distribution in Eq. (2.9) [22]. In particular, the mean value of the reduced size variable x is $\langle x\rangle$, and the relative standard deviation, $s_x=\langle x\rangle^{-1}[\langle x^2\rangle-\langle x\rangle^2]^{1/2}$, is given by $[t+1]^{-1/2}$. For large values of $\langle x\rangle$ and low values of s_x, Eq. (2.9) is similar to a Gaussian distribution function (*c.f.*, left panel of Fig. 2.5). When s_x becomes large (*c.f.*, right panel of Fig. 2.5), Eq. (2.9), vanishing for negative values of x, differs clearly from a Gaussian distribution. Our fit of Eq. (2.9) to the experimental radius- and thickness-histograms gives mean values $\langle R\rangle=44.2$ nm and $\langle h\rangle=7.66$ nm, and relative standard deviations of $s_R=17.3\%$ and $s_h=55.3\%$, respectively.

Note here that the histogram of gibbsite platelet radii in the left panel of Fig. 2.5 is well-described by the fitted $P_S(R,\langle R\rangle,t)$, whereas the thickness histogram scatters considerably, with the indication of a bimodal distribution with the two centers at $h\approx 4$ nm and $h\approx 9$ nm. For the distribution of the gibbsite platelet thickness, $P_S(h,\langle h\rangle,t)$ is therefore only an analytic first approximation. However, as we have checked, the mean aspect ratio, $p=\langle h\rangle/(2\langle R\rangle)=0.087$, of gibbsite platelets is so small that the ultrathin disk limit ($h\to 0$) can be applied to reasonable accuracy for all the static and dynamic properties of gibbsite studied in the present thesis. Therefore, the details of the thickness distribution are of minor importance, and our usage of a unimodal Schulz-Zimm distribution is justified. Moreover, despite the large thickness polydispersity of $s_h=55.3\%$, the gibbsite platelets studied here can be regarded as approximately monodisperse. The reason for this is the rather small polydispersity of $s_R=17.3\%$ in the platelet radius.

2.4.2 Static and dynamic light scattering

DMSO is a polar, aprotic, and low-viscous solvent of dielectric constant $\varepsilon=47.2$ at $T=293K$ and viscosity $\eta_0=2\times10^{-3}$ Pa·s, in which the platelets are charge-stabilized, forming a suspension that remains transparent up to the isotropic-liquid crystal (I/LC) transition. Different from aqueous gibbsite suspensions, which are turbid already at low concentrations, gibbsite in DMSO systems are transparent and show no multiple scattering in the investigated concentration range. Moreover, there is no residual CO_2 contamination such as in water, and no solvent self-dissociation, so that systems with low ionic strengths can be easily prepared. Thus, we can use (D)DLS to study the rotational and translational diffusion as a function of the gibbsite number concentration up to the I/LC transition point. Our standard (D)DLS/SLS apparatus is equipped with a krypton ion laser of wavelength $\lambda_0=647$ nm as a light source, and a $\lambda/2$ plate used as polarizer and analyzer (Bernhard Halle Nachfl., Berlin, Germany). Each sample was

measured both in vertical-unpolarized (VU) and vertical-horizontal (VH) scattering geometry, for values of the wave number, q, smaller than the value, q_m, where the primary peak of the mean scattered intensity, $I(q)$, occurs. DLS data were recorded for a large number of gibbsite volume fractions $\phi = M/(\rho_m V)$ up to the I/Lc transition occurring at $\phi_{\mathrm{I/Lc}} \approx 8\%$. Here, M is the total mass of added gibbsite of known mass density ρ_m, and V is the suspension volume. Using the same apparatus as for the DLS measurements, we have measured the static mean scattered intensity, $I(q)$, by SLS.

2.4.3 Viscosity measurements

To obtain the low shear-rate static viscosity of gibbsite suspended in DMSO, using an ArG2 rheometer from Ares, the viscosity was measured for various platelet volume fractions, ranging from 1.45 to 7.6 vol%. The results are presented and discussed in Section 6.4.

CHAPTER

THREE

Theory of pair-structure

In this chapter, various analytical schemes are introduced, each of which allows to compute approximately the static pair-correlation functions in a fluid of monodisperse spheres interacting by the HSY pair potential in Eq. (2.6). Special emphasis is laid on the description of our newly developed, analytically solvable and highly accurate MPB-RMSA integral equation scheme [14, 15], and its predecessors PB-RMSA [97], RMSA [98], and MSA [4] (the four acronyms are defined in due course) upon which this new scheme is based. For comparison, two routinely used, non-analytic integral equation schemes are discussed, namely the hypernetted chain (HNC) [99] and Rogers-Young (RY) [100] schemes.

Before all these integral equation schemes are discussed in Sections 3.3 and 3.4, two brief introductions are in place, concerning the definitions of the computed pair-structure functions given in Section 3.1, and the underlying Ornstein-Zernike equation in Section 3.2.

3.1 Pair-structure functions

In thermodynamic equilibrium, the probability density function for N particles to assume the center-of-mass positions $\mathbf{r}^N = (\mathbf{r}_1, \mathbf{r}_2, \ldots \mathbf{r}_N)$ in a volume V at temperature T, is given by

$$P_N(\mathbf{r}^N) = \frac{e^{-\beta U(\mathbf{r}^N)}}{\int\limits_{V^N} d\mathbf{r}^N e^{-\beta U(\mathbf{r}^N)}}. \tag{3.1}$$

Here, $U(\mathbf{r}^N)$ is the potential energy of the N particles. For a homogeneous and isotropic system, where $P_N(\mathbf{r}_1, \ldots \mathbf{r}_N) = P_N(\mathbf{r}_1 + \mathbf{t}, \ldots \mathbf{r}_N + \mathbf{t})$ for an arbitrary displacement vector $\mathbf{t}$, the

radial distribution function (rdf) is [4]defined as

$$g(r) = \lim_{\infty} \frac{N(N-1)}{n^2} \int_{V^{N-2}} d\mathbf{r}_3 \cdots d\mathbf{r}_N P_N(\mathbf{r}^N), \tag{3.2}$$

where $\lim_\infty$ denotes the thermodynamic limit $N \to \infty$ and $V \to \infty$, with $n = N/V$ fixed, characterizing a macroscopic system. In the present thesis, only such model systems are considered for which the total potential energy can be written as $U(\mathbf{r}^N) = 1/2 \sum_{l,j=1,l\neq j}^{N} u(|\mathbf{r}_l - \mathbf{r}_j|)$*i.e.* as the pairwise additive sum of an external potential u_{ext} and an isotropic pair-interaction potential $u(r)$.

The positive-valued function $g(r)$ quantifies the conditional probability in an isotropic system of finding a particle a distance r from a given one. In a fluid system of particles with hard-core diameter σ, $g(r \gg \sigma) \approx 1$, and $g(r \leq \sigma) = 0$. Additional generic properties of $g(r)$ can be derived from its definition [4]. The rdf is intimately related to the scattering wavenumber-dependent static structure factor,

$$S(q) = \lim_{\infty} \left\langle \frac{1}{N} \sum_{l,j=1}^{N} e^{i\mathbf{q}\cdot(\mathbf{r}_l - \mathbf{r}_j)} \right\rangle \geq 0, \tag{3.3}$$

which, in a static scattering experiment on an ergodic system, is proportional to the scattered intensity $I(q)$ divided by its value at infinite dilution. The bracket $< \ldots >$ in Eq. (3.3) denotes an equilibrium ensemble average. It can be shown [4], that

$$g(r) = 1 + \frac{1}{2\pi^2 nr} \int_0^\infty dq\, q \sin(qr) \left[S(q) - 1\right], \tag{3.4}$$

and

$$S(q) = 1 + \frac{4\pi n}{q} \int_0^\infty dr\, r \sin(qr) \left[g(r) - 1\right]. \tag{3.5}$$

In very dilute suspensions [4],

$$g(r) = g_0(r) + \mathcal{O}(\phi), \qquad \text{with} \qquad g_0(r) = e^{-\beta u(r)}. \tag{3.6}$$

Insertion of Eq. (3.6) into Eq. (3.5) gives the structure factor to first order in the volume fraction, according to

$$\begin{aligned} S(y) &= S_1(y) + \mathcal{O}(\phi^2), \\ S_1(y) &= 1 + 24\phi \int_0^\infty dx x^2 \left[e^{-\beta u(x)} - 1\right] \frac{\sin(xy)}{xy}. \end{aligned} \tag{3.7}$$

Here, $y = q\sigma$, and we adhere to the standard physics convention of using the same function

names for g and S when expressed in differing units, with the employed units identified by the argument variable. This convention is used also for all other functions.

3.2 Ornstein-Zernike equation

The one-component Ornstein-Zernike (OZ) equation,

$$h(x) = c(x) + \frac{6\phi}{\pi} \int d\mathbf{x}' \, c(x') \, h(|\mathbf{x} - \mathbf{x}'|), \tag{3.8}$$

for a homogeneous and isotropic fluid system has been originally introduced by Ornstein and Zernike around 1914 [101]. In Eq. (3.8), $\mathbf{x} = \mathbf{r}/\sigma$ and $\mathbf{x}' = \mathbf{r}'/\sigma$. The OZ equation relates the total correlation function, $h(r) = g(r) - 1$, to the direct correlation function $c(r)$. With the exception of limiting cases like, *e.g.* $c(r) = -\beta u(r)$ for $r \to \infty$ and $c(r) + 1 = \exp\{-\beta u(r)\}$ for $n \to 0$, that can be derived using (3.8) [4], the general form of the direct correlation function is not known in analytical closed form. Eq. (3.8) can be viewed alternatively as the definition of $c(r)$ in terms of $g(r)$.

However, the OZ equation is commonly employed as a tool to calculate $g(r)$ (or equivalently $S(q)$) from a given potential $u(r)$ in combination with an (approximate) closure relations for c as a functional of h and u. A general closure relation that applies to a good approximation for arbitrary $u(r)$ is not known. Instead, a variety of closures have been proposed, each of which is specially adapted to a certain class of pair potentials. Closures that apply decently well to the HSY pair potential in Eq. (2.6) are discussed in Sections 3.3 and 3.4.

Before embarking on different closures, we first use Eq. (3.8) to infer a general property for an important class of HSY fluids. For highly charged colloids at low salinity, where contact configurations are extremely unlikely, the hard-core part of the HSY potential is irrelevant. These systems have in common a practically zero contact value, $g(x = 1^+) \approx 0$, of the rdf. All these systems share the geometrical mean particle distance, $\tilde{d} = n^{-1/3}$, as their natural characteristic length unit. In terms of this length unit,

$$\beta u(\tilde{x} > \sigma/\tilde{d}) = \tilde{\gamma} \exp\{-\tilde{k}\tilde{x}\}, \tag{3.9}$$

with $\tilde{x} = r/\tilde{d}$ and reduced potential parameters $\tilde{\gamma} = \gamma\sigma/\tilde{d}$ and $\tilde{k} = k\tilde{d}/\sigma$. Since the hard core is of no physical relevance for these systems, the Yukawa potential in Eq. (3.9) can be extrapolated to $\tilde{x} = 0$ without affecting the microstructure. Thus,

$$h(\tilde{x}) = c(\tilde{x}) + \int d\tilde{\mathbf{x}}' \, h(\tilde{x}') \, c(|\tilde{\mathbf{x}} - \tilde{\mathbf{x}}'|), \tag{3.10}$$

where the volume fraction ϕ has dropped out. We see here that the class of HSY systems with practically zero contact value of the rdf are fully characterized by the two dimensionless parameters $\tilde{\gamma}$ and $\tilde{k}$. On the other hand, four dimensionless parameter groups which are

experimentally controllable to some extent, namely $\{L_B/\sigma, Z, n_s\sigma^3, \phi\}$, enter into the DLVO potential. Thus, different combinations of these four parameters sharing the same $(\tilde{\gamma}, \tilde{k})$ values have identical pair functions $S(\tilde{y})$ and $g(\tilde{x})$, under the proviso that the corresponding systems fall into the $g(x = 1^+) \approx 0$ class. The phase diagram of these effectively point-like Yukawa particles with masked hard-core interactions is quite simple, with a single fluid phase that can freeze into a fcc or bcc solid. The diagram has a single triple point but no critical point since the potential is purely repulsive [102–106]. A recent discussion of the critical point in hard-sphere plus attractive Yukawa-tail fluids is given in Ref. [107].

In Section 5.2, we apply our newly developed MPB-RMSA closure to compute the generic properties of $S(\tilde{y})$ and $g(\tilde{x})$ for point-Yukawa-like particles in the full fluid phase. Here, a peculiarity of the MPB-RMSA must be taken into account. The MPB-RMSA is build on two rescaling expressions for the parameters γ and k, leading to an enhanced accuracy of the method as compared to its predecessors, the RMSA and the PB-RMSA. In these two rescaling rules, the volume fraction ϕ enters explicitly. Therefore, even in the point-Yukawa like phase with $g(x = 1^+) = 0$, the MPB-RMSA-computed functions $S(\tilde{y})$ and $g(\tilde{x})$ depend on the three parameters $(\tilde{\gamma}, \tilde{k}, \phi)$. It is nevertheless possible to explore the boundaries of the point-like Yukawa phase using the MPB-RMSA, since the method reduces to the PB-RMSA in the dilute limit, and the rescaling rules used in the latter scheme are not explicitly ϕ-dependent.

The extended phase diagram including HSY systems with $g(x = 1^+) > 0$, *i.e.* systems where the rdf is discontinuous at contact distance, is somewhat more complicated than the phase diagram of point-Yukawa like particles, showing an additional fluid-fcc-bcc triple point [108, 109]. Systems where the hard core matters are characterized by three dimensionless parameters, namely by (γ, k, ϕ), with σ as the natural length unit. Here, systems of equal (γ, k, ϕ) share the same $S(y)$ and $g(x)$.

3.3 From the MSA to the MPB-RMSA closure relation

Only a single analytically solvable closure relation for the OZ equation is known to date, for the general case of a HSY pair-potential in the form of Eq. (2.6), at arbitrary volume fraction ϕ. In this so-called Mean Spherical Approximation (MSA) , the direct correlation function is approximated, for all non-overlap radii $x > 1$, by its asymptotic form $c(x) = -\beta u(x)$. While allowing for an analytic solution, the MSA has some undesired consequences. The main drawback is the unphysical prediction of negative values of $g(r)$ for pair potentials describing regions of strong, but finite repulsion such as, *e.g.*, the HSY potential in Eq. (2.6).

Certain rescaled versions of the MSA have been published in the past, all of which essentially conserve the analytic simplicity of the MSA, while increasing its accuracy to an eventually quantitative level. These rescaled version are based on the work by Gillan [110] and Hansen and Hayter [98], who introduced a semi-analytic rescaling rule for the hard-core diameter σ which should be used in the HSY potential in Eq. (2.6) when the MSA is employed.

In this so-called Rescaled Mean Spherical Approximation (RMSA), the prediction of unphysical negative values of the rdf is eliminated. The size-rescaling in RMSA is well-justified by the universality of all HSY-systems sharing the same long-ranged Yukawa tail, and with exceedingly unlikely hard-core contact configurations. Qualitative agreement is observed between the RMSA-calculated pair-structure functions $S(q)$ and $g(r)$, and highly accurate reference solutions obtained from Monte Carlo (MC) computer simulations. However, quantitative accuracy is missing in the RMSA, which is known to underestimate the height of the primary peak, $S(q_m)$, in the static structure factor.

This residual inaccuracy of the RMSA has been reduced in the subsequent work of Snook and Hayter, published in the year 1992 [97], which unfortunately, remained largely unnoticed. In this so-called Penetrating Background corrected Rescaled Mean Spherical Approximation (PB-RMSA) , both the coupling parameter γ and the screening parameter k of the HSY potential are altered using arguments based on an assumed, homogeneous, and hard-core penetrating microionic background. Although this penetrating background argument is not rigorous, it leads to a considerable improvement of the predicted pair-structure functions in comparison to the RMSA. In many cases, an almost quantitative agreement of the PB-RMSA calculated structure factor is observed in comparisons with MC simulation results. However, a remnant slight underestimation of $S(q_m)$ is still detected in the PB-RMSA result, in particular for highly structured, concentrated suspensions.

The reduction of this remnant underestimation of the pair-structure in PB-RMSA was the objective of work by the present author and collaborators, with results published in Refs. [14, 15]. In our work, we have demonstrated that a slight modification of the rescaling rules for γ and k, in the spirit of the penetrating background assumption, leads to an enhanced accuracy. We refer to this most recent MSA-based scheme as the Modified Penetrating Background corrected Mean Spherical Approximation (MPB-RMSA) . Section 5.1 contains a detailed comparison of pair-structure functions for the HSY model, obtained using MC simulations, our MPB-RMSA scheme, and additional, non-analytic integral equation schemes such as the Rogers-Young scheme [100]. While the peak in the MPB-RMSA rdf is still slightly underestimated in case of concentrated, low-salt suspensions, the MPB-RMSA static structure factor is in nearly perfect agreement with the computationally elaborate MC results, for arbitrary HSY potential parameters and colloid concentrations.

In the following subsections, the details of the MSA, RMSA, PB-RMSA, and MPB-RMSA schemes are discussed in a way that allows interested readers to easily implement the accurate MPB-RMSA scheme.

3.3.1 MSA closure

An important feature of the HSY model is that, in conjunction with the MSA closure relation [4],

$$c(x>1) = -\beta\, u(x)\,, \tag{3.11}$$

and the exact zero-overlap condition $g(x<1)=0$, an analytic solution of the Ornstein-Zernike equation is obtained for $S(q)$. This is a desirable feature since $S(q)$ is the key quantity determined in static scattering experiments. The MSA solution was first derived for general k by Waisman [111], and in the special limit of no screening ($k=0$) also by Palmer and Weeks [61]. The original MSA solution by Waisman includes a rather complex set of algebraic equations from which the unique, physically allowed structure factor must be deduced. The MSA solution was further simplified by Blum and Høye [112], and Cummings and Smith [113, 114]. A particularly simple form of the MSA solution was obtained more recently by Ginoza [115] (see also [63]), invoking a simple quartic algebraic equation from which the physical root is straightforwardly deduced. Many of the published analytic MSA solutions for HSY-like systems contain misprints that may be difficult to detect. Therefore, in Appendix A, we provide the corrected analytic MSA expressions used in our software package described in Appendix E.

While the MSA solution applies well to dense suspensions of more weakly charged macroions such as concentrated systems of charged micelles [44, 45], it is known to fail for the important case of strongly charged colloidal particles under low-volume fraction conditions such as, *e.g.*, suspensions of silica spheres in toluene-ethanol, or polystyrene spheres in water. Due to the non-exact treatment of shorter-ranged correlations in the MSA closure relation, which is only asymptotically exact for long distances, non-physical negative values of $g(x)$ are predicted for low concentrations and strong repulsion near the contact distance $x=1$ of two particles. This follows from the combination of Eq. (3.11) and Eq. (3.8) in the zero-concentration limit. In dilute systems, $g_{\rm MSA}(x>1) = 1-\beta\, u(x) + \mathcal{O}(\phi)$, attaining negative values for distances where $u(x) > k_B T$. Negative values of $g_{\rm MSA}(x)$ are found also when the MSA is applied to highly concentrated systems in the supercooled fluid regime for large values of the coupling parameter γ [116].

The undesired feature of negative rdf values is absent for an attractive Yukawa tail, where $u(x>1) \leq 0$. As shown by Hansen and Hayter [98], the severe deficiency of the MSA of predicting negative rdf values, can be remedied by increasing the hard-sphere diameter, σ, at fixed particle concentration, to a larger value $\sigma' > \sigma$. In performing this hard-core inflation, the Yukawa tail of the pair potential at non-overlap distances must be kept unchanged.

3.3.2 RMSA closure

Hansen and Hayter [98] have provided a simple rescaling prescription which remedies the shortcoming of the MSA solution for strongly repelling particles where the hard core plays no role. In the RMSA, one considers in place of the actual system a system of size-inflated spheres of rescaled hard-core diameter $\sigma' = \sigma/s$, and rescaled volume fraction $\phi' = \phi/s^3$, where the inflation parameter s, with $0 < s \leq 1$, is determined by the Gillan condition $g_{\mathrm{MSA}}(x' = 1^+; \phi') = 0$ for $x' = xs = r/\sigma'$ [110].

From the OZ equation (3.8), we note that the function $\gamma(x) = h(x) - c(x)$ (not to be confused with the HSY coupling parameter γ) is represented as an integral, and hence it is continuous for all $x \geq 0$. Using the zero overlap condition in

$$\begin{aligned} \gamma(x = 1^-) &= \gamma(x = 1^+) \\ \Rightarrow \quad -1 - c_{\mathrm{MSA}}(x = 1^-) &= g_{\mathrm{MSA}}(x = 1^+) - 1 + \beta u(x = 1^+), \end{aligned}$$

in combination with the analytic result for $c_{\mathrm{MSA}}(x)$ in Ref. [113], an analytic expression for

$$g_{\mathrm{MSA}}(x = 1^+) = -c_{\mathrm{MSA}}(x = 1^-) - \beta u(x = 1^+) \tag{3.12}$$

is obtained (see Appendix A), allowing for a straightforward determination of s using, *e.g.*, the Newton-Raphson method. In performing the hard-core inflation, the concentration n and the Yukawa tail are left unchanged. This implies that the parameters in Eq. (2.6) must be rescaled with respect to the inflated σ' according to

$$\gamma' = \gamma s \tag{3.13}$$

$$k' = k/s\,. \tag{3.14}$$

The RMSA solution is then given by $g_{\mathrm{RMSA}}(r) = g_{\mathrm{MSA}}(r; \phi', \sigma')$, which by construction is a non-negative function going continuously to zero at $r = \sigma'$. It approximates to reasonable accuracy the rdf of a family of strongly coupled HSY systems of varying particle sizes σ but equal concentration n and Yukawa tail (*i.e.*, equal $\gamma\sigma$ and equal k/σ). Since all members of this family share the same tail $u(r > \sigma')$, they have in particular the same potential value

$$\Gamma_{\mathrm{is}} = \beta u(r = d_{\mathrm{is}})\,, \tag{3.15}$$

at the ion-sphere diameter distance d_{is}, defined by

$$d_{\mathrm{is}} = \left(\frac{6}{\pi n}\right)^{1/3} = \sigma\,\phi^{-1/3} = \sigma'\,\phi'^{-1/3}\,. \tag{3.16}$$

The ion-sphere diameter is used in plasma physics as the characteristic length scale [4]. For

$k \to 0$, $\Gamma_{\rm is}$ reduces to the one component plasma (OCP) coupling constant. For strongly repulsive particles where the RMSA solution applies, the ordering relation $\sigma < \sigma' < d_{\rm is}$ is fulfilled.

The RMSA is widely used to this date as an efficient tool for calculating pair correlation functions, for fitting static scattering data (see, e.g., its implementation in Ref. [117]), and for delivering the static input to theoretical schemes predicting equilibrium and non-equilibrium colloidal transport properties and phase boundaries [23, 116, 118–120]. Note here that an extension of the RMSA to mixtures of hard-sphere Yukawa particles of differing diameters and Yukawa tails has been discussed by Ruiz-Estrada et al. [53].

Similar to a number of other integral equation schemes including the Percus-Yevick (PY) [121] and HNC approximations, the RMSA lacks thermodynamic consistency [4, 100]. Another artifact of the RMSA of minor importance is the kink in $g(r)$ at $r = \sigma'$ caused by the inflation of the diameter. Owing to its simplicity, the RMSA solution has been extensively applied to charged globular colloids and proteins. It tends to underestimate the principal peaks of the exact $g(r)$ and $S(q)$ as obtained in simulation calculations, with larger differences for large effective charges Z (see, *e.g.*, [23, 41, 122]). To obtain quantitative agreement with the simulation-generated peak values $S(q_m)$, the employed coupling parameter γ has to be enlarged above its physical value, for charged colloids usually by increasing the effective charge number in Eq. (2.5a). The so-adjusted RMSA $S(q)$ is overall in quantitative agreement with its simulation counterpart, and the RY scheme result. For the repulsive three-dimensional HSY model, the RY scheme has been shown to be highly accurate.

3.3.3 PB-RMSA closure

The necessity to treat γ as an adjustable parameter in RMSA calculations is rather unsatisfactory, in particular when accurate values of the effective charge number are searched for. To improve the RMSA, Snook and Hayter [97] have proposed a reinterpretation of the coupling and screening parameter based on a penetrating microion background (PB) correction argument. The PB-RMSA scheme by Snook and Hayter is in improved agreement with the simulation structure functions. In the following, we describe the PB-RMSA scheme and critically discuss the motivation of the employed PB correction. In Section 3.3.4, we will propose a straightforward modification of the PB-RMSA leading to a further improvement of its performance. In most considered cases, our MPB-RMSA scheme yields very good results, requiring no residual adjustment of the coupling parameter. Specific systems where the MPB-RMSA is less accurate are discussed in Section 5.1, including a summary of approximate global error bounds.

At this point already, we emphasize that the PB correction underlying the PB-RMSA and the modified PB-RMSA, is neither rigorous nor without alternatives. It is less general and less justified than the hard-core rescaling argument discussed before. Nevertheless, the PB correction improves significantly the performance of the RMSA in the full fluid-state parameter space.

The PB correction argument by Snook and Hayter relies on the observation that in the derivation of the effective HSY pair potential in Eq. (2.6), the degrees of freedom of all the point-like microions have been integrated out, so that their presence is articulated only through the values for γ and k. Snook and Hayter [1, 97] argue, in the spirit of the one-component plasma model (see Ref. [61]), that this is consistent with assuming vanishing spatial correlations,

$$g_{Ci}(r) \equiv 1 \quad \text{and} \quad g_{ij}(r) \equiv 1\,, \tag{3.17}$$

between colloids and microions, and among all microion species. Here, $g_{Ci}(r)$ and $g_{ij}(r)$ are, respectively, the colloid (C) - microion and microion-microion radial distribution functions, with indices i and j labeling the various microionic species. According to Eq. (3.17), the microions are uniformly smeared out in space, penetrating also the colloidal hard cores. While inserting Eq. (3.17) into the multi-component coupled Ornstein-Zernike equations [4] describing a primitive model system leads indeed to a description that couples the colloidal macroion species to itself only, one should notice that a DLVO-type HSY pair potential can be derived without invoking the crude assumption of a uniformly penetrating microion background. This has been shown, *e.g.*, in [52, 123–125], where the non-negligible inter-ionic correlations are described more realistically using combinations of MSA and HNC closure relations, which respects the hard core of the colloids.

In fact, the PB assumptions in Eqs. (3.17) are not only unnecessary in deriving the HSY potential. In addition, they are inconsistent with the static structure factor at small wavenumber values. This follows from the global electroneutrality condition,

$$\sum_{\mu} n_{\mu} Z_{\mu}, \tag{3.18}$$

in combination with the local electroneutrality conditions,

$$Z_{\nu} + \sum_{\mu} \int n_{\mu} Z_{\mu} g_{\nu\mu}(r) d^3 r = 0. \tag{3.19}$$

Here, ν and μ label the ionic species, and the sum includes the term $\mu = \nu$. For species ν, the number concentration is $n_{\nu} = N_{\nu}/V$, and Z_{ν} is the charge of an ion of species ν in units of e. Combining Eqs. (3.18) and (3.19) leads to

$$Z_C + n_C Z_C \hat{h}_{CC}(q \to 0) + \sum_{\mu \neq C} n_{\mu} Z_{\mu} \hat{h}_{C\mu}(q \to 0) = 0, \tag{3.20}$$

where the hat denotes a three-dimensional Fourier transform. Together with the PB assumptions in Eqs. (3.17), and the definition of the partial static structure factors,

$$S_{\mu\nu}(q) = \delta_{\mu_{\nu}} + \sqrt{n_{\mu} n_{\nu}} \hat{h}_{\mu\nu}(q), \tag{3.21}$$

one obtains $S(q \to 0) = S_{CC}(q \to 0) = 0$ for the zero-q colloid-colloid static structure factor, irrespective of the volume fraction and the potential parameters γ and k. This result based on Eqs. (3.17) in conflict with the PB-RMSA (and the MC simulation) results for the HSY fluid with $k > 0$, fulfilling $S(q \to 0) > 0$.

To allow for analytic progress, let us nevertheless accept the PB assumptions in Eq. (3.17) as a useful first approximation. Then, the total charge of uniformly smeared out added salt ions inside the colloidal cores is zero. The monovalent counterions released from the colloid surfaces, however, lead to a reduction of the total charge inside a colloidal sphere from Z to $Z(1-\phi)$. For small values of ϕ, encountered in low-salinity charge-stabilized systems, the charge-reduction effect predicted on the basis of Eq. (3.17) often appears to be negligibly small. However, the systems of masked hard-core interactions must be described by the rescaled version of the MSA which invokes a much larger rescaled volume fraction ϕ'. To correct for the charge reduction within the RMSA picture, the colloid charge number should be enlarged from Z to

$$Z^* = \frac{Z}{1-\phi'} \,. \tag{3.22}$$

Incidentally, a relation analogous to Eq. (3.22), but with unrescaled volume fraction, relating the bare macroion charge to the effective one-component one follows from the primitive model when all direct correlations are treated in MSA, and when the high-temperature limit is taken for which $k \ll 1$ and $\gamma \ll 1$ [52, 124]. Only in this limit of dominating thermal kinetic energy, one is allowed to treat the microions as a uniform, non-penetrating background [123].

The corrected Z^* substituted into Eq. (2.5a) leads to the enlarged background-corrected coupling parameter

$$\gamma^* = \frac{\gamma'}{(1-\phi')^2} \,. \tag{3.23}$$

If γ^* is used in the RMSA with unchanged screening parameter k', a system is modeled with a pair potential larger than the original one, for all distances r. Thus, the RMSA screening parameter k' must be corrected (enlarged) as well. Snook and Hayter argue that the background correction $\gamma' \to \gamma^*$ should be accompanied by a screening parameter correction $k' \to k^*$, with $k^* > k'$, performed such that the background-corrected HSY potential $u^*(r)$ remains unchanged at the ion-sphere diameter, *i.e.* they demand that $\beta u^*(d_{\rm is}) = \Gamma_{\rm is}$, with $\Gamma_{\rm is}$ according to Eq. (3.15). This yields the correction

$$k^* = k' - 2\phi'^{1/3} \log(1-\phi') \,, \tag{3.24}$$

in units of the rescaled diameter σ'. The PB correction rules in Eqs. (3.23) and (3.24) are easily implemented into the standard RMSA algorithm by applying them in each incremental step of the hard-core inflation from the actual value σ to $\sigma' = \sigma/s$, with s determined by the Gillan condition. The rescaled diameter σ' in PB-RMSA is larger than in RMSA, owing to the stronger repulsive forces derived from the steeper potential $u^*(r)$ (see Fig. 3.1).

By comparing the PB-RMSA predictions to MC simulations of $g(r)$ for a series of systems with $g(\sigma^+) = 0$, Snook and Hayter have demonstrated the improved performance of the PB-RMSA relative to that of the RMSA. The PB correction is independent of the hard-core inflation. Therefore, it can be applied also to systems with $g(\sigma^+) > 0$ and $s = 1$. In Section 5.1, we demonstrate that the PB-RMSA for positive contact value systems, which we denote as the PB-MSA, is also of improved accuracy, here in comparison to the unrescaled MSA.

The potential parameters in Eqs. (3.23) and (3.24), obtained from the simplifying uniform microion background assumption in Eq. (3.17), describe a severely altered pair potential as illustrated in Fig. 3.1. The Yukawa tail of the pair potential, $u^*(r)$, used in the PB-RMSA, decays more steeply than the tail of $u(r)$, intersecting the latter at $r = d_{\rm is}$, *i.e.* at $x = \phi^{-1/3}$. In contrast to the PB-RMSA, the RMSA size-rescaling leaves $u(r)$ unchanged not only at the ion-sphere diameter, but for all distances except for the inflated hard-core region which is virtually never probed by the colloids.

There is some ambiguity in selecting $d_{\rm is}$ as the distance where the pair potential value is kept fixed. With equal right, one could select the potential value at the somewhat smaller simple-cubic geometric distance $\tilde{d} = n^{-1/3} \approx 0.8\, d_{\rm is}$. However, results for $g(r)$ and $S(q)$ which we have obtained from our PB-RMSA code using $\tilde{d}$ in place of $d_{\rm is}$, are of similarly good accuracy in general with no overall improvement. Therefore, following Snook and Hayter, in our PB-RMSA code we keep the pair potential value fixed at $r = d_{\rm is}$.

The PB correction in Eq. (3.23) is based on the assumption that γ is independent of k. Within the primitive model of charged colloids leading to the effective DLVO potential, on first sight it seems more reasonable to enforce the condition $u^*(d_{\rm is}) = u(d_{\rm is})$ for k^* determined from Eq. (2.5a) in combination with Eq. (3.22). The resulting variant of the PB-RMSA, which we denote as the implicit PB-RMSA, gives an implicit equation for k^*, the solution of which can be expressed in terms of Lambert's W-function. The k^* and γ^* values of the implicit PB-RMSA are larger than the values given by Eqs. (3.23) and (3.24), therefore describing a steeper pair potential. We have tested the performance of the implicit PB-RMSA, finding that as a consequence of the steeper $u^*(r)$, the RMSA-typical underestimation of the peak values in $S(q)$ and $g(r)$ is rendered into a severe overestimation. For this reason, the implicit PB-RMSA has to be dismissed.

In view of the inadequacy of the uniform background assumption and the discussed ambiguities in formulating the PB-correction of $u(r)$, we conclude that the PB-RMSA is justified in essence only by its success in improving the performance of the RMSA solution of the HSY model, with the additional benefit of maintaining its analytic simplicity.

3.3.4 MPB-RMSA closure

The PB-RMSA scheme of Snook and Hayter discussed so far improves the accuracy of the underlying RMSA. Yet, for identical physical values of γ and k used in the PB-RMSA, MC

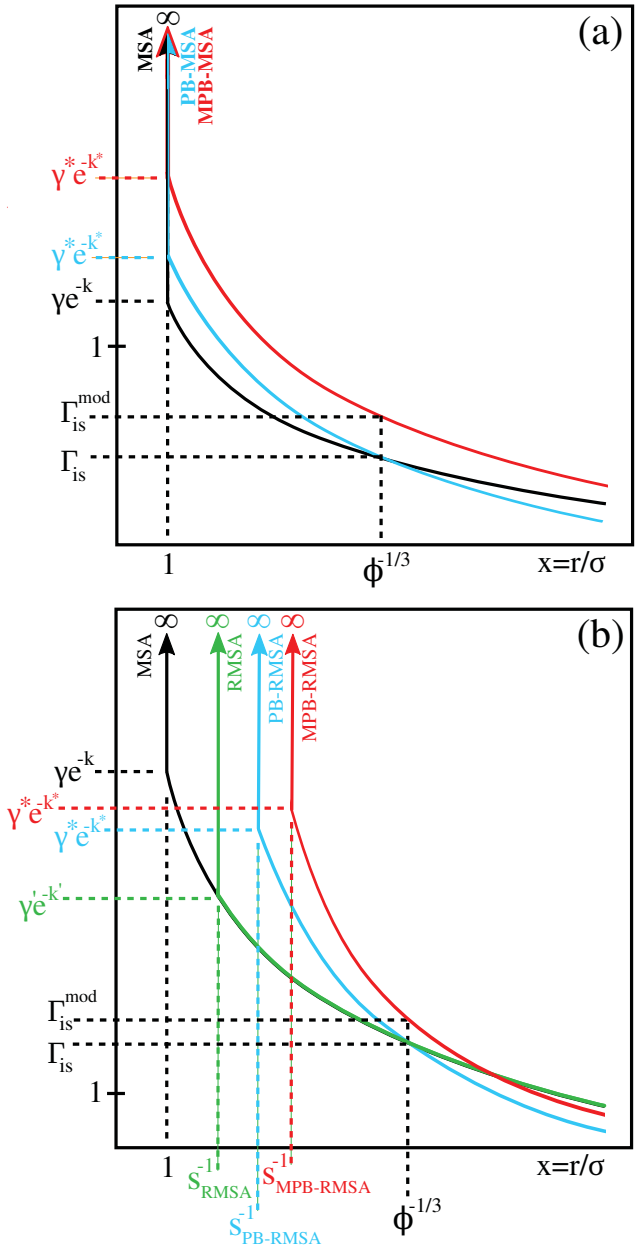

Fig. 3.1: *(a) Sketch of HSY pair potentials in units of k_BT (not to scale) used in the PB-MSA and MPB-MSA schemes, respectively, for a system requiring no hard-core rescaling. (b) As in (a), but for a system requiring hard-core rescaling. The solid black curve, labeled as MSA, represents the physical pair potential $u(x)$. Blue curves: $\beta u^*(x)$; red curves: $\beta u^*_{mod}(x)$. In (b), the indicated $1/s = \sigma'/\sigma$ values are those of the various rescaled diameters σ' in units of the physical diameter σ. Note here that $\sigma < \sigma'_{RMSA} < \sigma'_{PB-RMSA} < \sigma'_{MPB-RMSA} = \sigma^*$.*

simulations, and in the RY scheme discussed further down, the PB-RMSA still noticeably underestimates the principal peak value of $S(q)$ and $g(r)$.

In order to further improve the accuracy of the PB-RMSA, we propose an additional concentration rescaling motivated by the specific form of the screening parameter k in Eq. (2.5b). As noted before, the factor $1/(1-\phi)$ in Eq. (2.5b) corrects for the free volume accessible to the pointlike (on the scale of the colloids) microions. On the other hand, within the simplifying uniform microion background picture underlying the PB-RMSA, the free volume has been already corrected for in using Eq. (3.22). Thus, in order to avoid double correction of the screening parameter in doing a PB-RMSA calculation, we propose to replace the screening parameter k and the coupling parameter γ (depending on k via Eq. (2.5a)), in the set of given physical input parameters (k,γ,ϕ) by the modified values

$$k_{\rm mod} = k\sqrt{1-\phi}, \tag{3.25}$$

and

$$\gamma_{\rm mod} = \gamma \exp(k_{\rm mod}-k)\left(\frac{1+k/2}{1+k_{\rm mod}/2}\right)^2. \tag{3.26}$$

Note that ϕ is the unrescaled, physical volume fraction. This straightforward modification of the input values k and γ constitutes the MPB-RMSA, which we refer to as the MPB-MSA scheme in the special case of $s=1$. Note that our modification of the PB-RMSA simply consists of replacing the HSY input parameters $\{\gamma,k,\phi\}$ by $\{\gamma_{\rm mod},k_{\rm mod},\phi\}$.

Fig. 3.1 illustrates that the modified pair potential, $u^*_{\rm mod}(r)$, used in the MPB-RMSA calculation always lies above the PB-RMSA potential $u^*(r)$, so that $u^*_{\rm mod}(d_{\rm is}) = \Gamma^{\rm mod}_{\rm is} > \Gamma_{\rm is}$. Therefore, the rescaled diameter σ^* in the MPB-RMSA scheme is somewhat larger than the rescaled one in the PB-RMSA scheme.

As mentioned already in Section 3.2, it is important to note a subtle qualitative difference in the PB-RMSA and MPB-RMSA rescaling rules. On first sight, the rescaling rules for the coupling and screening parameter in Eqs. (3.23) and (3.24), used in PB-RMSA in every iteration step of hard-core inflation, appear to be of the same nature as the additional rescaling in Eqs. (3.25) and (3.26) that constitute the MPB-RMSA. In each of these four expressions, the parameters of the HSY pair-potential are rescaled as a function of the volume fraction, ϕ, or likewise the rescaled volume fraction, ϕ'. However, the PB-RMSA rescaling in Eqs. (3.23) and (3.24) are constructed in such a way that ϕ^* is a function of $\tilde{\gamma}$ and $\tilde{k}$ only, whereas $\phi^* = \phi^*(\tilde{\gamma},\tilde{k},\phi)$ in MPB-RMSA. This means that $S(\tilde{y})$ and $g(\tilde{x})$ in MPB-RMSA depend on the three parameters $(\tilde{\gamma},\tilde{k},\phi)$, even if the contact value of the rdf vanishes. This is the price to pay in using the MPB-RMSA which, on the other hand, is the most accurate of all MSA-based schemes discussed in this thesis.

With decreasing ϕ, the MPB-RMSA solution for $S(q)$ approaches the PB-RMSA and RMSA solutions. In the limit $\gamma \to 0$ (*e.g.*, $Z \to 0$) or $k \to \infty$, of a vanishing Yukawa tail, the (M)PB-RMSA and RMSA solutions all reduce to the analytic Percus-Yevick [121] solution

for neutral hard spheres (HS) . The latter provides accurate pair-structure functions of hard-sphere systems provided that $\phi \lesssim 0.35$. At larger ϕ, the PY scheme underestimates $g(x = 1^+)$ and slightly overestimates $S(q_m)$.

Once again, it should be noted that the simple replacements $k \to k_{\mathrm{mod}}, \gamma \to \gamma_{\mathrm{mod}}$ in the HSY input parameters are not based on a rigorous argument. They are only heuristically motivated, and draw their justification from the very good performance of the MPB-RMSA for an arbitrary repulsive HSY system. In Section 5.1, we show that the MPB-RMSA is in general in excellent agreement with pair structure functions obtained from simulations, RY calculations, and light scattering experiments. To facilitate the implementation of the (M)PB-RMSA by an interested reader, a comprehensive description of its algorithm is given in Appendix B.

3.4 HNC and RY closure relations

The (M)(PB)-RMSA schemes are based on the analytic MSA solution for the HSY model. There exist alternative integral equation schemes which have been applied to the HSY model, but these allow in general for purely numerical solutions only. The most frequently used numerical schemes for charge-stabilized colloids, are the hypernetted chain (HNC) [99] and Rogers-Young [100] methods which, however, are computationally more expensive. Therefore, the HNC and RY methods should be preferred over the MPB-RMSA only if a significant gain in accuracy is achieved. As we will show in Section 5.1, this requirement rules out the HNC method for most HSY-like systems. The HNC approximation underestimates systematically the principal peak values both of $S(q)$ and $g(r)$, while being only mildly superior to the numerically much faster RMSA. Except for not showing the non-physical kink in $g(r)$ at $r = \sigma'$ predicted by the MPB-RMSA as well as the PB-RMSA and RMSA solutions, we did not find system parameters $\{\sigma, \gamma, k, \phi\}$ for which the accuracy of the HNC matches that of the MPB-RMSA.

The elaborate RY method was found, from comparison with simulation results of $S(q)$ and $g(r)$, to perform excellently for the repulsive HSY model. We have confirmed this finding for all considered systems which cover a broad range of system parameters.

In our calculations, we have used the standard RY scheme, which interpolates continuously between the PY closure at short and the HNC closure at long distances, by a single-parameter mixing function. The RY hybrid closure is motivated by the observation made for the repulsive HSY potential, and for purely repulsive inverse power potentials, that the exact $S(q)$ is bracketed at small q and, at q_m, by the PY and HNC solutions for $S(q)$. The RY mixing parameter is determined by imposing local thermodynamic self-consistency, *i.e.*, by enforcing equality between the compressibility equation of state

$$\lim_{q \to 0} S(q) = k_B T \left(\frac{\partial n}{\partial p} \right)_T , \tag{3.27}$$

and the isothermal compressibility obtained from the density (concentration) derivative of the virial pressure

$$p_v = nk_BT - \frac{2\pi}{3}n^2 \int_0^\infty dr\, r^3\, g(r)\, \frac{\partial u(r)}{\partial r}\,. \tag{3.28}$$

In taking the density derivative, the weak density dependence of the mixing parameter is disregarded (imposing local consistency only), and for colloids also the concentration dependence of the effective pair potential. For monodisperse colloids, $S(q \to 0)$ relates to the osmotic isothermal compressibility. How precisely a state-dependent effective pair potential modifies the pressure, energy and compressibility equations of state is a subtle issue still under some debate [126–133]. The present work is concerned with the pair structure in HSY fluids only, not addressing its relation to the thermodynamic properties of systems with state-dependent interactions.

Different from the RY scheme, the (M)PB-RMSA and HNC methods are thermodynamically inconsistent. Owing to its local thermodynamic consistency, the RY scheme is expected to give accurate values of $S(q)$ in particular at small q. In Section 5.1.4, we use the RY scheme to test the predictions of the MPB-RMSA for $S(q \to 0)$, and to quantify the improvement in thermodynamic consistency in going from the RMSA to the MPB-RMSA scheme.

A general conclusion drawn from the comparison of the MPB-RMSA and RY scheme structure functions with MC data described in Section 5.1, is that the static structure factor is nearly always predicted with excellent accuracy by both methods for the same system parameters, while a remnant principal peak underestimation in $g(r)$ is found for the MPB-RMSA. Recall, however, that the computational load of the RY scheme is much higher. Moreover, the RY scheme does not give analytic expressions for $S(q)$ and $g(r)$ which could be used, *e.g.*, as input into dynamic theories.

3.5 Decoupling approximation for aspherical and polydisperse particles

In addition to the nearly perfectly spherical and monodisperse silica particles described in Section 2.2, the present thesis is concerned also with more complex shaped, aspherical particles. The aspherical particles considered are either monodisperse in size, such as the BSA proteins discussed in Section 2.3, or size-polydisperse, such as the gibbsite platelets in Section 2.4. A further complication arises from the distribution of charges on the particles, which, in general, is unknown and may well be non-spherically symmetric.

Integral equation theories for the pair-distribution functions of interacting aspherical, polydisperse particles with non-uniform surfaces have been applied successfully in the past. We note here the reference interaction site model (RISM), and the polymer reference interaction site model (PRISM) [4, 134–136], in which the correlations between interacting surface groups are treated in a way that is alike to a multi-component OZ equation description.

For a variety of non-spherical and polydisperse particles including rodlike viruses [137–140], platelets and rigid dendrimers [141–143], the arising generalized OZ integral equations have been solved using site-site closure relations such as the PY, HNC, and the Laria-Wu-Chandler [144, 145] closures.

When the effects of polydispersity or orientational ordering need to be accounted for, RISM, PRISM, and elaborate computer simulations are the methods of choice. None of these methods, however, is (semi-) analytically solvable with a small computational effort comparable to that of the MPB-RMSA method for monodisperse HSY fluids discussed in Section 3.3. Moreover, the dynamics of aspherical particles is considerably complicated by their complex hydrodynamic interactions. The calculation of transport properties for aspherical, hydrodynamically interacting objects requires therefore the performance of elaborate computer simulations. The aim of the present thesis is to present a set of semi-analytical schemes for the microstructure and (short-time) dynamics of colloidal suspensions. Hence, effects of asphericity and polydispersity are accounted for using simplifying approximations only, allowing for an analytic treatment. In the so-called decoupling approximation, it is assumed that the interactions in all pairs of particles are identical, independent of size, shape or relative orientation. In this approximation, polydispersity and asphericity are taken into account in the scattering amplitude distributions only [22].

Since we are dealing with charged particles, a short discussion on the neglected anisotropy in the electric double layer around a non-spherically symmetric particle is in order here. The mean electrostatic potential, $\Phi(r,\mu,\varphi) = \sum_{l=0}^{\infty}\sum_{m=-l}^{l}\Phi_l^m(r)Y_l^m(\mu,\varphi)$, of a particle with aspherical charge distribution immersed in an electrolyte solution, includes in general higher-order multipoles with $(l,m) \neq (0,0)$. Here, r is the distance of the particle center to the field point, $\mu = \cos\vartheta$ is the cosine of the polar angle, φ is the azimuthal angle, and the Y_l^m's are spherical harmonics.

For large r, all multipoles decay asymptotically equally fast according to [146–151]

$$\Phi_l^m(r) \sim f_l^m \frac{e^{-\kappa r}}{r}, \tag{3.29}$$

where κ denotes the inverse electrostatic screening length, and the f_l^m are determined by the charge distribution. In principle, this implies that the pair-interaction energy of two aspherical charge-distributions depends on their relative orientation even for $r \gg \kappa^{-1}$. However, the multipolar strengths, f_l^m, for a moderately aspherical particle can be expected to be small for larger l or m. Moreover, since after orientational averaging, $\left\langle Y_l^m(\mu,\varphi)\right\rangle_{\mu,\varphi} = 0$ for all $l > 0$, the neglect of anisotropic pair interaction contributions can be expected to be reasonable, for systems where the particles can rotate essentially freely.

Assuming the validity of the Rayleigh-Gans-Debeye approximation and single scattering, the static scattered intensity, $I(\mathbf{q})$, for polarized scattering from a scattering volume containing

$N_s \geq 1$ particle species of equal, constant dielectric properties reads

$$\frac{I(\mathbf{q})}{I_0} = \frac{\langle E(\mathbf{q})E^*(\mathbf{q})\rangle}{|E_0|^2} \propto \sum_{\alpha,\beta=1}^{N_s} v_\alpha v_\beta \sum_{j=1}^{N_\alpha}\sum_{k=1}^{N_\beta} \left\langle \tilde{f}_\alpha(\mathbf{q},\Omega_j)\tilde{f}^*_\beta(\mathbf{q},\Omega_k)\exp\left\{i\mathbf{q}\cdot\left(\mathbf{r}_j^\alpha - \mathbf{r}_k^\beta\right)\right\}\right\rangle . \tag{3.30}$$

Here, $E(\mathbf{q})$ is the modulus of the scattered electric field, and $I_0 = |E_0|^2$ is the intensity of the incoming monochromatic (laser or X-ray) beam. The star denotes complex conjugation, the scattering wave vector is denoted as $\mathbf{q}$, v_γ is the volume, and N_γ is the number of particles of species γ. Furthermore, $\tilde{f}_\gamma(\mathbf{q},\Omega_l)$ and $\mathbf{r}_l^\gamma$ are the form amplitude and the center-of-mass position, respectively, of particle l of species γ, oriented in direction of the solid angle Ω_l. The form amplitudes fulfill $\tilde{f}_\gamma(\mathbf{q}\to 0,\Omega) = 1$. In evaluating Eq. (3.30), we split the outermost sum into a self-part, $\alpha = \beta$, denoted by $\sum_1$, and a distinct part $\alpha \neq \beta$, denoted by $\sum_2$. Then, $I(\mathbf{q})/I_0 = \sum_1 + \sum_2$, and, for vanishing or neglected correlations between particle orientations and center-of-mass positions, one obtains

$$\sum\nolimits_1 \propto N\sum_{\alpha=1}^{N_s} x_\alpha P_\alpha(q) + \sum_{\alpha=1}^{N_s} v_\alpha^2 N_\alpha(N_\alpha - 1)\left\langle \tilde{f}_\alpha(\mathbf{q},\Omega)\right\rangle_\Omega^2 \langle \exp\{i\mathbf{q}\cdot(\mathbf{r}_1^\alpha - \mathbf{r}_2^\alpha)\}\rangle . \tag{3.31}$$

Here, $N = \sum_\gamma N_\gamma$ is the total number of particles, and $x_\gamma = N_\gamma/N$ is the molar fraction of species γ. The bracket $< \ldots >_\Omega$ denotes the orientational average, $\mathbf{r}_1^\alpha$ and $\mathbf{r}_2^\alpha$ are the position vectors for a representative pair of particles of species α, and

$$P_\gamma(q) = \left\langle \left| f_\gamma(\mathbf{q},\Omega)\right|^2\right\rangle_\Omega , \tag{3.32}$$

with scattering amplitude $f_\gamma(\mathbf{q},\Omega) = v_\gamma\tilde{f}_\gamma(\mathbf{q},\Omega)$. On assuming $N_\gamma \gg 1$ for all γ, and the definition

$$S_{\alpha\beta}(q) = \delta_{\alpha\beta} + \sqrt{N_\alpha N_\beta}\left\langle \exp\left\{i\mathbf{q}\cdot\left(\mathbf{r}_1^\alpha - \mathbf{r}_2^\beta\right)\right\}\right\rangle \tag{3.33}$$

of partial static structure factors in an isotropic multi-component suspension, with $\delta_{\alpha\beta}$ denoting the Kronecker delta, Eq. (3.31) can be written as

$$\frac{\sum_1}{N} \propto \sum_{\alpha=1}^{N_s} x_\alpha P_\alpha(q) + \sum_{\alpha=1}^{N_s} x_\alpha v_\alpha^2 \left\langle \tilde{f}_\alpha(\mathbf{q},\Omega)\right\rangle_\Omega^2 [S_{\alpha\alpha}(q) - 1] . \tag{3.34}$$

Note that our standard definition of $S_{\alpha\beta}(q)$, with $S_{\alpha\beta}(q\to\infty) = \delta_{\alpha\beta}$, agrees with that of Ashcroft and Langreth [152].

In addition to the translational-orientational decoupling approximation, we assume identical pair-correlations for all particle species, so that $S_{\alpha\alpha}(q)$ in Eq. (3.34) can be replaced by the structure factor

$$S(q) = 1 + N\langle \exp\{i\mathbf{q}\cdot(\mathbf{r}_1 - \mathbf{r}_2)\}\rangle , \tag{3.35}$$

of an ideally monodisperse suspension. Using that $[S_{\alpha\alpha}(q)-1] = x_\alpha[S(q)-1]$, this leads to

$$\frac{\Sigma_1}{N} \propto \sum_{\alpha=1}^{N_s} x_\alpha P_\alpha(q) + \sum_{\alpha=1}^{N_s} x_\alpha^2 v_\alpha^2 \left\langle \tilde{f}_\alpha(\mathbf{q},\Omega)\right\rangle_\Omega^2 [S(q)-1]\,. \tag{3.36}$$

We proceed by considering in decoupling approximation the distinct $(\alpha \neq \beta)$ part of Eq. (3.30). On assuming again vanishing correlations between orientations and center-of-mass positions, we obtain

$$\sum\nolimits_2 \propto \sum_{\substack{\alpha,\beta=1 \\ \alpha\neq\beta}}^{N_s} v_\alpha v_\beta \sqrt{N_\alpha N_\beta}\left\langle \tilde{f}_\alpha(\mathbf{q},\Omega)\right\rangle_\Omega \left\langle \tilde{f}_\beta^*(\mathbf{q},\Omega)\right\rangle_\Omega S_{\alpha\beta}(q). \tag{3.37}$$

On assuming again the particles of all species to be equal in terms of their interactions, we can use $S_{\alpha\beta}(q) = (x_\alpha x_\beta)^{1/2}[S(q)-1]$ for $\alpha \neq \beta$. This results in

$$\frac{\Sigma_2}{N} \propto \left[\sum_{\alpha=1}^{N_s} x_\alpha v_\alpha \left\langle \tilde{f}_\alpha(\mathbf{q},\Omega)\right\rangle_\Omega\right]^2 \times [S(q)-1] \qquad \text{for } N_s > 1. \tag{3.38}$$

The sum of Eqs. (3.36) and (3.38) is the static scattered intensity expression used in this thesis for BSA proteins and gibbsite platelets, based on assuming translational-orientational decoupling and interaction monodispersity:

$$I(q) \;\propto\; I_0 N\, P_m(q)\, S_m(q), \tag{3.39a}$$

$$S_m(q) \;=\; \Big[1 - X(q)\Big] + X(q) S(q). \tag{3.39b}$$

Here, $P_m(q)$ and $S_m(q)$ are the measurable form factor and the measurable structure factor, respectively, and

$$X(q) = A(q) + B(q), \tag{3.40}$$

with

$$A(q) = \frac{\sum_{\alpha=1}^{N_s} x_\alpha^2 v_\alpha^2 \left\langle \tilde{f}_\alpha(\mathbf{q},\Omega)\right\rangle_\Omega^2}{P_m(q)\sum_{\alpha=1}^{N_s} x_\alpha v_\alpha^2}, \tag{3.41a}$$

$$B(q) = \frac{sgn(N_s-1)\times\left[\sum_{\alpha=1}^{N_s} x_\alpha v_\alpha \left\langle \tilde{f}_\alpha(\mathbf{q},\Omega)\right\rangle_\Omega\right]^2}{P_m(q)\sum_{\alpha=1}^{N_s} x_\alpha v_\alpha^2}, \tag{3.41b}$$

(3.41c)

and

$$P_m(q) = \frac{\sum_{\alpha=1}^{N_s} x_\alpha P_\alpha(q)}{\sum_{\alpha=1}^{N_s} x_\alpha P_\alpha(q\to 0)} = \frac{\sum_{\alpha=1}^{N_s} x_\alpha v_\alpha^2 \left\langle \left|\tilde{f}_\alpha(\mathbf{q},\Omega)\right|^2\right\rangle_\Omega}{\sum_{\alpha=1}^{N_s} x_\alpha v_\alpha^2}. \tag{3.42}$$

Note that $0 \le X(q) \le 1$ and $P_m(q\to 0) = 1$. In Eq. (3.41b), *sgn* denotes the signum function. The function $X(q)$, referred to as the decoupling amplitude, assumes its maximum at low values of q. It decreases with increasing q, and stays close to zero at large q-values.

In the special case of a system containing only a single scattering species ($N_s = 1$), such as the solutions of monodisperse aspherical BSA proteins studied in this thesis, the sum over distinct species in Eq. (3.37), and hence the function $B(q)$ in Eq. (3.41b) vanish. The decoupling amplitude simplifies then to

$$X(q) = \frac{\left\langle \tilde{f}(\mathbf{q},\Omega)\right\rangle_\Omega^2}{P_m(q)} = \frac{\left\langle \tilde{f}(\mathbf{q},\Omega)\right\rangle_\Omega^2}{\left\langle \left|\tilde{f}(\mathbf{q},\Omega)\right|^2\right\rangle_\Omega}, \qquad (N_s = 1), \tag{3.43}$$

where now $X(q\to 0) = 1$, independent of the particle size or shape. Hence, in decoupling approximation applied to monodisperse particles, orientational disorder has no effect on the scattered intensity in forward direction. Any deviation of $X(q\to 0)$ from one must be due to size-polydispersity.

Curves of $X(q)$ for isotropic systems of monodisperse and polydisperse aspherical particles are displayed in Figs. 5.14 and 5.16, respectively. In decoupling approximation, the general effect of polydispersity and orientational disorder is a damping of the oscillations in $P_m(q)$ and $S_m(q)$, as compared to those in the form and structure factors, $P(q)$ and $S(q)$, of ideally monodisperse spheres. For all the aspherical and polydisperse particle suspensions treated in this thesis, the $S(q)$ entering into Eq. (3.39b) is calculated using the MPB-RMSA, for a

representative system of monodisperse effective spheres interacting via the HSY pair potential given in Eq. (2.6).

CHAPTER

FOUR

Theory of short- and long-time dynamics

4.1 Short-time dynamics: General expressions

To characterize the colloidal short-time regime, one considers the momentum relaxation time, $\tau_B = m/(3\pi\eta_0\sigma)$, the time scale $\tau_H = \sigma^2\rho_S/(4\eta_0)$ of hydrodynamic vorticity diffusion across a diameter σ, and the interaction time $\tau_I = \sigma^2/(4d_{t,0})$ [21, 22], where m is the mass of a colloidal sphere, $d_{t,0} = k_BT/(3\pi\eta_0\sigma)$ is the translational free diffusion coefficient for stick hydrodynamic surface boundaries, and ρ_S and η_0 are the mass density and shear viscosity of the suspending Newtonian solvent, respectively. For a coarse-grained time-resolution where $t \gg \tau_B \sim \tau_H$, the motion of a colloidal particle is erratic and overdamped. An essential part of the present thesis deals with the colloidal short-time regime $\tau_B \ll t \ll \tau_I$, during which a particle has moved a tiny fraction of its size only. This allows for calculating (equilibrium) short-time properties using pure equilibrium averages.

Diffusion properties can be measured by a variety of scattering techniques, which commonly determine the intermediate scattering function [4],

$$S(q,t) = \lim_{\infty} \left\langle \frac{1}{N} \sum_{l,j=1}^{N} \exp\left\{ i\mathbf{q} \cdot \left[\mathbf{r}_l(0) - \mathbf{r}_j(t) \right] \right\} \right\rangle, \tag{4.1}$$

as a function of scattering wavenumber q and correlation time t. Here, N is the number of colloid particles in the scattering volume, $\mathbf{q}$ is the scattering wave vector, and $\mathbf{r}_n(t)$ is the position vector pointing to the center of the n-th globular colloidal particle at time t. On the colloidal short-time scale, $S(q,t)$ decays exponentially according to [153]

$$\frac{S(q,t)}{S(q)} = \exp\left[-q^2 D(q) t \right], \tag{4.2}$$

where $D(q)$ is the wavenumber-dependent short-time diffusion function. A statistical-

mechanical expression for $D(q)$ follows from the generalized Smoluchowski equation in form of the ratio [21, 22, 153]

$$D(q) = d_{t,0}\frac{H(q)}{S(q)}, \tag{4.3}$$

of the hydrodynamic function

$$H(q) = \lim_{\infty}\left\langle \frac{1}{\mu_0 N}\sum_{l,j=1}^{N}\hat{\mathbf{q}}\cdot\mu_{lj}^{tt}(\mathbf{r}^N)\cdot\hat{\mathbf{q}}\exp\left\{i\mathbf{q}\cdot[\mathbf{r}_l-\mathbf{r}_j]\right\}\right\rangle, \tag{4.4}$$

and the static structure factor $S(q) = S(q,t=0)$. Here, $\mu_0 = d_{t,0}/k_BT = 1/(3\pi\eta_0\sigma)$ is the translational single-sphere mobility for stick hydrodynamic boundary conditions, $\hat{\mathbf{q}}$ is the unit vector in the direction of the scattering wave vector $\mathbf{q}$, and $\mu_{lj}^{tt}(\mathbf{r}^N)$ is a translational hydrodynamic mobility tensor linearly relating the hydrodynamic force on a sphere j to the translational velocity of a sphere l. This mobility depends in general on the instantaneous positions, $\mathbf{r}^N$, of all N particles through the specified hydrodynamic boundary conditions. In this work, stick hydrodynamic boundary conditions are assumed throughout.

The positive-valued hydrodynamic function $H(q)$ is a measure of the influence of HIs on short-time diffusion. In the (hypothetical) case of hydrodynamically non-interacting particles, $H(q) \equiv 1$, independent of q. The hydrodynamic function can be interpreted as the reduced short-time generalized mean sedimentation velocity measured in a homogeneous suspension subject to a weak force field collinear with $\mathbf{q}$ and oscillating spatially as $\cos(\mathbf{q}\cdot\mathbf{r})$. Hence,

$$\lim_{q\to 0} H(q) = \frac{U_{\text{sed}}}{U_0} \equiv K \tag{4.5}$$

is equal to the concentration-dependent (short-time) sedimentation velocity, U_{sed}, of a slowly settling suspension of spheres in units of the sedimentation velocity, $U_0 = \sigma^2 g(\rho - \rho_S)/(18\eta_0)$, of a single sphere at infinite dilution. Here, g is the gravitational acceleration, and ρ is the volume-averaged mass density of a colloidal sphere.

The function $H(q)$ can be expressed as the sum,

$$H(q) = \frac{d_s}{d_{t,0}} + H^d(q), \tag{4.6}$$

of a q-dependent distinct part, $H^d(q)$, accounting for all contributions with $l \neq j$ in Eq. (4.4) and vanishing for $q \to \infty$, and a self-part ($l = j$ in Eq. (4.4)) equal to the reduced short-time translational self-diffusion coefficient $d_s/d_{t,0}$. As illustrated in Fig. 4.1, the diffusion coefficient d_s is equal to the short-time slope of the mean-squared displacement, $W(t) = 1/6 < [\mathbf{r}(t) - \mathbf{r}(0)]^2 >$, of a colloidal particle [21]. Here, the factor $1/6$ accounts for the three spatial dimensions.

Two additional diffusion coefficients related to $D(q)$ are the short-time collective diffusion

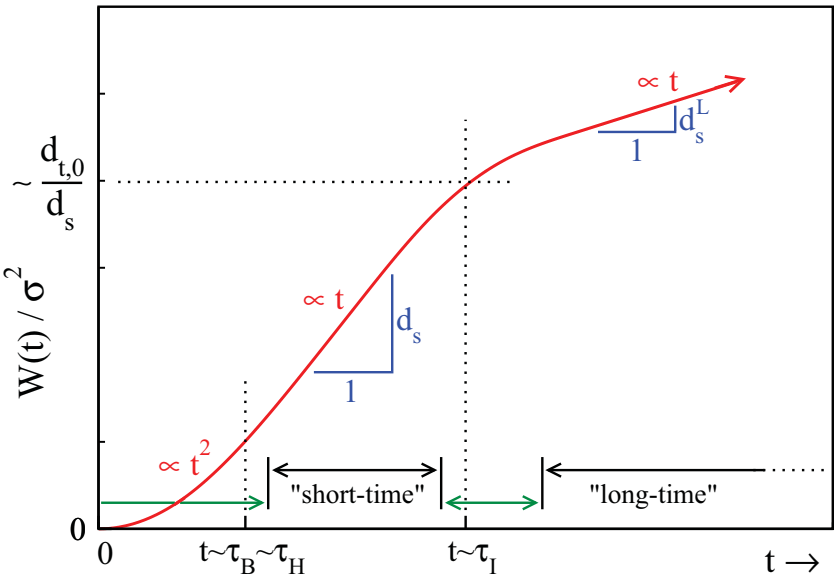

Fig. 4.1: *Sketch of the mean-squared displacement, $W(t)$, of a spherical Brownian particle in units of σ^2, as a function of correlation time t. The particle motion is diffusive, with $W(t) \propto t$, both in the short-time regime $\tau_B \sim \tau_H \ll t \ll \tau_I$, and in the long-time regime $t \gg \tau_I$. During a time $t \sim \tau_I$, diffusive motion has led to an average displacement $\sim \sigma$, of the particle from its initial position. Our definition of $W(t)$ in three spatial dimensions incorporates a factor of $1/6$, so that d_s and d_s^L are equal to the slopes of $W(t)$ at short and long times, respectively. Time regimes not considered in the present work are marked by green arrows: For $t \lesssim \tau_B \sim \tau_H$, the particle moves essentially ballistically, with $W(t) \propto t^2$. At transient times $t \sim \tau_I$, the particle motion is subdiffusive, with $W(t)$ increasing weaker than linear in time.*

coefficient $d_c = d_{t,0}K/S(q \to 0)$, and the short-time cage diffusion coefficient $d_{\mathrm{cge}} = D(q_m)$. These two coefficients characterize the decay rates, respectively, of thermally induced concentration fluctuations of macroscopic wavelengths, and of a wavelength related to the size, $2\pi/q_m$, of the dynamic nearest-neighbor cage formed around a particle.

So far only diffusion properties have been discussed. A rheological short-time property of interest is the high-frequency limiting viscosity, η_∞, which linearly relates the average deviatoric suspension shear stress to the applied rate of strain in a low-amplitude, oscillatory shear experiment with frequency $\omega \gg 1/\tau_I$. The statistical-mechanical expression for η_∞ is [154]

$$\eta_\infty = \eta_0 + \lim_{\infty} \frac{1}{10V} \sum_{\alpha,\beta=1}^{3} \left\langle \sum_{l,j=1}^{N} \mu_{lj}^{dd}{}_{\alpha\beta\beta\alpha}(\mathbf{r}^N) \right\rangle, \tag{4.7}$$

invoking the Cartesian components, $\mu_{lj}^{dd}{}_{\alpha\beta\beta\alpha}$, of the $3 \times 3 \times 3 \times 3$ dipole-dipole mobility tensor μ_{lj}^{dd}, that relate the symmetric hydrodynamic force dipole moment tensor of sphere l to the rate of strain tensor related to sphere j. For stick hydrodynamic boundary conditions, $\eta_\infty = \eta_0[1 + 2.5\phi + \mathcal{O}(\phi^2)]$ [155–157], where η_0 is the solvent viscosity. The $\mathcal{O}(\phi^2)$ contribution is due to particle interactions. Note here that $< ... >$ describes an equilibrium average with respect to the unsheared system. Direct interactions affect η_∞ only through their influence on the equilibrium particle distribution.

The great difficulty in evaluating Eqs. (4.4) and (4.7) to obtain $H(q)$ and η_∞, respectively, lies in the calculation of the hydrodynamic tensors $\mu_{lj}^{tt}(\mathbf{r}^N)$ and $\mu_{lj}^{dd}(\mathbf{r}^N)$, and in the associated many-particle average. Except for numerically expensive simulations [23–26], it is practically impossible to gain precise results for concentrated systems. In searching for methods which allow to calculate $H(q)$ and η_∞ to decent accuracy with moderate numerical effort, one has to resort to approximate methods. Two of these methods, namely the so-called pairwise additive (PA) approximation, and the $\delta\gamma$ scheme by Beenakker and Mazur supplemented by so-called self-part corrections, are discussed in the next sections. The methods are presented in a self-contained way to facilitate their implementation by an interested reader. Both methods have in common that they require $S(q)$, or equivalently $g(r)$, as the only input. The pros and cons of both methods are assessed in Chapter 6 in comparison to elaborate computer simulations.

4.2 Approximation of pairwise additive hydrodynamic interactions

In the PA approximation, the N-particle translational mobility tensors, $\mu^{tt}_{lj}(\mathbf{r}^N)$, are approximated by the sum of two-body mobilities according to

$$\frac{1}{\mu_0}\mu^{tt}_{lj}(\mathbf{r}^N)\Big|_{\mathrm{PA}} = \delta_{lj}\left[\mathbb{1}+\sum_{n\neq l}^{N}\mathbf{a}_{11}(\mathbf{r}_l-\mathbf{r}_n)\right]+(1-\delta_{lj})\mathbf{a}_{12}(\mathbf{r}_l-\mathbf{r}_j). \tag{4.8}$$

The 3×3 mobility tensor $\mathbb{1}+\mathbf{a}_{11}$ relates, for an isolated pair of particles in a quiescent fluid, the force on particle 1 to its own velocity. Correspondingly, $\mathbf{a}_{12}$ relates the force on particle 2 to the velocity of particle 1. The axial symmetry of the two-sphere problem allows to split the reduced mobilities into longitudinal and transverse components,

$$\mathbf{a}_{ij}(\mathbf{r})+\delta_{ij}\mathbb{1} = x^a_{ij}(r)\hat{\mathbf{r}}\hat{\mathbf{r}}+y^a_{ij}(r)\left[\mathbb{1}-\hat{\mathbf{r}}\hat{\mathbf{r}}\right], \tag{4.9}$$

where we use the notation from Ref. [158], with $\hat{\mathbf{r}}=(\mathbf{r}_1-\mathbf{r}_2)/|\mathbf{r}_1-\mathbf{r}_2|$. The mobility components $x^a_{ij}(r)$ and $y^a_{ij}(r)$ can be expanded analytically in powers of $\sigma/r=1/x$ using recursion formulas [158–160].

In a homogeneous fluid system, the ensemble average of a function f depending on two particle coordinates can be expressed in the thermodynamic limit as

$$\left\langle f(\mathbf{r}_l-\mathbf{r}_j)\right\rangle = \lim_{V\to\infty}\frac{1}{V}\int_V d\mathbf{r}\; g(r)f(\mathbf{r}). \tag{4.10}$$

The combination of Eqs. (4.4), (4.8), and (4.10) leads to the following PA results for d_s,

$$\frac{d_s}{d_{t,0}}\Big|_{\mathrm{PA}} = 1+8\phi\int_1^\infty dx\, x^2 g(x)\left[x^a_{11}(x)+2y^a_{11}(x)-3\right], \tag{4.11}$$

and for the distinct part of the hydrodynamic function,

$$\begin{aligned} H^d(y)\Big|_{\mathrm{PA}} &= -15\phi\frac{j_1(y)}{y} \\ &+ 18\phi\int_1^\infty dx\, xh(x)\left[j_0(xy)-\frac{j_1(xy)}{xy}+\frac{j_2(xy)}{6x^2}\right] \\ &+ 24\phi\int_1^\infty dx\, x^2 g(x)\tilde{y}^a_{12}(x)j_0(xy) \\ &+ 24\phi\int_1^\infty dx\, x^2 g(x)\left[\tilde{x}^a_{12}(x)-\tilde{y}^a_{12}(x)\right]\times\left[\frac{j_1(xy)}{xy}-j_2(xy)\right]. \end{aligned} \tag{4.12}$$

Here, $y = q\sigma$ is the diameter-scaled wavenumber, j_n is the spherical Bessel function of first kind and order n, and h is the total correlation function defined by $h(x) = g(x) - 1$.

We have introduced here the short-range mobility parts

$$\tilde{x}^a_{12}(x) = x^a_{12}(x) - 3/4x^{-1} + 1/8x^{-3}, \tag{4.13}$$

$$\tilde{y}^a_{12}(x) = y^a_{12}(x) - 3/8x^{-1} - 1/16x^{-3}, \tag{4.14}$$

which include all terms in the series expansion except for the far-field terms up to the dipolar (Rotne-Prager) level, which are subtracted off.

For pair-distances $x > 3$, we use analytic $\mathcal{O}(x^{-20})$-expansions for the two-body mobility functions x^a_{ij} and y^a_{ij}. The expansion coefficients are given in Tab. C.1 of Appendix C, and in Ref. [159]. Since the expansions in $1/x$ converge slowly at small separations, we employ accurate numerical tables for $x \leq 3$, which in particular account for lubrication at near-contact distances. These tables have been calculated by Jeffrey and Onishi [158] by combining the near-contact Eqs. (C.2) in Appendix C, with many orders (up to $n = 220$) of the $1/x$ expansions (C.1), resulting in a smooth transition of the near-field expressions to the far-field expressions.

Fig. 4.2 illustrates the behavior of the pair mobilities for four selected, highly symmetric two-sphere mobility problems, with the associated mobilities plotted as functions of the dimensionless separation, $\chi = x - 1$, of the sphere surfaces. In each of the four cases considered in Fig. 4.2, the forces $\mathbf{F}_1$ and $\mathbf{F}_2$ acting on spheres 1 and 2, respectively are equal in their magnitude $F = |\mathbf{F}_1| = |\mathbf{F}_2|$, acting either orthogonal, parallel or anti-parallel to $\hat{\mathbf{r}}$. Due to symmetry the velocities $\mathbf{V}_1$ and $\mathbf{V}_2$ of spheres 1 and 2 are equal in magnitude, with $\mathbf{F}_1 \parallel \mathbf{V}_1$ and $\mathbf{F}_2 \parallel \mathbf{V}_2$.

Panels (a) and (b) of Fig. 4.2 correspond to parallel and in-line sedimentation, respectively, without Brownian motion. From Eqs. (4.8) and (4.9), it follows that the sedimentation velocity $V_{\text{sed}} \equiv |\mathbf{V}_1| = |\mathbf{V}_2|$ for parallel and in-line sedimentation is given by $\mu_0 V_{\text{sed}}/F = [y^a_{11}(x) + y^a_{12}(x)]$ and $\mu_0 V_{\text{sed}}/F = [x^a_{11}(x) + x^a_{12}(x)]$, respectively.

Panels (c) and (d) of Fig. 4.2 illustrate snapshots of sliding and squeezing motion of two equal spheres. According to Eqs. (4.8) and (4.9), the instantaneous relative velocity, $\Delta V \equiv |\mathbf{V}_1 - \mathbf{V}_2|$, in panel (c) and (d) is given by $\mu_0 \Delta V/F = 2[y^a_{11}(x) - y^a_{12}(x)]$ and $\mu_0 \Delta V/F = 2[x^a_{11}(x) - x^a_{12}(x)]$, respectively.

In Fig. 4.2, blue dotted curves and blue solid lines represent the far-field mobility expansion results in Eqs. (C.1) of Appendix C, truncated at $n = 6$ and $n = 20$, respectively. Note from Tab. C.1 in Appendix C that $n = 6$ is the lowest order of the expansions in Eqs. (C.1) that is non-trivial in all coefficients, *i.e.* containing non-zero values of $x^{a\,(n)}_{ij}$ and $y^{a\,(n)}_{ij}$ for all $i, j \in \{1, 2\}$. Black solid lines in Fig. 4.2 represent the near-contact mobility Eqs. (C.2) in Appendix C. Red solid lines represent the mobilities used for $x \leq 3$ in our PA scheme implementation, calculated by Jeffrey and Onishi [158] by combining expansions up to $\mathcal{O}(x^{-220})$ with the near-contact Eqs. (C.2). Note from Fig. 4.2 the practically perfect agreement of the numerical tabulated values (red lines) with the $\mathcal{O}(x^{-20})$ and $\mathcal{O}(x^{-6})$ expansions (blue lines and

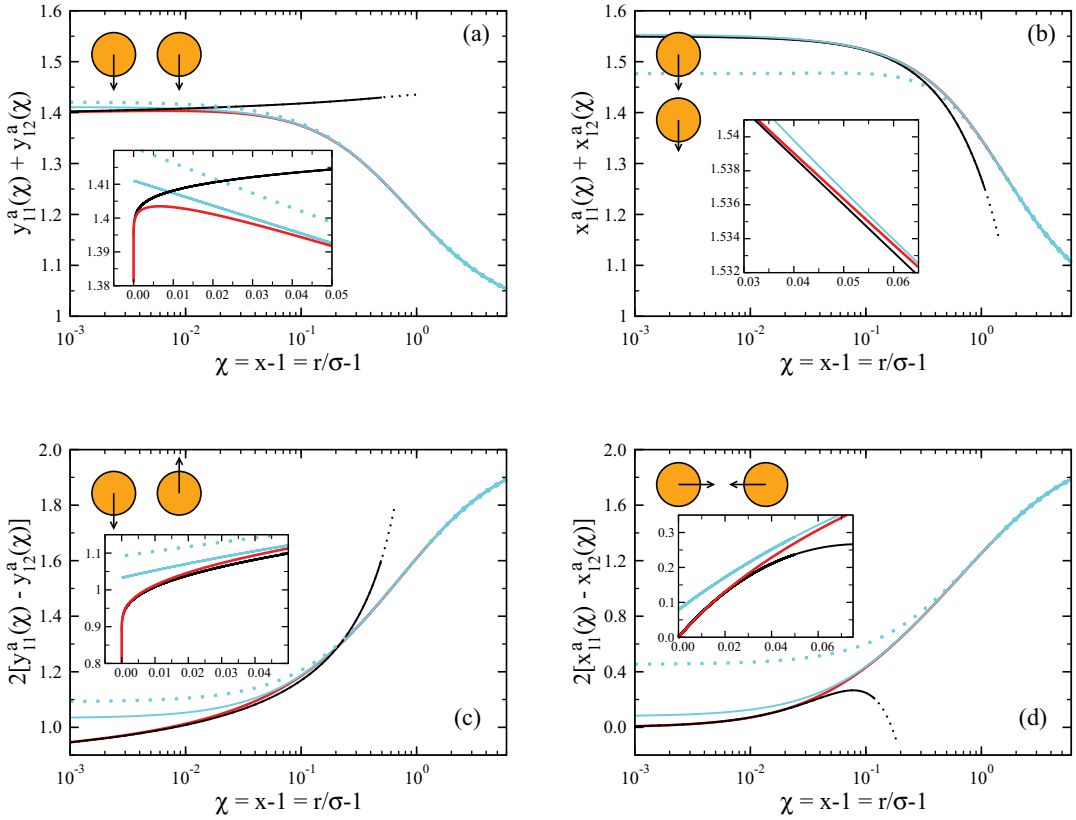

Fig. 4.2: *Hydrodynamic two-body mobility problems of four specifically selected highly symmetric geometries. Top left: parallel sedimentation, top right: in-line sedimentation, bottom left: sliding motion, bottom right: in-line squeezing motion. The black arrows represent the forces acting on the particles, and are in line with the instantaneous particle velocities. Blue dotted curves and blue solid curves represent the* $1/x$ *mobility expansions in Eqs.* (C.1) *of Appendix C, truncated at powers of* $n = 6$ *and* $n = 20$*, respectively. Black solid lines represent the near-contact mobility Eqs.* (C.2) *in Appendix C. Red solid lines represent the mobilities calculated by Jeffrey and Onishi [158], which combine many orders (up to* $n = 220$*) of the* $1/x$ *expansions in Eqs.* (C.1) *with the near-contact Eqs.* (C.2)*. The insets with double linear scales magnify the details of the transition region between near-field and far-field HIs. In our PA scheme implementation, we use the tables by Jeffrey and Onishi (red lines) for* $x \leq 3$*, and the* $1/x$ *expansions truncated at* $n = 20$ *(blue lines) for* $x > 3$*.*

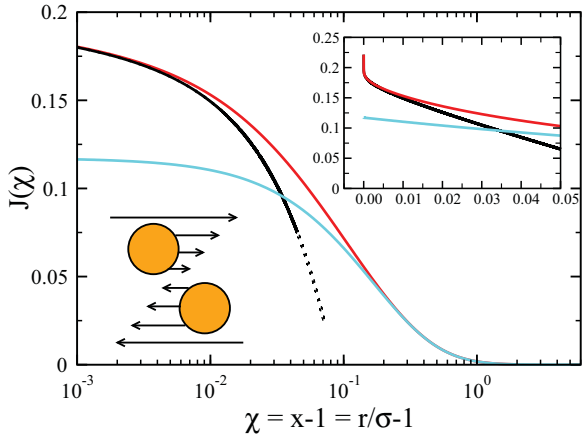

Fig. 4.3: *Two-body shear-mobility function. Blue line: leading-order far-field expansion* $J(x) = 15/128x^{-6}$. *Black line: near-contact shear-mobility function given in Eq.* (C.3) *of Appendix C. Red line: values from numerical tables by Jeffrey [161–163]. In our PA scheme implementation, we use the tables by Jeffrey for* $x \leq 3$, *and the leading-order far-field expression for* $x > 3$.

blue dotted curves) at $x = 3$. Hence, our usage of the $\mathcal{O}(x^{-20})$-expansion for $x > 3$ in the PA scheme is well justified.

Analogous to the translational diffusivity tensors, the dipole-dipole mobility tensors are approximated in the PA scheme by their self- and distinct two-body contributions $\mu^{dd\,(2)}_{11}(\mathbf{r})$, and $\mu^{dd\,(2)}_{12}(\mathbf{r})$, respectively. In hydrodynamically semi-dilute suspensions, the high-frequency viscosity of colloidal spheres at low shear-rate is obtained from [23, 157, 164]

$$\frac{\eta_\infty}{\eta_0} = 1 + \frac{5}{2}\phi(1+\phi) + 60\phi^2 \int_1^\infty dx\, x^2 g(x) J(x), \tag{4.15}$$

with

$$J(x) = \frac{6}{25\pi\sigma^3}\left[\mu^{dd\,(2)}_{11,\alpha\beta\beta\alpha}(\mathbf{x}) + \mu^{dd\,(2)}_{12,\alpha\beta\beta\alpha}(\mathbf{x})\right]. \tag{4.16}$$

Here, the rapidly decaying two-body shear mobility function, $J(x)$, accounts for the two-body HIs. For stick hydrodynamic boundary conditions, $J(x) = 15/128\, x^{-6} + \mathcal{O}(x^{-8})$.

Similar to our treatment of the mobilities x^a_{ij} and y^a_{ij}, we use the leading-order far-field expression, $J(x) = 15/128\, x^{-6}$, for the shear mobility function at $x > 3$, and accurate numerical tables to account for near-field HIs at $x \leq 3$ [161–163]. Fig. 4.3 illustrates $J(x)$ in its near-contact form, given in Eq. (C.3) of Appendix C (black line), in its leading-order far-field form

(blue line), and for all distances using the accurate numerical tables as employed in our PA code, matching both the near-field and far-field expressions (red line).

Using the zeroth-order concentration-expansion in Eq. (3.6), for the rdf of hard spheres given by $g_0^{\mathrm{HS}}(x) = \Theta(x-1) + \mathcal{O}(\phi)$, with Θ denoting the unit step function, we have checked that our PA code precisely reproduces the truncated virial expressions

$$\frac{d_s^{\mathrm{HS}}}{d_{t,0}} = 1 - 1.8315\phi + \mathcal{O}(\phi^2), \tag{4.17a}$$

$$K^{\mathrm{HS}} = 1 - 6.546\phi + \mathcal{O}(\phi^2), \tag{4.17b}$$

$$\frac{\eta_\infty^{\mathrm{HS}}}{\eta_0} = 1 + \frac{5}{2}\phi + 5.0023\phi^2 + \mathcal{O}(\phi^3), \tag{4.17c}$$

which were obtained in Refs. [165–167] using a mobility series expansion including terms up to $\mathcal{O}(x^{-1000})$, plus a near-field HI correction.

All PA results for $H(q)$ and η_∞ discussed in the present work are based on Eqs. (4.11), (4.12) and (4.15), with $g(r)$ computed in MPB-RMSA. Dynamical properties predicted by the PA scheme are exact to linear order in ϕ. Thus, the PA scheme is especially well-suited for hydrodynamically, but not necessarily structurally, dilute systems. Charge-stabilized suspensions at low salinity and concentration, where near-contact configurations are very unlikely, are prime examples of hydrodynamically dilute, but structurally ordered systems, showing pronounced fluid-like oscillations in $S(q)$ and $g(r)$.

Moreover, the PA scheme can be used to check the accuracy of other approximate schemes, such as the (self-part corrected) $\delta\gamma$ scheme, in the low concentration regime. At larger volume fractions, however, and for diffusion properties like d_c and K, where non-pairwise additive HIs are particularly influential, the PA approximation is bound to fail. Note that, while in the present work particles with stick hydrodynamic boundary conditions are considered, the PA scheme can be easily generalized to permeable particles, and to particles with slip-stick hydrodynamic boundary conditions, simply by using the corresponding two-body mobility functions given, e.g., in [159].

4.3 $\delta\gamma$ scheme

Different from the PA scheme, which cannot be applied to concentrated systems, the renormalized concentration fluctuation (termed $\delta\gamma$) expansion method of Beenakker and Mazur [28, 29] is applicable to fluid disordered systems also at large values of ϕ, where three-body and higher-order HI contributions are important. The $\delta\gamma$ method is an effective medium approach based on a partial resummation of many-body HI contributions. While applicable at all ϕ, its results for $H(q)$ and η_∞ reveal moderate inaccuracies at all concentrations, including the very dilute regime where the PA approach becomes exact. These inaccuracies can be partially

traced back to the approximate expressions for $\mu_{lj}^{tt}(\mathbf{r}^N)$ and $\mu_{lj}^{dd}(\mathbf{r}^N)$ used in the derivation of the $\delta\gamma$-scheme where, in particular, lubrication corrections are disregarded. Higher-order terms in the $\delta\gamma$ expansion require as input static correlation functions of increasing order (pair, triplet, and so on) swiftly increasing the difficulties in their evaluation.

In the present study, we use the easy-to-implement standard version of the $\delta\gamma$ method for which (like for the PA scheme) only $S(q)$ is required as input. The latter is calculated using the MPB-RMSA scheme. This amounts to the zeroth-order $\delta\gamma$ approximation regarding $H(q)$, and the second-order $\delta\gamma$ approximation regarding η_∞.

The zeroth-order $\delta\gamma$ scheme for $H(q)$ has been applied in the past both to neutral and charged colloidal particles, but the second-order $\delta\gamma$ scheme for η_∞ was used so far for neutral hard spheres only. To our knowledge, the present work provides the first test of the $\delta\gamma$ scheme for charged, Yukawa-type particles.

The zeroth-order $\delta\gamma$-scheme expression for $H(q)$ consists of a microstructure-independent part,

$$\left.\frac{d_s(\phi)}{d_{t,0}}\right|_{\delta\gamma} = \frac{2}{\pi}\int_0^\infty dy \left[\frac{\sin(y)}{y}\right]^2 \cdot \left[1+\phi S_{\gamma_0}(y)\right]^{-1}, \tag{4.18}$$

and a structure factor dependent distinct hydrodynamic function part,

$$\left.H^d(y)\right|_{\delta\gamma} = \frac{3}{2\pi}\int_0^\infty dy' \left[\frac{\sin(y')}{y'}\right]^2 \cdot \left[1+\phi S_{\gamma_0}(y')\right]^{-1} \times \int_{-1}^{1} d\mu (1-\mu^2)\left[S(|\mathbf{q}-\mathbf{q}'|)-1\right], \tag{4.19}$$

where μ is the cosine of the angle between $\mathbf{q}$ and $\mathbf{q}'$ [168]. The function $S_{\gamma_0}(y)$, which should not be confused with the static structure factor, is given in Refs. [28, 168] as an infinite sum of wavenumber-dependent contributions with inter-related scalar coefficients $\gamma_0^{(n)}$, $n = 0\ldots\infty$. Numerical results for $\gamma_0^{(n)}$ obtained from a computation truncated at $n = 5$ have been given in Tab. 1 of the original paper by Beenakker and Mazur [28]. Taking advantage of the nowadays available computing power, we have been able to extend these earlier computations to more terms with truncations at $n = 10$ and 15. However, our more accurate results for $\gamma_0^{(n)}$ differ from the original results by Beenakker and Mazur by no more than 3%, and the differences in $H^d(y)|_{\delta\gamma}$, $d_s(\phi)|_{\delta\gamma}$, and $\eta_\infty|_{\delta\gamma}$ are in fact negligible for all practical purposes. In Appendix D, the definition of the function S_{γ_0} is given, along with our table of the coefficients $\gamma_0^{(n)}$, truncated at $n = 10$.

The high-frequency limiting viscosity in the second-order $\delta\gamma$-scheme is given by [29]

$$\left.\frac{\eta_\infty}{\eta_0}\right|_{\delta\gamma} = \frac{1}{\lambda_0+\lambda_2}, \tag{4.20}$$

$$\lambda_0 = \left[1+\frac{5}{2}\phi\tilde{\gamma}_0^{(2)}\right]^{-1} = 1-\frac{5}{2}\phi+\frac{215}{168}\phi^2+\mathcal{O}(\phi^3), \tag{4.21}$$

$$\lambda_2 = \frac{30\phi}{4\pi}\left[\lambda_0\tilde{\gamma}_0^{(2)}\right]^2\int_0^\infty dy\,\frac{j_1^2(y/2)\,[S(y/\sigma)-1]}{1+\phi S_{\gamma_0}(y/2)}, \tag{4.22}$$

where $\tilde{\gamma}_0^{(2)} = \gamma_0^{(2)}/n = 1+167/84\phi+\mathcal{O}(\phi^2)$.

Evaluation of the low-concentration expansion in Eq. (3.7) gives $S_1^{\rm HS}(y) = 1-24\phi\, j_1(y)/y+\mathcal{O}(\phi^2)$ for the static structure factor of neutral hard spheres. Insertion of $S_1^{\rm HS}(y)$ into Eqs. (4.18), (4.19), and (4.20) gives, after a straightforward calculation, the first-order virial expansion results

$$\left.\frac{d_s^{\rm HS}}{d_{t,0}}\right|_{\delta\gamma} = 1-\frac{131}{56}\phi+\mathcal{O}(\phi^2) \approx 1-2.339\phi+\mathcal{O}(\phi^2), \tag{4.23a}$$

$$\left.K^{\rm HS}\right|_{\delta\gamma} = 1-\frac{411}{56}\phi+\mathcal{O}(\phi^2) \approx 1-7.339\phi+\mathcal{O}(\phi^2), \tag{4.23b}$$

$$\left.\frac{\eta_\infty^{\rm HS}}{\eta_0}\right|_{\delta\gamma} = 1+\frac{5}{2}\phi+\frac{1255}{168}\phi^2+\mathcal{O}(\phi^3) \approx 1+\frac{5}{2}\phi+7.47\phi^2+\mathcal{O}(\phi^3), \tag{4.23c}$$

as predicted by the $\delta\gamma$ scheme. The magnitudes of the linear virial coefficients of $d_s^{\rm HS}/d_{t,0}$ and $K^{\rm HS}$, and of the quadratic coefficient of $\eta_\infty^{\rm HS}/\eta_0$, overestimate the precise values given in Eqs. (4.17a), (4.17b), and (4.17c) by 28%, 12%, and 49% respectively. The effect of HIs on these quantities on the pair-level is thus overestimated by the $\delta\gamma$ scheme. Clearly, the PA scheme is the method of choice when dilute systems are considered. We note further that $H^d_{\delta\gamma}(q\to 0) = -5\phi+\mathcal{O}(\phi^2)$ for hard spheres, a result quite close to the exact result of $H^d(q\to 0) = -4.714\phi+\mathcal{O}(\phi^2)$. This indicates that the zeroth-order $\delta\gamma$ scheme is in general a better approximation for the distinct part, $H^d(q)$, of the hydrodynamic function than for its self-part d_s.

Interestingly enough, the first-order in ϕ result for $H^d(q\to 0)$ for hard-spheres predicted by the $\delta\gamma$-scheme, is identical to the one obtained from the Rotne-Prager (RP) approximation of the HIs, where only the leading order monopole and dipole terms in the $1/x$ expansion of μ_{lj}^{tt} are retained. For hard spheres, the first-order virial expansion result, $H(q_m) = 1-1.35\phi$, for the principal peak height of $H(q)$ remains valid to high accuracy up to the volume fraction $\phi_f = 0.494$ at freezing [23], whereas in the RP approximation, peak values of $H(q)$ larger

than one are predicted. The main reason for this failure of the RP approximation lies in its prediction of $d_s = d_{t,0}$ at all ϕ, whereas the actual d_s of hard spheres is significantly decreasing with increasing ϕ, down to the value $d_s^{\rm HS}(\phi_f) \approx 0.2 \times d_{t,0}$ at freezing [23, 169].

In low-salinity charge-stabilized systems at low concentrations, where $q_m\sigma \approx 2\pi\sigma n^{1/3} \ll 1$, the $\delta\gamma$-scheme gives predictions for $H^d(q)$ close to those by the RP approximation. Indeed, these are precisely the systems where the RP approximation can be expected to perform well, explaining in part the overall success of the $\delta\gamma$ scheme in making reliable predictions for the distinct part of $H(q)$ for charge-stabilized systems.

4.4 Self-part corrected $\delta\gamma$-scheme

The key observation regarding the zeroth-order $\delta\gamma$ expression for $H^d(q)$ is that it gives overall good results both for neutral and charged Yukawa-type spheres. In contrast, the zeroth-order $\delta\gamma$ expansion for d_s in Eq. (4.18) depends on ϕ only, independent of the employed pair-potential. Comparisons with accelerated Stokesian Dynamics (ASD) simulation results [23], and experimental data for d_s for charged colloids [16, 170], show that Eq. (4.18) is a decent approximation of d_s for neutral hard spheres only.

The self-diffusion coefficient of charged spheres is in fact larger than the one for neutral spheres at the same ϕ [171], since for the latter near contact configurations are more likely. Using leading-order far-field mobilities applicable to strongly charged colloids characterized by $q_m \propto \phi^{1/3}$, one finds the limiting concentration scaling predictions [16, 22, 171–174],

$$K \approx 1 - a_s\,\phi^{1/3} \tag{4.24a}$$

$$d_s/d_{t,0} \approx 1 - a_t\,\phi^{4/3} \tag{4.24b}$$

$$H(q_m) \approx 1 + p_m\,\phi^{1/3}, \tag{4.24c}$$

differing qualitatively from the regular hard-sphere virial results in Eqs. (4.17). The coefficients $a_s \simeq 1.4 - 1.8$ and $a_t \simeq 2.5 - 2.9$ in the fractional power laws vary to a certain extent with the particle sizes and charges. The coefficient $p_m > 0$ depends also on Z and κa [23, 120]. All coefficients are typically larger for more structured suspensions, signalled by a higher value of $S(q_m)$. As we will show, the concentration interval $\phi \lesssim 0.1$ where Eq. (4.24b) for d_s applies, is broader than the corresponding intervals for the collective properties K and $H(q_m)$.

For suspensions of strongly charged spheres where $\phi \lesssim 0.15$, it has been shown [16] that the PA result for d_s in Eq. (4.11) is in better agreement with ASD simulation results and experimental data than the corresponding $\delta\gamma$-scheme result based on Eq. (4.18). For larger concentrations $\phi \gtrsim 0.15$, the PA scheme overestimates the slowing hydrodynamic influence on d_s, since it does not account for the shielding of the HIs in pairs of particles by other intervening particles. Hydrodynamic shielding is a many-body effect which lowers the strength but

not the range of the HIs. It should be distinguished from the screening of HIs by spatially fixed obstacles or boundaries which absorb momentum from the fluid, thereby causing a faster than $1/r$ decay of the flow perturbation created by a point-like force. The neglect of hydrodynamic shielding (i.e., of three-body and higher-order HIs) by the PA scheme is more consequential for the sedimentation coefficient K than for d_s. To K, the PA scheme is applicable to decent accuracy only up to $\phi \approx 0.1$ [16], whereas for larger ϕ, K becomes increasingly underestimated. The coefficient d_s, on the other hand, is less sensitive to the neglect of higher-order HI contributions, since the leading-order far-field contributions to $x_{11}^a(x)$ and $y_{11}^a(x)$ are of $\mathcal{O}(x^{-4})$, i.e., of shorter range than the leading-order $\mathcal{O}(x^{-1})$ contribution to K.

As a simple improvement over the zeroth-order $\delta\gamma$ scheme for the $H(q)$ of charged particles, which preserves its analytic simplicity, we therefore use the self-part corrected expression

$$H(y)|_{\delta\gamma_{\text{corr}}} = \left.\frac{d_s}{d_{t,0}}\right|_{\text{PA}} + H^d(y)\Big|_{\delta\gamma}, \tag{4.25}$$

with d_s according to Eq. (4.11) and $H^d(q)$ according to Eq. (4.19), bearing in mind that $[d_s/d_{t,0}]_{\text{PA}}$ is less reliable for $\phi \gtrsim 0.15$.

For the limiting case of neutral hard spheres at larger ϕ, it is therefore preferential to use in place of $[d_s/d_{t,0}]_{\text{PA}}$ the accurate expression,

$$\left.\frac{d_s}{d_{t,0}}\right|^{HS} \approx 1 - 1.8315\phi\left(1 + 0.1195\phi - 0.70\phi^2\right) \tag{4.26}$$

which, for $\phi \leq 0.5$, agrees well with ASD [23] and hydrodynamic force multipole [175] results, with an accuracy better than 3%. Note that the linear and quadratic order coefficients in Eq. (4.26) have been selected identical to the numerically precise values -1.8315 and $-0.219 = -1.8315 \times 0.1195$, of the respective virial coefficients derived in Ref. [165]. We have determined the cubic coefficient in Eq. (4.26) from a best fit to recent simulation results in [175] and [23]. The coefficient 0.70 differs somewhat from the coefficient 0.65 in Ref. [175], where simulation results only up to $\phi \leq 0.45$ were considered.

A self-part corrected version of the $\delta\gamma$ scheme for $H(q)$ was used already in earlier applications, where d_s was considered simply as an adjustable parameter [168], or in more recent work where it was determined using elaborate ASD simulations [23]. For practical purposes, however, it is far more convenient to use the analytic d_s corrections in Eqs. (4.11), (4.25) and (4.26). In the present work, numerous ASD simulation results for $H(q)$, d_s, and η_∞ have been generated to provide precise benchmarks for assessing the accuracy of the proposed self-part corrected $\delta\gamma$ scheme (see Chapter 6).

While the $\delta\gamma$ scheme for $H(q)$ has been used already for charge-stabilized colloids, to our knowledge the application of the $\delta\gamma$ scheme for η_∞ in Eqs. (4.20)-(4.22) was restricted so far to colloidal hard spheres, where the predicted values for $\eta_\infty(\phi)$ are in good agreement, for $\phi \lesssim 0.4$, with experiments and simulation data. In Section 6.1.4, we are going to assess the

performance of the $\delta\gamma$-scheme expression for the η_∞ of charged particles by comparison with ASD simulation data. Our analysis shows that the second-order $\delta\gamma$ contribution, $\lambda_2(\phi) < 0$, to η_∞/η_0 is only weakly dependent on the shape of the static structure factor. Moreover, the zeroth-order contribution, $\lambda_0(\phi) > 0$, which is dependent on ϕ only, dominates for small ϕ the contribution λ_2. As a consequence, the $\delta\gamma$-predicted values for η_∞ change only slightly when going from neutral to charged particles, whereas simulations and experiments [176] reveal significantly smaller viscosity values, in particular at low salinities. Thus, the $\delta\gamma$-scheme result in Eqs. (4.20)-(4.22) applies to neutral hard spheres only. However, for the interesting case of low-salinity systems, where the viscosity differences to neutral spheres at equal concentration are largest, the $\delta\gamma$ scheme can be modified (corrected) in an ad-hoc way, according to

$$\left.\frac{\eta_\infty}{\eta_0}\right|_{\delta\gamma_{\rm corr}} = 1 + \frac{5}{2}\phi(1+\phi) - \frac{1}{\lambda_0} + \frac{1}{\lambda_0+\lambda_2}. \tag{4.27}$$

The motivation for this correction follows from the PA expression in Eq. (4.15): For a low-salinity system of strongly repelling particles, one has the scaling relation $r_m \propto \phi^{-1/3}$ for the peak position, r_m, of the rdf, where $g(r \lesssim r_m) \approx 0$. Since $J(x) \sim \mathcal{O}(x^{-6})$, for these systems the integral in Eq. (4.15) is of $\mathcal{O}(\phi^3)$. Hence, to quadratic order in ϕ, η_∞ is determined basically by the microstructure-independent contribution, $1 + 2.5\phi(1+\phi)$, to Eq. (4.15).

In Eq. (4.27), we correct approximately for this limiting behavior of η_∞ by subtracting the structure-independent "self part", $1/\lambda_0$, from $[\eta_\infty/\eta_0]_{\delta\gamma}$, which renders the remainder of $\mathcal{O}(\phi^2)$ small, while adding the term $1 + 2.5\phi(1+\phi)$. As we will show in the following, the so-corrected $\delta\gamma$ scheme is in very good agreement with the ASD viscosity data of low-salinity systems, even up to the freezing transition concentration. We point out here that Eq. (4.27) is restricted in its applicability to the low-salinity regime of strongly repelling particles. In contrast, the d_s-corrected $\delta\gamma$-scheme for $H(q)$ in Eq. (4.25) applies to HSY systems for any set of system parameters $\{\gamma, k, \phi\}$, provided $\phi \lesssim 0.15$, including the crossover regime from neutral to deionized, highly charged particle systems. For neutral hard spheres, the (uncorrected) $\delta\gamma$ scheme for η_∞ performs quite well.

The design of a simple, corrected $\delta\gamma$ scheme which operates well for arbitrary $\{\gamma, k, \phi\}$, including systems of intermediate salinity, is obstructed by the limited separability of λ_0 and λ_2 which are both of $\mathcal{O}(\phi^2)$ in general, and by significant many-body HI contributions for more concentrated systems of nearly hard-sphere-like particles at high salinity. For small values $\phi \lesssim 0.1$, the PA method can be used to produce reliable predictions of η_∞, for arbitrary salinities.

4.5 Mode-coupling expressions for long-time dynamic properties

Various types of dynamic properties can be approximately calculated in the long-time regime $t \gg \tau_I$ using the mode-coupling theory (MCT) of Brownian systems. For introductory texts on MCT, the interested reader is referred to Refs. [4, 177, 178]. Note that the emphasis of the present work lies on the short-time dynamic properties of colloidal particles, with no efforts invested to further develop the MCT of long-time diffusion and rheology. However, some of the experiment results discussed further down, namely the rheologic and dynamic scattering data from BSA protein solutions and gibbsite platelet suspensions, have been recorded in the long-time regime. Since dynamic properties like the self-diffusion coefficient and the effective suspension viscosity can be quite different regarding their short-time and long-time values, we have included MCT results to our theoretical modeling, with a partial account of far-field HIs.

The BSA protein solutions and gibbsite platelet suspensions considered in the present thesis are rather dilute, with structure factor maxima $S(q_m) \lesssim 1.7$. Therefore, simplified MCT expressions with approximate account, or even without HIs, can be reasonably applied.

4.5.1 Long-time self-diffusion coefficient

As sketched in Fig. 4.1, the long-time self-diffusion coefficient is defined as $d_s^L = \lim_{t\to\infty} dW(t)/dt$, *i.e.* by the long-time slope of the mean-squared displacement. Including far-field HIs up to the dipolar Rotne-Prager level, the simplified implicit MCT expression

$$\frac{d_s^L}{d_{t,0}} = \left[1 + \frac{1}{36\pi\phi}\int_0^\infty dq\, q^2 S(q) \frac{\left[1 - H^{\mathrm{RP}}(q)/S(q)\right]^2}{d_s^L/d_{t,0} + H^{\mathrm{RP}}(q)/S(q)}\right]^{-1}, \tag{4.28}$$

for d_s^L has been derived in [179]. The integral in Eq. (4.28) is convergent only provided that that $d_s/d_{t,0} = H(q \to \infty) = 1$. On the RP ($\mathcal{O}(x^{-3})$) level, this requirement is fulfilled since the leading-order far-field contribution to d_s is of $\mathcal{O}(x^{-4})$ (see Eq. (4.11) and Tab. C.1). In evaluating Eq. (4.28) applicable to rather dilute suspensions, for $H_d(q)$ one can use the $\delta\gamma$-scheme result which, to first order in ϕ, is equal to $H_d^{\mathrm{RP}}(q)$. Starting from an initial seed $d_s^L = d_{t,0}$, Eq. (4.28) can be solved iteratively for d_s^L, requiring usually less than ten iterations to converge to a relative residual of 10^{-4}.

4.5.2 Static shear viscosity

In long-time rheological measurements on colloidal suspensions under low-amplitude steady shear, there is a non-zero shear-stress relaxation part, $\Delta\eta$, contributing to the static viscosity $\eta = \eta_\infty + \Delta\eta$. This contribution is influenced both by HIs and direct interaction forces. While a version of the MCT for $\Delta\eta$ with far-field HIs has been discussed already in earlier work

together with an extension to multicomponent systems [180], for analytical simplicity we use here the standard one-component expression

$$\Delta\eta^{MCT} = \frac{k_B T}{60\pi^2} \int_0^\infty dt \int_0^\infty dq\, q^4 \left[\frac{S(q,t)}{S(q)} \frac{d}{dq} \log S(q) \right]^2, \tag{4.29}$$

as derived, *e.g.*, in Ref. [180] under the neglect of HIs. In principle, $\Delta\eta^{MCT}$ should be calculated self-consistently in combination with the corresponding MCT memory equation for $S(q,t)$ [119]. However, as we have thoroughly checked in comparison to fully self-consistent MCT calculations, for systems with rather weakly coupled particles, $\Delta\eta^{MCT}$ can be obtained more simply in a first iteration step where $S(q,t)$ in the integral of Eq. (4.29) is approximated by its short-time form $S(q,t)/S(q) = \exp[-q^2 d_{t,0}\, t/S(q)]$, valid without HI.

For the weakly coupled systems to which the first iteration solution as described by Eq. (4.29) applies, $\Delta\eta$ augments η_∞ by a small relative amount. For example, $\Delta\eta < 0.1 \times \eta_\infty$ in case of the BSA solutions studied in this thesis. Therefore, the neglect of HIs in $\Delta\eta^{MCT}$ can be expected to be rather insignificant for the systems considered, since the dominant effect of HIs is included already in η_∞. Theoretical results for η shown in the present work are all based on the first iteration solution for $\Delta\eta^{MCT}$, and on η_∞ calculated using the self-part corrected $\delta\gamma$ or PA schemes.

CHAPTER

FIVE

Pair-structure results: Theory, simulation and experiment

5.1 Validation of the MPB-RMSA using simulations and alternative closures

5.1.1 Monte Carlo computer simulation results

The Monte Carlo simulations for suspensions of colloidal hard-sphere Yukawa particles, with results presented in this chapter, and related accelerated Stokesian Dynamics simulations with results presented in Chapter 6, have been performed by Prof. Adolfo J. Banchio at the National University of Córdoba, Argentina, within our joint theoretical-computer simulation project.

The MC simulations were performed using in general $N = 512$ particles interacting via the pair potential in Eq. 2.6, placed in a periodically repeated cubic simulation box. In strongly correlated particle systems with long-range Yukawa repulsion, a larger number of $N = 800$ particles was used, to gain improved statistics and resolution of the principal peak region of $S(q)$.

5.1.2 Systems with strong Yukawa repulsion

Systems with strong Yukawa repulsion, where $\beta u(\sigma^+) = \gamma \exp\{-k\} \gg 1$, are characterized by a (practically) zero likelihood for contact configurations so that the hard core plays no role. Strong Yukawa repulsion of colloidal particles is observed for large charge numbers and sufficiently low salt concentrations.

As a representative class of colloidal systems with strong and long-ranged Yukawa repulsion, we consider here spheres of diameter $\sigma = 200$ nm and effective charge number $Z = 100$, immersed under zero-added salt conditions ($n_s = 0$) in a weakly polarizable solvent ($\varepsilon = 10$,

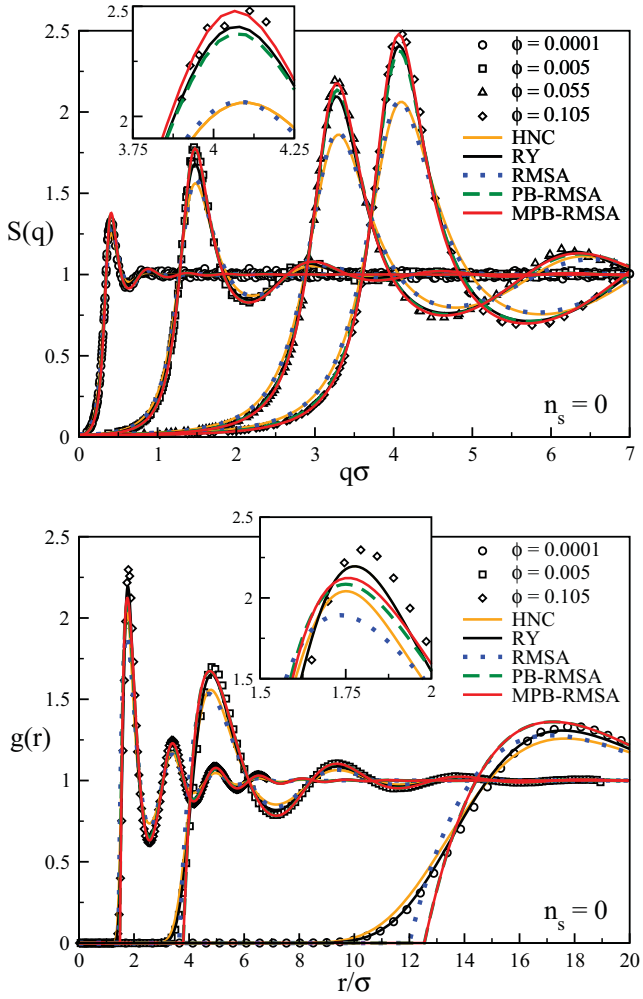

Fig. 5.1: *Static structure factor, $S(q)$, and radial distribution function, $g(r)$, of a zero-salinity system at volume fractions, ϕ, as indicated. Open symbols: MC simulation data. Orange and black solid lines, blue dotted curves, green dashed curves, and red solid lines: HNC, RY, RMSA, PB-RMSA, and MPB-RMSA scheme results, respectively. For $\phi = 0.055$, $g(r)$ is not shown to avoid obstructing the figure. The insets magnify the principal peak regions of the most concentrated system. The corresponding hydrodynamic functions are plotted in Fig. 6.1. System parameters are: $Z = 100, L_B = 5.62$ nm, $\sigma = 200$ nm.*

$T = 297$K) of Bjerrum length $L_B = 5.62$ nm. For these parameters, the potential at contact is typically quite large, *e.g.* $\beta u(x = 1^+) = 260$ for $\phi = 10^{-4}$, and $\beta u(x = 1^+) = 140$ for $\phi = 0.105$. Fig. 5.1 shows integral equation and MC simulation results for $S(q)$ and $g(r)$ at various volume fractions. The considered volume fractions from $\phi = 10^{-4}$ to 0.105 cover the concentration range from dilute systems with moderate particle correlations up to more concentrated systems with strong pair correlations. MC simulation results are represented in Fig. 5.1 by open symbols. Orange and black solid lines represent the HNC and RY schemes, respectively. Blue dotted curves are RMSA, green dashed curves unmodified PB-RMSA, and red solid lines are MPB-RMSA results.

The depicted RMSA curves in Fig. 5.1 are in fair qualitative agreement with the MC generated results for $g(r)$ and $S(q)$. As expected, the RMSA underestimates the principal peak heights $S(q_m)$ and $g(r_m)$. The HNC approximation improves only slightly the accuracy of the RMSA. The RY-scheme, on the other hand, is in excellent agreement with the MC data at all considered ϕ. It slightly underestimates the MC-$S(q_m)$ for the largest considered concentration only.

The MPB-RMSA and PB-RMSA results are in very good overall agreement with the MC data, except for a kink in $g(r)$ at the rescaled diameter which becomes most noticeable at low concentrations, and except for a slight underestimation of $g(r_m)$ at larger ϕ. The MPB-RMSA and the PB-RMSA results coincide at low ϕ but, as a general rule, the MPB-RMSA performs better at larger volume fractions. At $\phi = 0.105$, the MPB-RMSA happens to predict a principal peak height, $S(q_m)$, in even better agreement with the simulation data than the RY scheme.

The discussed characteristics of the considered integral equation scheme results persist when the concentration, n_s, of added 1-1 electrolyte is increased. This is demonstrated in Figs. 5.2 and 5.3, where $S(q)$ and $g(r)$ are plotted for the same system as in Fig. 5.1, but now using volume fractions $\phi = 0.055$, 0.105, and 0.15, and coion concentrations $n_s = 10^{-6}$, 10^{-5}, and 10^{-4} M. To allow for a straightforward comparison, both in Figs. 5.2 and 5.3 identical axis scales are used in the nine panels. The panels are ordered by ϕ increasing from top to bottom, and by n_s decreasing from left to right. Thus, interparticle correlations increase from left to right, and from top to bottom. In Figs. 5.2 and 5.3, the same color code is used for the various employed methods as in Fig. 5.1. Results by the unmodified PB-RMSA scheme are not included in Figs. 5.2 and 5.3 to not obstruct the figures.

The rightmost columns of panels in Figs. 5.2 and 5.3 present results for three systems of strongly charged particles with a very low residual, but experimentally still accessible, salt content. In the most concentrated system in panel (i), for which $\phi = 0.15$ and $n_s = 10^{-6}$ M, a peak value $S(q_m) \approx 2.5$ is attained according to the MC simulations. The very same peak value is predicted by the MPB-RMSA and RY integral equation schemes. According to the empirical Hansen-Verlet freezing rule, the system in panel (i) is rather close to the freezing transition point [103, 181, 182]. The screening parameter k assumes rather low values of 2.67, 3.24, and 3.68 in panels (c), (f), and (i), and the corresponding ratios k_c^2/k_s^2 are 1.1, 2.1, and

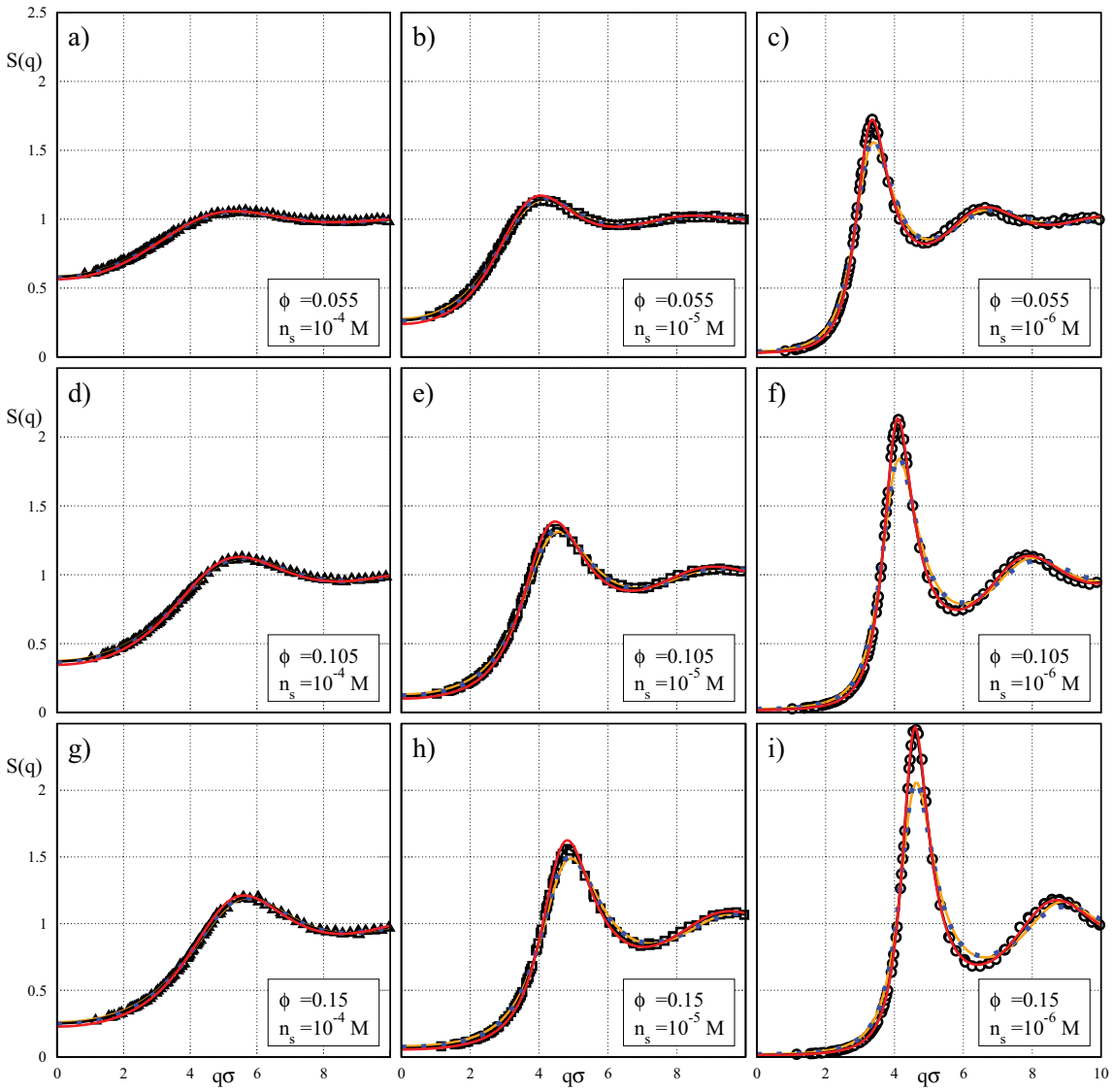

Fig. 5.2: *Static structure factor for systems of various volume fractions, ϕ, and salt concentrations, n_s, as indicated in each panel. The panels are ordered by ϕ, which increases from top to bottom, and by n_s, decreasing from left to right. Open symbols: MC simulations. Orange and black solid lines, blue dotted curves, and red solid lines: HNC, RY, RMSA, and MPB-RMSA scheme results, respectively. Corresponding radial distribution functions and hydrodynamic functions are displayed in Figs. 5.3 and 6.2. System parameters are: $L_B = 5.617$ nm, $\sigma = 200$ nm, and $Z = 100$.*

3.0, respectively. The rather high values for k_c^2/k_s^2 indicate that salt microions play a minor role in the electrostatic screening, which is dominated instead by the surface-released counterions.

In the leftmost columns of panels, the salt concentration $n_s = 10^{-4}$ M is chosen so large that electrostatic repulsion is almost fully screened. This can be noticed from the rdfs in panels (a), (d), and (g) of Fig. 5.3. Similar to neutral hard spheres, where $x_m = r_m/\sigma = 1$, in each of theses systems $g(x_m)$ is located at $x_m \approx 1$. Other indicators for the closeness to the HS limit are the high values $k = 18.5, 18.6$, and 18.7 of the screening parameter, and the low ratios $k_c^2/k_s^2 = 0.01, 0.02$, and 0.03, corresponding to panels (a), (d), and (g), respectively.

The added-salt systems in Figs. 5.2 and 5.3 exemplify our general observation that the MPB-RMSA slightly overestimates the pair ordering at intermediate salt concentrations. At the largest considered salinity $n_s = 10^{-4}$ M, *i.e.* in the leftmost columns of panels in Fig. 5.3, both the RY and HNC schemes predict a small but non-zero contact value, whereas $g(x = 1^+) = 0$ according to the MSA-based schemes. Except for a narrow interval at $r \approx \sigma$, the rdfs of all considered integral equation schemes agree with each other in the high-salinity case. The rdf in panel (a) of Fig. 5.3, where $\phi = 0.055$ and $n_s = 10^{-4}$ M, has a visible maximum $g(x_m) > 1$ at the nearest-neighbor shell distance $x_m \approx 1.2$. This clearly distinguishes it from the infinite dilution limit, $g_0(x) = \exp\{-\beta u(x)\}$, which has no maximum at finite x.

5.1.3 Systems with non-zero contact values

Complementary to the strong Yukawa coupling regime where $g(x = 1^+) \approx 0$, there is the regime of weak Yukawa repulsion characterized by non-zero contact values. For weak Yukawa coupling is $\gamma e^{-k} \lesssim 1$, which for the DLVO parameters in Eqs. (2.5) holds true for sufficiently low Z and sufficiently large coion concentrations n_s. Even for a non-zero probability of two macroions in contact, in many cases there is still a principal maximum $g(x_m) > g(1^+)$ at $x_m > 1$. caused by the Yukawa tail. This clearly distinguishes these systems from neutral hard-sphere suspensions where $\gamma = 0$ or $k \to \infty$ (see Fig. 5.5 for an example). HSY systems with non-zero contact values are difficult to realize experimentally, since for colloids, *e.g.*, one needs to worry about residual van der Waals forces which become strong at contact. Irrespective of any experimental realizations, it is of interest to test the performance of the (M)PB-MSA under conditions where no rescaling is required. We do this in the following by a comparison with MC simulations and RY calculations.

We start by investigating the contact value of the rdf which, in the weak coupling regime, is an indicator for the accuracy of an integral equation scheme. In Fig. 5.4, we present results for $g(x = 1^+)$ by the various integral equation schemes in comparison to MC data. The system parameters are representative of a low-salinity, aqueous solution of nano-sized apoferritin proteins [41]. Three different effective charge numbers, $Z = 36$, 20.5 and 1, are considered.

For $Z = 1$, the limit of neutral hard spheres is practically reached, with tiny differences in the hard-sphere contact value only. For hard spheres, $g_{\rm HS}(x = 1^+) = (1 - 0.5\phi)/(1 - \phi)^3$ according to the Carnahan-Starling equation of state [4, 7]. In the limit of zero Yukawa coupling

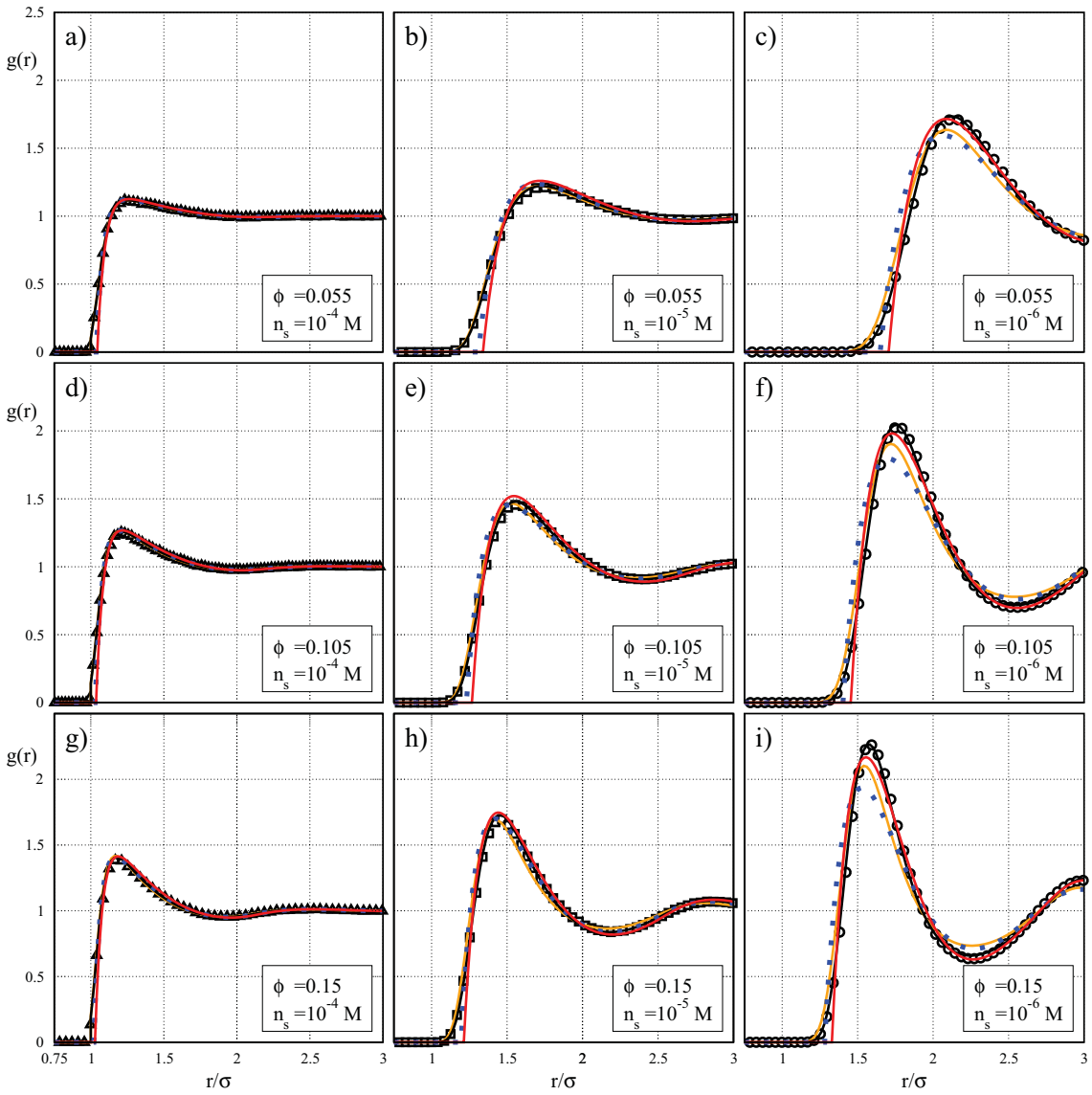

Fig. 5.3: *Radial distribution function $g(r)$ for systems of various volume fractions, ϕ, and salt concentrations, n_s, as indicated in each panel. The panels are ordered by ϕ, which increases from top to bottom, and by n_s, decreasing from left to right. Open symbols: MC simulations. Orange and black solid lines, blue dotted curves, and red solid lines: HNC, RY, RMSA, and MPB-RMSA scheme results, respectively. Corresponding static structure factors and hydrodynamic functions are displayed in Figs. 5.2 and 6.2. System parameters are: $L_B = 5.617$ nm, $\sigma = 200$ nm, and $Z = 100$.*

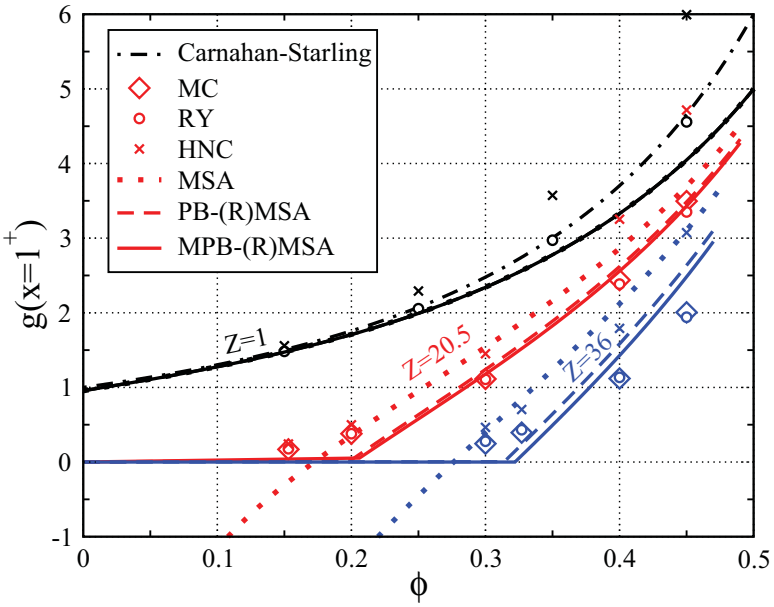

Fig. 5.4: *Rdf contact value $g(x = 1^+)$, obtained by MC simulation (diamonds), RY (circles), HNC (crosses), MSA (dotted lines), PB-(R)MSA (dashed lines), and MPB-(R)MSA (solid lines). Black (top): $Z = 1$, red (middle): $Z = 20.5$, blue (bottom): $Z = 36$. Dashed-dotted black line: Carnahan-Starling contact value for hard spheres. Common parameters are: $L_B = 0.71$ nm, $\sigma = 13.8$ nm, and $n_s = 10^{-5}$ M.*

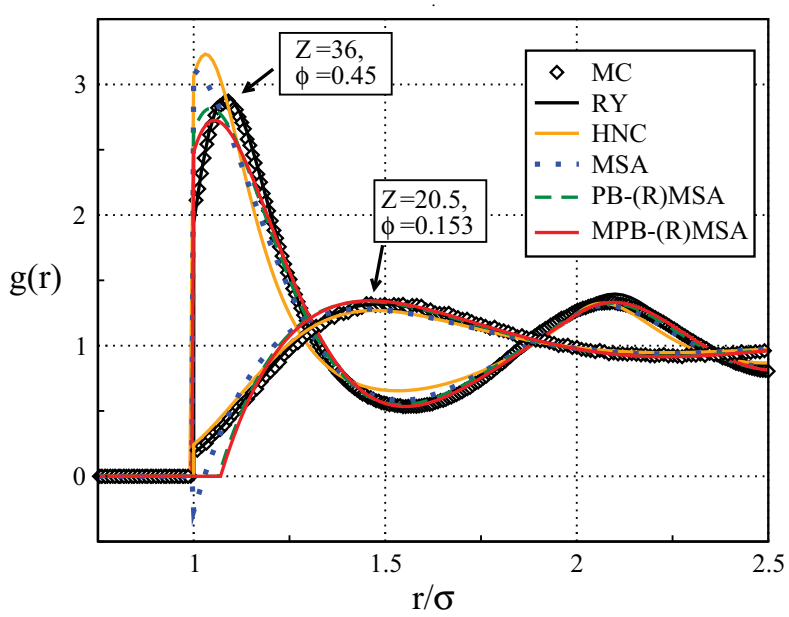

Fig. 5.5: *Radial distribution function $g(r)$ for two systems selected from Fig. 5.4. Common parameters are: $L_B = 0.71$ nm, $\sigma = 13.8$ nm, and $n_s = 10^{-5}$ M. Charge numbers and volume fractions as indicated.*

($Z = 0$), the (M)PB-MSA and the MSA reduce to the Percus-Yevick solution for hard spheres, which is known to underestimate the exact $g_{\mathrm{HS}}(x = 1^+)$ at larger volume fractions (*i.e.*, for $\phi \gtrsim 0.35$). On the other hand, the RY predictions for $g(r)$, including the contact value, are in excellent accord with the MC simulation results, for all considered values of Z (see Fig. 5.5). The HNC is known to deteriorate in its accuracy when systems with shorter-ranged repulsive potentials are considered, in predicting a too pronounced nearest neighbor shell and a too large contact value of the rdf.

The supremacy of the (M)PB-MSA schemes over the MSA in the no-rescaling regime of positive contact values shows up most clearly when the charge number is increased so that the electrostatic and excluded volume interactions are of comparable importance. Our analysis of a large number of systems with finite contact values and various charge numbers, hard-core diameters, and electrolyte concentrations has revealed that all three MSA-based schemes tend to overestimate the increase of $g(x = 1^+)$ with increasing ϕ as described by the MC and RY methods, when $\gamma e^{-k} \gtrsim 3.0$. Among all MSA-based schemes, the weakest overestimation is observed for the MPB-(R)MSA method. See for example the system with $Z = 36$ in Fig. 5.4.

Consider next the rdf of a dense system at $\phi = 0.45$ and $Z = 36$, as depicted in Fig. 5.5. For this system, $g(x = 1^+) = 2.01$, 2.48 and 2.64 in MC, MPB-MSA and PB-MSA, respectively. While the MPB-MSA performs better than the PB-MSA regarding the contact value,

the primary Yukawa-tail peak of $g(x)$ at $x_m > 1$ is slightly more underestimated by the modified PB-MSA version. A general observation for systems with weak Yukawa coupling is that, while contact and Yukawa-tail peak values are not precisely reproduced, the overall shape of the (M)PB-MSA rdf is still in good accord with the MC and RY results.

5.1.4 Test of thermodynamic consistency

Out of all integral schemes considered in this thesis, the RY scheme is the only one being thermodynamically self-consistent regarding the osmotic compressibility. By its construction, the zero-q limiting value of the RY static structure factor agrees with the concentration derivative, $\beta\,(\partial p_v/\partial n)_T$, of the virial pressure in Eq. (3.28). In taking the derivative, a possible concentration dependence of $u(r)$ and the RY-mixing parameter has been ignored (see the discussion in Section 3.4).

We can use the RY results for $S(q \to 0)$ as accurate reference values to quantify the degree of thermodynamic inconsistency for each of the other considered integral equation schemes, by comparing the results for $S(q \to 0)$ with those for $k_BT\,(\partial n/\partial p_v)_T$, the latter obtained by a numerical differentiation of the virial pressure p_v as done also in the RY case.

In a HSY system with strong and long-range Yukawa repulsion, $S(q \to 0)$ attains values close to zero. Therefore, to clearly reveal the differences, in Fig. 5.6 we plot the predictions for $1/S(q \to 0)$ (solid lines) by the various integral equation schemes along with the corresponding results for $\beta\,(\partial p_v/\partial n)_T$ (dashed lines). The system parameters $L_B = 8.64$ nm, $\sigma = 200$ nm, $n_s = 10^{-6}$ M, and $Z = 200$ are representative of a low-salinity system of strongly repelling macroions. The volume fraction interval covers the complete fluid-phase regime up to $\phi = 0.15$, with a peak height $S(q_m) \approx 3.1$ where, according to the empirical Hansen-Verlet freezing rule, a system with long-range Yukawa repulsion is close to the freezing transition point [103, 181, 182].

In Fig. 5.6, it can be noted that all considered integral equation schemes except for the RY scheme are thermodynamically inconsistent, with the relative difference between compressibility and virial results extending up to 53% for the HNC, 45% for the RMSA, 34% for the PB-RMSA, and 24% for the MPB-RMSA. The self-consistent RY result for the inverse reduced compressibility is bracketed by the HNC, RMSA and PB-RMSA solutions, but not by the MPB-RMSA results. The predictions for $1/S(q \to 0)$ by the various schemes grow roughly linear in concentration for $\phi > 0.025$, where $\phi \approx 0.025$ is the concentration value for which $k_s = k_c$.

Fig. 5.6 shows that, as a consequence of the improvement of the RMSA-predicted pair structure by the modified PB correction, also the degree of thermodynamic consistency is improved. Unlike HNC and RMSA, the MPB-RMSA result for $S(q \to 0)$ is in reasonably good accord with the RY data even up to the freezing concentration. Thus, the MPB-RMSA can be used to obtain a quick estimate of the (osmotic) compressibility. However, if quantitative accuracy is required at $q \to 0$, the RY-method is still the method of choice.

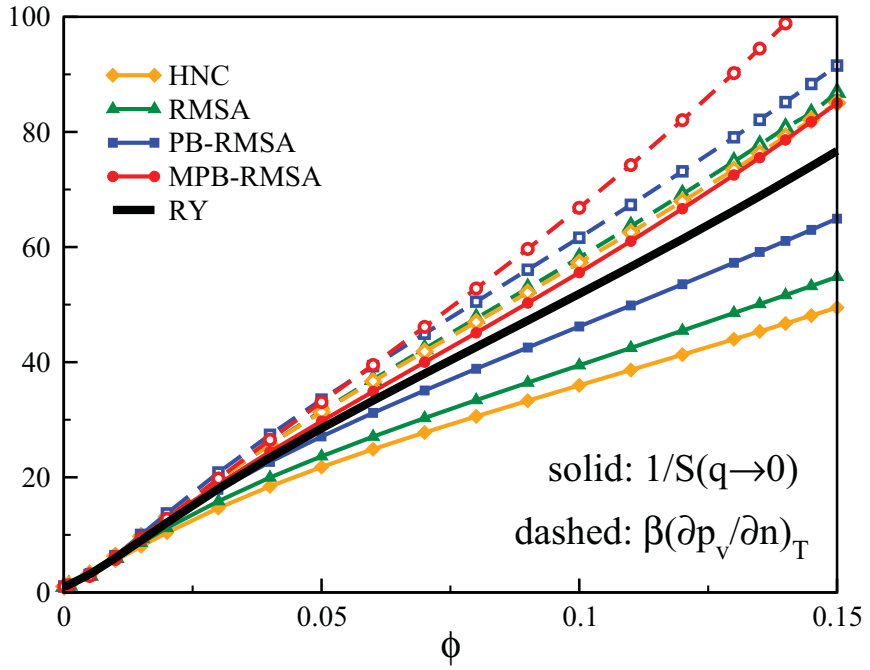

Fig. 5.6: *Test of local thermodynamic consistency. Solid lines with filled symbols:* $1/S(q \to 0)$ *as a function of* ϕ*, for different integral equation schemes as indicated. Dashed lines with open symbols: corresponding predictions for* $\beta\,(\partial p_v/\partial n)_T$*, obtained from the concentration derivative of the virial pressure in Eq.* (3.28)*. System parameters are:* $L_B = 8.64$ *nm,* $\sigma = 200$ *nm,* $n_s = 10^{-6}$ *M, and* $Z = 200$*.*

5.2 Concentration scaling and fluid-phase behavior

Having established the good accuracy of the MPB-RMSA in comparison to MC and RY results, we demonstrate now its capability as a fast tool to explore generic features in the pair structure and fluid-phase behavior of HSY systems. The explorations discussed below have required extensive parameter scans. We focus in the following again on systems with strong Yukawa repulsion, characterized by $g(x = 1^+) \approx 0$.

As a first application of the MPB-RMSA, in Fig. 5.7 we investigate the generic concentration dependence of the principal peak positions at x_m and $y_m = q_m\sigma$ of $g(x)$ and $S(y)$, respectively, for suspensions of strongly charged colloidal macroions. For these systems, one expects that the particles minimize their configurational free energy by maximizing the radius of the nearest-neighbor shell. Thus, x_m should scale in concentration according to $x_m = r_m/\sigma \sim \tilde{d}/\sigma = n^{-1/3}/\sigma$, and y_m according to $y_m \sim 2\pi\sigma/\tilde{d}$.

Fig. 5.7 demonstrates that the scaling relations $x_m = \tilde{d}/\sigma$, and $y_m = 1.1 \times 2\pi\sigma/\tilde{d}$, are obeyed indeed to good accuracy, provided the coion concentration n_s is not too large, and the volume fraction is not too small. In the experimentally not realizable case of zero salinity ($n_s = 0$), the geometric scaling of the peak positions with the colloid concentration remains valid down to very low values of n. With increasing salt content, the concentration of coions eventually surpasses the concentration of surface-released counterions, leading to a significant reduction in the reduced Debye screening length, $1/k$, and the pair potential contact value $\gamma\exp(-k)$ at $x = 1$. This softens the Yukawa tail, allowing two particles to come closer than $r = n^{-1/3}$, reflected in Fig. 5.7 by deviations of x_m and y_m from the $n^{\pm 1/3}$ scaling behavior. As a crude criterion for the transition to the geometric concentration scaling behavior, we can use $k_c > k_s$, or equivalently, $n > 2n_s/|Z|$, where k_c according to Eq. (2.5b) is the contribution to k due to the monovalent counterions released from the colloid surfaces. This simple criterion is qualitatively confirmed in Fig. 5.7, where the colloid concentrations $n = 2n_s/|Z|$ are marked by short vertical lines. Note that the geometric scaling of x_m and y_m necessarily fails at very high concentrations when $\tilde{d}$ approaches σ.

For systems where x_m and y_m obey geometric concentration scaling, one might anticipate that the reduced pair structure functions

$$g_{\rm red}(R) = \frac{g(r/r_m) - 1}{g(r_m) - 1}, \tag{5.1a}$$

$$S_{\rm red}(Q) = \frac{S(q/q_m) - 1}{S(q_m) - 1}, \tag{5.1b}$$

with $R = r/r_m = x/x_m$ and $Q = q/q_m = y/y_m$, are approximately universal except for small values of their arguments. By definition, $g_{\rm red}(R)$ and $S_{\rm red}(Q)$ are equal to one at $R = Q = 1$, converging to zero for $R, Q \to \infty$. The function $S_{\rm red}(Q)$ is non-universal at $Q \approx 0$, since even for the subclass of low-compressibility systems where $S(q \to 0) \approx 0$ and $S_{\rm red}(Q \to 0) \approx$

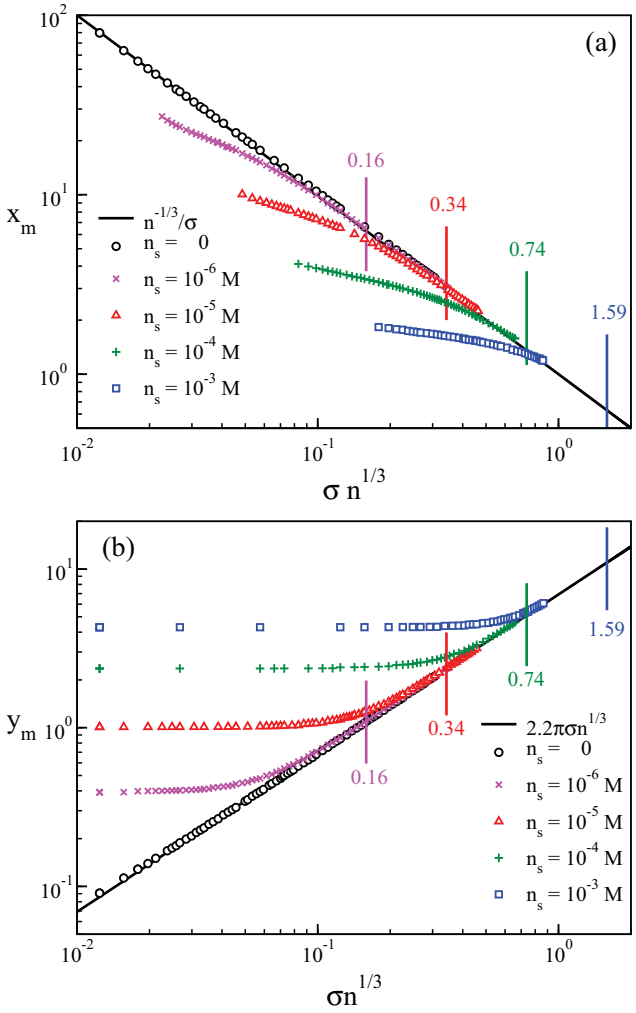

Fig. 5.7: *Dimensionless radial position, x_m, of the principal maximum in $g(x)$, and dimensionless wavenumber location, y_m, of the principal maximum in $S(y)$, plotted versus the inverse geometric pair distance $1/\tilde{d} = n^{1/3}$ in units of σ. Results for various salt contents (as indicated) were generated using the MPB-RMSA. Abscissa values where $k_s = k_c$ holds are marked by vertical lines. The parameters $L_B = 0.716$ nm, $\sigma = 100$ nm, and $Z = 300$ are representative of an aqueous suspension of strongly charged macroions.*

$-1/(S(q_m)-1)$, different values for $S_{\rm red}(Q\to 0)$ are obtained for different principal peak heights. By the same token, $g_{\rm red}(R)$ behaves non-universally at $R\approx 0$.

In Fig. 5.8, MPB-RMSA results for $g_{\rm red}(R)$ and $S_{\rm red}(Q)$ are displayed for a large number of fluid-ordered HSY systems with $S(q_m)\leq 3.2$, masked hard-core interactions, and geometric concentration scaling of x_m and y_m. There are pronounced variations in the width of the principal peaks, and in the undulations of the following minimum and maximum. The sharpest peaks are found for the most strongly structured, low-compressibility systems. These systems show additionally the largest values of $g_{\rm red}(Q\to 0)$ and $S_{\rm red}(Q\to 0)$. The figure clearly illustrates that the reduced structure functions are non-universal even away from the small argument (*i.e.*, small Q or small R) regime.

According to Eq. (3.4), a universal $g_{\rm red}(R)$ for systems where $x_m=\tilde{d}/\sigma$ would imply a linear relationship between $S(y_m)-1$ and $g(x_m)-1$. This would allow the rephrasing of the Hansen-Verlet freezing criterion for $S(y_m)$ in terms of $g(x_m)$. However, such a simple 1-1 relation between $S(y_m)$ and $g(x_m)$ does not exist in general. This will be explicitly demonstrated as a by-product of the following discussion.

Up to this point, parameters including ϕ, $n_{\rm s}\sigma^3$ and $L_{\rm B}/\sigma$ have been scanned which are to a certain extent under experimental control. However, as noted in Section 3.2, strong Yukawa systems for which $g(x=1^+)=0$ are fully characterized by two independent parameters, namely $\tilde{\gamma}$ and $\tilde{k}$ appearing in Eq. (3.9). In discussions of the phase behavior, it is more convenient to use the pair $(\tilde{T},\tilde{k})$ in place of $(\tilde{\gamma},\tilde{k})$, with the reduced temperature

$$\tilde{T}=\frac{k_{\rm B}T}{u(r=\tilde{d})}=\frac{\exp(\tilde{k})}{\tilde{\gamma}}\,, \tag{5.2}$$

measuring the thermal energy relative to the potential energy of a pair of particles at distance $\tilde{d}=n^{-1/3}$. Different sets, $\{\sigma, L_{\rm B}/\sigma, Z, n_{\rm s}\sigma^3, \phi\}$, of experimentally controllable parameters can describe the same state point $(\tilde{T},\tilde{k})$.

At this point, it is necessary to address again a peculiarity of the MPB-RMSA scheme, discussed already in Sections 3.2 and 3.3.4. In principle, a given state point $(\tilde{T},\tilde{k})$ corresponds to unique pair-structure functions $g(\tilde{x})$ and $S(\tilde{y})$, under the proviso that $g(x=1^+)\approx 0$. Here, $\tilde{y}=q\tilde{d}$, and $\tilde{x}=x/\tilde{d}$. In MPB-RMSA, however, $g(\tilde{x})$ and $S(\tilde{y})$ depend on the three parameters $(\tilde{T},\tilde{k},\phi)$, or $(\tilde{\gamma},\tilde{k},\phi)$, even when $g(x=1^+)=0$. This undesired feature of the MPB-RMSA scheme is a consequence of the rescaling in Eqs. (3.25) and (3.26), into which the (unrescaled) volume fraction ϕ enters irrespective of the value of $g(x=1^+)$, thereby violating the two-dimensional $(\tilde{T},\tilde{k})$, or $(\tilde{\gamma},\tilde{k})$, parametrization of strongly coupled HSY fluids where $g(x=1^+)\approx 0$. Hence, the shift of the strongly coupled HSY-fluid parameter space from two to three parameters is a side effect of the rescaling rules that render the MPB-RMSA into a quantitatively accurate method. This artificially enforced ϕ-dependence of the microstructure of point-Yukawa like fluids should not be confused with the ϕ-dependence that naturally occurs for HSY-fluids with non-negligible contact values $g(x=1^+)>0$. The latter class of

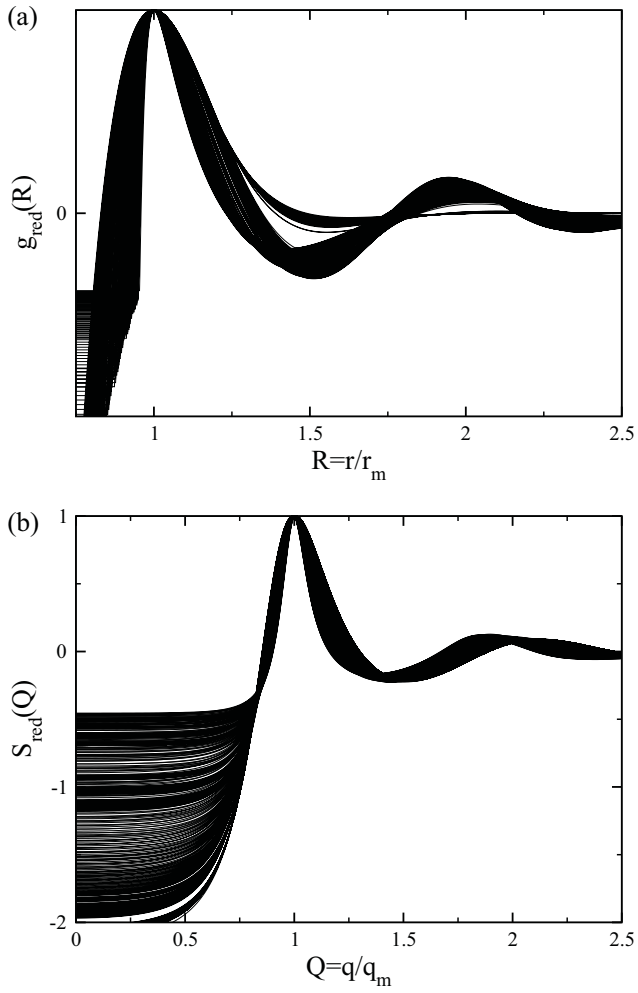

Fig. 5.8: *(a) Reduced radial distribution function $g_{red}(R)$, and (b) reduced static structure factor $S_{red}(Q)$, for a large number of systems with $\phi = 0.01$, $g_{MPB\text{-}RMSA}(x = 1^+) = 0$ and $S(y_m) \leq 3.2$. The systems in panel (a) satisfy additionally that $0.99 \leq x_m\sigma/\tilde{d} \leq 1.01$, and in panel (b) that $0.99 \leq y_m\tilde{d}/\sigma/(2.2\pi) \leq 1.01$.*

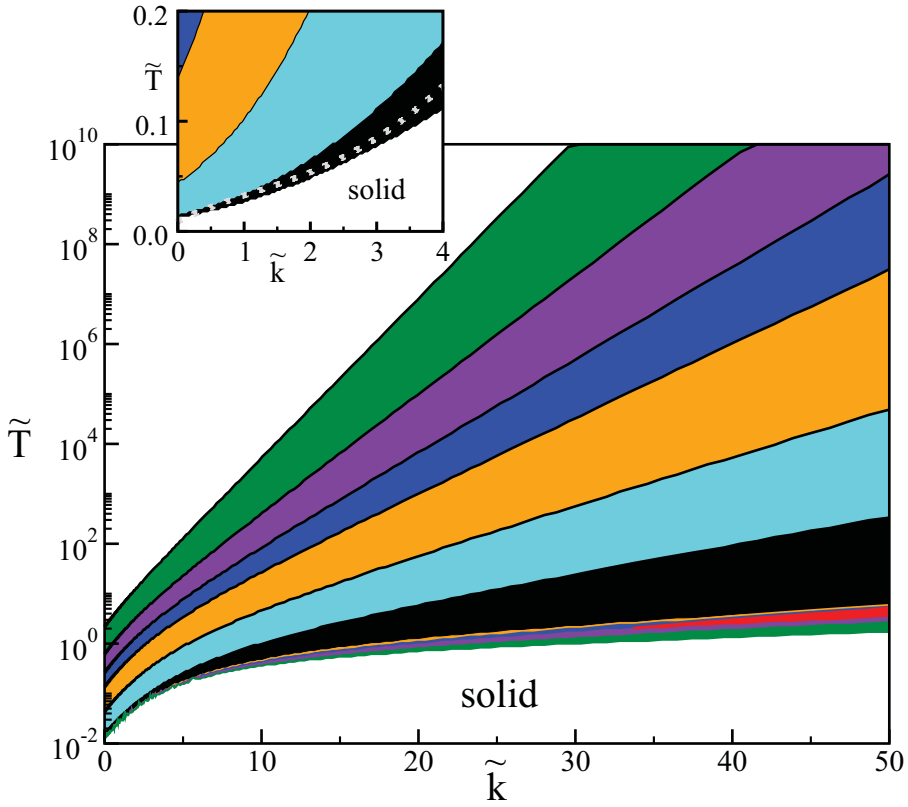

Fig. 5.9: *Fluid-phase diagram, obtained using the MPB-RMSA, for HSY systems with* $g_{\text{MPB-RMSA}}(x = 1^+) = 0$. *The fluid phase is characterized by the Hansen-Verlet criterion* $S(q_m) < 3.2$. *A specifically colored areal facet corresponds to a specific volume fraction, namely (from top to bottom) green:* $\phi = 1\%$, *violet:* $\phi = 5\%$, *blue:* $\phi = 10\%$, *orange:* $\phi = 15\%$, *light blue:* $\phi = 25\%$, *black:* $\phi = 35\%$, *and red:* $\phi = 45\%$. *A facet of given* ϕ *is bounded from above by the curve determined from* $g(\sigma^+, \phi) = 0$, *and from below by the freezing line* $S(q_m) = 3.2$. *Inset: lower-*$\tilde{k}$ *phase diagram part using a linear scale. The dotted curve is the solid-liquid coexistence line for point-Yukawa particles predicted by Pistoor and Kremer [104].*

systems requires in general three independent parameters such as, *e.g.* $(\tilde{T},\tilde{k},\phi)$, to span the phase space. Arbitrary HSY systems of equal $(\tilde{T},\tilde{k},\phi)$ have the same $S(y)$ and $g(x)$ in common. Note for $\phi \to 0$, that the MPB-RMSA reduces to the PB-RMSA which, in turn, reduces to the RMSA. The latter two methods do not share the MPB-RMSA-specific volume-fraction dependence of the point-Yukawa like microstructural functions. Therefore, the MPB-RMSA can be used to map out the boundaries of the point-Yukawa like phase in $(\tilde{T},\tilde{k})$-space, provided that a very low volume fraction is selected.

Keeping in mind this artifact of the MPB-RMSA, we proceed by discussing the fluid-phase diagram part of HSY systems with masked hard-core interactions, characterized in principle by two parameters $\tilde{T}$ and $\tilde{k}$. The diagram is constructed using the MPB-RMSA predictions for $S(q_m)$ in combination with the empirical Hansen-Verlet rule. For a neutral hard-sphere system with no long-ranged repulsion, $S(q_m) = 2.85$ at freezing. Computer simulations [103, 181, 182] and density functional theory calculations [183] have shown that $S(q_m)$ at freezing varies between 2.85 and 3.3 for HSY systems, in going from short-ranged to long-ranged Yukawa tails. In the present study, a fixed value of 3.2 was selected for simplicity, in agreement with the freezing peak value of $S(q)$ found experimentally in our low-salinity charged silica system.

Fig. 5.9 shows our result for the $\tilde{T} - \tilde{k}$ phase diagram, for a very extended range, $\tilde{T} = 10^{-3} - 10^{10}$ and $\tilde{k} = 10^{-4} - 50$, of state points. Fluid-phase systems are characterized by peak values $S(q_m) < 3.2$. The inset shows the lower-$\tilde{k}$ part of the diagram on a linear scale. A uniformly colored areal segment in the diagram includes the state points of fluid systems of equal volume fraction. Seven different volume fractions ϕ from 0.01 to 0.45 are considered. An areal segment of given ϕ is bounded from above by the line determined from $g_{\text{MPB-RMSA}}(\sigma^+;\phi) = 0$, and from below by the freezing line $S(q_m) = 3.2$. The same phase diagram, computed in PB-RMSA instead of the MPB-RMSA, is depicted in Fig. 12 of Ref. [14, 15]. For the reasons explained above, the two diagrams are indistinguishable at low volume fractions, differing noticeably only when both $\tilde{k}$ and ϕ are large. In particular, the inset of Fig. 5.9 remains practically unchanged when, in place of the MPB-RMSA, the PB-RMSA is used.

Increasing the temperature $\tilde{T}$ in systems of given ϕ and $\tilde{k}$ increases the likelihood of near-contact configurations, until the upper boundary of the fixed-ϕ segment is reached defined by the largest $\tilde{T}$ where $g_{\text{MPB-RMSA}}(\sigma^+) = 0$. On further increasing the temperature, $g(\sigma^+) > 0$ and the systems of a given ϕ no longer belong to the considered class of HSY systems with masked hard-core interactions. As expected and noted from the phase diagram, the region of fluid-state points describing systems with masked hard-core interactions narrows with decreasing screening length and increasing volume fraction.

According to the inset in Fig. 5.9, the solid-fluid coexistence line bounding the fluid-state diagram from below, is in good accord with the polynomial fit to the melting line,

$$\tilde{T}_m(\tilde{k}) = 0.009 + 0.0303\,\tilde{k} - 0.00997\,\tilde{k}^2 + 0.0035\,\tilde{k}^3 - 0.000245\,\tilde{k}^4\,, \tag{5.3}$$

reported by Pistoor and Kremer [104] (see also [184]). The Hansen-Verlet criterion does not allow to distinguish the fluid-bcc transition appearing at smaller screening parameters from the fluid-fcc transition at larger $\tilde{k}$. However, the value of the reduced temperature at the isochoric fluid-bcc transition point in the OCP limit, is predicted by the MPB-RMSA method as $\tilde{T}(\tilde{k}=0) \approx 0.01$. This value is in agreement with Eq. (5.3), and with the molecular dynamics simulation result by Hamaguchi *et al.* [105]. This points to the internal consistency and accuracy of the fluid-phase diagram in Fig. 5.9. Note here that the fluid-solid coexistence region of the HSY at smaller values of $\tilde{k}$ is very narrow, with vanishing relative density difference (vanishing miscibility gap) at $\tilde{k}=0$ [102, 105, 183].

A short discussion is in order here regarding the number of considered state points on which Fig. 5.9 is based. For each of the seven considered volume fractions, the MPB-RMSA pair structure functions have been calculated and stored in a database for 500×500 state points $(\tilde{T},\tilde{k})$, of values representatively distributed over the depicted $\tilde{T}$ and $\tilde{k}$ intervals. Such an extensive calculation was done in about 5 h of cpu time on a standard desktop PC. It was made possible owing to the rapidity and stability of the MPB-RMSA code. Out of this large number, systems with $S(q_m) < 3.2$ and $g_{\text{MPB-RMSA}}(x=1^+)=0$ were selected constituting the state points in Fig. 5.9. An additional filtering for systems obeying geometric concentration scaling has led to Fig. 5.8.

In Fig. 5.10, we have sorted the zero-contact-value systems in Fig. 5.9 according to values of the principal peak positions and locations, and the location, x_{dip}, of the first minimum in $g(x)$ to the right of the principal peak (see inset in Fig. 5.10(c)). Each colored dot in the figure represents a system where the MPB-RMSA structure functions have been calculated. The subset of systems of lowest $\phi = 0.01$ (green dots), *e.g.*, extends actually over the whole dotted phase space part. However, like in Fig. 5.9, it is partially overlayed (in Fig. 5.10(a) nearly completely) by the more concentrated subsets of systems colored as in Fig. 5.9.

Fig. 5.10(a) shows explicitly that for a given value of $S(y_m)$, there exist a variety of systems of different peak values $g(x_m)$ and different volume fractions. As we have discussed in relation to Fig. 5.8 and the Hansen-Verlet criterion for $S(y_m)$, there is no unique value of $g(x_m)$ characterizing the onset of freezing. For instance, for $S(y_m)=3.2$, values for $g(x_m)$ occur in between 2.2 and 3.8.

Fig. 5.10(b) extends the discussion of Fig. 5.7 by showing that, with increasing ϕ, all systems approach geometric scaling behavior where $\tilde{x}_m = x_m\sigma/\tilde{d} = 1$ and $\tilde{y}_m/(2\pi) = y_m\tilde{d}/(2\pi\sigma) = 1.1$. The most concentrated systems at $\phi = 0.45$ (in red) cover only a tiny patch centered around this geometric scaling point.

In Fig. 5.10(c), all fluid systems are sorted according to the locations, x_m and x_{dip}, of the principal peak and the subsequent minimum of $g(x)$. There is very roughly a linear relationship between x_{dip} and x_m (with some significant spread, however) independent of the considered volume fraction. Quite interestingly, the systems obeying geometric concentration scaling are located, for any considered ϕ, in a small patch centered at $\tilde{x}_{\text{dip}} = r_{\text{dip}}/\tilde{d} = 1.4$ and $\tilde{x}_m = r_m/\tilde{d} = 1$, with constant ratio $\tilde{x}_{\text{dip}}/\tilde{x}_m = x_{\text{dip}}/x_m \approx 1.4$ (as long as the fluid systems are well structured).

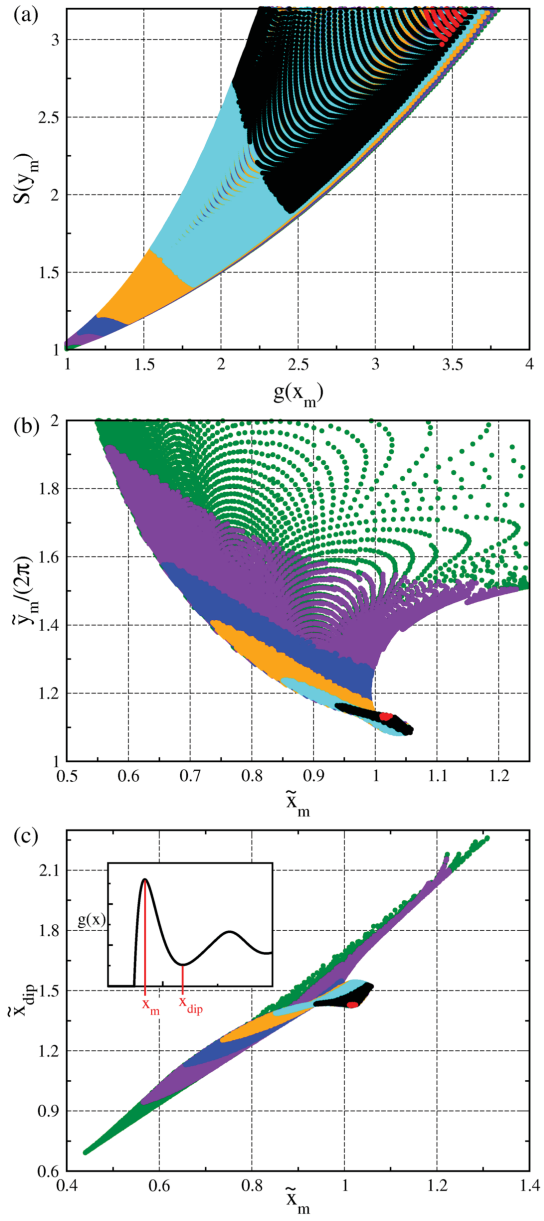

Fig. 5.10: *(a) $S(y_m)$ versus $g(x_m)$, and (b) $\tilde{y}_m/(2\pi) = y_m\tilde{d}/(2\pi\sigma)$ versus $\tilde{x}_m = x_m\sigma/\tilde{d}$, and (c) $\tilde{x}_{dip} = x_{dip}\sigma/\tilde{d}$ versus $\tilde{x}_m = x_m\sigma/\tilde{d}$, for the zero-contact value fluid systems at the seven volume fractions considered in Fig. 5.9, using the same color code. Each colored dot represents a considered system. The inset in (c) illustrates the locations of x_m and x_{dip}.*

This finding of a constant ratio for systems obeying geometrical density scaling can be motivated by the following simplifying consideration. The rdf of a strongly correlated HSY system with well-developed principal peak is crudely described by

$$g(r) \approx \Theta(r - r_m) + \frac{A}{4\pi n r_m^2}\,\delta(r - r_m)\,, \tag{5.4}$$

where $\Theta(r)$ is the unit step function. The δ-distribution part is a crude sketch of the peak region of $g(r)$. On noting that

$$N_{\rm nn} = 4\pi n \int_0^{r_{\rm dip}} dr\, r^2\, g(r) \tag{5.5}$$

defines the number, $N_{\rm nn}$, of nearest neighbors, and using $r_m = \tilde{d}$, integration of Eq. (5.4) leads to

$$\left(\frac{r_{\rm dip}}{r_m}\right)^3 = \frac{3}{4\pi}\,(N_{\rm nn} - A) + 1\,. \tag{5.6}$$

Provided A and $N_{\rm nn}$ are independent of ϕ, a constant ratio $r_{\rm dip}/r_m$ is obtained. In strongly correlated systems, $S(q \to 0) \approx 0$, which in conjunction with the Fourier transform of Eq. (5.4) leads to $A = 4\pi/3 - 1$. Assuming $N_{\rm nn} = 12$ consistent with the values $12 - 13$ obtained from Eq. (5.5) when the MPB-RMSA rdf's are used, $r_{\rm dip}/r_m = \tilde{x}_{\rm dip}/\tilde{x}_m \approx 1.38$ is obtained which somewhat fortuitously is close to the ratio 1.4 noted from Fig. 5.10(c).

5.3 Static structure of charged silica spheres

The high accuracy of the MPB-RMSA for systems of strongly correlated particles shows its capability as a conveniently fast tool for evaluating scattering data. To illustrate this, we use the MPB-RMSA in the following to fit experimental $S(q)$ which we have obtained from SLS experiments on suspensions of negatively charged TPM coated silica spheres suspended in toluene-ethanol. Details of the silica sphere system, and the conducted experiments, are given in Section 2.2.

The experimental $S(q)$ has been obtained by division of the static scattered intensity $I(q)$ by the particle concentration and the light scattering determined form factor, $P(q)$. The latter can be well fitted by a core-shell form factor model with spherical silica core of diameter 264 nm, and a surrounding spherical TPM shell of thickness 4 nm, differing in its refractive index from that of the silica core [185]. Note that the outer diameter, $\sigma = 272$ nm, in this core-shell model is in agreement with the diameter that has been independently determined from fitting SAXS intensities at large q-values by a (polydisperse) sphere form factor. Since the X-ray scattering length densities of silica and TPM are both distinctively different from that of the toluene-ethanol solvent mixture, a form factor of homogeneously scattering spheres applies in fitting the SAXS intensities. In light scattering, however, the refractive indices of silica, TPM, and

the toluene-ethanol solvent are quite similar, so that the more complicated core-shell model for $P(q)$ has been used.

The residual salinity, $n_s = 0.7 \times 10^{-6}$ M, in the system was determined as a global fit-parameter from a concentration series of SLS measurements of $S(q)$, fitted by the MC, RY and MPB-RMSA results. The only ϕ-dependent fitting parameter in our analysis has been the effective charge number Z, which was adjusted in each of the employed methods to match the structure factor peak height. The suspension freezes at a volume fraction of $\phi \approx 0.16$, where the experimental $S(q)$ attains a principal peak value of about 3.2.

The upper panel of Fig. 5.11 exemplifies our theoretical analysis of the concentration series experiments by showing the peak-height adjusted $S(q)$ of the MC, RY and (M)PB-RMSA methods, for the least concentrated system ($\phi = 0.057$) in the series, and for a concentrated system ($\phi = 0.15$) close to the freezing transition. The fraction of surface-released counterions is large enough even at $\phi = 0.057$, where $k_c = 0.93 \times k_s$, to guarantee a small value of the osmotic compressibility. All three methods considered in the top panel of Fig. 5.11 reproduce the experimental $S(q)$ with excellent accuracy in the whole experimentally accessible q-range. In the lower panel of Fig. 5.11, the deduced effective charges are plotted for the complete concentration series. Interestingly enough, the MC, RY and MPB-RMSA methods all give the same values for the effective charges, with uncertainties comparable to the symbol sizes. This highlights the capability of the MPB-RMSA to deliver reliable results for the effective charge with little numerical effort. In contrast, the (unmodified) PB-RMSA version of Snook and Hayter over-predicts the values of Z systematically, but not to such an extent as the HNC and RMSA schemes which overestimate the effective charge of the silica spheres roughly by a factor of two.

The RMSA and HNC peak values of $S(q)$ for $\phi > 0.06$ cannot be tuned large enough to reach the experimental peak heights, for any reasonable value of Z. For the most concentrated system ($\phi = 0.159$) right at the freezing point, even the PB-RMSA calculated $S(q_m)$ remains well below the experimental $S(q_m)$, for any value of Z. This inability of the RMSA and HNC schemes to reach the experimental peak heights in certain low-salinity systems, like the considered silica samples, can be explained by the competing influence of added salt ions and surface-released counterions [see Eqs. (2.5)]: When Z is increased from small values at a given ϕ, $S(q_m)$ increases initially since γ increases with Z for nearly constant k, as long as the concentration of surface-released counterions is much less than the concentration of salt ions. When Z becomes large, however, the cross-over point described by $k_c^2(Z) = k_s^2$ is surpassed, and the surface-released counterions start to dominate the electrostatic screening. Then, $S(q_m)$ decreases with increasing Z since the effect of the increasing coupling parameter γ on the pair structure is overcompensated by the likewise increasing screening parameter k. Consequently, $S(q_m)$ goes through a maximum as a function of Z. In a recent experimental study by Wette *et al.* [186, 187], it has been shown that a similar mechanism can lead to a reentrant fluid-crystalline-fluid phase behavior when the 1-1 electrolyte NaOH is added to suspensions of silica spheres. The strong dependence of the pH-value on the amount of added NaOH leads to

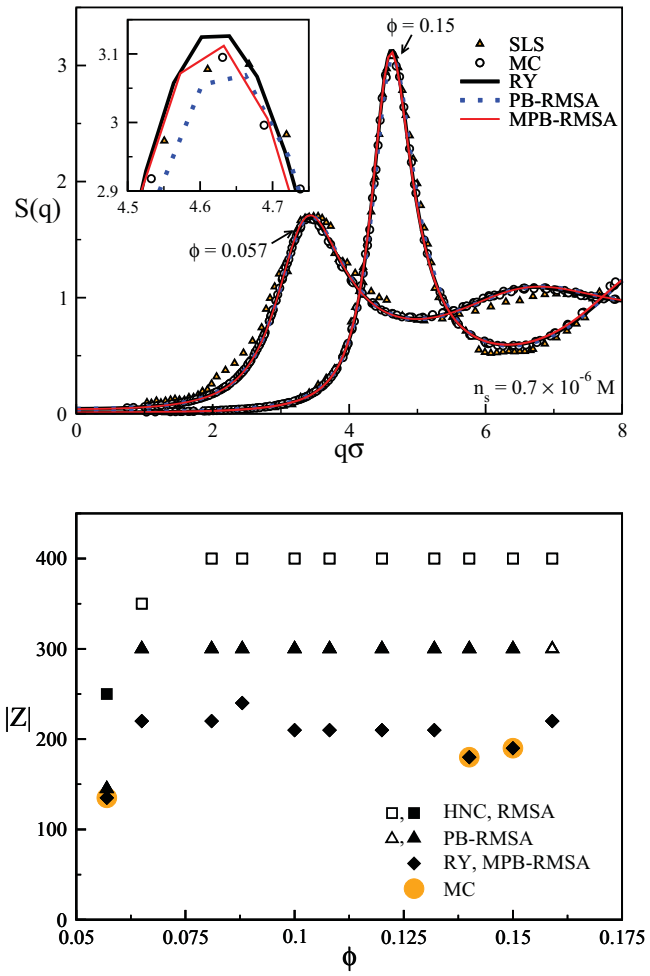

Fig. 5.11: *Top panel: Structure factor of TPM-coated, charged silica spheres dispersed in a toluene-ethanol mixture. Filled triangles: SLS experiment data. Open circles: MC simulation data. Black solid lines, blue dotted curves, and red solid lines: RY, PB-RMSA, and MPB-RMSA schemes, respectively. The charge numbers determined from fitting the experimental data, are identical for the MC, RY and MPB-RMSA methods, namely* $Z = (135, 190)$ *for* $\phi = (0.057, 0.15)$*. The non-modified PB-RMSA predicts different values, namely* $Z = (145, 300)$*. Bottom panel: Effective charge number,* $|Z|$*, used in the various schemes for a best approximation of the SLS-*$S(q_m)$ *in the concentration series of charged silica spheres. Orange filled circles: MC simulations. Diamonds: RY and MPB-RMSA schemes. Triangles: PB-RMSA. Squares: HNC and RMSA. Filled symbols are used when the experimental* $S(q_m)$ *can be reproduced, and open symbols when it is underestimated at any* $|Z|$*. In the latter case, the lowest* $|Z|$ *is plotted which minimizes the peak-height underestimation. Common parameters (in both panels) are :* $L_B = 8.64$ *nm,* $\sigma = 272$ *nm, and* $n_s = 0.7 \times 10^{-6}$ *M.*

a rapid increase in Z when small amounts of NaOH are added to an aqueous silica suspension. The accompanying increase in the coupling parameter γ can induce a freezing transition. At higher concentrations of added NaOH, the continued increase in Z is overcompensated by the increased screening due to Na^+ and OH^- microions and surface-released counterions. As a result, the silica suspension can re-melt at a large concentration of added NaOH. When $S(q_m)$ is calculated by a method such as the RMSA which underestimates the structure of strongly correlated particles, the predicted maximum of $S(q_m)$ as a function of Z may be not large enough to match the experimental peak value.

In summary, we conclude that out of all considered methods only the RY and MPB-RMSA schemes, and of course the MC simulation method, allow for a fully consistent fit of experimental structure factors of strongly coupled charged spheres, providing thus trustworthy values for the effective charge. Out of these three schemes, only the RY and MC methods have been well-established so far, with the former method routinely used to fit scattering data. However, the fitting procedure can be quite cumbersome, due to the non-analytic nature of these two methods, causing thus long execution times. On a standard desktop PC, one MC run of good statistics typically takes several hours, and about 10 seconds are usually needed for the RY calculated pair structure functions of a given system. An additional complication in applying the RY scheme is caused by its internal iterative algorithm which interpolates between HNC and the Percus-Yevick closure to achieve local thermodynamic consistency. Convergence of this algorithm depends on an initial seed for the mixing parameter which has to be provided by the user. To our experience, it is occasionally difficult to find an appropriate seed that allows the RY-scheme to converge.

The MPB-RMSA code, on the other hand, is rapidly evaluated for any system, with a typical cpu-time of less than 0.1 seconds. This has allowed us to implement the MPB-RMSA with a convenient graphical user interface, described in Appendix E, in which an imported experimental $S(q)$ or $g(r)$ can be readily fitted. Input parameters such as Z and ϕ can be tuned with real-time response of the MPB-RMSA structure functions, resulting in a fast and versatile fitting tool of quantitative accuracy.

5.4 Static structure of bovine serum albumin proteins

In this section, we describe in detail the simplifying spheroid-Yukawa model for the BSA proteins that has been introduced in Section 2.3. Static scattered intensities determined by SAXS are shown, in comparison to our theoretical fit expressions. The BSA suspension characteristics are determined from this comparison.

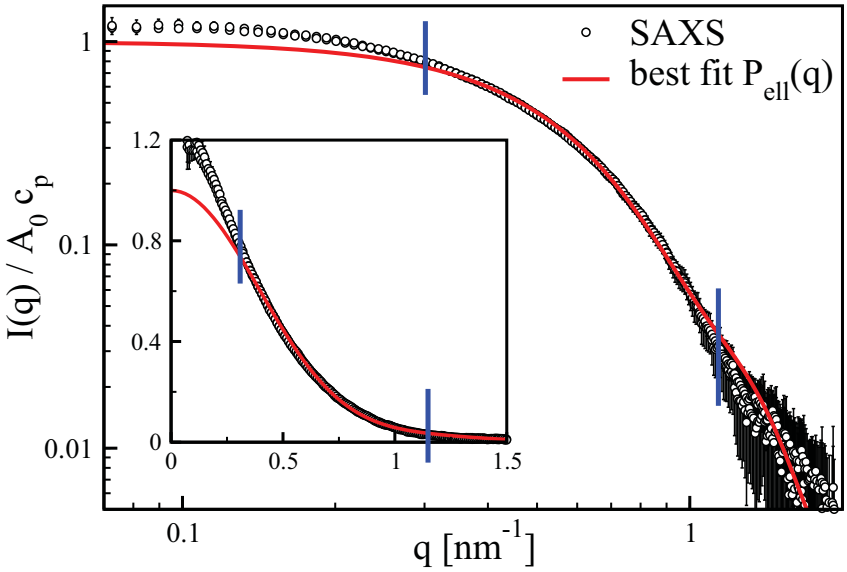

Fig. 5.12: *BSA form factor fit. Open circles: SAXS intensities at two protein concentrations of $c_p = 1$ and 2 g/l, for 0.15 M of added NaCl. The SAXS intensities have been divided by c_p, and by a common, q-independent factor A_0. Red solid line: Angular-averaged spheroid form factor according to Eqs. (5.8), fitted to the SAXS data within $0.3\ nm^{-1} < q < 1.15\ nm^{-1}$, as indicated by the blue vertical line segments. The obtained fit values are $a = 1.75$ nm and $b = 4.74$ nm. Inset: Intensity on a double linear scale.*

5.4.1 Form factor fitting

At low protein concentration and sufficiently large amount of added salt, inter-protein correlations are negligible. The scattered intensity, $I(q)$, is then solely determined by the form factor $P(q)$, *i.e.* $I(q) \propto P(q)$. Crystallographic measurements [72–74] have revealed a flat and roughly heart-shaped structure of albumin proteins. The computation of single-particle properties such as $P(q)$, $d_{t,0}$, and the intrinsic viscosity $[\eta]$, with an account of the complex particle shape of biomolecules, can be done by elaborate simulations only [74, 188] and is beyond the scope of this thesis. The aim of the present study is rather to give an essentially analytic description of the microstructure, and the dynamics, of interacting BSA proteins with low computational cost. We therefore employ a simple oblate spheroid model of the protein form factor. Note that a similar spheroidal model of BSA, as illustrated in Fig. 2.3, with isotropic pair-interactions has been used before by Kotlarchyk and Chen [189]. In this earlier work, however, the protein dynamics were not described theoretically.

In Fig. 5.12, SAXS intensities for BSA solutions of very small protein weight concentrations, $c_p = 1$ and 2 mg/ml, and 0.15 M of added NaCl, are shown along with the best-fit oblate

spheroid form factor. To check for a residual effect of interparticle correlations on $I(q)$, $S(q)$ was calculated for the present two systems to first order in ϕ using Eq. (3.7) in combination with the full DLVO pair potential in Eq. (2.1). As an upper bound for the magnitude of the repulsive and the attractive parts of the DLVO potential, an effective charge $|Z| = 34$ and a Hamaker constant $A_H = 3$ were used. As judged from our results of fitting a whole concentrations series of BSA suspensions, with fit parameter results presented in Tab. 5.1, the effective charge value $|Z| = 34$ can be safely considered as an upper bound. Likewise, the Hamaker constant is an upper bound to the values reported in literature [190, 191]. The cutoff Δ in Eqs. (2.2) and (2.3) is selected as $0.1\ \text{nm}/\sigma$, and the Bjerrum length as $L_B = 0.711$ nm, corresponding to water at room temperature. The remaining parameter required to uniquely specify the DLVO potential is the effective diameter σ. As argued in Section 5.4.2, the value of $\sigma = 7.40$ nm is a reasonable choice for BSA proteins.

The DLVO potential for these parameters is displayed in the inset of Fig. 5.13, along with its attractive part, u_{vdW}, and the HSY potential approximation. With a maximum of about 0.7 k_BT attained at $x \approx 1.07$, the electrostatic barrier height of u_{DLVO} is expectedly low. For shorter distances, u_{vdW} dominates the pair energy, predicting the binding energy of a BSA dimer to be stronger than $-4\ k_BT$ at the reduced cutoff distance $1 + \Delta$.

Note from Fig. 5.13 that for $u = u_{HSY}$, the first-order in ϕ structure factor $S_1(q)$ and the MPB-RMSA $S(q)$ agree almost perfectly. Since the latter is quite accurate for any fluid-state volume fraction, we conclude that $\mathcal{O}(\phi^2)$ corrections to $S_1(q)$ are small for the considered BSA system. All structure factors in Fig. 5.13 oscillate very mildly, with the largest deviation from unity occurring at $q \to 0$, where $S_1 \approx 0.99$ for the full DLVO potential. Therefore, the SAXS intensities in Fig. 5.12 contain no appreciable particle correlations. However, considering the rather strong dimer binding energy obtained for the employed DLVO potential parameters, we expect that a smaller part of the BSA proteins forms oligomers.

To fit the measured intensity in Fig. 5.12, we have used Eq. (3.39a) for $I(q)$ with $S_m(q)$ set equal to one, so that

$$I(q) = A c_p P_{\text{ell}}(q). \tag{5.7}$$

Here, A is a q-independent factor (of dimension velocity^3), that should be the same for all intensity measurements corrected for recording time and source intensity. The form factor is modeled by that of monodisperse, homogeneously scattering, and isotropically ordered oblate spheroids with semi-axis of revolution a and radius b . For oblate spheroids, the orientationally averaged form factor in Eq. (3.32) can be calculated as [185]

$$P_{\text{ell}}(q) = \int_0^1 d\mu |\tilde{f}_{\text{ell}}(q,\mu)|^2 \tag{5.8}$$

with

$$\tilde{f}_{\text{ell}}(q,\mu) = 3\frac{j_1(u)}{u} \tag{5.9}$$

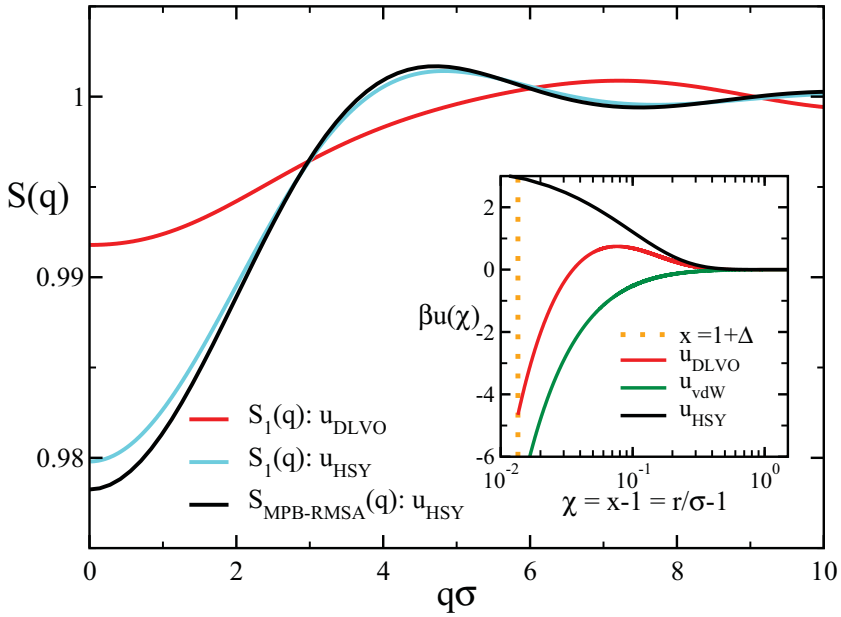

Fig. 5.13: *Estimates for the static structure factor for a dilute BSA suspension with* 0.15 *M of added NaCl. The red and light blue solid lines are structure factors using the full DLVO pair-potential in Eq.* (2.1)*, and the HSY pair-potential in Eq.* (2.6)*, respectively, calculated to first order in* ϕ *according to Eq.* (3.7)*. The black solid line is the MPB-RMSA prediction for* $S(q)$*, using the same HSY pair potential as in the* $\mathcal{O}(\phi)$ *calculation. The employed BSA parameters are* $A_H = 3$*,* $\Delta = 0.1$ *nm*$/\sigma$*,* $L_B = 0.711$ *nm,* $n_s = 0.15$ *M,* $\sigma = 7.40$ *nm, and* $\phi = 0.015$*, with all DLVO potential parts depicted in the inset.*

and

$$u = q\sqrt{a^2\mu^2 + b^2(1-\mu^2)}. \tag{5.10}$$

Here, $j_1(x) = (\sin x - x\cos x)/x^2$ is the spherical Bessel function of the first kind, and μ is the cosine of the angle between the ellipsoid symmetry axis and the scattering wave vector $\mathbf{q}$.

Using an automatic weighted least-squares minimizer implemented into the software package described in Appendix E, the spheroid semi-axes a and b entering into $P_{\rm ell}(q)$ were varied to achieve a best fit intensity in Eq. (5.7) for a given prefactor A. This fitting procedure was iterated for different values for A, until optimal agreement with the SAXS intensities in the range $0.3\ \text{nm}^{-1} < q < 1.15\ \text{nm}^{-1}$ was achieved, resulting in $a = 1.75$ nm and $b = 4.74$ nm. These values for the spheroid semi-axes are in good accord with previously reported values, and in reasonable agreement with the linear dimensions of the reported heart-shape like crystal structure of albumins [72–74, 192]. In a related recent study [46], similar values $a = 1.80 \pm 0.05$ nm and $b = 4.60 \pm 0.15$ nm have been determined, in decent agreement with the values obtained here. The optimized value for A, denoted by A_0, has been also used in our SAXS intensity fits for systems without added salt, discussed in Section 5.4.3.

The best-fit form factor, $P_{\rm ell}(q)$, depicted in Fig. 5.12 deviates from the SAXS intensities outside the fitted q-range. For $q \gtrsim 1.15\ \text{nm}^{-1}$, corresponding to length scales $2\pi/q \lesssim 6$ nm $\lesssim \sigma$, the complex internal structure of BSA is probed, which is not accounted for in the simplifying spheroid-Yukawa (SY) model. The deviations visible for $q \lesssim 0.3\ \text{nm}^{-1}$, corresponding to distances of roughly 20 nm or larger, are likely due to additional scattering species consisting of larger particles such as BSA oligomers or impurities. Since the size-, form-, and charge-distributions of oligomers and impurities are unknown, our choice of the lower q-boundary in fitting $I(q)$ is somewhat more ambiguous than the upper boundary. Therefore, we have repeated the intensity fitting for various low-q boundaries, finding that the weighted least squares deviation increases dramatically if the boundary is selected below $0.3\ \text{nm}^{-1}$. Moreover, the fit values for a and b remain essentially constant when the lower q-boundary is selected larger than $0.3\ \text{nm}^{-1}$.

The parameters of the spheroid form factor fitted to the SAXS data of proteins in general depend slightly on the measured q range, the prepared protein concentration, solvent and salt conditions, and the background subtraction. In the context of the present study, the related changes of the spheroid model parameters are all small compared to the experimental error bars, and will be further discussed in Section 5.4.3.

5.4.2 Effective sphere diameter

When protein correlations come into play at higher concentrations or lower salinities, the spheroid model of BSA is still too complex for an analytic treatment. Therefore, as far as the protein-protein interactions are concerned, in an additional approximation we describe

the proteins as effective spheres of diameter σ. Depending on the considered single-particle property, different definitions for σ can be given.

Consider first the geometric effective diameter, $\sigma_{geo} = 8(ab^2)^{1/3} = 6.80$ nm, following from equating the volume of the effective sphere to that of the spheroid. This effective diameter reflects the volume of the protein and the hydration layer visible to SAXS, but does not include thermo- and hydrodynamic effects of non-sphericity [193]. Thus, it should be considered as a lower boundary to the effective sphere diameter.

A thermodynamic effective diameter, $\sigma_{B_2} = 7.40$ nm, follows from demanding equal second virial coefficients, $B_2(T)$, of hard spheroid and effective hard sphere [194].

Alternatively, dynamic single-particle properties can be used to define an effective diameter. For hydrodynamic stick-boundary conditions and $a < b$, the translational free diffusion coefficient of an isolated spheroid is given by [74, 195, 196]

$$d_{t,0}^{ell}(a,b) = \frac{k_B T S(a,b)}{12\pi\eta_0 a}, \tag{5.11}$$

with $S(a,b) = 2$ atan $\xi(a,b)/\xi(a,b)$ and $\xi(a,b) = \sqrt{|a^2-b^2|}\,/a$. Equating $d_{t,0}^{ell}$ to the diffusion coefficient, $d_{t,0} = k_B T/(3\pi\eta_0\sigma_{d_{t,0}})$, of an effective sphere leads to $\sigma_{d_{t,0}} = 7.38$ nm.

One can derive another effective diameter from considering the intrinsic viscosity

$$[\eta] = \lim_{\phi\to 0} \frac{\eta(\phi)-\eta_0}{\eta_0\phi}, \tag{5.12}$$

where ϕ is the particle volume fraction. For a spheroid with hydrodynamic stick-boundary conditions [197, 198],

$$[\eta]^{\text{ell}} = \frac{5}{2} + \frac{32}{15\pi}\left[\frac{b}{a} - 1\right] - 0.628\left[\frac{1-a/b}{1-0.075a/b}\right], \tag{5.13}$$

which, for $a = b$, reduces to the Einstein result, $[\eta]^{\text{sph}} = 2.5$, for a solid sphere. Note here that $[\eta]^{\text{ell}} > 2.5$ for $a \neq b$. We obtain $[\eta]^{\text{ell}} = 3.25$ for the best fit values a and b given in Fig. 5.12. On demanding equality of the interaction-independent linear terms in the virial expansions of the viscosity,

$$\frac{\eta}{\eta_0} = 1 + [\eta]\phi + \mathcal{O}(\phi^2), \tag{5.14}$$

between spheroids and effective spheres, and on using $\phi^{\text{ell}} = (4\pi/3)ab^2 n$ and $\phi^{\text{sph}} = (\pi/6)\sigma_{[\eta]}{}^3 n$ for the same number density n, an effective diameter $\sigma_{[\eta]} = 7.42$ nm is obtained. Since the spheroid aspect ratio, $p = a/b = 0.37$, is rather close to unity, the four discussed effective diameters are all quite similar in magnitude. We use $\sigma = \sigma_{B_2} = 7.40$ nm in all our calculations of the static and dynamic properties of BSA discussed in this thesis.

5.4.3 Concentration series results

Concentrated protein solutions exhibit pronounced inter-particle correlations which are reflected in the static scattering intensity. Strong correlations are observed also in dilute, low-salinity solutions where the proteins show long-ranged electrostatic repulsion.

In order to allow for an analytical theoretical treatment, we assume that the static scattering intensity of interacting BSA proteins can modeled by the orientational-translational decoupling approximation Eqs. (3.39), rewritten as

$$I(q) = Ac_p P_{\rm ell}(q) S_m(q), \tag{5.15a}$$

$$S_m(q) = \Big[1 - X(q)\Big] + X(q) S(q), \tag{5.15b}$$

and

$$X(q) = \frac{1}{P_{\rm ell}(q)} \left[\int_0^1 d\mu \, f_{\rm ell}(q,\mu) \right]^2 . \tag{5.16}$$

Here, $S(q)$ is the structure factor of ideally monodisperse effective spheres of diameter $\sigma = \sigma_{B_2}$ and screened Coulomb repulsion of HSY type. In Fig. 5.14, the decoupling amplitude $X(q)$ for the BSA spheroid model is plotted. For wavenumbers $q \lesssim 0.5$ nm^{-1}, $X(q)$ remains close to unity, decaying for larger q steeply towards its first zero value at $q \approx 1.3$ nm^{-1}. For $q > 1.3$ nm^{-1}, $X(q) < 0.04$. The orientational disorder assumed in the decoupling approximation has the effect of damping the oscillations in $S_m(q)$. While $S_m(q)$ is practically equal to one for $q \gtrsim 1.3$ nm^{-1}, irrespective of the still visible oscillations in $S(q)$, the effect of orientational disorder on $S_m(q)$ is weak in the range $q \lesssim 0.5$ nm^{-1}, where the most distinctive features in $S(q)$ occur. We further note for monodisperse systems that $S_m(q \to 0) = S(q \to 0)$, a feature which plays an important role in the upcoming discussion of collective diffusion.

Fig. 5.15 includes the SAXS intensities for all explored BSA solutions without added salt, that we could fit using the decoupling approximation in Eq. (5.15), with $S(q)$ calculated in MPB-RMSA based on Eq. (2.6). To highlight differences in the intensities in Fig. 5.15, the intensity datasets are divided by their respective amplitudes A, and by the protein concentrations c_p. The most concentrated solution shown here is the one for $c_p = 90$ mg/ml. The intensities for two even more concentrated systems with $c_p = 180$ and 270 mg/ml are not depicted in the figure, since these could not be fitted reasonably well by the SY model.

In order to fit the experimental intensity data using Eq. (5.15), some deviations of the prefactor A from the optimized form factor fit value A_0 have to be allowed for (see Tab. 5.1). The fit of each individual intensity curve in Fig. 5.15 was made as follows: After dividing the SAXS intensity by A_0 and c_p, the weighted sum of quadratic deviations between SAXS data points, and the intensity according to Eqs. (5.15), was minimized by an automatic three-dimensional weighted least-squares minimizer with respect to the fitting parameters $\{|Z|, n_s, \phi\}$. For each concentration, the whole experimental dataset was used, for wavenumbers from 0.07 to about

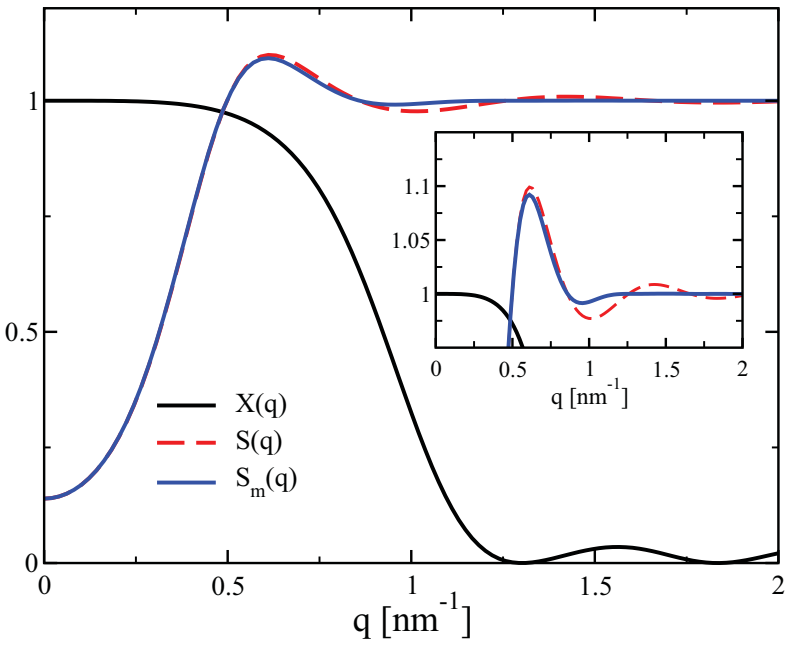

Fig. 5.14: *Static orientational-translational decoupling approximation results for a representative system at $c_p = 45$ mg/ml, selected from the low-salt BSA concentration series. The decoupling amplitude $X(q)$ is depicted as the black curve. The oscillations of the measurable structure factor, $S_m(q)$ (blue curve), decay faster than for the HSY structure factor $S(q)$ (dashed red curve), calculated in MPB-RMSA. The inset enlarges the peak region. Values $a = 1.75$ nm and $b = 4.74$ nm for the spheroid semi-axes are used. The parameters entering into the calculation of $S(q)$ are listed in Tab. 5.1.*

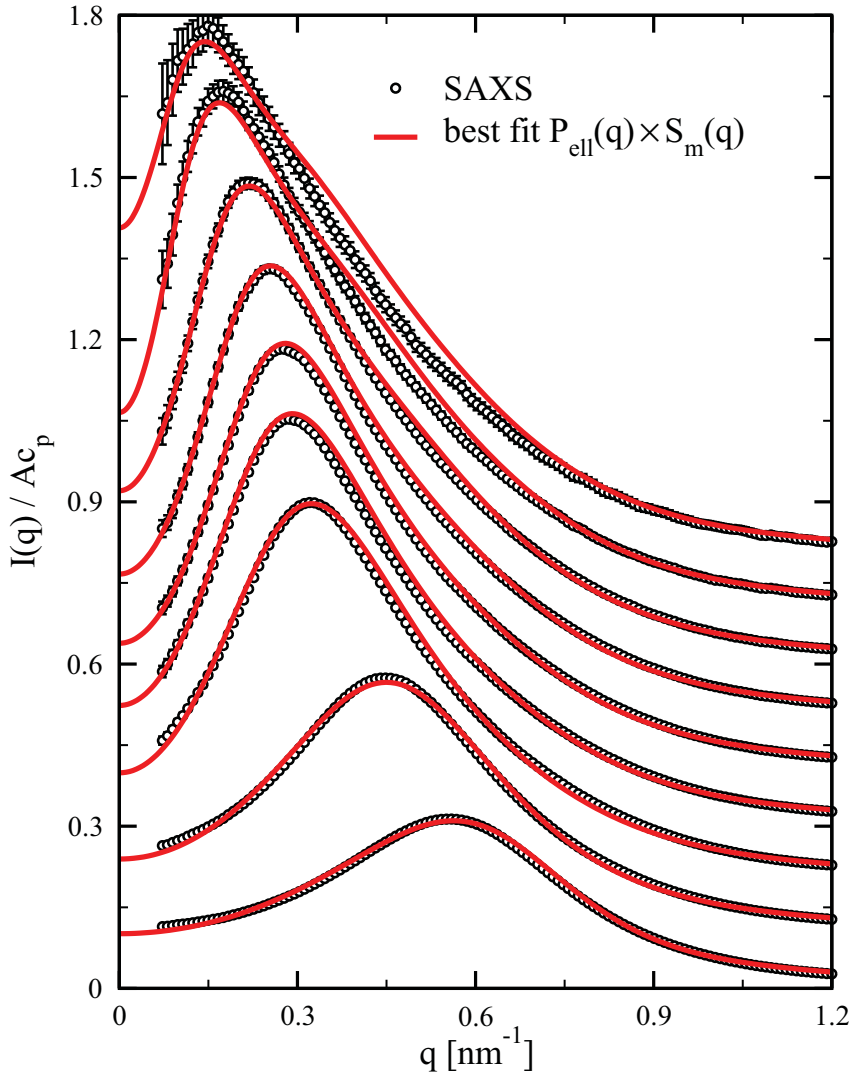

Fig. 5.15: *SAXS intensities of BSA solutions at various c_p, and without added salt, divided by Ac_p. From top to bottom: $c_p = 0.9, 1.8, 4.5, 7.2, 9, 13.5, 18, 45,$ and 90 mg/ml. The intensity curves are displaced in steps of 0.1 along the vertical axis for better visibility. SAXS-data in the extended range $q \lesssim 4$ nm^{-1} were taken into account in the fits, shown here only up to $q = 1.2$ nm^{-1}. Red solid lines: best fits according to Eqs. (5.15), with $S(q)$ calculated in MPB-RMSA. The fit parameters are listed in Tab. 5.1.*

Tab. 5.1: *Fit parameters ϕ, $|Z|$, n_s, and A/A_0, for the BSA concentration series without added NaCl, with intensities shown in Fig. 5.15. The additional parameters $L_B = 0.711$ nm, $\sigma = \sigma_{B_2} = 7.40$ nm, $a = 1.75$ nm, $b = 4.74$ nm are kept fixed, and A_0 is taken from the form factor fit in Fig. 5.12. The fit values at $c_p = 0.9, 1.8, 45,$ and 90 mg/ml should be taken with a pinch of salt (see related text). The listed values for c_p are according to Eq. (2.7).*

$\mathbf{c_p}$ [mg/ml]	ϕ	$\mathbf{\lvert Z\rvert}$	$\mathbf{n_s}$ [μM]	$\mathbf{A/A_0}$
0.9	5.19×10^{-4}	34.5	1216	1.20
1.8	1.34×10^{-3}	18.8	608	1.08
4.5	3.72×10^{-3}	19.1	1278	0.96
7.2	6.97×10^{-3}	16.7	1497	0.97
9	1.04×10^{-2}	14.6	1510	1.05
13.5	1.28×10^{-2}	12.6	1297	0.81
18	2.06×10^{-2}	10.8	1292	0.85
45	8.19×10^{-2}	9.47	2375	1.0
90	1.74×10^{-1}	8.52	3323	1.0

4 nm^{-1}. If the fit was unsatisfactory, the prefactor A was slightly altered, and the optimization with respect to $\{|Z|, n_s, \phi\}$ was repeated. This procedure was iterated until convergence in all fit parameters was achieved. For all considered concentrations, $L_B = 0.711$ nm, $\sigma = \sigma_{B_2} = 7.40$ nm, $a = 1.75$ nm, and $b = 4.74$ nm were kept fixed. Tab. 5.1 summarizes the obtained best fit parameters.

While the overall intensity fits for the two lowest concentrations, $c_p = 0.9$ and 1.8 mg/ml, look reasonably good, they contain some peculiarities. A shoulder is present in the fit intensity extending from $q \approx 0.3$ to 0.8 nm^{-1}, overshooting the experimental data by several standard deviations. Moreover, the prefactor A in both cases is substantially larger than A_0, and the fitted $|Z|$ assumes a questionably large value of 34.5 for $c_p = 0.9$ mg/ml. These peculiarities can be attributed to impurity contributions neglected in Eq. (5.15). Note also that the maximal intensities in both systems occur at wavenumbers well below 0.3 nm^{-1}, where impurities are found to obstruct also the form factor fit in Fig. 5.12.

All our attempts to remedy these fitting problems for the two most dilute samples have failed. Since we lack information on the shape and size distribution, and the interactions of the impurities, we cannot improve on Eq. (5.15). Restricting the wavenumber interval in the fitting procedure to $q \gtrsim 0.3$ nm^{-1} gives no improvement, either. While Eq. (5.15) is expected to be quite accurate in this restricted q-range, the maximum in $I(q)$ is not included. The intensity for $q > 0.3$ nm^{-1} is a monotonically decaying curve, almost completely determined by the form factor. It therefore lacks distinct features coming from particle correlations, rendering the fit with respect to $\{|Z|, n_s, \phi\}$ into an overdetermined problem. For all these reasons,

our fit parameters in Tab. 5.1 for $c_p = 0.9$ and 1.8 mg/ml should be considered as being not quantitatively accurate.

Except for the two most dilute systems, all other systems with concentrations ranging from $c_p = 4.5$ to 90 mg/ml shown in Fig. 5.15 can be excellently fitted by Eq. (5.15). The obtained effective charges, salt concentrations, and volume fractions all assume reasonable values, showing systematic dependencies on the BSA concentration. Note, however, that for $c_p = 45$ and 90 mg/ml, the SY model is pushed to its limit. On assuming a Hamaker constant of 3 k_BT [191], the repulsive barrier height of the DLVO potential becomes very small, with values of 1.3 and 0.5 k_BT at $c_p = 45$ and 90 mg/ml, respectively. The contact value of $g(x)$ at $x = 1$ is just barely zero for the more dilute system, whereas $g(x = 1^+) \approx 0.9$ in the more concentrated system. Obviously, the SY model with purely repulsive, spherically symmetric pair interactions is bound to fail when the particles are allowed to come into hard-core contact. Thus, the system with $c_p = 45$ mg/ml, and fitted volume fraction $\phi = 8.19\%$, is clearly on the borderline of applicability of the SY model. Somewhat unexpectedly, and probably fortuitously, the system with $c_p = 90$ mg/ml can still be fitted with good accuracy. Summarizing, the fit values for the most concentrated systems with $c_p = 45$ and 90 mg/ml in Tab. 5.1 should be interpreted with caution, since the fit parameters might be significantly distorted by the discussed deficiencies of the SY model. Another indication for this are the obtained fit values for $\phi(c_p)$, which for the two most concentrated samples clearly overshoot the linear dependence on c_p found approximately for the less concentrated systems (see Tab. 5.1).

In closing our discussion of the static scattered intensities, we note that fit parameters slightly different from the ones in Tab. 5.1 are obtained, when in place of the BSA model with spheroid axes $(a,b) = (1.75\text{ nm}, 4.74\text{ nm})$, the values $(a,b) = (1.80\text{ nm}, 4.60\text{ nm})$ given in [46] are used. For instance, at $c_p = 4.5$ and 18 mg/ml, the best-fit values for $|Z|$ change to 18.4 and 10.7, respectively. Note that in comparison to Ref. [192], where the RMSA was employed in fitting $I(q)$, we use here the improved MPB-RMSA integral equation scheme for $S(q)$, resulting in more precise fit-values. Moreover, different from the earlier intensity fitting described in [192], the dephasing influence on $I(q)$ originating from the particle asphericity is accounted for approximately in the decoupling approximation used in the present study. The slightly different spheroid semi-axes $(a,b) = (1.80\text{ nm}, 4.60\text{ nm})$, and the correspondingly slightly changed fit-parameters, do not cause appreciable changes in the dynamical properties explored in Section 6.3. For instance, the collective diffusion coefficient changes by no more than 3%, and the changes in the static- and high-frequency viscosities are less than 0.1%. Note that using the somewhat smaller spheroid causes changes of the fitted volume fraction of about 5% which does not change absolute values but slightly rescales the protein concentration axis for the theoretical predictions.

5.5 Static structure of gibbsite platelets

To fit the static mean scattered intensity of gibbsite in DMSO, and to provide a basis for explaining the trends in the concentration dependence of the gibbsite platelet diffusion coefficients discussed in Section 6.4, we introduce here a simplifying model of the pair-interactions and the shape of the gibbsite platelets. In this circular cylinder-Yukawa (CCY) model, which is similar in spirit to our SY model for BSA proteins, the gibbsite platelets are described in terms of their scattering amplitudes as orientationally disordered, flat, circular cylinders with non-zero polydispersity both in their thickness- and radius distributions. In terms of the pair-interactions, the gibbsite platelets are treated in the CCY model as uniformly charged effective hard spheres of effective diameter σ, interacting by the HSY pair potential in Eq. (2.6).

5.5.1 Form factor

Recall from Section 5.4.1 our fitting procedure of the spheroid form factor to the SAXS-recorded mean scattered intensity of dilute, weakly coupled BSA protein solutions. As a result of this fit, the linear dimensions of the spheroid model of BSA proteins have been determined, allowing for further application of this model in calculating static and dynamic properties of BSA in dilute and concentrated solutions.

The reverse path is taken in the present section, in modeling the form factor in the CCY model of gibbsite platelets. Different from BSA proteins, the shape and size of gibbsite platelets is well known from our TEM and AFM pictures, with results shown in Figs. 2.4 and 2.5. However, static scattered intensities from dilute, weakly coupled gibbsite solutions, to which the form factor could be directly fitted, are not available. As noted from Fig. 5.16, under the low-salt conditions studied here, the scattered intensity shows pronounced signs of particle interactions even for the most dilute samples considered. In addition, the q-range accessible in the SLS experiments is too restricted for a reliable form factor fit, even if the range of electric repulsion was screened by the addition of salt.

Therefore, we use an ab initio calculation of the form factor in Eq. (3.42), used in the subsequent analysis of interaction gibbsite platelets in the framework of the translational-orientational and interspecies decoupling approximation. For continuous distributions of molar fractions x_α and the scatterer volumes v_α, the weighted sum in Eq. (3.42) can be expressed as

$$P_m(q) = \frac{\int_0^\infty dR \int_0^\infty dh \int_0^1 d\mu P_S(R) P_S(h) v^2(R,h) \left|\tilde{f}_{\mathrm{cyl}}(q,R,h,\mu)\right|^2}{\int_0^\infty dR \int_0^\infty dh \int_0^1 d\mu P_S(R) P_S(h) v^2(R,h)}, \tag{5.17}$$

where

$$\tilde{f}_{\mathrm{cyl}}(q,R,h,\mu) = \frac{4J_1(qR\sqrt{1-\mu^2})}{qR\sqrt{1-\mu^2}} \cdot \frac{\sin(qh\mu/2)}{qh\mu} \tag{5.18}$$

is the form amplitude of a circular cylinder [93, 185, 199] of radius R, height h and volume $v(R,h) = \pi R^2 h$, with J_1 denoting the cylindrical Bessel function of the first kind. Orientational averaging is achieved in Eq. (5.17) by integrating over $\mu = \cos(\vartheta)$, where ϑ is the polar angle between the cylinder symmetry axis and the scattering vector $\mathbf{q}$. A single integral suffices here for the orientational averaging, when approximating of the hexagonal shape of gibbsite platelets (*c.f.*, Fig. 2.4) by circular cylinders. The average over the distribution of platelet sizes is expressed by integrating with respect to R and h, on assuming that a normalized joint probability distribution $P(R,h)$ can be approximated by the product of two unimodal Schulz-Zimm distributions (2.9) for the marginal distributions $P_S(R)$ and $P_S(h)$. The best fits of $P_S(R)$ and $P_S(h)$ to the size-histograms obtained from our TEM and AFM pictures of the dried specimen, shown in Fig. 2.5, give mean values $\langle R\rangle = 44.2$ nm and $\langle h\rangle = 7.66$ nm, and relative standard deviations of $s_R = 17.3\%$ and $s_h = 55.3\%$, respectively.

5.5.2 Effective sphere diameter

The effective sphere diameter, σ, for the gibbsite platelets studied in this thesis is obtained from equating the second virial coefficient, $B_2(T)$, of neutral hard spheres of radius σ_{B_2} to that of neutral, non-overlapping cylindrical platelets of radius $\langle R\rangle$ and height $\langle h\rangle$, on assuming all orientations to be equally probable. According to [194], this results in

$$\sigma_{B_2}^3 = \frac{3}{2}\langle R\rangle^2 \langle h\rangle \left[1 + \frac{\langle h\rangle}{2\langle R\rangle}\left(1 + \frac{\langle R\rangle}{\langle h\rangle}\right)\left(1 + \frac{\pi\langle R\rangle}{\langle h\rangle}\right)\right], \tag{5.19}$$

giving $\sigma_{B_2} = 65$ nm.

As discussed already in Section 5.4.2 in the context of the SY model for BSA proteins, there are various alternatives to define an effective sphere diameter of aspherical colloids. For instance, by equating the mean geometric cylinder volume and the volume of the effective sphere, we would obtain the geometric effective diameter, $\sigma_{\mathrm{geo}} = [6\langle R^2 h\rangle]^{1/3} = 45$ nm, of a gibbsite platelet.

Accurate analytic expressions for free diffusion coefficients of Brownian cylinders with arbitrary aspect ratio are not available. Therefore, the calculation of effective sphere radii based on these dynamic quantities is less straightforward for circular cylinders than for the spheroids discussed in Section 5.4.2.

Nevertheless, estimates for the free diffusion coefficient of gibbsite platelets can be given. The mean aspect ratio, $p = \langle h\rangle/(2\langle R\rangle) = 0.087$, of the explored platelets is so small that the ultrathin disk limit ($h \to 0$) can be applied to reasonable accuracy. In this limit, one finds [160, 200] $d_{t,0} = (d_{t,0}^{\parallel} + 2d_{t,0}^{\perp})/3 = k_B T/(12\eta_0\langle R\rangle) \approx 3.8\times 10^{-12}$ m^2/s for the orientationally

averaged single-disk translational free diffusion coefficient, and $d_{r,0}^{\perp} = 3k_BT/(32\eta_0\langle R\rangle^3) \approx 2.2\times10^3/\mathrm{s}$ for the (end-over-end tumbling) rotational free diffusion coefficient. Note here that for $p \to 0$, $d_{r,0}^{\perp}$ is equal to the rotational diffusion coefficient $d_{r,0}^{\parallel}$, characterizing rotation with respect to the platelet rotational symmetry axis at infinite dilution. A small but finite value of p lowers somewhat the values both of $d_{t,0}$ and $d_{r,0}^{\perp}$, and $d_{r,0}^{\parallel}$ and $d_{r,0}^{\perp}$ become different. Equating the ultrathin disk limit result for $d_{t,0}$ and $d_{r,0}$ with the translational and rotational free diffusion coefficients $d_{t,0} = k_BT/(3\pi\eta_0\sigma_{d_{t,0}})$ and $d_{r,0} = k_BT/(\pi\eta_0{\sigma_{d_{t,0}}}^3)$ of spheres, results in the effective sphere diameters $\sigma_{d_{t,0}} = 56$ nm and $\sigma_{d_{r,0}} = 66$ nm, of the gibbsite platelets.

Tirado and García de la Torre [201, 202] have provided precise polynomial fits to their simulation data for the single particle diffusion coefficients of cylindrical platelets as a function of p. The allowed aspect ratio range, $p > 0.1$, of these fits, however, excludes the small aspect ratio of the present gibbsite platelets. However, we can estimate the influence of a non-zero p value using the analytic result in Eq. (5.11) for the translational free diffusion coefficient of spheroids, and the expression [196]

$$d_{r,0}^{\mathrm{ell},\perp} = \frac{k_BT}{8\pi\eta_0 ab^2 f_{\mathrm{rot}}(a,b)} \tag{5.20a}$$

$$f_{\mathrm{rot}} = \frac{4}{3}\times\frac{(b/a)^2-(a/b)^2}{2-S(a,b)[2-(b/a)^2]} \tag{5.20b}$$

for the rotational end-over-end tumbling free diffusion coefficient of oblate ($b > a$) spheroids, with the function $S(a,b)$ defined already in Section 5.4.2. Choosing a spheroid of equal aspect ratio $p = a/b = \langle h\rangle/(2\langle R\rangle)$ and volume $v = \pi/6ab^2 = \pi\langle R^2h\rangle$, as in the cylinder model of gibbsite, gives $d_{t,0}^{\mathrm{ell}} = 3.13\times10^{-12}$ m^2/s and $d_{r,0}^{\mathrm{ell},\perp} = 1.4\times10^3/\mathrm{s}$. These values, which are 18% and 36% smaller than their respective ultrathin disk-limit counterparts, suggest that the non-zero thickness of gibbsite platelets has a rather small, yet non-negligible influence on the translational and rotational free diffusion coefficients.

Finally, on employing the power-law representation of simulation data in [88] for the intrinsic viscosity of thin cylinders, we obtain $[\eta]^{\mathrm{cyl}} \approx 6.8$ at $p = 0.087$. Note that this value for $[\eta]$ is similar to the one found experimentally for uncharged gibbsite platelets in [198], and that a spheroid of equal aspect ratio has a distinctly larger intrinsic viscosity of $[\eta]^{\mathrm{ell}} \approx 9.1$. Demanding equality of the interaction-independent linear terms in the virial expansions in Eq. (5.14) for the viscosity of cylindrical platelet and effective sphere suspensions, and on using $\phi^{\mathrm{cyl}} = \pi\langle R^2h\rangle n$ and $\phi^{sph} = (\pi/6){\sigma_{[\eta]}}^3 n$ for equal number density n, an effective diameter $\sigma_{[\eta]} = 63$ nm for gibbsite platelets is obtained.

In summary, the small aspect ratio, $p = 0.087$, of gibbsite platelets implies a rather wide spread in the various effective sphere diameters discussed here, with the largest relative deviation of 46% between σ_{geo} and $\sigma_{d_{r,0}}$. In comparison, the different effective sphere diameters of BSA proteins at $p = 0.37$, discussed in Section 5.4.2, show a maximum spread of less than 10%.

5.5.3 Static mean scattered intensity

To model the static mean scattered intensity of gibbsite solutions recorded by SLS, we employ again the translational-orientational decoupling approximation Eqs. (3.39) with monodisperse interactions assumed. Like the form factor in Eq. (5.17), the decoupling amplitude $X(q)$ is expressed here as a ratio of integrals comprising the radius- and thickness distributions of the model cylinders, with

$$X(q)P_m(q)\int_0^\infty dR\int_0^\infty dh\int_0^1 d\mu P_S(R)P_S(h)v^2(R,h) = \int_0^\infty dR\int_0^\infty dh P_S^2(R)P_S^2(h)v^2(R,h)\left[\int_0^1 d\mu\,\tilde{f}_{\rm cyl}(q,R,h,\mu)\right]^2 + \left[\int_0^\infty dR\int_0^\infty dh\int_0^1 d\mu P_S(R)P_S(h)v(R,h)\tilde{f}_{\rm cyl}(q,R,h,\mu)\right]^2, \tag{5.21}$$

And $P_m(q)$ evaluated according to Eq. (5.17). Due to the small aspect ratio p, $P_m(q)$ and $X(q)$ are practically independent of h. The function $X(q)$ is well approximated by a constant value of 0.72 in the range $q \lesssim 2/\langle R\rangle$, including the full q-range accessible to SLS (*c.f.*, Fig. 5.16).

The structure factor $S(q)$, entering into Eqs. (3.39), has been calculated in MPB-RMSA, on assuming that the pair interaction of charged gibbsite platelets can be approximated by the repulsive HSY pair potential in Eq. (2.6), evaluated for monodisperse effective spheres with a hard-core diameter $\sigma = \sigma_{B_2} = 65$ nm. As further input into Eqs. (2.5) for the HSY screening and coupling parameters, we use $L_B = 1.18$ nm, for DMSO at $T = 293K$, and a residual 1-1 electrolyte concentration of $n_s = 7\times 10^{-6}$ M.

The HSY input parameters that remain to be determined are the effective particle charge Z, and the number concentration, $n_{\rm eff} = 6\phi_{\rm eff}/(\pi\sigma^3)$, of effective spheres. Recalling our discussion in Section 5.5.2 regarding the various effective sphere diameter definitions for gibbsite, we note that the volume fraction, $\phi_{\rm eff}$, of effective spheres is typically different from the physical volume fraction, $\phi = M/(\rho_m V)$, of gibbsite platelets. Here, M is the total mass of suspended gibbsite of known mass density ρ_m, and V is the suspension volume. It can be expected, however, that $\phi_{\rm eff}$ scales linearly in ϕ, and that $\phi_{\rm eff} = 0$ for $\phi = 0$.

Fig. 5.16 includes the experimentally determined intensities (open symbols), for platelet volume fractions $\phi = 0.16\%$ (black) and 0.88% (red). The experimentally recorded intensities have been divided by their respective, experimentally determined value for ϕ, which in Eq. (3.39a) is proportional to N, and by the q-independent factor I_0 that is the same for all intensity measurements corrected for source intensity, recording time, and scattering volume. The resulting experiment data have been fitted by $P_m(q)\times S_m(q)$, with best fits depicted as solid lines in Fig. 5.16.

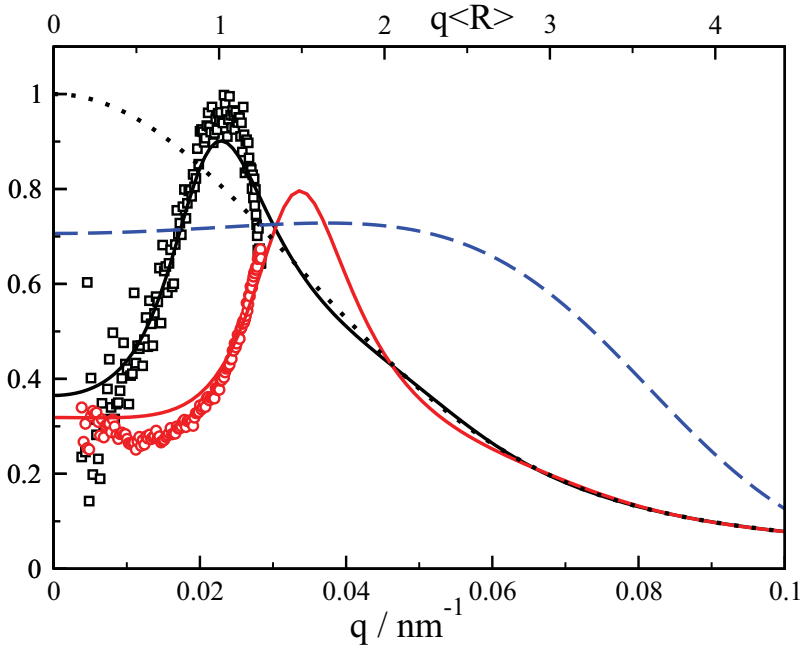

Fig. 5.16: *Normalized experimental mean scattered intensity, $I(q)/(I_0\phi)$, of gibbsite platelets in DMSO, for $\phi = 0.16\%$ (black squares) and $\phi = 0.88\%$ (red circles), in comparison to the fit functions $P_m(q) \times S_m(q)$ with $\phi_{eff} = 0.43\%$ (black line) and $\phi_{eff} = 1.68\%$ (red line). Black dotted curve: measurable form factor $P_m(q)$. Blue dashed curve: decoupling amplitude $X(q)$.*

Since an accurate determination of Z relies on fitting the maximum in $I(q)$, which unfortunately is not located inside the SLS-resolved q-range for most of the considered concentrations, we alternatively estimate Z by the observed I/LC transition concentration, which according to our experiments occurs at $\phi_{\text{I/LC}} = 8\%$, at low salinity. Simulations predict the isotropic-nematic transition of neutral hard disks to occur at $n_{\text{I/LC}}d^3 \approx 4$ [203, 204], where $n_{\text{I/LC}}$ is the (isotropic phase) number density at the transition, and d is the disk diameter. Using this relation, we estimate the charge on a gibbsite platelet by assuming that $d = 2[\langle R\rangle + \kappa^{-1}]$ and $n_{\text{I/LC}} = \phi_{\text{I/LC}}/(\pi\langle R^2 h\rangle)$, with $\kappa^2 = 4\pi L_B(n_{\text{iso}}|Z| + 2n_s)/(1-\phi_{\text{I/LC}})$. For the considered large concentration at the I/LC transition point, the residual salt contribution to κ can be neglected. Solving for the platelet effective charge leads to $Z = 71$ This effective charge value is used in all our calculations, independent of ϕ, since the dependence of Z on ϕ and n_s is unknown to date. According to Ref. [205], $Z = 71$ is a quite reasonable value for gibbsite platelets.

As demonstrated in Fig. 5.16, decently good fits of the experimental $I(q)$ are obtained from adjusting the only remaining fit parameter, ϕ_{eff}, which enters into the MPB-RMSA calculation of $S(q)$. The global factor I_0 in Eq. (3.39a) only sets the overall scale, and is system independent. Assuming a linear homogeneous relation $\phi_{\text{eff}}(\phi)$, from our fit we obtain $\phi_{\text{eff}} = 1.93\phi$.

While the theoretical fit to the experimental $I(q)$ is satisfying, future SAXS experiments are desirable to obtain $I(q)$ in a more extended q-range, covering all the structural features in $I(q)$, and allowing for a more detailed fitting.

CHAPTER

SIX

Diffusion and Rheology results: Theory, simulation and experiment

6.1 Short-time diffusion and high-frequency viscosity in simulation and theory

6.1.1 Accelerated Stokesian Dynamics computer simulations

The accelerated Stokesian Dynamics simulations of suspensions of colloidal HSY particles, with results presented in this chapter, as well as the related Monte Carlo simulations with results presented in Chapter 5, and the Molecular Dynamics simulations for the equilibrium structure of uncharged spheres, have been performed by Prof. Adolfo J. Banchio at the National University of Córdoba, Argentina, in the framework of our joint theoretical-computer simulation project.

The simulation data for $H(q)$ and η_∞ in the HSY systems explored in this work, have been generated using an accelerated Stokesian Dynamics (ASD) simulation code. The details of the simulation method have been explained in Ref. [24]. It allows to simulate short-time properties of a larger number of spheres, typically up to $N = 1000$, placed in a periodically replicated simulation box, allowing for improved statistics. Since short-time properties are obtained from single-time equilibrium averages, we have used equilibrium configurations generated using a Monte-Carlo simulation method for charged spheres, and a Molecular Dynamics algorithm for neutral hard spheres, with the many-sphere HIs accounted for using the ASD scheme. The computed hydrodynamic function, $H_N(q)$, shows a strong system-size dependence, even when N is not small. We therefore extrapolate $H_N(q)$ to the thermodynamic limit using the finite-size

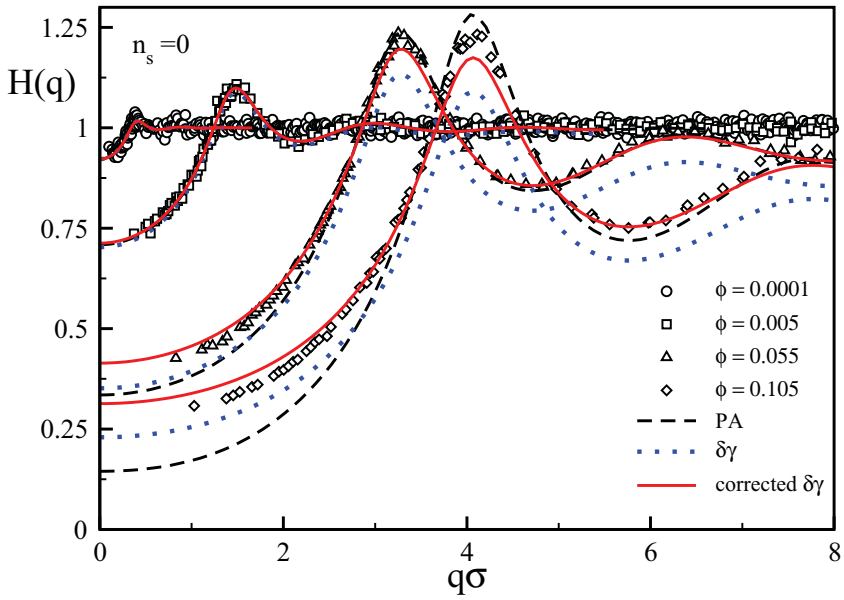

Fig. 6.1: *Hydrodynamic function of a zero-salinity system at volume fractions, ϕ, as indicated. Open symbols: ASD simulation data. Black dashed lines, blue dotted curves, and red solid lines: PA scheme, $\delta\gamma$ scheme, and self-part corrected $\delta\gamma$-scheme results, respectively. As input to the analytical short-time schemes, $S(q)$ and $g(r)$ have been computed in MPB-RMSA. These static functions are displayed in Fig. 5.1. System parameters are: $Z = 100, L_B = 5.62$ nm, and $\sigma = 200$ nm.*

scaling correction [206, 207],

$$H(q) = H_N(q) + 1.76\, S(q) \frac{\eta_0}{\eta_\infty(\phi)} \left(\phi/N\right)^{1/3}, \tag{6.1}$$

which, for $q \to 0$ and $q \to \infty$, includes the finite-size corrections for K and d_s, respectively. This finite-size correction formula was initially proposed by Ladd for hard spheres [206, 208, 209], and has been subsequently applied also to charged spheres [23], and solvent-permeable particles [26]. As pointed out by Ladd [206], and explained by Mo and Sangani [207], η_∞ is not critically dependent on N so that a finite size scaling extrapolation to $N \to \infty$ is not needed (see also [25]). The simulation results discussed in following are obtained from averaging over 2000 configurations, for systems of typically $N = 512$ particles.

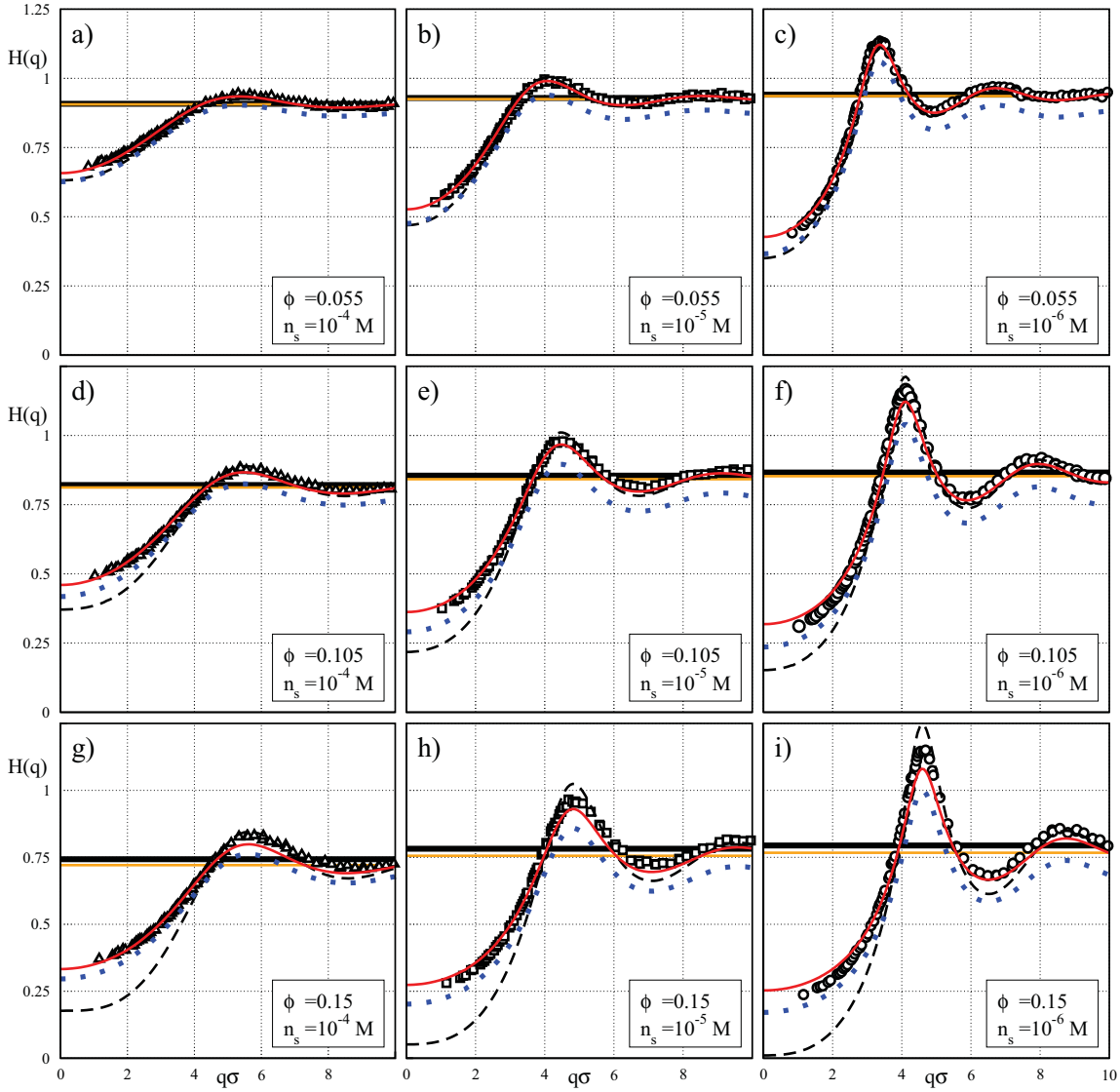

Fig. 6.2: *Hydrodynamic function $H(q)$ for systems at various volume fractions, ϕ, and salt concentrations, n_s, as indicated in each panel. The panels are ordered by ϕ, increasing from top to bottom, and by n_s, decreasing from left to right. Open symbols: ASD simulations. Black dashed lines, blue dotted curves, and red solid lines: PA scheme, $\delta\gamma$ scheme, and self-part corrected $\delta\gamma$-scheme results, respectively. In the latter scheme, the self-diffusion coefficient has been calculated using the PA scheme according to Eqs. (4.25) and (4.11). The horizontal black and orange lines mark the values for $d_s/d_{t,0}$ obtained by ASD simulations and in the PA scheme, respectively. As input to the analytical short-time schemes, $S(q)$ and $g(r)$ have been computed in MPB-RMSA. These functions are displayed in Figs. 5.2 and 5.3, respectively. System parameters: $L_B = 5.617$ nm, $\sigma = 200$ nm, and $Z = 100$.*

6.1.2 Diffusion properties of charged particles

The results for $H(q)$ obtained by the ASD simulations and all analytic short-time schemes described in Chapter 4, are included in Figs. 6.1 and 6.2. Open symbols represent ASD simulation data, black dashed curves are our PA results, blue dotted curves the zeroth-order $\delta\gamma$ scheme, and red solid lines the self-part corrected $\delta\gamma$-scheme predictions. In Fig. 6.1, salt-free suspensions are considered, with the corresponding pair-structure functions $S(q)$ and $g(r)$ displayed in Fig. 5.1.

The systems considered in Fig. 6.2 are for three different finite salt concentrations, with the corresponding functions $S(q)$ and $g(r)$ displayed in Figs. 5.2 and 5.3, respectively. The black and orange horizontal lines in each panel of Fig. 6.2 mark the reduced short-time self-diffusion coefficient, $d_s/d_{t,0} = H(q \to \infty)$, obtained from the ASD simulations and the PA scheme, respectively.

As discussed already in Section 5.1.2, the rightmost column of panels in Fig. 6.2 presents results for three systems of strongly charged particles with very low residual, but experimentally still accessible salt content. The most concentrated system in panel (i) is rather close to the freezing transition point.

Different from neutral hard spheres, where $H(q_m)$ decreases linearly with increasing ϕ, the hydrodynamic function peak heights of the three low-salinity systems depends non-monotonically on ϕ, with ASD predicted values $H(q_m) = 1.13$, 1.17, and 1.15 for the systems in panels (c), (f), and (i), respectively. Such a non-monotonic ϕ-dependence of $H(q_m)$ is typical for low-salinity systems, as discussed in Refs. [23] and [120]. The ASD results for the reduced self-diffusion coefficient, $d_s/d_{t,0}$, and the corrected $\delta\gamma$-scheme results for the sedimentation coefficient K in panels (c), (f), and (i), follow closely the concentration-scaling Eqs. (4.24b) and (4.24a), with $a_t = 2.63$ and $a_s = 1.44$.

We proceed in our discussion by considering the systems in the leftmost column of panels. The salt concentration, $n_s = 10^{-4}$ M, of these systems is so large that the neutral hard-sphere (HS) limit is practically reached. The comparison with the $H(q)$ of genuine neutral hard spheres at volume fractions equal to those in panels (a), (d), and (g), shows relative differences of less than 6% in all three cases. The proximity to genuine neutral hard-sphere systems is manifest also in the large values, $k = 18.5, 18.6$, and 18.7, of the screening parameter, and in the small ratios $k_c^2/k_s^2 = 0.01, 0.02$, and 0.03, for the systems in panels (a), (d), and (g), respectively.

For the smallest considered concentration $\phi = 0.055$ (top row of panels in Fig. 6.2), the differences in the respective $H(q)$ predicted by the analytic methods and the ASD simulations are very small. Since the PA scheme becomes exact at low ϕ, this illustrates that, despite their overall inaccuracies, the self-part corrected, and even the uncorrected $\delta\gamma$-scheme, can be used to obtain good estimates of $H(q)$ also for more dilute suspensions.

With increasing ϕ, pronounced differences are observed in Fig. 6.2 between the PA-scheme and ASD results for $H(q)$. This reflects the expected failure of the PA scheme in concentrated

suspensions, where three-body and higher-order HI contributions become influential. The deviations of the PA-scheme results from the precise simulation data are most pronounced for the peak value $H(q_m)$, which is overestimated by the PA scheme, and in the sedimentation coefficient, $K = H(q \to 0)$, which is underestimated. In fact, for the system in panel (i), the PA prediction for K is just barely larger than zero, turning to unphysical negative values when the volume fraction surpasses $\phi = 0.154$ at a fixed $n_s = 10^{-6}$ M. However, the PA-scheme values for $d_s/d_{t,0}$ remain in very good agreement with the ASD results, with a relative deviation of less than 3.5% even at $\phi = 0.15$. The values for $d_s/d_{t,0}$ predicted by the uncorrected $\delta\gamma$ scheme are generally in less good agreement with the simulation data, clearly revealed in Fig. 6.2 by the parallel offset of the corresponding $H(q)$.

The self-part corrected $\delta\gamma$-scheme results for $H(q)$ in Fig. 6.2 (red solid lines) illustrate that this hybrid scheme combines the good accuracy of the PA scheme regarding d_s, and of the $\delta\gamma$ scheme regarding $H^d(q)$. Indeed, the corrected $\delta\gamma$-scheme results for $H(q)$ are in overall good agreement with the ASD simulation data for all considered systems, with the largest deviation of 6% for $H(q_m)$ observed in panel (i).

In closing our discussion of Fig. 6.2, a short comment is in order regarding the computational cost caused by the considered methods of computing $H(q)$. The fast and accurate evaluation of $S(q)$ and $g(r)$ by the MPB-RMSA method, in combination with the easily evaluable integrals in Eqs. (4.11), (4.12), and (4.19), has allowed us to implement a convenient graphical user interface code, described in Appendix E. Using this code, MPB-RMSA results for $S(q)$ and $g(r)$, and PA-, $\delta\gamma$-, and self-part corrected $\delta\gamma$-scheme results for $H(q)$, are obtained in less than 1 second of cpu time, for a given set of input parameters $\{L_B, \sigma, Z, n_s, \phi\}$. Thus, all curves depicted in Fig. 6.2, except for the ASD simulation data, have been obtained altogether in less than a minute on a standard desktop PC. In comparison, the computation of just one of the computer simulation curves in Fig. 6.2 required on a standard desktop PC typically 5 hours of cpu time for generating 2000 equilibrated configurations (using our MC method) and approximately 8 hours of cpu time for computing $H(q)$ with the ASD scheme. The overall accuracy and fast performance of the hybrid $\delta\gamma$ scheme in Eqs. (4.25)-(4.27) make this scheme well-suited for the real-time fitting, even of large sets of experimentally recorded data for $H(q)$ and $D(q)$ [20].

6.1.3 Hybrid $\delta\gamma$ scheme for diffusion of neutral hard spheres

The main virtue of the d_s-corrected (zeroth-order) $\delta\gamma$ scheme lies in its good applicability to charge-stabilized systems. However, it is interesting to assess in more detail its performance in the limiting case of neutral hard spheres, in particular when the values of $H(q)$ at $q = 0$ and $q = q_m$ are considered. Recall for hard spheres that the accurate expression for $d_s^{\rm HS}$ in Eq. (4.26) should be preferentially used instead of the approximate PA result. For neutral spheres, higher-order HI contributions to d_s begin to matter at somewhat smaller concentrations than for charge-stabilized particles, where near-contact configurations are unlikely.

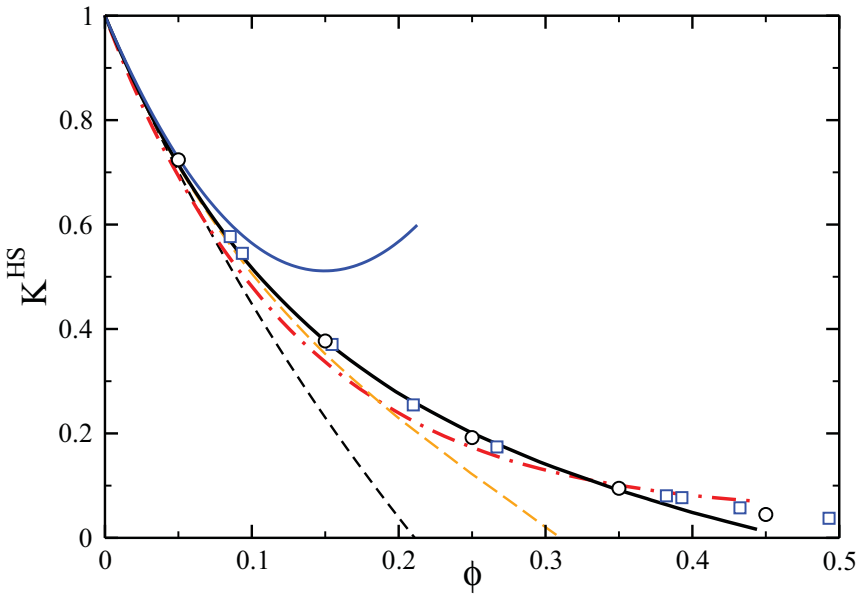

Fig. 6.3: *Reduced short-time sedimentation coefficient, K^{HS}, of neutral hard spheres. Open circles: Hydrodynamic force multipole simulation data by Abade et al. [26]. Open Squares: Lattice-Boltzmann simulation data by Segrè et al. [208]. Black dashed line: PA-scheme result. Dashed-dotted red line: uncorrected $\delta\gamma$-scheme result. Dashed orange line: self-part corrected $\delta\gamma$-scheme result, with $d_s/d_{t,0}$ taken from the PA-scheme. Solid black line: self-part corrected $\delta\gamma$-scheme result, with $d_s/d_{t,0}$ according to Eq. (4.26). Solid blue line: second-order virial result $K^{HS} = 1 - 6.546\phi + 21.918\phi^2$ [166]. The static structure factor input was obtained using the analytic Percus-Yevick solution.*

In Fig. 6.3, numerically precise Lattice Boltzmann [208] and hydrodynamic force multipole simulation results [26] for $K^{\mathrm{HS}}(\phi)$ are compared with the predictions of all considered analytical schemes. For $\phi \lesssim 0.35$, the uncorrected $\delta\gamma$ scheme underestimates the simulation data, showing the opposite trend of a slight overestimation for $\phi \gtrsim 0.35$. The corrected $\delta\gamma$ scheme with d_s-input according to Eq. (4.26), on the other hand, is in excellent agreement with the simulation data up to $\phi \approx 0.4$, reflecting the accuracy of the $\delta\gamma$-scheme predictions for $H^d(q)$ also for neutral spheres.

For large volume fractions $\phi \gtrsim 0.4$, however, the distinct part, $K^{\mathrm{HS}} - d_s^{\mathrm{HS}}/d_{t,0}$, of the sedimentation coefficient is considerably underestimated by the $\delta\gamma$ scheme, to such an extent that the self-part corrected $\delta\gamma$ scheme prediction for K^{HS} assumes unphysical negative values for $\phi \gtrsim 0.45$. Up to $\phi \approx 0.2$, the corrected $\delta\gamma$-scheme prediction for K^{HS}, with d_s^{HS} obtained by the PA scheme, lies closer to the simulation data than the uncorrected $\delta\gamma$-scheme result. This can be explained by the precise account of (two-body) lubrication effects in the PA-scheme, which are not included in the uncorrected $\delta\gamma$ scheme. At larger concentrations, however, the corrected $\delta\gamma$ scheme, with PA input for d_s, increasingly underestimates the sedimentation coefficient up to the point that, for $\phi \gtrsim 0.31$, unphysically negative values for K^{HS} are attained. This is a consequence of the already noted many-sphere hydrodynamic shielding effect, disregarded in the PA scheme, which lowers the strength of the HIs without reducing their range, leading to a larger self-diffusion coefficient than predicted on basis of hydrodynamic pair-interactions alone. The neglect of shielding effects by the PA scheme, both in the self- and distinct parts of K^{HS}, is the reason for the crossover of the PA curve of K^{HS} to negative values already at $\phi \approx 0.21$.

Regarding again Fig. 6.3, we note that the second-order virial result,

$$K^{\mathrm{HS}} = 1 - 6.546\phi + 21.918\phi^2 + \mathcal{O}(\phi^3), \tag{6.2}$$

derived in Ref. [166], ceases to be applicable for $\phi \gtrsim 0.15$, where the representing curve bends up to larger values. This is the reason why this second-order virial result cannot be used, different from the corresponding virial results for d_s^{HS}, $\eta_\infty^{\mathrm{HS}}$, and $H^{\mathrm{HS}}(q_m)$, to construct analytic extrapolation formulas, which are valid for all concentrations up to the freezing transition.

We proceed by discussing the concentration dependence of the peak value, $H^{\mathrm{HS}}(q_m)$, of the hydrodynamic function of neutral spheres. As noted in Sec. 4.1, $H(q_m)$ is related to the short-time cage diffusion coefficient, $d_{\mathrm{cge}} = d_{t,0}H(q_m)/S(q_m)$, characterizing the initial decay rate of density fluctuations of wavelength equal to the nearest-neighbor cage size. Fig. 6.4 displays the decline of the hard-sphere $H(q_m)$ with increasing ϕ. To excellent accuracy up to the freezing volume fraction, this decline is described by the first-order virial result [23]

$$H^{\mathrm{HS}}(q_m) = 1 - 1.35\phi. \tag{6.3}$$

Indeed, all the depicted ASD [23] and hydrodynamic force multipole [26] values for $H(q_m)$

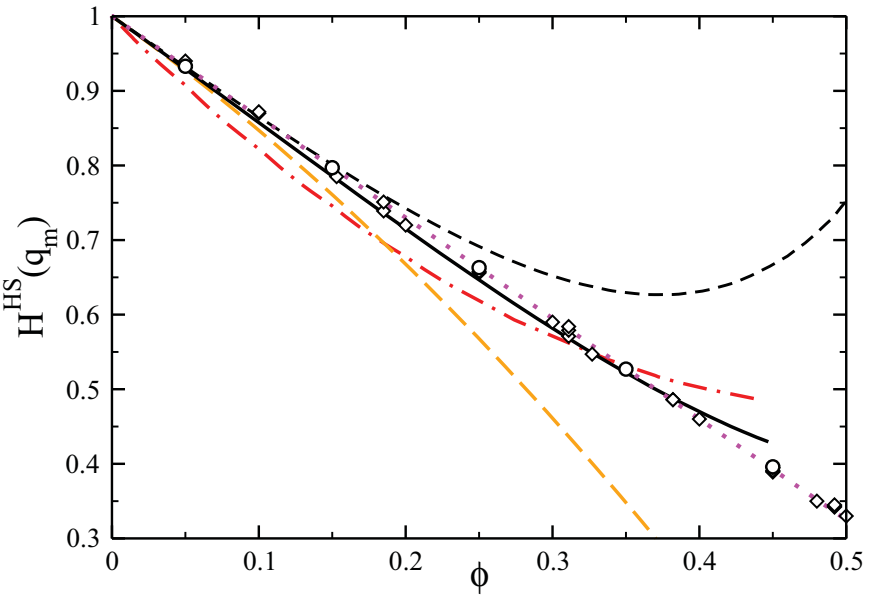

Fig. 6.4: *Hydrodynamic function peak value, $H(q_m)$, of neutral hard spheres. Open circles: Hydrodynamic force multipole simulation results by Abade et al. [26]. Open diamonds: ASD simulation data [23]. Black dashed line and dashed-dotted red line: PA-scheme and uncorrected $\delta\gamma$-scheme results, respectively. Dashed orange line: self-part corrected $\delta\gamma$-scheme results, with $d_s/d_{t,0}$ taken from PA-scheme calculations. Solid black line: self-part corrected $\delta\gamma$-scheme results, with $d_s/d_{t,0}$ according to Eq. (4.26). Dotted curve in magenta: $1-1.35\phi$. The static structure factor input was obtained using the analytic Percus-Yevick solution.*

follow this line, indicating that, for a so far unknown reason, all higher order virial contributions cancel out. According to Fig. 6.4, the uncorrected $\delta\gamma$ scheme significantly underestimates $H^{\rm HS}(q_m)$ for $\phi \lesssim 0.35$, overestimating it instead for $\phi \gtrsim 0.4$. In contrast, the corrected $\delta\gamma$-scheme result with the precise $d_s^{\rm HS}$ according to Eq. (4.26), is distinctly more accurate in that it only very slightly underestimates the linear decay in Eq. (6.3) for $\phi \lesssim 0.4$. Moreover, for $\phi > 0.4$, the positive-valued deviations from $1 - 1.35\phi$ are substantially smaller than those of the uncorrected $\delta\gamma$ scheme.

The corrected $\delta\gamma$-scheme prediction for $H^{\rm HS}(q_m)$, with d_s calculated using the PA scheme, is a decent approximation up to $\phi \lesssim 0.15$. Its bending over to smaller values occurs for $H^{\rm HS}(q_m)$ at somewhat larger ϕ than in the sedimentation case, indicating that $\delta\gamma$-scheme results for $H^d(q)$ are more accurate at $q = q_m$ than at $q \approx 0$. The curve for $H^{\rm HS}(q_m)$ predicted by the PA scheme bends over to larger values at a concentration $\phi \approx 0.37$ vastly beyond its range ($\phi \lesssim 0.1$) of applicability. The total neglect of many-body HIs in the PA scheme implies, at larger ϕ, an underestimation of d_s, but to a larger extent an overestimation of $H^d(q_m)$. As a net result, $H^{\rm HS}(q_m)$ at large ϕ is strongly overestimated by the PA scheme.

In summarizing our discussion of hard-sphere systems, the key message conveyed by Figs. 6.3 and 6.4 is that the corrected $\delta\gamma$ scheme, with d_s according to Eq. (4.26), describes $H^{\rm HS}(q)$ quite precisely for $\phi \lesssim 0.4$.

6.1.4 High-frequency viscosity in simulation and theory

In the following, we compare viscosity results obtained by the various methods described in Sec. 4, for the two limiting cases of deionized (low-salinity) charged-sphere and neutral hard-sphere suspensions. Results for systems with intermediate added salt are in between these two limiting cases.

In Fig. 6.5, we display our viscosity results for neutral hard spheres (HS) with those for two deionized suspensions of highly charged spheres (CS) where $n_s = 0$. Results by all the methods in Section 4 are shown. We point out that, in addition to the CS system of Fig. 6.2 with parameters $L_B = 5.617$ nm, $\sigma = 200$ nm, and $Z = 100$ (referred to here as system CS-1), whose ASD results for η_∞ in Fig. 6.5 are indicated by filled red circles, we additionally show viscosity results for another zero-salt system where $L_B = 0.71$ nm, $\sigma = 50$ nm, and $Z = 70$ (labeled CS-2), whose ASD data for η_∞ are represented by red diamonds filled in blue. The reason for including in Fig. 6.5 results for two different deionized systems, is that system CS-1 freezes at $\phi \approx 0.15$, whereas systems CS-2 stays fluid up to $\phi \sim 0.3$, allowing us to test the predictions of our analytical methods in a more extended volume fraction range. The ASD simulation data for $\eta_\infty(\phi)$ for systems CS-1 and CS-2 merge continuously, overlapping nearly perfectly within $0.1 < \phi < 0.15$. This indicates that the limiting behavior of η_∞ for highly correlated charged spheres is practically reached in both systems. Therefore, the depicted CS-results for η_∞ were calculated in the analytic schemes using the parameters of system CS-2

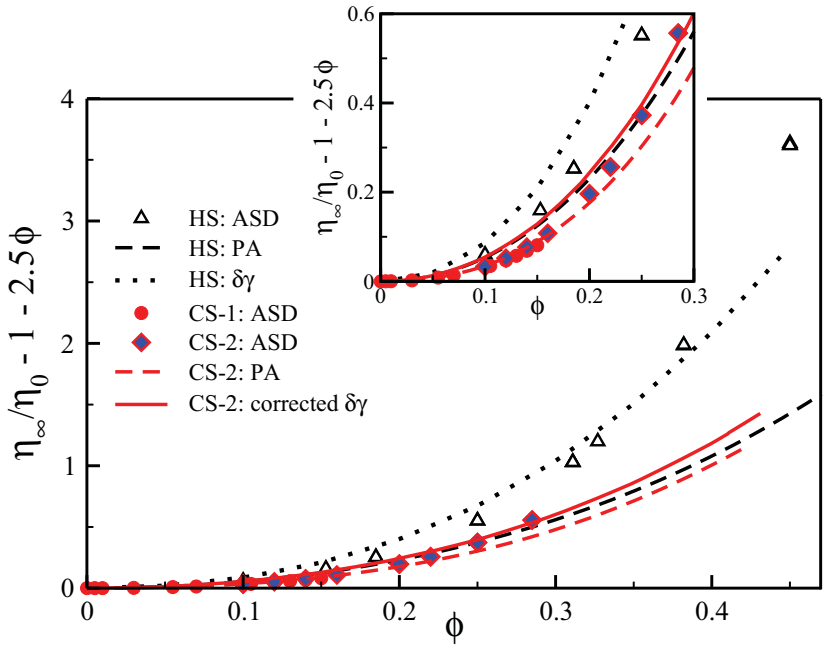

Fig. 6.5: *Reduced high-frequency viscosity, η_∞/η_0, as a function of ϕ, for a suspension of neutral hard spheres (HS, in black), and two deionized charged-sphere suspensions (CS-1 and CS-2, in red). The leading-order Einstein contribution, $1+2.5\phi$, is subtracted off to expose the differences. Symbols: ASD simulation results. Dashed lines: PA-scheme results according to Eq. (4.15). Dotted lines: $\delta\gamma$-scheme results according to Eqs. (4.20)-(4.22). Solid lines: self-part corrected $\delta\gamma$-scheme results according to Eqs. (4.27), (4.21), and (4.22). All analytic schemes use the MPB-RMSA $S(q)$ as input. The CS-1 viscosity results represented by red filled circles are ASD data for $L_B = 5.617$ nm, $\sigma = 200$ nm, and $Z = 100$. The ASD data for the more weakly charged, smaller particles of system CS-2, with $L_B = 0.71$ nm, $\sigma = 50$ nm, and $Z = 70$ are indicated by red diamonds filled in blue. The parameters of system CS-2 have been used in the analytic calculations. The inset magnifies the details at lower ϕ.*

only. The deviations in η_∞ for the two CS systems are minuscule in all considered analytic schemes.

Consider first the performance of the PA scheme. By its definition, the PA result for η_∞ is in very good agreement with the ASD simulation data at low ϕ, but the agreement becomes poorer with increasing volume fraction. While the deviations between the ASD and PA results for low-salt systems are very small up to $\phi \lesssim 0.2$, for neutral spheres significant differences are visible already for $\phi \gtrsim 0.1$. These differences originate from the fact that in charged-sphere suspensions, near-contact configurations are disfavored by the electric repulsion, i.e., charged-sphere systems are hydrodynamically more dilute than neutral sphere suspensions. Since higher-order HI effects on η_∞ in low-salinity charged systems are weaker, for many such systems (including system CS-1), which freeze already at $\phi \lesssim 0.2$, the accuracy of the PA-scheme for η_∞ is sufficiently good in the whole fluid regime. Regarding $H(q)$, however, the PA-scheme predictions for charged spheres deviate significantly from the ASD data already at $\phi \gtrsim 0.1$ (see again Fig. 6.2). At larger ϕ, and in contrast to the ASD data, the PA scheme predicts only a slight enlargement of η_∞ in going from charged to neutral spheres. The distinctly larger values of η_∞ for concentrated hard-sphere suspensions are thus mostly due to near-field, many-body HIs which enlarge the viscous dissipation. Overall, however, η_∞ is rather insensitive to the range of the pair potential, at least in comparison to the static (zero frequency) viscosity which for concentrated systems can become very much larger than η_∞ [210].

The self-part modified $\delta\gamma$ scheme for η_∞, defined by Eq. (4.27), agrees overall very well with the ASD data for charged spheres in the whole fluid-state concentration regime. Small deviations from the simulation data are noticed at low ϕ values only. Regarding neutral hard spheres, a similar observation applies to the unmodified second-order $\delta\gamma$ scheme, which describes the ASD simulation data quite well up to $\phi \approx 0.4$. The slight overestimation of $\eta_\infty^{\mathrm{HS}}$ at lower ϕ can be attributed to the non-exact treatment of two-body HI contributions by the $\delta\gamma$ scheme.

Overall, the high-frequency viscosity of charged-sphere systems at low salinity is well captured by the modified $\delta\gamma$-scheme in Eq. (4.27), and for neutral hard spheres by the unmodified $\delta\gamma$ scheme (up to $\phi \approx 0.4$). Different from the self-part corrected $\delta\gamma$ scheme for $H(q)$, which makes reliable predictions for arbitrary salinities, the modified $\delta\gamma$ scheme for η_∞ applies to low-salinity systems only, and the unmodified $\delta\gamma$ scheme only to neutral hard spheres. The reasons for this have been discussed already in Section 4.4.

Before closing our discussion of η_∞, it is of interest to compare the numerical efforts required by the employed methods. The computation of the 45 ASD data points for neutral and charged spheres included in Fig. 6.5 required about 500 hours of cpu time on a modern desktop PC. This large time investment should be compared to the few minutes computation time on a comparable PC which were required for the results by all considered analytic schemes, amounting to more than one thousand data points on a dense mesh of ϕ values.

6.1.5 Short-time relations between viscosity and diffusion properties

Having quite accurate analytic methods for short-time properties at our disposal, we are in the position to analyze possible relations between these properties in the whole fluid-state concentration regime. Specifically, we want to test the validity of two generalized Stokes-Einstein (GSE) relations,

$$\frac{D^*(\phi)}{d_{t,0}} \times \frac{\eta_\infty(\phi)}{\eta_0} \approx 1, \tag{6.4}$$

for $D^*(\phi) = d_s(\phi)$ and $D^*(\phi) = d_{\mathrm{cge}}(\phi)$. In addition, we probe the validity of the Kholodenko-Douglas GSE (KD-GSE) relation [30],

$$\frac{d_c(\phi)}{d_{t,0}} \times \frac{\eta_\infty(\phi)}{\eta_0} \times \sqrt{S(q \to 0, \phi)} \approx 1, \tag{6.5}$$

between the collective diffusion coefficient, $d_c = K/S(q \to 0)$, η_∞, and the square root of the isothermal osmotic compressibility given by $S(q \to 0)$. In particular the KD-GSE relation has been used in various biophysical and soft matter studies [31–34].

All three considered GSE relations are exact at $\phi = 0$ only. The approximate validity of a GSE relation in concentrated systems is an important issue in microrheological studies, since it allows to infer a rheological property more easily from a diffusion measurement. For testing the GSE relations in Eqs. (6.4) and (6.5), we consider here again the two limiting HSY cases of a low-salinity charge-stabilized system and neutral spheres, since the differences in the respective short-time dynamic properties are here largest.

For a precise test of the GSE relations in the case of hard spheres, we take advantage of simple analytic expressions available for all short-time properties appearing in Eqs. (6.4) and Eq. (6.5), with the exception of K, for which we use the quite accurate self-part corrected $\delta\gamma$-scheme result depicted in Fig. 6.3. The analytic expressions for hard spheres, which apply to excellent accuracy up to $\phi = 0.5$, are Eq. (6.3) for $H^{\mathrm{HS}}(q_m)$, Eq. (4.26) for d_s^{HS}, and the generalized Saitô-type expression for $\eta_\infty^{\mathrm{HS}}$ [25],

$$\frac{\eta_\infty^{\mathrm{HS}}}{\eta_0} = 1 + \frac{5}{2}\phi\frac{1+S}{1-\phi(1+S)}, \tag{6.6}$$

where $S = 1.001\phi + 0.95\phi^2 - 2.15\phi^3$. Moreover, we use the precise formula for the structure factor peak height [210]

$$S^{\mathrm{HS}}(q_m) \approx 1 + 0.644\phi g^{HS}(x = 1^+), \tag{6.7}$$

where $g^{\mathrm{HS}}(x = 1^+) = (1 - 0.5\phi)/(1-\phi)^3$ is the Carnahan-Starling contact value for the hard-sphere rdf. For $S^{\mathrm{HS}}(q \to 0)$ in Eq. (6.5), we employ the Carnahan-Starling equation of state [4, 7], which gives $S^{\mathrm{HS}}(q \to 0) = (1-\phi)^4/[(1+2\phi)^2 + \phi^3(\phi - 4)]$.

In testing the GSE relations in Eqs. (6.4) and (6.5) for low-salinity systems, for the diffusion

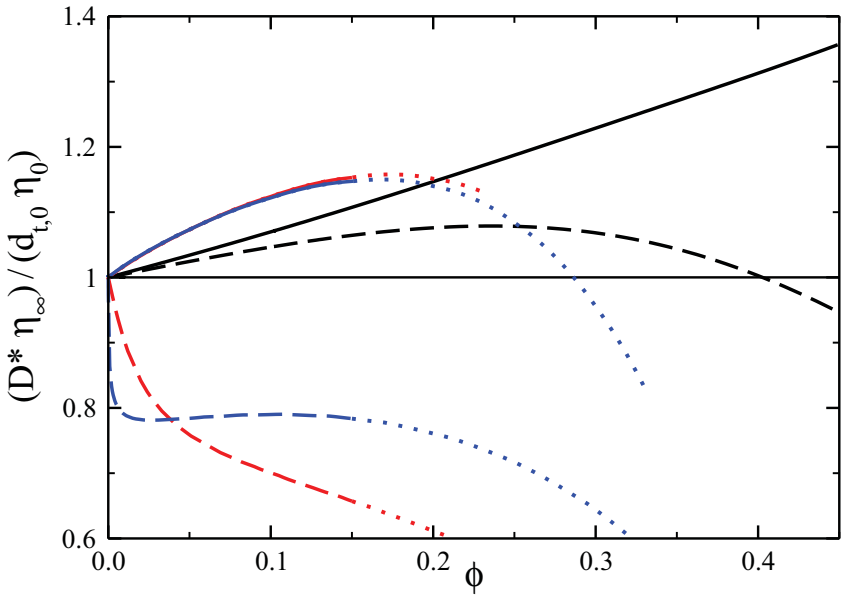

Fig. 6.6: *Test of the two GSE relations in Eq. (6.4), relating η_∞ to $D^* = d_s$ and $D^* = d_{cge}$, respectively. Solid lines: $(d_s/d_0) \times (\eta_\infty/\eta_0)$ vs. ϕ. Dashed lines: $(d_{cge}/d_0) \times (\eta_\infty/\eta_0)$ vs. ϕ. Black curves are hard-sphere results obtained from Eqs. (4.26), (6.3), (6.6), and (6.7). Red and blue curves are corrected $\delta\gamma$-scheme results for the low-salinity charged-sphere systems CS-1 and CS-2, respectively, both assuming a residual salt content of $n_s = 10^{-6}$ M. The corrected $\delta\gamma$-scheme results have been calculated using Eqs. (4.27), (4.21), and (4.22) for η_∞, and Eqs. (4.25) and (4.11) for d_s and $d_{cge} = d_0 H(q_m)/S(q_m)$. As input to all analytic schemes, MPB-RMSA results for $S(q)$ have been used.*

properties we use the self-part corrected $\delta\gamma$ scheme, with d_s calculated by the PA scheme. For η_∞ we use the corrected $\delta\gamma$ scheme according to Eq. (4.27).

The validity of the two GSE relations in Eq. (6.4) is examined in Fig. 6.6. A valid GSE relation is reflected by a horizontal line of unit height. For neutral hard spheres (black lines), the product $(d_s^{\rm HS}/d_{t,0}) \times (\eta_\infty^{\rm HS}/\eta_0)$ is well approximated, for all displayed ϕ, by its first-order in ϕ expansion given by $1 + 0.67\phi$, showing a more than 20% violation of this GSE relation for $d_s^{\rm HS}$ when $\phi \gtrsim 0.3$.

Different from $d_s^{\rm HS}$, the GSE scaling for $d_{\rm cge}^{\rm HS}$ is approximately satisfied with a maximal deviation from one of 8%. Thus, for hard-sphere like colloidal particles available only in amounts too small for a mechanical rheological experiment, one can determine η_∞ approximately from a dynamic scattering experiment measuring $D(q_m)$.

According to Fig. 6.6, in low-salinity systems of charged particles, the GSE-relation for d_s is overall of similar accuracy as that for hard spheres, although the deviations from one are larger at smaller ϕ. The curves for $(d_s/d_{t,0}) \times (\eta_\infty/\eta_0)$ obtained for the two low-salinity

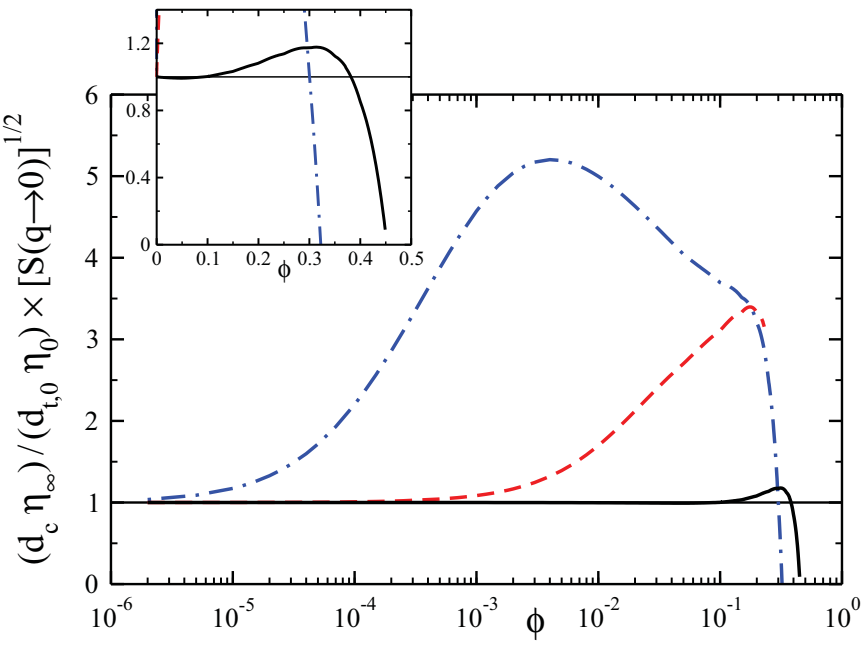

Fig. 6.7: *Test of Kholodenko-Douglas GSE relation in Eq. (6.5). Black curves: neutral hard-sphere results based on the precise analytic result in Eq. (6.6) for η_∞^{HS}, $S^{HS}(q\to 0)$ according to the Carnahan-Starling equation of state, and K^{HS} calculated by the self-part corrected $\delta\gamma$-scheme Eq. (4.25), using in place of $[d_s/d_0]_{PA}$ the, for hard spheres, more accurate expression $[d_s/d_0]^{HS}$ given in Eq. (4.26). Red (dashed) and blue (dashed-dotted) curves are self-part corrected $\delta\gamma$-scheme results for the low-salinity systems CS-1 and CS-2 (with $n_s = 10^{-6}$ M), respectively, using Eqs. (4.27), (4.21), and (4.22) for η_∞, and Eqs. (4.25) and (4.11) for $d_c = d_0 H(q\to 0)/S(q\to 0)$. As input to all analytic schemes, MPB-RMSA results for $S(q)$ have been used.*

systems coincide practically for $\phi \lesssim 0.15$. The downturn of these two curves at larger $\phi \gtrsim 0.18$, indicated by the dotted curve continuations in Fig. 6.6, is not shared by the ASD simulation data (c.f., Fig. 25 in [23]). This is an artifact of the PA scheme which, as discussed already in relation to Fig. 6.2, tends to underestimate d_s at larger ϕ.

Different from neutral hard spheres, in low-salinity systems the GSE relation for $d_{\rm cge}$ is manifestly violated already at very low ϕ. The strong difference in the $(d_{\rm cge}/d_{t,0})\times(\eta_\infty/\eta_0)$ curves for the two considered low-salinity systems is due to the different ϕ-dependence of their respective $S(q_m)$. The pronounced decline of both curves at low ϕ is mainly triggered by the sharp low-ϕ rise of $S(q_m)$ in low-salinity systems.

Kholodenko and Douglas [30] have proposed the GSE relation in Eq. (6.5) using mode-coupling theory like arguments. For neutral spheres at low ϕ, we can check this relation analytically using the numerically precise second-order virial expansion results for $K^{\rm HS}$ in Ref. [166], $\eta_\infty^{\rm HS}$ in Ref. [167], and $S^{\rm HS}(q\to 0)$ given by the Carnahan-Starling equation of

state. This leads to

$$\frac{d_c^{\mathrm{HS}}}{d_{t,0}} \times \frac{\eta_\infty^{\mathrm{HS}}}{\eta_0} \times \sqrt{S^{\mathrm{HS}}(q \to 0, \phi)} = 1 - 0.046\phi + 1.3713\phi^2 + \mathcal{O}(\phi^3), \tag{6.8}$$

where the first-order virial coefficient is indeed close to zero. Using the analytic expressions for $\eta_\infty^{\mathrm{HS}}$ in Eq. (6.6), and K^{HS} calculated in the self-part corrected $\delta\gamma$-scheme with d_s according to Eq. (4.26), we can test the KD-GSE relation in fact in the full fluid-state regime of neutral spheres. According to the inset in Fig. 6.7, the KD-GSE for neutral spheres is valid to decent accuracy up to $\phi \lesssim 0.4$, with a maximal positive-valued deviation from one at $\phi \approx 0.3$ of less than 18%. Strong negative-valued deviations from one are observed for $\phi \gtrsim 0.4$, where the KD-GSE relation ceases to be applicable to neutral hard spheres.

The corrected $\delta\gamma$-scheme results included in Fig. 6.7 demonstrate the striking violation of the KD-GSE relation, when low-salinity systems of charged particles are considered. A clear violation of this relation is observed for all concentrations $\phi \gtrsim 10^{-4}$ in the case of the low-salinity system CS-1, and for $\phi \gtrsim 10^{-2}$ in the case of system CS-2, where, for both systems, a residual salt concentration of $n_s = 10^{-6}$ M has been assumed. The maximal (positive-valued) violation of the KD-GSE relation occurs roughly at a volume fraction where the $d_c(\phi)$ of charged spheres attains its maximum. The maximum in $d_c(\phi)$, in turn, is the result of a competition, with increasing ϕ, between decreasing compressibility and decreasing sedimentation coefficient. The concentration at the peak of $d_c(\phi)$ is determined roughly from $k_c^2(\phi) = k_s^2$ [18]. The downturn of the $d_c\eta_\infty\sqrt{S(q \to 0)}/(d_{t,0}\eta_0)$ curve at large ϕ, observable in Fig. 6.7 for neutral and charged spheres alike, is triggered by the large-ϕ decline both of K and η_∞.

6.2 Short-time diffusion of silica spheres

6.2.1 Self-diffusion

Fig. 6.8 includes the prediction by the PA scheme for the normalized short-time self-diffusion coefficient, $d_s/d_{t,0}$, of charged and neutral hard spheres, respectively, in comparison with ASD simulation results, and our DLS data for the TPM coated charged silica spheres in toluene-ethanol discussed in Section 2.2. The comparison of the PA scheme result with the ASD data allows for deducing quantitatively the contribution to d_s by the non-pairwise additive part of the HIs that arises from the solvent-mediated interactions of three and more particles.

The large scattering wavenumber regime related to self-diffusion is usually not accessible by DLS. Therefore, using an argument by Pusey [211], we identify d_s approximately as $d_s \approx D(q^*)$ (crosses in Fig. 6.8), where q^* is the first wavenumber located to the right of q_m where $S(q^*) = 1$ (see top part of Fig. 6.10). Simulations of charged and neutral spheres have shown that d_s is determined in this way to within 5 - 10% accuracy [23, 26, 212]. A comment is in order here on a false proposition by Robert [213], who claims that it has been predicted

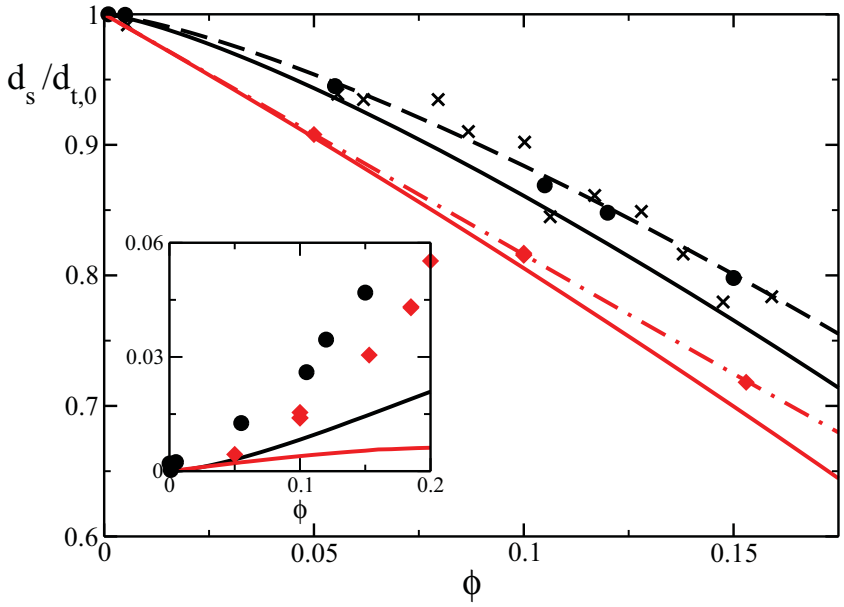

Fig. 6.8: *Normalized short-time self-diffusion coefficient, $d_s/d_{t,0}$, of a deionized suspension of charged spheres (CS, black) and hard spheres (HS, red). Crosses: DLS data for TPM coated charged silica spheres. Circles and diamonds: accelerated Stokesian Dynamics (ASD) results for CS and HS, respectively. Solid black and red lines: PA-scheme results for CS and HS, using MPB-RMSA input for $S(q)$. Dashed black line: $1-2.5\,\phi^{4/3}$. Dashed-dotted red line: 3^{rd}-order virial Eq. (4.26) for HS. Inset: $d_s/d_{t,0}$ as predicted by the PA scheme (lines), and by ASD simulation (symbols), with the leading-order far-field HIs part for CS (black) and HS (red), subtracted off.*

theoretically that there is no difference in the concentration dependence of d_s for charged and neutral particles. Quite the contrary, Nägele *et al.* have shown for charged spheres at low salinity that $d_s/d_{t,0} \approx 1 - a_t\,\phi^{4/3}$ (cf. Eq. (4.24b)), *i.e.*, d_s in these systems has a fractional ϕ-dependence qualitatively different from that of hard spheres [22, 172, 173]. Only the self-diffusion coefficient of neutral hard spheres can be described by a regular virial series, with the first three coefficients given in (4.26). The correct second-order virial coefficient, $-0.219\,\phi^2$, in Eq. (4.26) differs even in its sign from the erroneous result, $+0.88\,\phi^2$, used in Ref. [213].

The $\phi^{4/3}$ dependence of $d_s/d_{t,0} - 1$ was confirmed both by the experiments of Overbeck *et al.* [171], and by ASD simulations based on the OMF model [23]. The depicted ASD data for a low salinity system of charged spheres are overall well described by the fractional ϕ relation in Eq. (4.24b) for $a_t \approx 2.5$, over an extended range of volume fractions.

Our DLS data for the charged silica spheres depicted in Fig. 6.8 are fully consistent with the ASD simulation data, the PA-scheme result, and the $\phi^{4/3}$ scaling prediction for d_s in (4.24b), with $a_t = 2.5$. The hydrodynamic self-mobility related to d_s is rather short-ranged, decaying

like $1/r^4$ for a large separation r of two spheres. Consequently, the difference between d_s and its infinite dilution value $d_{t,0}$ is smaller for charged spheres than for neutral ones, since electric repulsion disfavors near-contact configurations. As discussed already in Section 6.1.3, the PA scheme overestimates the strength of the HIs in dense suspensions, for it does not account for the shielding of the HIs between a pair of particles by intervening ones. This is the reason why, at higher concentration, the ASD and experimental data for d_s are larger than the PA-scheme prediction. The PA-scheme result for $d_s/d_{t,0}$ is also well described by Eq. (4.24b), but for a somewhat larger parameter value of $a_t \approx 2.9$.

The inset in Fig. 6.8 shows $d_s/d_{t,0}$, as obtained by the PA scheme and ASD simulations, with the far-field part originating from the leading-order self-mobility part proportional to $1/r^4$ subtracted off. According to the inset, d_s is rather insensitive to the near-field two-body part of the HIs, causing a small increase in d_s only. Three-body and higher-order HIs contributions come into play for $\phi \gtrsim 0.1$, with an enlarging influence on d_s originating from hydrodynamic shielding.

6.2.2 Sedimentation

In principle, one needs to distinguish between the short-time and the long-time sedimentation coefficients, but the latter is smaller than the first one by at most a few percent. The two coefficients are practically equal in dilute systems where the two-body HIs part dominates.

Fig. 6.9 includes theoretical, simulation and experimental results for the (short-time) sedimentation coefficient, $K = U_{\text{sed}}/U_0$, of homogeneous systems for charged and neutral spheres. The key message conveyed by this figure is the qualitative difference in the ϕ-dependence of K for charged and neutral particles. This difference is more pronounced than the one for the self-diffusion coefficient discussed earlier. Charged spheres sediment more slowly than uncharged ones since near-contact configurations are disfavored. Thus, stronger laminar friction takes place between the back-flowing solvent, and the solvent layers dragged along with the settling spheres because of the stick hydrodynamic boundary condition. The solvent backflow is created by a pressure gradient directed towards the container bottom which balances the non-zero, buoyancy-corrected total gravitational force on the spheres.

At smaller ϕ and low salinity, K is well described by the non-linear Eq. (4.24a), with a coefficient $a_s \approx 1.4 - 1.8$ depending to some extent on the strength of the electrostatic pair interactions. The exponent $1/3$ arises from the 2-body far-field part of the HIs which dominates the near-field part for $\phi \lesssim 0.08$, and the scaling relation, $q_m \propto \phi^{1/3}$, valid in low-salinity systems for the wavenumber location of the structure factor peak [23]. As a consequence, the $\phi^{1/3}$ concentration dependence of K is observed both for dilute fluid and crystalline systems of charged particles.

The experimental results of Rojas-Ochoa [214] for the low-salinity sedimentation coefficient of a suspension of charged polystyrene spheres in an ethanol/water mixture ($\sigma = 117$ nm, $n_s = 10^{-6}$M, $L_B = 1.48$ nm), and also our data for the charged silica spheres in toluene-

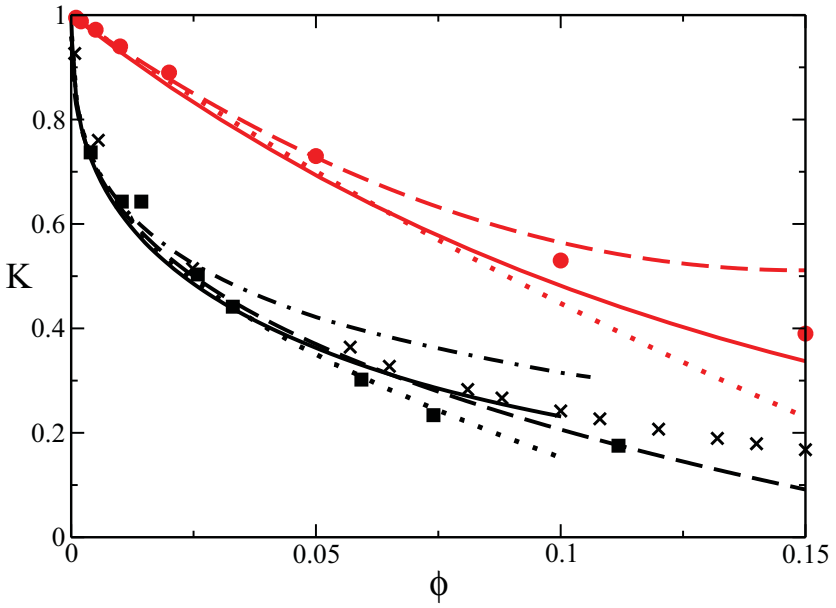

Fig. 6.9: *Normalized sedimentation velocity, $K = U_{sed}/U_0$, of charged spheres at low salinity versus that of neutral hard spheres. Experimental DLS/SLS data are shown for charged polystyrene spheres in an ethanol-water mixture taken from [214] (squares), and for our TPM coated silica spheres (crosses). Solid (dotted) black lines: $\delta\gamma$-scheme (PA-scheme) results, respectively, for the low-salinity polystyrene spheres system, obtained using the MPB-RMSA input for $S(q)$ with a fixed charge number $Z = 200$. Dashed-dotted black line: self-part corrected $\delta\gamma$ scheme result. Dashed black line: scaling form $1 - 1.71\,\phi^{1/3}$ according to Eq. (4.24a). Circles: hard-sphere simulation results by Ladd [206]. Dashed red line: 2^{nd}-order virial result for HS given in Eq. (6.2). Solid (dotted) red lines: $\delta\gamma$-scheme (PA-scheme) results, respectively, for HS with MPB-RMSA input for $S(q)$. For HS, the MPB-RMSA reduces to the Percus-Yevick closure.*

ethanol system, are in accord with the OMF-based prediction of a steep (as compared to neutral spheres) $\phi^{1/3}$-like decay of the sedimentation coefficient. The experimental values of K in both systems discussed in Fig. 6.9 have been deduced from small-q DLS and SLS measurements of $D(q)$ and $S(q)$, extrapolated to $q = 0$. Therefore, there is an unavoidable scatter in the extrapolated data, in particular since the osmotic compressibility coefficient $S(q \to 0)$ of low-salinity systems is very small.

In contrast to charged particles, the small-ϕ dependence of K is well represented for neutral spheres by a regular virial expansion. In fact, the second-order virial expression in Eq. (6.2) coincides, for $\phi \lesssim 0.08$, with the simulation data for K^{HS} by Ladd [206]. At larger ϕ, shielding arising from the higher-order HIs terms comes into play, contributing to K through the higher-order virial coefficients. Since shielding is disregarded in the PA scheme, the PA scheme notably overestimates the strength of the HIs for $\phi \gtrsim 0.1$. When applied to concentrations beyond its range of applicability, too small and eventually even non-physical negative values for K are predicted (see the dotted lines in Fig. 6.9).

Fig. 6.9 displays additionally, both for neutral spheres and for the system parameters of the charged polystyrene spheres system [214], the predictions for K by the $\delta\gamma$ scheme and by the PA scheme. As input to both schemes, $S(q)$ in MPB-RMSA was used, which reduces to the Percus-Yevick solution for HS. At small ϕ, the PA-scheme result for K follows precisely the scaling prediction $1 - a_s\,\phi^{1/3}$, with $a_s = 1.71$. The $\delta\gamma$ scheme at very small ϕ is less accurate than the PA scheme, owing to its incomplete account of two-body HIs contribution, notably its neglect of lubrication which plays a role for neutral spheres. Lubrication occurs in the thin fluid layer between two almost touching spheres in a relative squeezing or shearing motion. It is more influential to self-diffusion than to sedimentation, since in the latter case the (monodisperse) spheres move with equal mean velocity in the direction of the applied force field. In self-diffusion, on the other hand, a tagged particle is thermodynamically driven in a squeezing motion towards particles in front of it.

The $\delta\gamma$ scheme captures the overall ϕ dependence of K decently well, both regarding the two considered charge-stabilized systems, and neutral hard spheres. The self-part corrected $\delta\gamma$ scheme result for charged spheres lies at larger ϕ above the experimental data for K. This exemplifies a general observation, made also in Figs. 6.1, 6.2, 6.11 and 6.12, that the self-part corrected $\delta\gamma$ scheme overestimates somewhat the ASD-$H(q)$ at small q. For all larger values of q, however, including the principal peak region of $H(q)$, it is in distinctly better agreement with the simulation data for $H(q)$ than the uncorrected version.

6.2.3 Diffusion function

We proceed by discussing the short-time diffusion function, $D(q)$, defined in Eq. (4.2), which is measured in short-time DLS and XPCS experiments. DLS data of its inverse, $d_{t,0}/D(q)$, are included in the bottom part of Fig. 6.10, for a low-salinity system of charged silica spheres at a volume fraction $\phi = 0.15$ rather close to the freezing transition value. The experimental

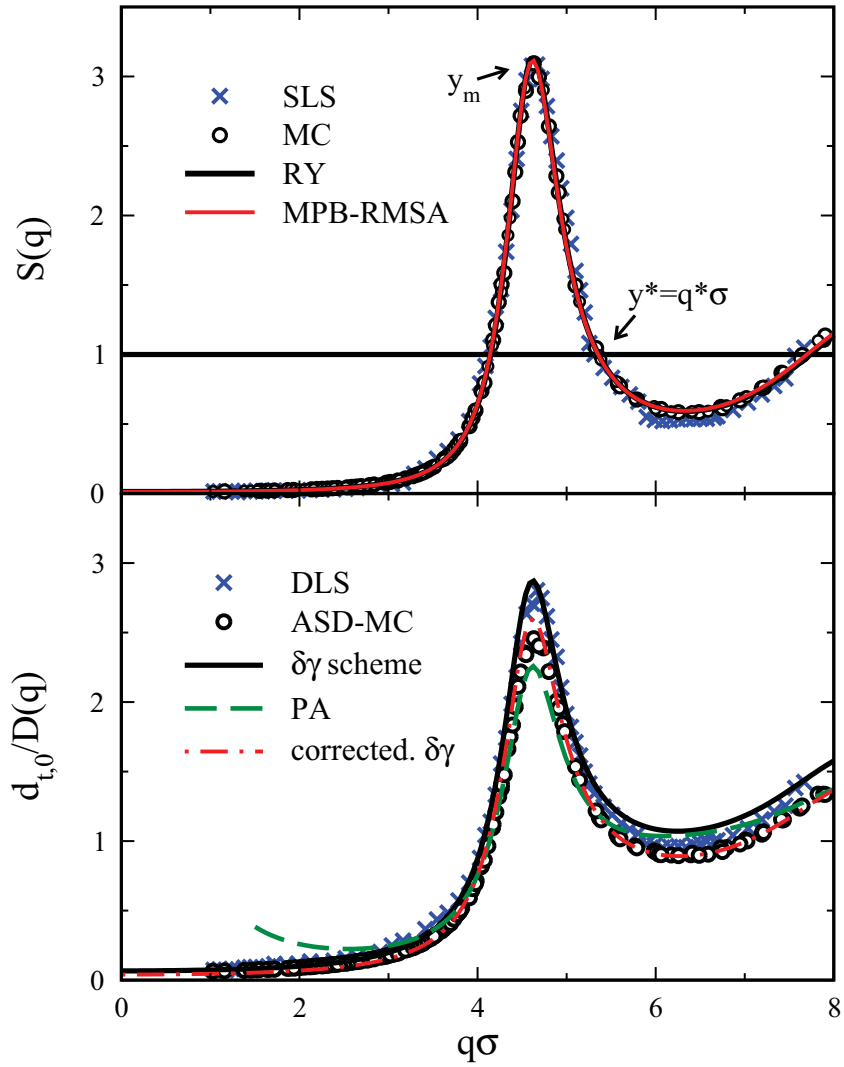

Fig. 6.10: *Top: static structure factor, $S(q)$, obtained by static light scattering (SLS, crosses), versus MPB-RMSA and RY results (red and black lines, respectively) and MC simulation data (open circles) for a common $Z = 190$. Bottom: short-time inverse diffusion function, $d_{t,0}/D(q)$, for a low-salinity system of charged silica spheres. Crosses: DLS data. Open circles: ASD-MC simulation data. Solid black line, dashed green line, and dashed-dotted red line: $\delta\gamma$-scheme, PA-scheme, and self-part corrected $\delta\gamma$-scheme predictions, respectively. The system parameters are: $\sigma = 272$ nm, $\phi = 0.15$, $n_s = 0.7 \times 10^{-6}$ M, and $L_B = 8.64$ nm.*

data are compared with our ASD simulation result for $D(q)$, and the (self-part corrected) $\delta\gamma$-scheme result where the d_s-part is taken from the ASD simulation result. For the two analytic schemes, the MPB-RMSA input for $S(q)$ was used, shown in the top part of Fig. 6.10.

The shape of $d_{t,0}/D(q)$ is similar to that of $S(q)$, owing to $d_{t,0}/D(q) = S(q)/H(q)$ according to Eq. (4.3). The analytic MPB-RMSA scheme predicts a structure factor in excellent agreement with our MC simulation data, and with the $S(q)$ obtained from the numerically elaborate RY scheme. The excellent agreement between all $S(q)$ depicted in the top part of Fig. 6.10, for all displayed wavenumbers, points to the accuracy of our scattering data. The only adjustable parameter in calculating $S(q)$ has been the effective charge number, uniquely determined as $Z = 190$ by the MPB-RMSA, RY and MC methods, from matching the experimental $S(q_m)$.

We recall from Eq. (4.3) that $D(q \to \infty) = d_s$ and $D(q \to 0) = d_{t,0}\, U_{\rm sed}/[U_0 S(q \to 0)] = d_c$. Here, d_c is the short-time collective diffusion coefficient which quantifies the initial decay rate of long-wavelength thermal concentration fluctuations. The short-time d_c is only slightly larger than its long-time counterpart d_c^L, even when a concentrated system is considered. The relative osmotic compressibility coefficient, $S(q \to 0)$, in the considered low-salinity system is very small, so that d_c is exceedingly larger than $d_{t,0}$, reflected in Fig. 6.10 in the low-q values of $d_{t,0}/D(q)$ close to zero. The function $D(q)$ attains its minimum at q_m, where its value is equal to the cage diffusion coefficient $d_{\rm cge}$. With increasing concentration and pair interactions, the nearest-neighbor cage stiffens, *i.e.*, it becomes more sharply structured, as reflected by a smaller value of $d_{\rm cge}$.

According to the bottom part of Fig. 6.10, there is good agreement between the ASD simulation data for $d_{t,0}/D(q)$, and the self-part corrected $\delta\gamma$-scheme prediction with its MPB-RMSA input. The ASD simulation peak height is somewhat overestimated by the uncorrected $\delta\gamma$ scheme which uses a too small value for the self-diffusion coefficient of charged spheres. For the charged silica particles system considered here, the experimental peak height of $d_{t,0}/D(q)$ happens to be somewhat closer to that of the uncorrected $\delta\gamma$ scheme. However, the first minimum of $d_{t,0}/D(q)$ to the right of q_m is in better accord with the self-part corrected $\delta\gamma$-scheme prediction.

To illustrate the failure of the PA scheme for concentrations $\phi \gtrsim 0.1$ where many-body HIs are strong, we have included its prediction into Fig. 6.10. It deviates from the experimental and simulation data most strongly at $q \approx 0$ and near q_m, reflecting its overestimation of the HIs at the large volume fraction $\phi = 0.15$, by giving a too small value for K, and a too large value for $H(q_m)$.

6.2.4 Hydrodynamic function

In Fig. 6.11, the experimental findings by Philipse and Vrij [65] for the $H(q)$ and $S(q)$ of a well-structured, charge-stabilized suspension of silica spheres suspended in a 70:30 toluene-ethanol mixture ($\varepsilon = 10$ at $T = 298$ K), are compared with our theoretical and simulation predictions based on the OMF model discussed in Section 2.1. The MPB-RMSA, RY and

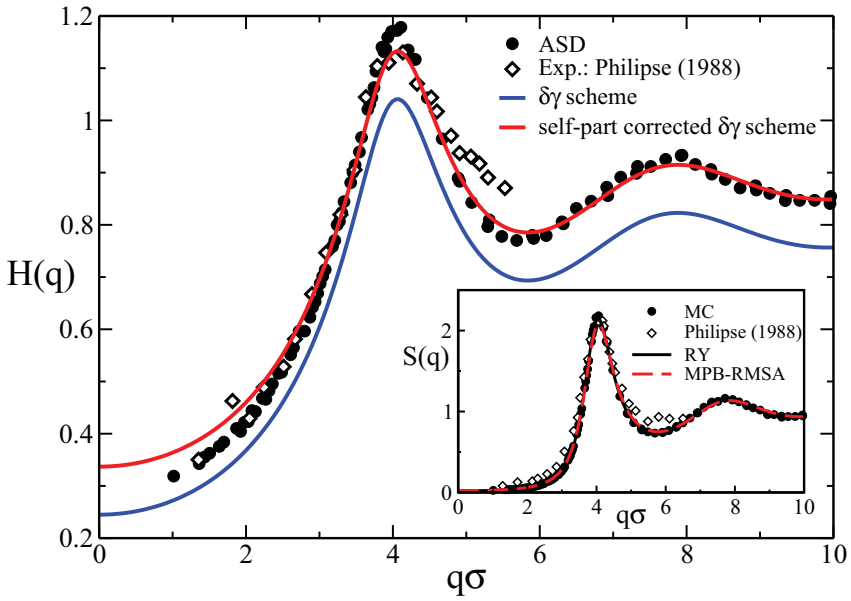

Fig. 6.11: *Open Diamonds: DLS and SLS data for $H(q)$ and $S(q)$ (in inset), taken from [65], for a charge-stabilized system at $\phi = 0.101$, in comparison with corresponding ASD and MC data predictions (filled black circles). Solid blue and red lines: uncorrected and self-part corrected $\delta\gamma$-scheme result, respectively. Black solid and dashed red lines in inset: RY and MPB-RMSA $S(q)$, respectively, for $Z = 100$, $a = 80$ nm, $n_s = 2 \times 10^{-6}$ M and $L_B = 5.62$ nm.*

MC $S(q)$ of common charge number $Z = 100$ shown in the inset, coincide practically in the depicted q-range.

There is good overall agreement between the experimental $H(q)$, and the ASD and self-part -corrected $\delta\gamma$-scheme results (with d_s taken from the ASD simulation) for $H(q)$ which have been obtained from multiplying the experimental data for $D(q)$ by those for $S(q)$. The self-part corrected $\delta\gamma$ scheme underestimates to some extent the ASD $H(q_m)$, but except for the precise peak value the overall shape of $H(q)$ is well reproduced. Figs. 6.10 and 6.11 exemplify that the self-part corrected $\delta\gamma$ scheme allows for predicting consistently, and to almost quantitative accuracy, the short-time generic features of many charge-stabilized systems including small proteins and large colloidal spheres.

Low-salinity systems are typically characterized by a peak value of $H(q_m)$ larger than one. In a recent study based on the OMF model, the upper limiting freezing line for $H(q_m)$ was derived [120], from which it follows that $H(q_m)$ never exceeds the value of 1.3. However, $H(q_m)$ in low-salt systems is not always larger than one. At very low ϕ, it increases monotonically according to $1 + p_m \phi^{1/3}$, with a moderately system-dependent coefficient $p_m > 0$ (see Eq. (4.24c)). At larger ϕ, where near-field HIs matter, $H(q_m)$ can pass through a maximum typically occurring at $\phi \sim 10^{-2} - 10^{-1}$, with an ensuing decline when ϕ is further increased. Provided the system remains fluid at larger ϕ, such as in apoferritin protein solutions [41], $H(q_m)$ can reach values smaller than one.

In the OMF model, $H(q_m)$ is bound from below by the corresponding peak height of neutral spheres. The latter decreases linearly in ϕ in the whole fluid phase regime according to Eq. (6.3). At fixed ϕ and with increasing salt content, $H(q_m)$ and d_s decrease monotonically, with q_m shifted to larger q values, towards the limiting hard-sphere values $H^{\mathrm{HS}}(q_m)$ and d_s^{HS}, respectively. Opposite to this, K increases monotonically with increasing salinity, for the reasons discussed earlier, towards its upper hard-sphere limit. In summary, the ordering relations

$$H(q_m) \geq H^{\mathrm{HS}}(q_m), \tag{6.9a}$$

$$d_s \geq d_s^{\mathrm{HS}}, \tag{6.9b}$$

$$K \leq K^{\mathrm{HS}}, \tag{6.9c}$$

are fulfilled. The equality sign holds for zero particle charge, $Z = 0$, and in the infinite salinity limit, $k \to \infty$. The OMF model ordering relations in Eq. (6.9) are obeyed by a large variety of experimentally studied charge-stabilized systems, including nanosized proteins [41] and suspensions of compact colloidal particles [43, 65, 214, 216–220].

In a series of articles, Robert, Grübel and coworkers [39, 213, 215, 221] reported on their observation of very small values for $H(q)$, for certain low-salinity suspensions of intermediately large volume fractions, which they studied by combining XPCS and SAXS techniques. At all probed wavenumbers, their $H(q)$ are substantially smaller than those of neutral hard

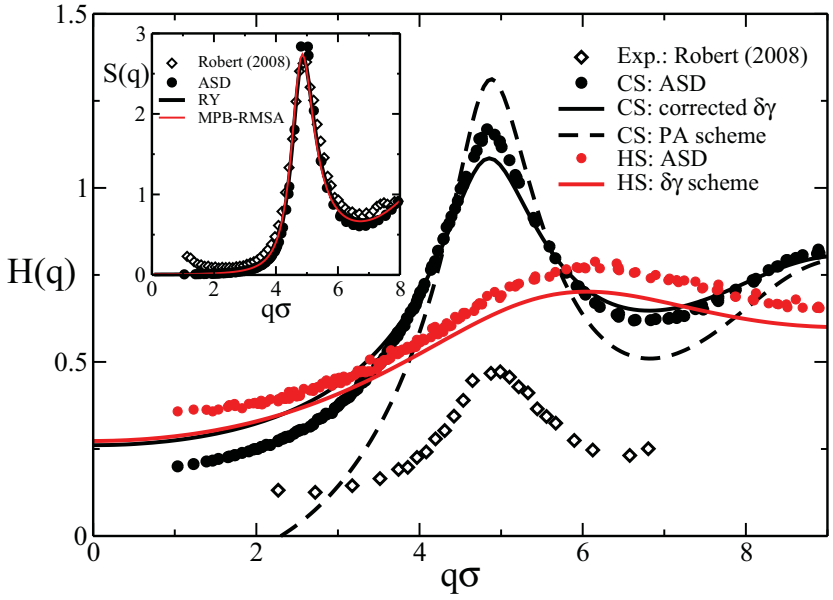

Fig. 6.12: *XPCS and SAXS data of $H(q)$ and $S(q)$ (in inset), taken from Ref. [215], for a low-salinity system of charged poly-perfluoropentylmethacrylate spheres (CS) with $\sigma = 125$ nm, $n_s = 1.6 \times 10^{-5}$ M, and $\phi = 0.18$ in a water/glycerol mixture at $T = 293$ K where $\varepsilon = 62.95$ and $L_B = 0.91$ nm (open diamonds). Inset: RY and MPB-RMSA $S(q)$ for $Z = 163$. Comparison with OMF model based ASD data, self-part corrected $\delta\gamma$ and PA-scheme results for $H(q)$, all obtained using $Z = 163$. The experimental $H(q)$ is substantially smaller than the ASD $H^{HS}(q)$ (red circles), and the $\delta\gamma$ scheme result for hard spheres (red line).*

spheres at the same ϕ. This findings of so-called ultra-small $H(q)$ is incompatible with the OMF model since the first two ordering relations in Eqs. (6.9) are violated.

A typical result for an ultra-small $H(q)$ with peak height $H(q_m) \approx 0.47$, taken from [215] for a system of poly-perfluoropentylmethacrylate spheres in a water/glycerol mixture at $\phi = 0.18$, is shown in Fig. 6.12, in comparison with our OMF model based simulation and theoretical results for $H(q)$, which predict a peak value for $H(q)$ larger than one. The inset displays the experimentally determined $S(q)$, and the peak-height adjusted MC, RY and MPB-RMSA results obtained for the common charge value $Z = 163$, and $n_s = 1.6 \times 10^{-5}$ M ($k = 2.92$). The experimental peak height, $S(q_m) \approx 2.63$, identifies the system as fluid-ordered according to the Hansen-Verlet freezing rule.

Just like in the silica system considered before, the self-part corrected $\delta\gamma$-scheme result for $H(q)$, based on the MPB-RMSA $S(q)$ input for its distinct part depicted in the inset, and the precise ASD simulation result for $d_s/d_{t,0}$, is in overall good agreement with the full ASD simulation result for $H(q)$. It underestimates the ASD peak height to some extent, but aside from the precise peak value the agreement with the ASD $H(q)$ is quantitatively good.

For completeness, Fig. 6.12 shows also the PA-scheme prediction for $H(q)$. The concentration is clearly too large here for the PA scheme to apply, with the consequence that nonphysical negative values of $H(q)$ are predicted for $q\sigma \lesssim 2.4$. This shows that for the present system, where $\phi = 0.18$, $H(q)$ is strongly influenced by many-body HIs. Quite notably, however, for the same particle system, an ultra-small hydrodynamic function, with $H(q_m) \approx 0.7 < H^{\mathrm{HS}}(q_m) = 0.95$, was reported by Robert *et al.* [215] even at $\phi = 0.04$, *i.e.*, for a concentration where two-body HIs dominate.

The experimental peak height in Fig. 6.12 is considerably smaller than the peak value, $H^{\mathrm{HS}}(q_m) = 0.76$, of hard spheres, the latter calculated according to Eq. (6.3). To allow for a comparison at all probed q values, Fig. 6.12 includes the ASD and $\delta\gamma$-scheme results for the $H(q)$ of hard spheres. The hard-sphere structure factor peak value is $S^{\mathrm{HS}}(q_m) = 1.19$ at $\phi = 0.18$.

Grübel, Robert and coworkers originally tried to explain their observation of strikingly low values for $H(q)$ as the result of HIs screening [39, 222]. To support their assertion, they presented a Brinkman fluid-type calculation of $H(q)$ [39], wherein only the leading-order far-field part of the hydrodynamic pair mobility is considered, treating the Brinkman screening length as a fitting parameter. However, in a later experimental-theoretical study [220], it was pointed out that hydrodynamic screening does not occur in fluid-ordered, unconfined suspensions of mobile colloidal particles (see here also Ref. [223]). Furthermore, the assumed screening of the HIs conflicts with the fact that the short-time diffusion and viscosity properties of many charge-stabilized systems, at concentrations and interaction parameters similar to the ones probed by Robert *et al.*, are well explained by OMF model based methods without any necessity to invoke HIs screening. The low-salinity system in Fig. 6.10, for example, is in the concentration range where an ultra-slow $H(q)$ should be observable.

More recently, Robert *et al.* retracted from their interpretation of ultra-small $H(q)$'s as being

due to HIs screening. In an alternative attempt to explain their findings [215], they introduced a correction factor, $f = \eta_0/\eta_{\text{eff}} < 1$, multiplying the OMF model based $\delta\gamma$-scheme $H(q)$, with the value of f determined such that the ultra-small experimental $H(q)$ is overall matched. Furthermore, they conjecture that f can be identified by the ratio of the solvent viscosity and some effective suspension viscosity η_{eff}, leaving it unspecified, however, whether η_{eff} should be identified with the high-frequency viscosity, η_∞, or with the substantially larger static suspension viscosity $\eta = \eta_\infty + \Delta\eta$. This ad-hoc modification of the $\delta\gamma$ scheme lacks a sound physical basis, for the $\delta\gamma$-scheme expression for $H(q)$ describes a genuine diffusion property. The values for f obtained from fitting the ultra-small $H(q)$ given by [215], are neither consistent with calculated [23] nor experimental [224] results for η_0/η_∞.

6.2.5 Influence of additional particle interactions

In this section, we analyze the effect on $H(q)$ caused by particle interaction contributions not considered in the OMF model. On a qualitative level, we discuss the influence of particle porosity, residual attractive forces and microion kinetics on the shape of $H(q)$. None of these effects is likely to be responsible for an ultra-small $H(q)$ like the ones reported by Robert, *et al.*, discussed in Section 6.2.4.

The effect of particle porosity on the $H(q)$ of dense suspensions of neutral porous spheres has been explored in a recent simulation study [26, 212]. A non-zero solvent permeability has the effect to weaken the HIs, reducing thus the deviations of $H(q)$ at all q from its zero-concentration limiting value of one. For the same reason, a suspension of porous particles is less viscous than a suspension of impermeable ones [25, 225]. Porosity is less influential when the particles are charged since near-contact configurations are then unlikely. The particles studied by Robert *et al.* are only very weakly porous, if at all. Thus, porosity can not explain the findings of ultra-small $H(q)$'s. On the contrary, significant porosity would lead to a $H(q)$ overall closer to one.

An attractive interaction contribution enlarges both $S(q \to 0)$ and the sedimentation coefficient K [226]. The enlargement of the latter is overcompensated by the former, at least at smaller ϕ [227]. Thus, in dispersions of moderately charged particles such as bovine serum albumin or Lysozyme proteins with sufficiently strong short-range attraction, the collective diffusion coefficient, $d_c = d_0 K/S(0)$, can attain values smaller than d_0 [36, 38, 42, 228].

Opposite to sedimentation, attraction tends to slow self-diffusion, resulting in smaller values of the short-time and long-time self-diffusion coefficients [228, 229]. Attraction-induced slowing of self-diffusion is accompanied by an augmentation of the short-time (high-frequency) and long-time (static) suspension viscosities [163]. Attraction fosters the formation of short-lived, transient particle pairs and clusters, which are better shielded from the solvent backflow so that sedimentation is enhanced. In self-diffusion, however, the mean velocity of a weakly forced particle driven towards its next-neighbor cage particles becomes smaller with increasing attraction, owing to the larger tendency of nearby particles to form a transient cluster. This

picture also explains why attraction-induced slowing of long-time self-diffusion is found not only in colloidal systems, where HIs are present, but also in atomic liquids [230]. Sedimentation is different in the sense that all particles, not just a single tagged one, are forced to move, on the average, in the direction of the external force. Summarizing, the overall effect of attraction is to lower the difference between $H(q \to \infty) - H(q \to 0)$, and to shift the peak position q_m to larger values.

The data by Robert *et al.* for $S(q)$ and $H(q)$ give no hint on an appreciable attractive interaction part. The short-range van der Waals attraction acting between the particles is masked in low-salinity systems by the strong and long-ranged electric forces to such an extent that it can not influence $H(q)$ significantly. Moreover, the experimental $S(q)$ given by Robert *et al.* can be described to good accuracy by the OMF model based structure factor. Significant attraction would enlarge at low q the gap between the OMF model and the ultra-small $H(q)$ in Fig. 6.12, instead of reducing it.

On first sight, the non-instantaneous electrokinetic relaxation of counter- and coions forming overlapping electric double layers around the charged colloids is a more promising candidate for causing ultra-small $H(q)$'s. Indeed, the relaxation of the microion clouds has a slowing influence on colloid diffusion, referred to as the electrolyte friction effect. This effect can lower $H(q \to 0)$ [41] to a smaller extent, and also the values of the short-time and long-time self-diffusion coefficients [231]. However, electrolyte friction scales with the ratio, $d_{t,0}/d_m$, of the free diffusion coefficient, $d_{t,0}$, of the slowly moving colloids relative to the (mean) free diffusion coefficient, d_m, of the small microions [37, 41, 231]. Because of the huge difference in these two free diffusion coefficients, it is unlikely that electrokinetics can explain the strikingly low values for $H(q)$ reported on by Robert and collaborators. Whereas the electrokinetic influence on colloid diffusion is very small for larger colloidal spheres, it can be significantly strong for small, nanosized macroions such as proteins.

6.3 Long-time collective diffusion and static viscosity of bovine serum albumin

In the following Sections 6.3.1-6.3.3, we compare the DLS data for the collective diffusion coefficient of BSA solutions, and the static shear viscosity measured using the suspended couette-type rheometer described in Ref. [78], to the results of the dynamic schemes discussed in Chapter 4. Moreover, we test the validity of the generalized Stokes-Einstein relation proposed by Kholodenko and Douglas, using our experimental and theoretical data for short and long timescales. We reemphasize here that the employed theoretical schemes use $S(q)$ and $g(r)$ as the only input. With $S(q)$ and $g(r)$ determined in Section 5.4 from the fits to the SAXS-intensities, all theoretical results for d_c, η_∞ and η are thus obtained without any additional adjustable parameters.

6.3.1 Collective diffusion

Fig. 6.13 includes our SLS/DLS data for $1/S(q \to 0)$ (upper part) and d_c^L (lower part), for aqueous BSA solutions in comparison with the theoretical predictions. Systems without added salt, and for concentrations $n_s = 5 \times 10^{-3}$ and 0.15 M of added NaCl, are considered. Additional measurements using 0.5 M of added NaCl (data not shown) agree almost perfectly with the data for $n_s = 0.15$ M, indicating that electrostatic repulsion is fully screened already at $n_s = 0.15$ M. As the input to the dynamics schemes, $S(q)$ and $g(r)$ were generated by the MPB-RMSA, using concentration-interpolated input parameters $\phi(c_p)$ and $Z(c_p)$ based on Tab. 5.1. For no added salt, $n_s(c_p)$ was interpolated using Tab. 5.1, while $n_s = 5 \times 10^{-3}$ and 0.15 M were kept fixed (independent of c_p) in the corresponding theoretical calculations. The value $d_{t,0}^{ell} = 5.82$ Å^2/ns of the spheroid translational free diffusion coefficient was used to obtain d_c in experimental units from the dimensionless results for $d_c/d_{t,0}$ as obtained by both theoretical schemes.

For no added salt, the experimental $d_c^L(c_p)$ assumes a maximum at $c_p \approx 10-20$ mg/ml. This maximum is qualitatively reproduced by both theoretical schemes (corrected $\delta\gamma$ and PA), but its location is predicted to occur at somewhat larger concentrations $c_p \approx 20-30$ mg/ml. For BSA concentrations larger than the concentration at the maximum value for d_c, the PA-predicted $d_c(c_p)$ reduces strongly, eventually reaching unphysical negative values for $c_p \gtrsim 110$ mg/ml. This illustrates the expected failure of the PA scheme at higher concentrations, indicating that three-body contributions to HIs, totally left out in the PA, but not in the $\delta\gamma$ scheme, come into play for $c_p \gtrsim 30$ mg/ml. Up to the concentration value at the maximum of d_c, both schemes agree very well, with residual differences not visible for $c_p \lesssim 20$ mg/ml on the scale of Fig. 6.13. Despite its residual small inaccuracies, the self-part corrected $\delta\gamma$ expansion will therefore be used in the following calculations of the d_c for BSA proteins.

The physical origin of the non-monotonous concentration dependence $d_c(c_p)$ at low concentrations of salt can be understood on the basis of Eq. (4.3), rewritten using $d_c^L \approx d_c$ as

$$\frac{d_c}{d_{t,0}} = \lim_{q\to 0} \frac{H(q)}{S(q)}. \tag{6.10}$$

The ratio in Eq. (6.10) consists of two competing factors. The factor $1/S(q \to 0)$, inversely proportional to the isothermal osmotic compressibility of ideally monodisperse particles, increases monotonically as a function of the BSA concentration. Owing to the larger coupling constant γ in Eq. (2.5a), a much steeper initial increase of $1/S(q \to 0)$ is observed for weakly screened systems, than for systems with added salt (c.f. the top panel of Fig. 6.13). As c_p is further increased, the amount of surface-released counterions increases correspondingly, leading to an enhanced electrostatic screening. As a consequence, the rate of change of $1/S(q \to 0)$ with c_p reduces significantly at a colloid concentration roughly set by the criterion, $k_c^2(c_p) = k_s^2$, of equal surface released counterion and salt-co-ion contributions to the screening parameter in Eq. (2.5b).

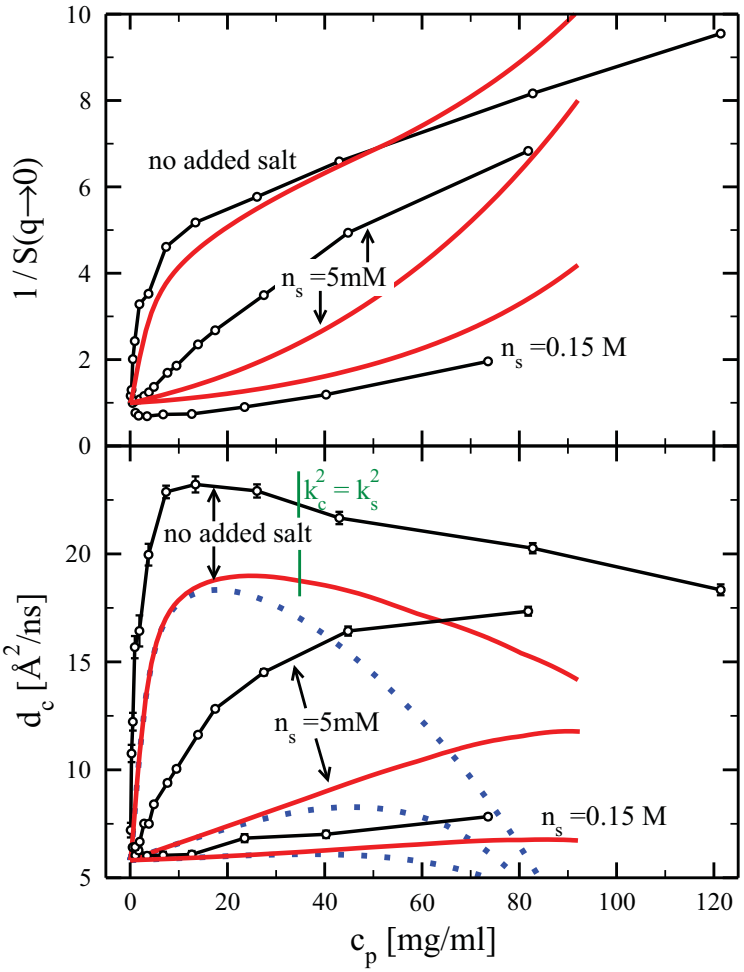

Fig. 6.13: *Top panel: Inverse zero-wavenumber limiting static structure factor, $S(q \to 0)$, of BSA solutions, obtained from SLS (connected black circles) and our MPB-RMSA scheme (red solid lines). Number concentrations, n_s, of added NaCl as indicated. Bottom panel: Fast mode coefficient, $D_1 = d_c^L$, obtained from the discussed double-exponential fit to the DLS data of BSA solutions (connected black circles), and d_c calculated by the self-part corrected $\delta\gamma$ scheme (red solid lines), and the PA scheme (blue dotted curves). All theoretical curves are based on input parameters $\phi(c_p)$ and $Z(c_p)$ interpolated from Tab. 5.1. In the zero added-salt case, the $n_s(c_p)$ values were also interpolated using Tab. 5.1. Theoretical results for added NaCl are obtained using fixed salt concentrations of $n_s = 5 \times 10^{-3}$ and 0.15 mM. The input parameters $L_B = 0.711$ nm, $\sigma = \sigma_{B_2} = 7.40$ nm, $a = 1.75$ nm, $b = 4.74$ nm, and $d_{t,0} = d_{t,0}^{ell}(a,b) = 5.82$ Å^2/ns are kept fixed throughout. For the zero added-salt case, the green vertical line segment at $c_p \approx 34$ mg/ml marks the protein mass-concentration where the surface-released counterion contribution to k^2 in Eq. (2.5b) is equal to the coion contribution.*

The nominator in Eq. (6.10) is the reduced sedimentation velocity, $H(q \to 0)$, which is known from theory and experiment [16] to decrease monotonically, for not too large concentrations and low salinity according to Eq. (4.24a) in the case of highly charged particles, and according to Eq. (6.2) for neutral hard spheres. For strongly correlated particles, the competition between decreasing compressibility and decreasing sedimentation coefficient with increasing c_p leads thus to a maximum in $d_c(c_p)$, at a concentration roughly determined from $k_c^2(c_p) = k_s^2$.

The DLS-measured values for d_c are not quantitatively reproduced by the self-part corrected $\delta\gamma$ scheme. Both in the zero added-salt case, and for $n_s = 0.15$ M, d_c^L is underestimated by the corrected $\delta\gamma$ scheme prediction by about 25%. The difference might be simply due to the complex-shaped BSA proteins having a translational free diffusion coefficient larger than the value $d_{t,0}^{ell} = 5.82$ Å^2/ns used in the SY model. In fact, an extrapolation of the experimental data for d_c^L to zero concentration leads to a larger value for $d_{t,0}$ in the range of $6-7$ Å^2/ns, which can completely explain the differences in d_c between experiment and theory. However, this low-concentration extrapolation should not be over-interpreted as being conclusive, since the experimental data are rather noisy for low concentrations.

While the agreement between the theoretical and the experimental d_c's is overall rather satisfying for very low and very high salt content, strong differences are found for the intermediate added NaCl concentration of 5 mM. This is not surprising, however, since already the zero added-salt experiments led to fit values for n_s of 1 to 3 mM. Therefore, n_s is most probably a function of c_p also in the 5 mM added NaCl case, instead of being constant as assumed in the calculations. Moreover, there is no obvious reason to expect that the relation $Z(c_p)$, interpolated from Tab. 5.1, remains valid at arbitrary added salt concentrations. Additional future SAXS measurements at 5 mM added NaCl are necessary to determine, for this case, the precise dependence of n_s and Z on c_p.

6.3.2 Static viscosity

The rheometric results for the zero-shear rate limiting static viscosity η without added salt, and with 0.15 M of added NaCl, are plotted in Fig. 6.14 as a function of c_p, and compared to the theoretical predictions. Apart from pronounced differences at lower concentrations, discussed in detail further down, the experimental data agree overall decently well with the theoretical predictions. Due to the rather weak microstructural ordering of the BSA proteins, characterized by structure factor peak heights less than 1.2 even for the most concentrated samples, the shear-stress relaxation term $\Delta\eta$ contributes only little to η, with a maximum relative contribution of about 10% near $c_p = 100$ mg/ml. The dominant contribution to η is given by η_∞, which is predicted to good accuracy both by the PA scheme and the corrected $\delta\gamma$ scheme, with practically equal results. The PA scheme is applicable to the whole experimentally probed concentration range of $c_p \lesssim 100$ mg/ml, since three-body and higher order HI contributions

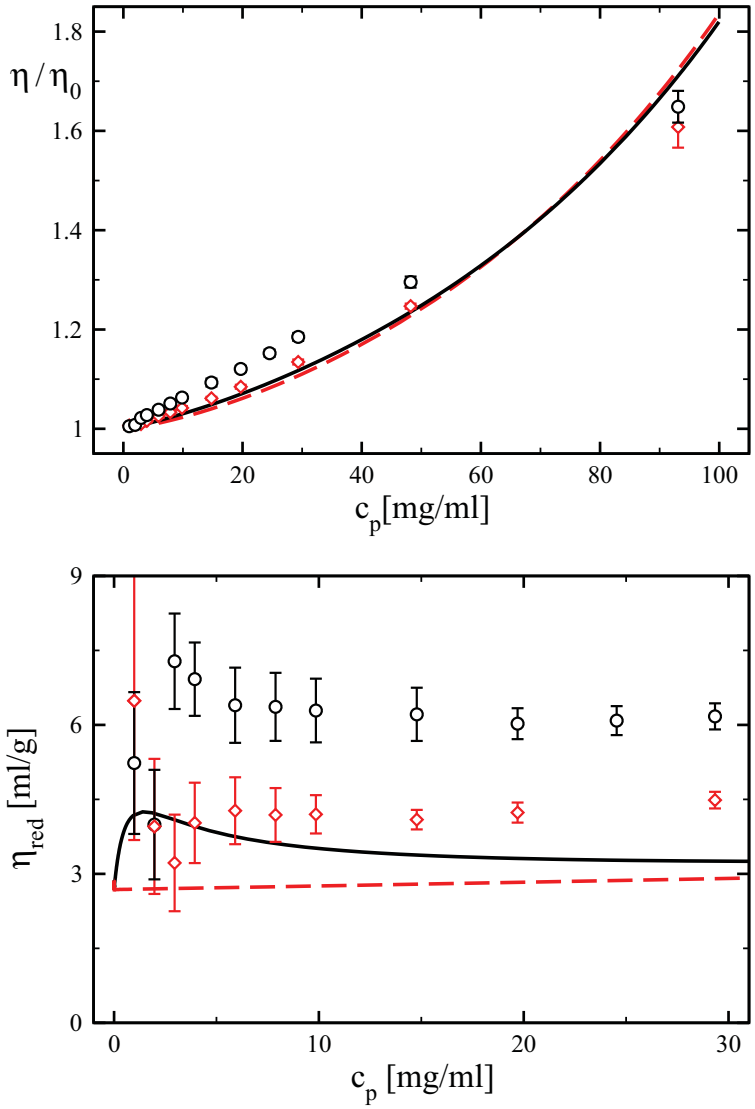

Fig. 6.14: *Static relative viscosity η/η_0 (top panel) of BSA and reduced (bottom panel) viscosity η_{red}, for $T = 25°$ C, as functions of c_p. Theoretical curves are based on input parameters $\phi(c_p)$ and $Z(c_p)$, concentration-interpolated using Tab. 5.1. Symbols: experimental data without added salt (black circles) and with $n_s = 0.15$ M (red diamonds). Lines: theoretical results without added salt (black solid line, $n_s(c_p)$ interpolated using Tab. 5.1) and with a fixed salt concentration of $n_s = 0.15$ M (red dashed curve). Note the different c_p-ranges in the two panels.*

affect η_∞ to a lesser extent than d_c (c.f. here Fig. 6.13, showing the failure of the PA-scheme prediction for d_c already for $c_p \lesssim 50\ g/l$).

The addition of larger amounts of salt lowers the values for η, as can be noticed from the two experimental data sets depicted in Fig. 6.14. The reason for this is the enhanced electrostatic screening, causing $\Delta\eta$ to decrease with increasing salinity in going from strongly structured, charged spheres to basically neutral hard spheres. In contrast, η_∞ is known from theory and experiment [23] to *increase* upon the addition of salt (*c.f.*, Fig. 6.5), due to the enlarged influence of near-field HIs when the particles are allowed to get closer to each other in electrostatically screened systems. Thus, η_∞ and $\Delta\eta$ have opposite trends in their dependencies on the concentration of added salt. These competing trends are the reason for the weak crossover in the two theoretical curves for η, noticed in the top panel of Fig. 6.14 at $c_p \approx 67$ mg/ml. For particle concentrations larger than this c_p value, the increase of η_∞ overcompensates the decrease in $\Delta\eta$ when, in place of the zero added-salt system, a system with $n_s = 0.15$ M is considered. That such a weak crossover is not observed in the experiment data in Fig. 6.14, points to an underestimation of the crossover concentration by our simplifying theories for η, possibly due to the neglect of HIs in the $\Delta\eta$ calculation.

A remarkable feature is noticed from the bottom panel of Fig. 6.14, where we plot the so-called reduced viscosity,

$$\eta_{\text{red}}(c_p) = \frac{\eta(c_p) - \eta_0}{\eta_0 c_p}, \tag{6.11}$$

as a function of c_p. The function $c_p\eta_{\text{red}}/\phi$ reduces to the intrinsic viscosity, $[\eta]$ at very low volume fractions where $\eta \to \eta_0 + [\eta]\phi$. Features of dilute systems are more clearly revealed in η_{red} than in η.

Both experimental data sets in the bottom panel of Fig. 6.14 show a local maximum of η_{red} at low c_p values, which for the zero added-salt system (black open circles) is visible as a weak non-monotonicity near $c_p \approx 3$ mg/ml. For the system with 0.15 M added NaCl (red open diamonds), the experimental maximum is represented essentially by a single data point at $c_p = 1$ mg/ml, where $\eta_{\text{red}} \approx 6.5$ ml/g, whereas the remaining data points describe a nearly constant plateau value of 4.5 ml/g. This plateau value is in good overall agreement with reported values for η_{red} at low c_p, in the range of 3.8 to 4.9 ml/g [232–235].

Regarding the large experiment error bars on the figure at very low c_p, we cannot attribute physical significance to the single-point maximum in the $n_s = 0.15$ M system. A more refined data resolution in a future experimental study is clearly needed here. Even the maximum in η_{red} for the zero added-salt case might be disputable on basis of the experimental data alone. However, the existence of such a maximum in η_{red} draws its credibility from the comparison to the theoretical results, showing a maximum in $\eta_{\text{red}}(c_p)$ at a slightly lower value of c_p. A similar non-monotonic behavior of $\eta_{\text{red}}(c_p)$, with a pronounced peak at low c_p, has been measured also in polyelectrolyte systems [236–238], in low-salinity suspensions of charged silica spheres [239], and in microgels [240]. The effect has been described theoretically by scaling

arguments [241], by the Rice-Kirkwood equation [242] for the shear viscosity in combination with a screened Coulomb potential [243], and for rod-like particles using a MCT scheme similar to ours [244]. In these earlier treatments, HI has been disregarded altogether. In our approach, HI is included in the for the present systems dominating η_∞ part of η.

To rule out that the non-monotonicity of the theoretical $\eta_{\rm red}(c_p)$ is caused by BSA-specific dependencies of $|Z|$ and n_s on c_p, (c.f. Tab. 5.1), we have investigated additionally a model system for fixed $|Z| = 20$ and $n_s = 1$ mM, where we find again a maximum in $\eta_{\rm red}(c_p)$. Thus, the maximum in $\eta_{\rm red}(c_p)$ is a generic effect in weakly screened HSY fluids. It is entirely due to the shear-stress relaxation term $\Delta\eta$, for $(\eta_\infty - \eta_0)/(\eta_0\phi)$ increases monotonically in c_p at arbitrary salt concentration. Since the HIs are neglected in our MCT treatment of the shear-stress relaxation part $\Delta\eta$, we conclude that the local maximum in $\eta_{\rm red}$ is basically a non-hydrodynamic effect, arising from electrostatic repulsion. We point out that the discussed physical mechanism underlying the non-monotonic behavior of $\eta_{\rm red}(c_p)$ is different from the one causing the maximum in d_c as a function of c_p. The latter maximum originates from a competition between electrostatic repulsion and hydrodynamic slowing in crowded systems. It is therefore not surprising that the maxima in $\eta_{\rm red}$ and d_c are located at considerably different protein concentrations. Whereas the maximum of d_c occurs at $c_p \approx 30$ mg/ml (c.f. Fig. 6.13), the maximum in $\eta_{\rm red}$ is observed at $c_p \lesssim 5$ mg/ml.

The theoretical values for $\eta_{\rm red}$ in Fig. 6.14 underestimate the experimental data by a factor of about $1/2$. In the low-concentration regime, the theoretical result for $\eta_{\rm red}c_p/\phi$ approaches $[\eta] = 2.5$, owing to the underlying effective sphere model. The intrinsic viscosity of BSA modeled as a spheroid is $[\eta]^{ell} = 3.25$, which is larger than the value for a sphere by a factor of 1.3 only. Therefore, this can not be the only cause for the observed deviation. However, the actual intrinsic viscosity of a heart-like shaped BSA protein is neither equal to that of a spheroid nor to that of an effective sphere. We recall here our discussion of Fig. 6.13, where we argued that $d_{t,0}$ for a BSA protein might well be about 25% larger than the free diffusion coefficient, $d_{t,0}^{ell}$, of the model spheroid. We can similarly argue that the observed differences between the experimental and theoretical $\eta_{\rm red}$ may be largely due to a value for the intrinsic viscosity of BSA of about $4-5$, which is $20-50\%$ larger than $[\eta]^{ell}$, and about twice as large as the $[\eta]$ value of spheres. This could explain the observed difference.

Note here that electrokinetic contributions to η, d_s and d_c, originating from the non-instantaneous response of the microion-clouds around each protein, are not included in our treatment. Microion electrokinetics has the effect of lowering somewhat the values of d_s and d_c [37, 41], while enlarging the viscosity η [245, 246]. These effects can be expected to be stronger when κ^{-1} is approximately equal to the particle size. Furthermore, electrokinetic effects are expected to be less significant at higher protein concentrations [47, 231].

6.3.3 Test of Kholodenko-Douglas relations

Using our theoretical short-time dynamic schemes in Section 6.1.5, we have tested the accuracy of the KD-GSE relation (6.5) on short time scales. Since we have experimental data sets for η, d_c^L, and $S(q \to 0)$ for BSA solutions with low and high salt content at our disposal, together with theoretical tools to calculate these properties, we are now in the position to scrutinize experimentally and theoretically the accuracy of the KD-GSE relation

$$\frac{d_c(\phi)}{d_{t,0}} \times \frac{\eta^*(\phi)}{\eta_0} \times \sqrt{S(q \to 0, \phi)} \approx 1, \tag{6.12}$$

for short and long time scales, using $\eta^* = \eta_\infty$ and $\eta^* = \eta$, respectively.

In their discussion of the GSE relation in Eq. (6.12), based on mode-coupling theory like arguments, Kholodenko and Douglas have considered explicitly a dilute suspension of colloidal hard spheres to first order in ϕ only, where η_∞ and η are identical, since $\Delta\eta = \mathcal{O}(\phi^2)$. For high concentrations, we test now the validity of both the long-time and short-time versions of the KD-GSE relation, on recalling that different from η_∞ and η, d_c and d_c^L are practically equal even at high concentrations. In Ref. [30], it was argued that for uncharged hard spheres (HS) the KD-GSE relation is valid to linear order in ϕ. On recalling that $d_c \approx d_c^L$, we can check this statement analytically for long time scales using numerically precise 2$^{\text{nd}}$ order virial expansion results for d_c^{HS} and η^{HS} [166, 167, 247], and with $S^{HS}(q \to 0, \phi)$ calculated from the precise Carnahan-Starling equation of state. In this way, we obtain

$$\frac{d_c^{HS}\eta^{HS}}{d_{t,0}\eta_0}\sqrt{S^{HS}(q \to 0)} = 1 - 0.046\phi + 2.282\phi^2 + \mathcal{O}(\phi^3), \tag{6.13}$$

which is identical to the short-time version of the KD-GSE relation for hard spheres in Eq. (6.8) to linear order in ϕ, with a coefficient, -0.046, which is not precisely vanishing but close to zero. However, to quadratic order in ϕ already, where particle correlations come into play and η_∞ needs to be distinguished from η, both the short- and long-time GSE variants have distinctly non-zero virial coefficients.

In Fig. 6.15, we plot the left-hand-side (lhs) function in Eqs. (6.12) in its short- and long-time form, as a function of c_p. Both BSA solutions without added salt, and solutions with $n_s = 0.15$ M are considered. Apart from a constant factor, which is related to the actual value of $d_{t,0}$ in BSA solutions discussed earlier, the theoretical curves compare reasonably well to the experimental data. There are only small differences in the short-time and long-time GSE curves in the case of BSA solutions.

With the hard-sphere-like behavior of the particles practically reached for $n_s = 0.15$ M, in the added-salt system the two KD-GSE variants apply for concentrations up to $c_p \approx 50$ mg/ml, corresponding to $\phi \approx 0.1$. For more concentrated systems, the lhs function in Eq. (6.12) increases initially, going trough a shallow maximum near $c_p \approx 90$ mg/ml. For zero added salt,

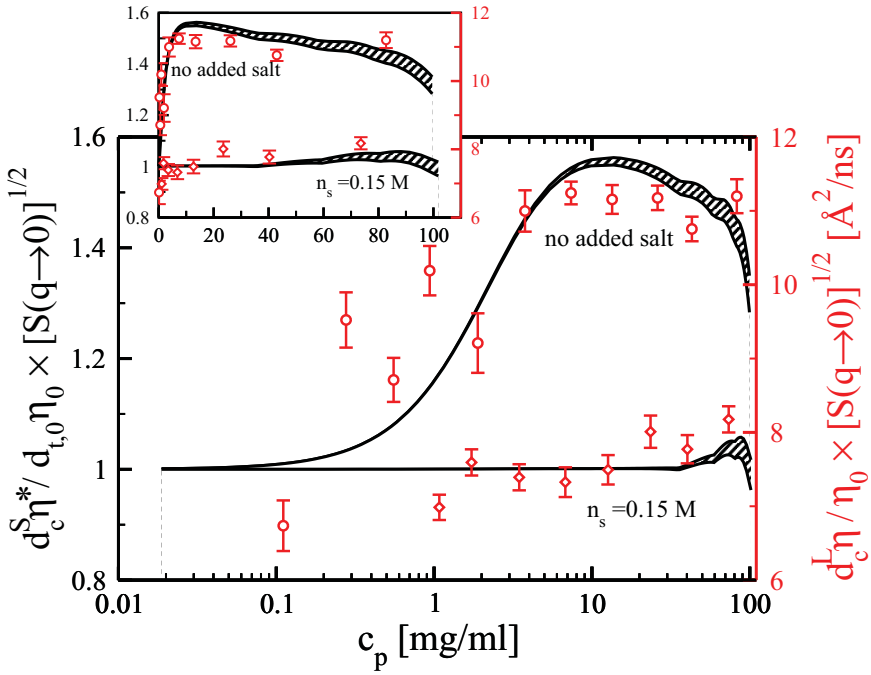

Fig. 6.15: *Test of the long-time and short-time KD-GSE relations in Eq. (6.12), with $\eta^* = \eta$ and $\eta^* = \eta_\infty$, respectively. Results for BSA solutions without added salt (upper datasets), and with 0.15 M of added NaCl (lower datasets) are shown. Red symbols: combination of d_c^L from DLS, η/η_0 from suspended couette rheometry, and $S(q \to 0)$ from SLS. Black lines: Theoretical results, combining $d_c \approx d_c^L$ and η_∞ calculated from the self-part corrected $\delta\gamma$ scheme with $S(q \to 0)$ from the MPB-RMSA scheme. For the long-time GSE version, $\eta = \eta_\infty + \Delta\eta$, where $\Delta\eta$ from MCT is used. Lower boundaries of the theoretical curves correspond to the short-time GSE, upper boundaries to the long-time version. The theoretical curves are based on $S(q)$-input with $\phi(c_p)$ and $Z(c_p)$ concentration-interpolated using Tab. 5.1. For zero added salt, $n_s(c_p)$ was also interpolated using Tab. 5.1. The parameters $L_B = 0.711$ nm and $\sigma = \sigma_{B_2} = 7.40$ nm are kept constant.*

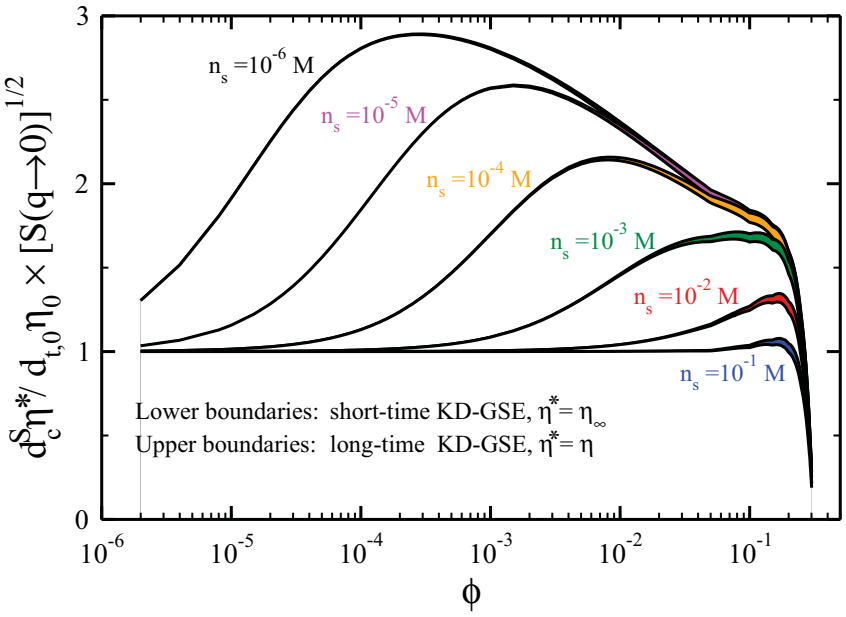

Fig. 6.16: *Test of the short- and long-time versions of the KD-GSE relation in Eq. (6.12) for volume fractions from very dilute values to $\phi = 30\%$, and various salt concentrations as indicated. The collective diffusion coefficient, $d_c/d_{t,0} \approx d_c^L/d_{t,0}$, and the high-frequency limiting viscosity, η_∞/η_0, are obtained from the self-part corrected $\delta\gamma$ scheme. The static viscosity, $\eta = \eta_\infty + \Delta\eta$, is calculated using MCT for $\Delta\eta$. Values for $S(q \to 0)$ are obtained from the MPB-RMSA method. The input parameters $L_B = 0.711$ nm, $\sigma = 7.40$ nm, and $|Z| = 10$ are kept constant.*

violation of the KD-GSE relations is observed theoretically at all non-zero concentrations, and can be noticed in the experimental data already for $c_p \lesssim 1$ mg/ml.

In our discussion of the KD-GSE relation, we proceed now by characterizing the crossover behavior in going from the low-salt to the high-salt regime. To this end, in Fig. 6.16, we plot the lhs of Eqs. (6.12) as a function of ϕ for various salt contents, using the parameters $L_B = 0.711$ nm, $\sigma = 7.40$ nm, and $|Z| = 10$. These parameters are typical of aqueous solutions of small globular proteins such as BSA, Lysozyme [248] and Apoferritin [41]. The charge number Z is kept constant here for simplicity. Theoretical results are plotted as a function of ϕ instead of c_p. In lowering the salt content in Fig. 6.16 stepwise by factors of 0.1, starting from a maximal value of $n_s = 0.1$ M, we find that the maximal (positive) deviation from one of the lhs function in Eq. (6.5) increases roughly logarithmically. For low salt content, $n_s \lesssim 10^{-3}$ M, the physical origin of the maxima in Fig. 6.16 is understood from comparing the theoretical results for d_c and η in Figs. 6.13 and 6.14, respectively: The maximal violation of the KD-GSE relations occurs roughly at a volume fraction where $d_c(\phi)$ attains its maximum, *i.e.* for ϕ determined

approximately from $k_c^2(\phi) = k_s^2$. Recalling that $k_c^2 \propto \phi$ and $k_s^2 \propto n_s$, this explains why the ϕ-location of the maxima in Fig. 6.16 shows a power-law dependence on n_s for $n_s \lesssim 10^{-3}$ M. For larger n_s, a crossover to hard-sphere-like behavior occurs, where the KD-GSE relations apply for $\phi \lesssim 0.1$.

To generate the datasets in Fig. 6.16, we have used the self-part corrected delta-scheme Eq. (4.27) for η_∞. In a strict sense, this expression applies only for highly charged particles at low salinity, as explained in Section 4.4. However, as noted from Fig. 6.5, in which the leading-order Einstein contribution to η_∞ has already been subtracted off, the difference in η_∞ between charged and uncharged spheres is moderate even at larger concentrations. The violation of the KD-GSE at low and intermediate values of n_s is therefore mostly due to ϕ-dependence of d_c, which we have calculated using the corrected $\delta\gamma$-scheme Eq. (4.25). Since the latter expression applies well for arbitrary amounts of added salt, the curves in Fig. 6.16, including the ones for intermediate salt concentrations, are reliable throughout.

6.4 Long-time diffusion and static viscosity of gibbsite platelets

Dynamic light scattering functions of gibbsite suspensions have been recorded in VH and VU geometry, for a large number of scattering wavenumbers and concentrations up to the volume fraction right at the I/LC transition. Results for the normalized intensity autocorrelation functions, $g_2^{\mathrm{VU}}(q,t)$, (filled symbols) and $g_2^{\mathrm{VH}}(q,t)$ (open symbols) for two different volume fractions $\phi = 0.8\%$ and 4.8% are shown in Fig. 6.17. We point out that $g_2^{\mathrm{VU}} \approx g_2^{\mathrm{VV}}$ to excellent accuracy, due to the very small optical anisotropy of the gibbsite platelets. The rather dilute system at $\phi = 0.8\%$ has only weak inter-platelet correlations, whereas the system at $\phi = 4.8\%$ is not very far from the I/LC transition.

Consider first the low-concentrated system in panel (a) of Fig. 6.17, where $g_2^{\mathrm{VU}}(q,t) - 1$ and $g_2^{\mathrm{VH}}(q,t) - 1$ are shown for four different q-values located well below q_m, with $q\langle R\rangle = 1.26$ at the largest considered q. At this low concentration, both IACF's are only slightly stretched, decaying basically single-exponentially. The stretching is due to the rather small polydispersity, $s_R = 17.3\%$, in the disk radius R. Due to the small value of p, the more pronounced polydispersity in h of value $s_h = 55.3\%$ has very little influence only on the particle diffusion coefficients, and on the scattering amplitudes in the experimentally accessed q-range where $q\langle R\rangle \lesssim 1$ and thus $q\langle h\rangle \lesssim 0.1$. The time relaxation of $g_2^{\mathrm{VH}}(q,t)$ is faster than that of $g_2^{\mathrm{VU}}(q,t)$.

To globally account for polydispersity and particle correlation effects, which both give rise to a potentially continuous superposition of correlation times, we have fitted all of the measured functions $g_2(q,t) - 1$ in panel (a) of Fig. 6.17 by the Kohlrausch-Williams-Watts (KWW) stretched exponential, $\{\exp[-(t/\tau_i)^{\beta_i}]\}^2$, characterized by overall decay times τ_i and a stretching exponents $\beta_i \leq 1$ [249, 250]. A system decaying nearly single-exponentially has a

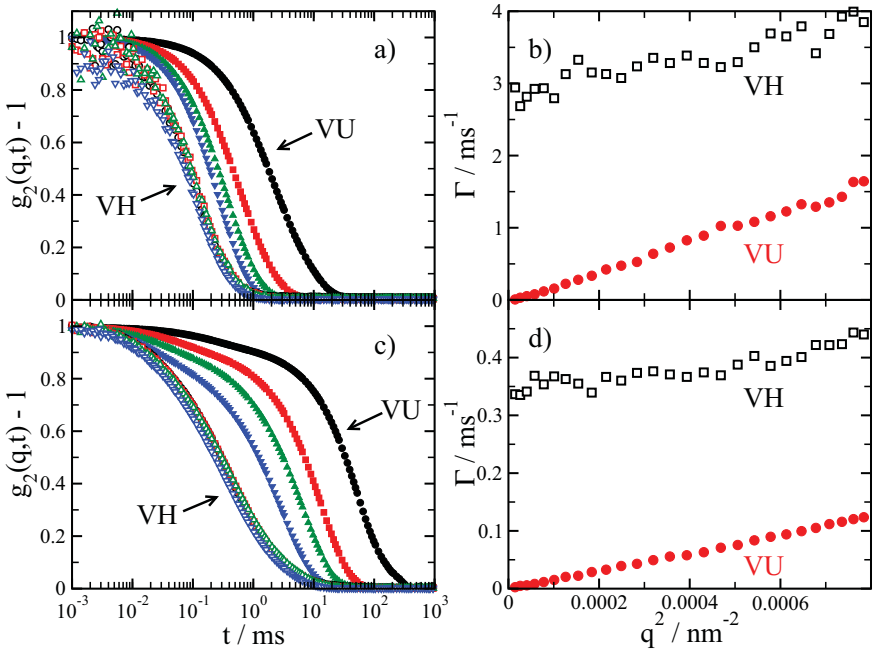

Fig. 6.17: *Panels a and c: Reduced intensity autocorrelation function, $g_2(q,t)-1$, versus correlation time t for gibbsite in DMSO. Panels b and d: (mean) relaxation rates Γ_i as functions of q^2. The gibbsite volume fraction is $\phi = 0.8\%$ in panels a and b, and $\phi = 4.8\%$ in panels c and d. Probed wavenumbers in a and c: $q = 7.6\times10^{-3}$ nm^{-1} (black circles), $q = 1.47\times10^{-2}$ nm^{-1} (red squares), $q = 2.08\times10^{-2}$ nm^{-1} (green triangles), and $q = 2.84\times10^{-2}$ nm^{-1} (blue triangles). Open symbols: VH scattering geometry. Filled symbols: VU ≈ VV scattering geometry.*

value of β close to one. For example, $\beta_i \approx 0.9$ for the low-concentration systems with IACFs depicted in panel (a) of Fig. 6.17. The mean KWW relaxation rates, Γ_i, were then calculated from $\Gamma_i = 1/[\tau_i \times \Gamma(1/\beta_i)/\beta_i]$ [251], with Γ denoting the gamma function. We note here that the area coherence factor C in the Siegert relation $Cg_1^2(q,t) = g_2(q,t) - 1$ is practically equal to one in all our experiments.

The resulting relaxation rates Γ_{VH} and Γ_{VU} at $\phi = 0.8\%$ are plotted as functions of q^2 in panel (b) of Fig. 6.17. At the small q-values with $q\langle R\rangle \lesssim 1$ considered here, the relaxation rates in VH and VU≈VV geometry can be expressed as $\Gamma_{VH} = 6D_r^{\perp} + \mathcal{O}(q^2)$ and $\Gamma_{VV} = D_t q^2 + \mathcal{O}(q^4)$, respectively [21, 92–94, 252], where D_t and $D_r^{\perp}$ are interpreted as the concentration- and interaction-potential dependent experimental translational and (end-over-end tumbling) rotational diffusion coefficients. Note here that we use capital D's to denote experimentally determined diffusion coefficients for gibbsite, to distinguish them from the theoretically computed diffusion coefficients. The latter are denoted by lower-case d's throughout. Polydispersity effects have been accounted for in an average way through the KWW determination of the relaxation rates. Contributions to Γ_{VV} of $\mathcal{O}(q^4)$ arising from rotational diffusion, and rotational-translational coupling, are not accounted for.

Regarding the low-concentration system in panels (a) and (b), there is no distinction required between short- and long-time diffusion coefficients. The slopes of Γ_{VU} and Γ_{VH} in panel (b) in the $q^2 \to 0$ extrapolation are approximately equal to the zero-concentration diffusion coefficients. A zero-ϕ extrapolation of all investigated systems, with the relaxation rates evaluated as described above, gives $D_{t,0} = 2.1 \times 10^{-12}$ m^2/s and $D_{r,0}^{\perp} = 0.34 \times 10^3/s$. Both values are somewhat smaller than the values obtained from the ultrathin platelet approximation, given in Section 5.5.2.

The data for Γ_{VH} in panel (b) shows an overall linear increase in q^2, but are more noisy than those for Γ_{VU}. This originates from the much lower scattering intensity in VH geometry which for the gibbsite system is by a factor of 10^{-4} smaller than in VU geometry.

At larger platelet concentration, where direct and hydrodynamic interactions come into play, one sees interesting changes in the scattering functions. The VU and VH normalized IACFs, and the corresponding KWW relaxation rates for the more concentrated system at $\phi = 4.8\%$, are depicted in panels (c) and (d) of Fig. 6.17, respectively. It is apparent from panel (c) that in VU geometry an additional fast relaxation mode is observed. Moreover, the slow-mode decay of $g_2^{VU}(q,t) - 1$ gets slightly more stretched out. In VH geometry, no additional mode is seen at this concentration but the decay is more stretched than in the $\phi = 0.8\%$ case. All these features are indicators of pronounced platelet correlations requiring now the distinction between short- and long-time diffusion properties. The subdiffusive transition regime is characterized by the structural relaxation time given by $\tau_I = 1/(6D_{r,0}^{\perp}) \approx 0.05$ ms.

Using again the Siegert relation, we can fit the two-mode decay of g_2^{VU} observed in panel

(c) in the probed time window by the two-exponential form,

$$g_2^{\mathrm{VU}}(q,t)-1=\left[Ae^{-\Gamma_t^{\mathrm{VU}}t}+(1-A)e^{-\Gamma_c^{\mathrm{VU}}t}\right]^2, \tag{6.14}$$

involving three fit parameters A,Γ_t^{VU} and Γ_c^{VU} with $0\leq A\leq 1$ and $\Gamma_c^{\mathrm{VU}}>\Gamma_t^{\mathrm{VU}}>0$. Both the fast-mode and slow-mode relaxation rates, $\Gamma_c^{\mathrm{VU}}=q^2D_c$ and $\Gamma_t^{\mathrm{VU}}=q^2D_t$, show the expected diffusive q^2-dependence, allowing for the determination of the associated diffusion coefficients D_c and D_t which obey (aside from experimental scatter) the ordering $D_c>D_{t,0}$ and $D_t<D_{t,0}$. In panel (d), $\Gamma_t^{\mathrm{VU}}\approx\Gamma^{\mathrm{VV}}=q^2D_t+\mathcal{O}(\phi^4)$ is plotted vs. q^2, with D_t inferred from the slope at small q. The corresponding fast mode rate, Γ_c^{VU}, is not shown in the figure. Here again, the associated diffusion coefficient, D_c, has been determined as the slope of Γ_c^{VU} as a function of q^2, extrapolated to $q\to 0$. Panel (d) also shows the relaxation rate, $\Gamma^{\mathrm{VH}}=6D_r^{\perp}+D_tq^2$, of the somewhat stretched out single-mode decay of $g_2^{\mathrm{VH}}(q,t)$, determined using the KWW analysis. Note here that the slope of the Γ^{VH} vs. q^2 curve is equal within experimental noise to that of Γ_t^{VU} vs. q^2. The slope in both cases is identified as the translational self-diffusion coefficient, D_t, of interacting platelets in the isotropic phase. Likewise, $D_r^{\perp}$ determined from the zero-q intercept of the Γ^{VH} plotted versus q^2 in panel (d), which fulfills $D_r^{\perp}<D_{r,0}^{\perp}=D_r^{\perp}(\phi\to 0)$, can be interpreted as the rotational self-diffusion coefficient at non-zero concentrations.

The same evaluation procedure as explicated in Fig. 6.17 for two selected concentrations, was applied to an extended set of concentrations up to the I/LC transition. The resulting reduced diffusion coefficients $D_t/D_{t,0}$, $D_r^{\perp}/D_{r,0}^{\perp}$, and $D_c/D_{t,0}$, are depicted in Fig. 6.18 as functions of ϕ.

According to this figure, D_t and $D_r^{\perp}$ are concentration-independent, within the experimental scatter, in the low-concentration range $\phi\lesssim 0.3\%$. This is the expected behavior for practically uncorrelated particles at low concentration. On the other hand, already around $\phi=1\%$, the fast-mode coefficient, D_c, has grown largely above its zero-concentration value $D_{t,0}$ whereas, as viewed from the extended vertical scale of Fig. 6.18, D_t and $D_r^{\perp}$ start to strongly decline below their respective infinite dilution values at $\phi\sim 1\%$.

A concentration dependence similar to that of D_c has been reported for the collective diffusion coefficient in polymers and flexible rod systems [253, 254]. However, the gibbsite platelets studied here have no flexible parts. Moreover, the onset of the strong increase in $D_c(\phi)$ is found at concentrations far below the platelet overlap concentration $\phi^*=(3/2)p$ of about 13%. Note here that an alternative definition of the overlap concentration invoking the random close packing volume fraction, $f=0.64$, of spheres according to $\rho^*(4\pi\langle R\rangle^3/3)=f$ results in $\phi^*=(3\langle h\rangle/4\langle R\rangle)f\approx 8.3\%$, *i.e.* a value fortuitously close to the concentration $\phi_{\mathrm{I/LC}}=8\%$, where the I/LC transition is observed experimentally.

Since the dynamics of freely rotating charged platelets at concentrations well below the overlap concentration ϕ^* is most strongly influenced by the monopolar terms in the far-field electrostatic and hydrodynamic interactions, $D_c(\phi)$ should behave similar to the collective dif-

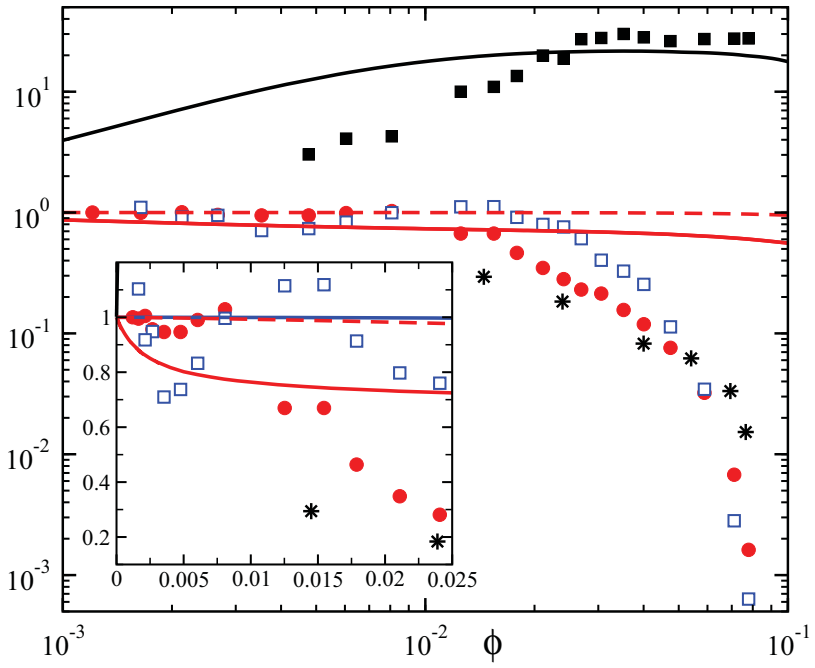

Fig. 6.18: *Volume fraction dependence of various dynamic properties including the experimental normalized fast-mode diffusion coefficient, $D_c/D_{t,0}$, (filled squares), and the experimental slow-mode diffusion coefficient, $D_t/D_{t,0}$, (filled circles), both obtained in VU geometry, and the experimental normalized (mean) rotational diffusion coefficient, $D_r^{\perp}/D_r^{0,\perp}$ (open squares), obtained from VH measurements. Stars: Inverse low-shear-rate viscosity $(\eta/\eta_0)^{-1}$, obtained from rheometric measurement. Solid black and dashed red lines: theoretical $d_c/d_{t,0}$ and $d_t^S/d_{t,0}$ predictions of the effective charged sphere model, calculated using the corrected $\delta\gamma$ scheme. Solid blue line (inset only): Scaling relation $d_r^S/d_r^0 = 1 - 1.3\phi_{eff}^2$ for the short-time rotational diffusion coefficient of effective spheres, using $\phi_{eff} = 1.93\phi$. Solid red line: $d_t^L/d_{t,0}$ of effective charged spheres, calculated using the simplified MCT scheme with far-field HIs correction. Note that experimentally determined diffusion coefficient of gibbsite are denoted by capital D's, to distinguish them from the theoretically predicted diffusion coefficients, denoted by lower-case d's.*

fusion coefficient $d_c(\phi)$, measured in low-salinity suspensions of globular charged colloids. The latter coefficient shows a sharp rise at low ϕ indeed (*c.f.*, Fig. 6.13, and the related discussion).

Fig. 6.18 includes the long-time value of the experimental translational self-diffusion coefficient D_t, which for interacting systems can become substantially smaller than its short-time counterpart, whose deviations from $d_{t,0}$ are comparatively small. That D_t should be interpreted as a long-time property follows from Eq. (6.14) in combination with the finding that $D_c > D_{t,0} > D_t$ for $\phi \gtrsim 0.5\%$. Due to the fast decay of the collective mode, Γ_t^{VU} is largely determined by D_t for times $t \gtrsim 1/(q^2 D_c)$ which define the long-time regime, $t \gg \tau_I \approx 0.05$ ms, when the zero-q extrapolation is made in determining D_t. Different from self-diffusion, the long-time form of d_c is practically equal to its short-time counterpart, for all concentrations in the isotropic regime [22, 255].

The effective sphere interaction model in combination with the rotational-translational decoupling approximation is easily generalized from the SLS intensity to the normalized time-dependent electric field autocorrelation function, which for small q in VV ($\approx$VU) geometry is given by

$$g_1^{\mathrm{VV}}(q,t) = [1-B]e^{-q^2 W(t)} + BS(q\to 0)e^{-q^2 d_c t}, \tag{6.15}$$

with $B = X(q\to 0)/[X(q\to 0) + (1-X(q\to 0))S(q\to 0)]$. Here, $W(t)$ is the mean-squared displacement of a charged effective sphere with initial (short-time) slope d_s, and final (long-time) slope d_s^L, where $d_s^L < d_s \leq d_{t,0}$ (*c.f.*, Fig. 4.1). Moreover, on ignoring the small difference between long- and short-time collective diffusion coefficients, noticeable at very high concentrations only, $d_c = d_{t,0}H(q\to 0)/S(q\to 0)$ [21, 22, 153]. Eq. (6.15) is fully consistent with the two-mode decay observed for gibbsite, fitted using Eq. (6.14), and it supports the interpretation of the experimental D_t as a long-time self-diffusion coefficient. We point out that in the simplifying model considered here, the diffusion coefficients of platelets are simply approximated by those of the effective charged spheres.

Using the effective sphere parameters $n_s = 7\mu$M, $\sigma = 65$ nm, $Z = 71$ determined in Section 5.5, and varying the (effective) volume fraction in small steps assuming a linear, homogeneous relationship $\phi_{\mathrm{eff}} = 1.93\phi$, we have generated a set of $S(q)$'s using the MPB-RMSA scheme, as input to the otherwise parameter-free self-part corrected $\delta\gamma$ scheme for $H(q)$.

Considering the approximations invoked in our simplifying model, the agreement of the theoretically calculated d_c with the experimental data in Fig. 6.18 is satisfying. The smooth increase of d_c with increasing ϕ to values about 20 times larger than $d_{t,0}$ is well captured. As explained already in Section 6.3.1, the theoretical d_c reaches a shallow maximum at $\phi \approx 3\%$ originating from the interplay of osmotic compressibility and sedimentation coefficient $H(q\to 0)$ [41].

The self-part corrected $\delta\gamma$ scheme result for the short-time self-diffusion coefficient, $d_s(\phi)$, is included into Fig. 6.18 (see also inset). In the explored ϕ-range, the theoretical $d_s(\phi)$ decreases only mildly with increasing ϕ, and is overall well described by the fractional power-

law Eq. (4.24b) with $a_t \approx 2.9$. For $\phi \gtrsim 2\%$, however, the decline of the experimental long-time D_t in Fig. 6.18 is very strong. For values $\phi \gtrsim 7\%$ near to $\phi_{\mathrm{I/LC}}$, D_t assumes values of less than 1% of $D_{t,0}$. This is similar to the slowing down of self-diffusion seen for block copolymers in a neutral solvent when the disordered-ordered transition is approached [256], in polymer solutions with increasing concentration [254], and also for polymer grafted clay particles [90]. The measured values of $D_t^L/D_{t,0}$ for gibbsite are much smaller than those reached by the long-time translational diffusion coefficient of low-salinity charge-stabilized spheres in the fluid phase, which reaches its minimal value of $d_t^L/d_{t,0} \approx d_t^L/d_t^S \approx 0.1$ at the freezing transition volume fraction ϕ_f [169, 176]. For the effective sphere model used here, ϕ_f can be estimated on basis of the empirical Hansen-Verlet freezing criterion $S(q_m, \phi_{\mathrm{eff}} = \phi_f) \approx 3.1$ for charged spheres at low salinity [103, 181, 182]. With $S(q)$ computed in MPB-RMSA, this results in the freezing transition volume fraction $\phi_{\mathrm{eff}} = 42\%$, corresponding to $\phi = \phi_{\mathrm{eff}}/1.93 = 22\%$. We attribute the strong decay of the experimental D_t at larger ϕ to the uprising influence of the anisotropic electro-steric interactions, and to the rotational-translational coupling effects in platelet systems. These effects, which are obviously not included in the effective sphere model, cause a further slowing down of the translational and rotational dynamics.

The short-time rotational self-diffusion coefficient, d_r, of colloidal charged-sphere systems at low salinity, follows to good accuracy the concentration scaling $d_r/d_{r,0} = 1 - a_r\phi^2$, with $a_r \approx 1.3$, in the whole ϕ-range of Fig. 6.18 [23, 40]. Note that $d_r/d_{r,0}$ decreases less strongly with increasing ϕ than $d_s/d_{t,0}$. This can be explained [40] by the shorter-ranged hydrodynamic self-coupling of the rotational motion. The experimental (long-time) diffusion coefficients D_t and $D_r^{\perp}$ depicted in Fig. 6.18, follow overall the same ordering $D_r^{\perp}(\phi) > D_t(\phi)$ as their short-time counterparts in the effective sphere model.

The low-q expression for $g_1^{\mathrm{VH}}(q,t)$ in our simplifying model is given by (see, e.g., [252, 257])

$$g_1^{\mathrm{VH}}(q,t) = e^{-q^2W(t)}G_r(t), \tag{6.16}$$

where $G_r(t) =< P_2(\hat{\mathbf{u}}(t)\cdot\hat{\mathbf{u}}(0)) >$ is the rotational self-dynamic correlation function of spheres, with the optical axis of a sphere characterized by the unit vector $\hat{\mathbf{u}}$, and with P_2 denoting the 2$^{\mathrm{nd}}$-order Legendre polynomial. In the derivation of Eq. (6.16), it has been assumed that the translational-rotational motions of a particle are decoupled [252]. This decoupling is exactly valid for hydrodynamically interacting spheres at short times only. For non-spherical particles, it is an approximation even to linear order in t.

At short times, $G_r(t) = \exp\{-6d_r^S t\}$ decays exponentially. At long times, however, $G_r(t)$ decays in principle non-exponentially, with an average decay rate somewhat smaller than d_r^S [252]. While a genuine long-time rotational self-diffusion coefficient does not exist, one can define instead a mean orientational self-diffusion coefficient, $\overline{d_r}$, determined by the time dependence of $G_r(t)$ for all times. A corresponding $\overline{d_r}$ of platelets, identified as the measured $D_r^{\perp}$, is shown indeed in Fig. 6.18, as obtained in panel (d) of Fig. 6.17 using the KWW analysis. The calculation of $\overline{d_r}$ for colloidal hard spheres in Ref. [252] suggests that $\overline{d_r}$ is only slightly

smaller than d_r^S, at least for smaller values of ϕ. The experimental mean rotational diffusion coefficient $D_r^{\perp}$ depicted in Fig. 6.18, however, decreases very strongly at larger ϕ, to an extent comparable to that of the experimental D_t. Like for D_t, we attribute this strong decline of $D_r^{\perp}$ at larger ϕ to the strong anisotropic electro-hydrodynamic coupling of the charged platelets.

CHAPTER

SEVEN

Conclusions and Outlook

A set of analytical theoretical schemes has been introduced, tested and applied in this thesis, that allow precise and quick computation of static pair correlations, diffusion properties, and the viscosity of HSY-like colloidal fluids. The accuracy and validity range of these easy-to-implement methods was assessed in the complete fluid-phase regime through extensive comparisons with static and dynamic simulations. Using our analytic methods, we calculated a variety of short-time dynamic properties, including the hydrodynamic function and the high-frequency viscosity, as functions of concentration, salt content, effective particle charge, and particle size. The long-time static viscosity and self-diffusion coefficient were calculated using a simplified MCT result including far-field HIs. The observed trends in the static and dynamic properties were explained also in terms of intuitive physical pictures. In addition, the theoretical methods were used to analyze experimental results, obtained by our collaborators, for three different systems: charge-stabilized colloidal silica spheres in toluene-ethanol, gibbsite platelets in DMSO, and globular BSA proteins in water.

The dynamic methods employed require the static structure factor, or likewise the rdf, as the only input. An analytic integral equation method was designed which allows for a fast and quantitatively accurate computation of $S(q)$ and $g(r)$. This so-called MPB-RMSA method is a simple modification of the PB-RMSA scheme originally devised by Snook and Hayter [97]. It can be easily implemented into a standard (R)MSA code (cf., Appendix B), making it appealing for practical applications.

Through extensive comparison with RY and MC calculations, we have established the MPB-RMSA as a fast and convenient tool for analyzing experimental scattering data on charge-stabilized suspensions in a wide range of concentrations, ionic strengths, and effective charge numbers, with a fast delivery of $S(q)$ and $g(r)$. Such a fast delivery is also required in dynamic methods including MCT and dynamic density functional theory. In these methods, static structure factors in an extended range of wavenumbers are required as input in calculations of non-equilibrium glass or gel lines.

As demonstrated in this thesis for silica spheres, BSA proteins, and gibbsite platelets, the MPB-RMSA is well-suited to the real-time fitting of experimentally obtained pair structure functions. The central fitting parameter, Z, can be obtained from matching the experimental structure factor peak heights. In most cases, the MPB-RMSA effective charge number is practically identical to that obtained from the more elaborate MC simulations and the RY method. However, the latter two methods are computationally more expensive by orders of magnitude.

We have demonstrated the capability of the MPB-RMSA as a fast tool for exploring generic features in the pair microstructure and the equilibrium fluid-phase behavior. Using the MPB-RMSA, the principal peak heights, $S(q_m)$ and $g(r_m)$, and the corresponding peak positions have been determined throughout the fluid $(\tilde{T},\tilde{k})$ phase-space. This has allowed us to unravel the conditions for which geometric concentration scaling of the peak positions is observed. The solid-fluid coexistence line determined in conjunction with the Hansen-Verlet freezing rule was shown to be in good agreement with MD simulation results for point-Yukawa particles, including the isochoric OCP transition point.

While the MPB-RMSA static structure functions are in good overall agreement with the MC and RY results, in some specific details there are small discrepancies. For low-salt systems of strongly correlated particles, $S(q_m)$ is overestimated by up to 5%. The peak value, $g(r_m)$, of the rdf is, in general, slightly underestimated, again by up to 5% for highly correlated particles. Furthermore, the (M)PB-RMSA $g(r)$ has a kink at the inflated (rescaled) hard core diameter that is not shared by the exact rdf. For HSY systems with weak Yukawa repulsion where the physical hard core matters, the MPB-MSA pair structure functions remain in good overall agreement with the MC and RY data, unless $\gamma e^{-k} \gtrsim 3.0$. Under the latter condition, the increase of the rdf contact value $g(\sigma^+)$ as a function of ϕ is overestimated.

Unlike the RY scheme, the MPB-RMSA is thermodynamically inconsistent, but to a lesser degree than the RMSA, HNC, and also the PB-RMSA schemes. The zero-q limit of $S(q)$ is predicted by the MPB-RMSA to a reasonable accuracy, with deviations from the RY result of less than 10% even at the freezing volume fraction.

The static functions $S(q)$ and $g(r)$, computed by the MPB-RMSA method, have been used as the only input required in the PA and (self-part corrected) $\delta\gamma$ schemes for the short-time dynamics. For arbitrary salt concentration, the PA scheme, which precisely, but only accounts for two-body HIs, is in excellent agreement with the simulation data for $H(q)$, provided that $\phi \lesssim 0.1$. With regard to the high-frequency viscosity, the PA-scheme predictions are in good agreement with the simulation data for volume fractions up to $\phi \approx 0.1$ in case of neutral hard spheres, and up to $\phi \approx 0.2$ for strongly charged spheres in the low salinity regime. At larger ϕ, three-body and higher-order HIs are influential, so that the self-part corrected $\delta\gamma$ scheme should be used.

The self-part corrected $\delta\gamma$ scheme for $H(q)$ of charged spheres is in good agreement with our ASD results at all ϕ and n_s values investigated. When it is applied to neutral hard spheres, using d_s^{HS} according to Eq. (4.26), $H^{\mathrm{HS}}(q)$ is predicted to very high degree of accuracy for concentrations up to $\phi \approx 0.4$, and including the small-q region.

We have shown that the (second-order) $\delta\gamma$-scheme expression for η_∞, given in Eqs. (4.20)-(4.22), is only applicable to hard-sphere like systems, that is at large screening or zero charge. Its predictions for $\eta_\infty^{\rm HS}$, however, agree well with the ASD data up to $\phi \lesssim 0.4$. At larger ϕ, it underestimates the high-frequency viscosity. Based on arguments applicable to low-salinity charge-stabilized systems only, we have introduced in Eq. (4.27) a simple correction to the $\delta\gamma$-scheme result for η_∞. This corrected $\delta\gamma$ scheme predicts to a high degree of accuracy the high-frequency viscosity of low-salinity systems, even up to the freezing transition concentration.

We have shown that a large body of experimental results for $D(q)$ and $H(q)$, for systems of different particle types and sizes, concentrations, salt contents and solvents, is well described by the OMF model, with all the ordering relations in Eqs. (6.9) satisfied. Residual attractive pair interactions or solvent permeability, and most likely also electrolyte friction, can not explain the ultra-small $H(q)$ findings of Robert and collaborators [215]. Ultra-small values of $H(q)$ have not been observed in our scattering experiments, nor in those of our collaborators and various other groups [65, 214, 216, 218].

We have investigated static and dynamic properties of aqueous BSA protein solutions in an integrated conceptual framework, by combining SLS/DLS, SAXS, and rheometric measurements with our analytical schemes. Protein solutions with physiological concentrations of NaCl have been studied, as well as low-salt solutions, showing distinct features in the concentration-dependence of the collective diffusion coefficient and the (reduced) viscosity. In our analytical theoretical approach to BSA proteins, we have used a simplifying spheroid-Yukawa model of BSA with isotropic, repulsive pair interactions, to calculate the static scattered intensity using the efficient MPB-RMSA method in combination with the orientational-translational decoupling approximation. The resulting static structure factors $S(q)$ have been used, without any further fitting, in calculating d_c, η_∞, and η on basis of our well-tested short-time dynamics schemes. Without including additional protein-specific features, we have used the spheroid-Yukawa model for $I(q)$, and the related effective sphere-Yukawa model for the dynamic properties, as minimal models to reveal their pros and cons.

The measured static and dynamic properties of BSA are captured reasonably well in our simplifying SY model, with an at least semi-quantitative accuracy, for mass concentrations up to $c_p \approx 100$ mg/ml. In the range of 2 mg/ml $\lesssim c_p \lesssim 50$ mg/ml, reliable values for the effective protein charge, and the residual electrolyte concentration, have been obtained from our fits of the SAXS intensities. The SAXS fits are considerably obstructed for $c_p \lesssim 2$ mg/ml by the presence of scattering impurities, and for $c_p \gtrsim 50$ mg/ml by the breakdown of the decoupling approximation.

A well-developed maximum in the concentration dependence of the collective diffusion coefficient of BSA was found at low salinity. This behavior is also seen in charge-stabilized colloidal suspensions. It is caused by the competition between electrostatic repulsion and hydrodynamic slowing down in crowded systems. Moreover, a non-monotonic concentration dependence of the reduced viscosity of low-salinity BSA solutions was predicted theoretically, and to some extent has been seen also experimentally. We have explained the local

maximum in the reduced viscosity $\eta_{\mathrm{red}}(c_p)$ as a non-hydrodynamic effect caused by the electric repulsion. A non-monotonic concentration-dependence of η_{red}, with a pronounced peak at low concentration, is also observed in polyelectrolyte solutions. Thus, the low-c_p peak in η_{red} is a generic feature of charge-stabilized dispersions at low salinity.

We have analyzed the validity of the short-time and long-time versions of a GSE relation by Kholodenko and Douglas [30], which connects the collective diffusion coefficient to the shear viscosity and to the isothermal osmotic compressibility. Despite their appealing simplicity, the KD-GSE relations fail to capture the essential richness of macromolecular collective diffusion. To decent accuracy, they apply to electrostatically screened solutions at high salinity, where a maximum positive-valued violation of 18% is found for volume fractions around 0.3. However, the KD-GSE relations are violated for more crowded high-salt solutions, and for all non-zero volume fractions under low-salt conditions. The key finding from our validity tests of various GSE relations is the strong dependence of their applicability on the range and character of the particle interactions.

Using (D)DLS and SLS, we have measured the long-time translational collective- and self-diffusion coefficients D_c and D_t^L, the mean rotational diffusion coefficient $D_r^{\perp}$, and the static scattered intensity, $I(q)$, of charged gibbsite platelets suspended in DMSO at low ionic strength. Our experiments cover the concentration range from very dilute systems up to the I/LC transition.

The usage of DMSO as a solvent that has a dielectric constant close to that of gibbsite, has enabled us to determine the translational and rotational diffusion properties without the necessity of invoking elaborate X-ray photon correlation spectroscopy measurements. Fast relaxation modes in the dynamic scattering data have frequently been reported in relation to the liquid-glass transition, the glassy state, and also for polymer-coated clays [84, 86, 258]. In the present study, a fast mode also has been found for the isotropic phase, and we have identified it as a collective diffusion mode.

With increasing ϕ, the measured collective diffusion coefficient increases to about twenty times the single-particle (orientationally averaged) translational diffusion coefficient. Different from the translational and rotational self-diffusion coefficients, which strongly decrease for $\phi \gtrsim 2\%$, the collective diffusion coefficient remains nearly constant for these larger concentrations even when the I/LC transition concentration is reached. The strong decay of the self-diffusion coefficients is accompanied by a comparatively pronounced increase of the zero-shear-rate limiting static shear viscosity. We have provided arguments, both experimentally and theoretically, that the coefficients D_t and $D_r^{\perp}$ obtained in the scattering modes analysis should be identified, respectively, with the translational long-time and the mean rotational self-diffusion coefficients of gibbsite platelets.

We have used a circular cylinder-Yukawa model for the thin gibbsite platelets in the isotropic fluid phase, similar to the spheroid-Yukawa model used for the moderately aspheric BSA proteins. At low concentrations, the mean scattered intensity $I(q)$ of gibbsite is well reproduced in the simplifying translational-rotational decoupling method, on neglecting cor-

relations between particle positions, sizes and orientations, and on approximating the direct platelet interactions by a spherically symmetric electro-steric repulsion of DLVO type.

Except for very low concentrations, the accessible q-range in light scattering experiments is restricted to wavenumbers smaller than the value where the principal structure peak in $I(q)$ occurs. The effective particle charge has therefore been estimated from the I/LC transition as $Z = 71$, and was kept constant in our model calculations independent of concentration and salinity. We note here that while the simple effective sphere model clearly fails in terms of quantitative predictions for the gibbsite platelet system, it allows for a correct assessment of qualitative features in the isotropic phase, such as the ordering of the values of the rotational and translational self-diffusion coefficients, and the plateau region of the collective diffusion coefficient at larger ϕ.

Upon increasing the concentration, peculiar observations have been made in the measured diffusion properties of the gibbsite/DMSO system. We find that D_c grows with increasing concentration, similar to suspensions of charge-stabilized colloidal spheres at low ionic strength. Since the value of d_c is nearly the same at long and short times, and since the increase in $d_c(\phi)$ is mainly due to the reducing osmotic compressibility $S(q \to 0)$, the basic features of the experimental $D_c(\phi)$ have been reproduced in our effective sphere model, using the self-part corrected $\delta\gamma$-scheme.

The effective sphere model of gibbsite is less accurate regarding the measured long-time dynamic quantities D_t^L and $D_r^\perp$, which are more sensitive to anisotropic direct and hydrodynamic interactions most influential on shorter length scales. The strong decay of both quantities to less than 1% of their respective infinite dilution values near $\phi_{\mathrm{I/LC}} = 8\%$, is not reproducible in an effective sphere model, where $D_t^L \gtrsim 0.1 \times D_{t,0}$ is predicted for all fluid-state concentrations.

Various extensions of the presented work can be thought of, that could be the starting point for future projects.

The MPB-RMSA scheme for the equilibrium pair-structure of HSY-like fluids can be used to implement a quicker version of the self-consistent renormalized jellium approach by Colla *et al.* [57], for calculating the colloidal renormalized charge. Here, the MPB-RMSA can replace the numerically more expensive RY scheme with practically no loss in accuracy.

Our comprehensive two-dimensional parameter scans of the point-Yukawa-like phase, presented in Section 5.2, could be extended to cover the full three-dimensional parameter space of HSY-like particles including non-zero contact values of the rdf. Using our fast and accurate schemes describing short-time dynamics, parameter scans of the scaling behavior of dynamic properties could be determined with high resolution in the full fluid phase regime. The results of such dynamic parameter scans could be used in systematic searches for possible GSE relations, combining various diffusion properties with the suspension viscosity and properties of the pair-structure functions.

A straightforward extension of the PA scheme of short-time colloid dynamics is obtained

using expressions for the pair-mobility functions $x_{ij}^a(x)$ and $y_{ij}^a(x)$, and the shear-mobility function $J(x)$, that apply to spheres with different non-stick hydrodynamic boundary conditions. The investigations presented in this thesis have been restricted to spheres with hydrodynamic stick boundaries. However, expressions for $x_{ij}^a(x)$, $y_{ij}^a(x)$ and $J(x)$ can also be computed for spheres with slip or mixed stick-slip boundaries, for spherical fluid droplets, and for permeable spheres, where solvent-permeability is accounted for using the Debye-Bueche-Brinkmann equation [259, 260]. Series expansions for $x_{ij}^a(x)$ and $y_{ij}^a(x)$ to $\mathcal{O}(x^{-20})$ for some selected types of hydrodynamic boundary conditions are tabulated in Ref. [159], and to $\mathcal{O}(x^{-7})$ for solvent-permeable spheres of arbitrary permeability in Ref. [261]. In a future project, these truncated two-body series expansions could be extended to a very high order in $1/x$ by methods discussed in Refs. [21, 158, 159, 162], with resulting mobility tables for pairs of spheres with varying solvent permeabilities or hydrodynamic slip lengths, and for fluid droplets. In combination with the MPB-RMSA method, a computationally highly efficient solver for short-time dynamic properties of charged and uncharged spheres, with various sorts of hydrodynamic boundary conditions could be implemented. A promising field of application for such a solver is the investigation of suspensions of charged and uncharged microgels that show a temperature-dependent swelling behavior with associated varying solvent permeability [262–264].

We recall from Chapter 6 that the PA-scheme results with stick hydrodynamic boundary conditions are accurate up to $\phi \approx 0.1$ regarding the $H(q)$ of both the CS and HS systems, and the η_∞ of HS, whereas the PA-scheme expression for the η_∞ of CS is applicable even up to $\phi \approx 0.2$. A non-zero hydrodynamic slip-length or a non-zero solvent permeability reduce the hydrodynamic drag on a single sphere. A weakening effect of slip and permeability should apply also to two-body HIs. Thus, the PA scheme is likely to be reasonably accurate for larger volume fractions when, in place of stick-boundary spheres, slip or permeable spheres are considered.

In contrast to the PA scheme, a straightforward generalization of the (self-part corrected) $\delta\gamma$ scheme to systems other than stick-boundary spheres is not in sight. However, short-time dynamic properties in concentrated suspensions of spheres with arbitrary hydrodynamic boundary conditions and interaction potentials, can be computed using a precise hydrodynamic force multipole method [265, 266]. This simulation method, which is computationally far more expensive than the analytical schemes discussed in the present thesis, takes accurate account of many-body HIs in systems consisting of a few hundred particles with periodic boundary conditions. This requires, in general, an extrapolation (finite size scaling) to a macroscopically large system. In combination with MC simulations for their microstructure, the multipole method has been used to calculate various short-time diffusion coefficients and the high-frequency viscosity of uncharged, uniformly permeable spheres, as functions of permeability and concentration [25, 26, 165–167, 175, 212, 225].

Different from the self-part corrected $\delta\gamma$ scheme for $H(q)$ in Eq. (4.25), which applies to any salt concentration under the condition that $\phi \lesssim 0.15$, the corrected $\delta\gamma$ scheme for η_∞

in Eq. (4.27) is valid at low salinities only. An appropriately corrected $\delta\gamma$ scheme for η_∞, applicable for arbitrary salinities, is still missing. Its development could be the topic of a future study.

Possible extensions of the SY model for globular protein solutions used in this thesis, which allow the theory to maintain analytical simplicity to some extent, are the inclusion of short-range attractive interactions for suspensions at larger salt content using, for instance, a two-Yukawa pair potential [267, 268], and the average inclusion of surface patchiness [248]. For the static viscosity of more strongly concentrated protein solutions than those considered in the present work, the shear stress relaxation contribution, $\Delta\eta$, can become large in comparison to η_∞. In calculating $\Delta\eta$, one then needs to account for HIs which tend to further enlarge the viscosity. An inclusion of HIs into $\Delta\eta$ can be accomplished starting from an extended MCT scheme discussed in Refs. [119, 180].

Future SAXS and XPCS measurements of gibbsite platelets are needed for an unambiguous determination of the gibbsite effective charge and its dependence on ϕ and n_s. Our simplifying CCY model of gibbsite could be improved by a more elaborate approach. In a more refined calculation of $I(q)$, one can account for shape-dependent direct interactions via the PRISM method [4, 134–136]. However, regarding dynamic quantities, it will be very difficult to include shape-dependent hydrodynamic interactions, on avoiding numerically expensive multi-particle collision, fluctuating Lattice-Boltzmann or Stokesian dynamics simulations. Finally, the similar measured concentration-dependencies of D_t^L, $D_r^\perp$, and of the inverse low shear-rate limiting viscosity, $(\eta/\eta_0)^{-1}$, of the gibbsite system discussed in this thesis, can be the starting point of a future examination of generalized Stokes-Einstein relations in concentrated platelet fluids.

APPENDIX

A

MSA solution

Except for the HSY pair-potential parameters $\{\gamma, k, \phi\}$, the static structure factor $S(q)$ and the rdf $g(r)$, the variable names used in this appendix are locally defined only. The index of abbreviations and symbols in this thesis, starting on page 165, does not apply to the local variable names used here.

A large body of literature [63, 113–115, 269–271], deals with analytic MSA solutions for $S(q)$ and $g(r)$ for particles interacting by the HSY pair potential in the form of Eq. (2.6). Unfortunately, there are various misprints scattered in the lengthy lists of coefficients in which $S(q)$ and $g(r)$ are expressed. To facilitate the implementation of the MSA solution by an interested user, we summarize here the analytic MSA solutions used in our software package described in Appendix E. The MSA expressions given here are the corrected ones by Cummings and Smith [113, 114], which have been obtained using a Wiener-Hopf factorization method [272].

For conciseness, we give only those results required for the implementation of the MPB-RMSA algorithm (see Appendix B), namely those for $g_{\mathrm{MSA}}(r=\sigma^+)$ and $S(q)$. There exist also analytic MSA expressions for the Laplace transform of $g(r)$, and for $c(r)$, which can be found in the literature on the MSA given cited this thesis.

According to Eq. (3.12), the MSA rdf contact value $g_{\mathrm{MSA}}(x=1^+)$ is obtained from $c_{\mathrm{MSA}}(x=1^-)$ and the pair potential at contact. Using the analytic MSA result for $c(r)$, one obtains

$$\begin{aligned} g_{\mathrm{MSA}}(x=1^+) \;=\; & a+b+K-\beta k f e^{-k}-6\phi\left\{\beta\frac{f+de^{k}}{k^2}\times\left[-\beta f k^2 e^{-k}+ak^2e^{-k}\right.\right. \\ & -2kbe^{-k}-2ae^{-k}+2bk^2e^{-k}-2\beta dk^2e^{-k}+2ae^{-2k}+2ake^{-2k} \\ & \left.\left.+2\beta dk^2e^{-2k}+\beta fk^2e^{-3k}+2bke^{-2k}\right]-\beta^2(f+de^{k})^2e^{-3k}\right\}. \end{aligned} \tag{A.1}$$

The MSA static structure factor is given in the zero-q limit by $S_{\mathrm{MSA}}(q\to 0)=a^{-2}$, and for arbitrary q by $S_{\mathrm{MSA}}(q)=\left[X_A^2+X_B^2\right]^{-1}$, with coefficients

$$\begin{aligned}
X_A &= 1-12\phi\left[a\frac{q\cos(q)-\sin(q)}{q^3}+b\frac{\cos(q)-1}{q^2}\right.\\
&\quad\left.+\beta d\frac{\sin(q)}{q}+\frac{\beta bf}{b^2+q^2}+\beta d\frac{b\cos(q)-q\sin(q)}{b^2+q^2}\right], \qquad (A.2)\\
X_B &= -12\phi\left[a\frac{q\sin(q)+\cos(q)-1-\frac{1}{2}q^2}{q^3}+b\frac{\sin(q)-q}{q^2}\right.\\
&\quad\left.+\beta d\frac{1-\cos(q)}{q}+\frac{\beta qf}{b^2+q^2}+\beta d\frac{b\sin(q)+q\cos(q)}{b^2+q^2}\right], \qquad (A.3)\\
a &= \frac{1+2\phi+\frac{12\phi\beta}{k}\times\left\{\left[1+2\phi-\frac{6\phi}{k}\right]\times[-f-d(1+k)]+3d\phi k\right\}}{(1-\phi)^2}, \qquad (A.4)\\
-b &= \frac{\frac{3}{2}\phi+\frac{12\phi\beta}{k}\times\left\{\left[\frac{3}{2}\phi+\frac{1-4\phi}{k}\right]\times[-f-d(1+k)]-\frac{kd}{2}\times(1-4\phi)\right\}}{(1-\phi)^2}, \qquad (A.5)\\
d &= \frac{(\beta D-K)e^{-k}+\beta^2E}{\beta^2F}, \qquad (A.6)\\
f &= \frac{6\phi}{F}\left[2-e^{-k}\right]-\frac{S\delta}{F}[\tau(1+k)-3\phi k]\\
&\quad+\frac{T\delta}{F}\left[\rho(1+k)+k(\frac{1}{2}-2\phi)\right]+\frac{K-\beta D}{\beta^2F}, \qquad (A.7)\\
\delta &= \frac{12\phi}{k(1-\phi)^2}, \qquad \tau=1+2\phi-\frac{6\phi}{k}, \qquad \rho=\frac{3}{2}\phi+\frac{1-4\phi}{k}, \qquad (A.8)\\
K &= -\gamma e^{-k}, \qquad T=\frac{12\phi}{k}\times\left[1-k-e^{-k}\right], \qquad (A.9)\\
S &= \frac{12\phi}{k^2}\times\left[1-\frac{k^2}{2}-(1+k)e^{-k}\right], \qquad (A.10)\\
F &= \delta\times\left\{S\times\left[\left(1+2\phi-\frac{6\phi}{k}\right)\times\left(1-(1+k)e^{-k}\right)+3\phi ke^{-k}\right]\right.\\
&\quad\left.-T\times\left[\left(\frac{3\phi}{2}+\frac{1-4\phi}{k}\right)\times\left(1-(1+k)e^{-k}\right)-\frac{1}{2}(1-4\phi)ke^{-k}\right]\right\}\\
&\quad-6\phi(1-e^{-k})^2, \qquad (A.11)
\end{aligned}$$

$$E = -6\phi + S\delta \times \left[1 + 2\phi - \frac{6\phi}{k}\right] - T\delta \times \left[\frac{3\phi}{2} + \frac{1-4\phi}{k}\right], \tag{A.12}$$

$$D = k - \frac{S(1+2\phi)}{(1-\phi)^2} + \frac{3T\phi}{2(1-\phi)^2}, \tag{A.13}$$

$$X = 6\phi \left\{ ke^{-k} - \frac{6\phi}{(1-\phi)k^2} \times \left[2 - 2k - (2-k^2)e^{-k}\right] - \frac{18\phi^2}{k^2(1-\phi)^2} \times \left[2 - k - (2+k)e^{-k}\right] \right\}, \tag{A.14}$$

$$Y = k - \frac{6\phi}{k^2(1-\phi)} \times \left[2 - k^2 - 2(1+k)e^{-k}\right] - \frac{18\phi^2}{k^2(1-\phi)^2} \times \left[2 - k - (2+k)e^{-k}\right]. \tag{A.15}$$

In Eqs. (A.1)-(A.15), ϕ, γ and k are the volume fraction and HSY coupling- and screening parameters, as defined in Eqs. (2.5).

Finally, β is the only root of the quartic equation,

$$36\phi^2\beta^4 - X\beta^3 + 12\phi K\beta^2 - KY\beta + K^2 = 0, \tag{A.16}$$

that vanishes when the double limit $K \to 0$ and $\phi \to 0$ is taken. The closed analytic form of this root, used in the combined microstructure and dynamics solver described in Appendix E, can be easily obtained using a computer algebra software such as MAPLE®, but is too lengthy to be displayed here. To identify the physical root, it is helpful to employ the low-ϕ expansions of the four roots of Eq. (A.16), given in Ref. [113]. Note that in the notation of Ref. [113], ξ equals the HSY screening parameter k, and η denotes the volume fraction ϕ.

An alternative, but computationally less efficient way to determine the physical root β of Eq. (A.16), was suggested in Ref. [269]. This method consists of calculating the MSA solutions for $S(q)$ using all four roots of (A.16), Fourier-transforming into the respective $g(r)$'s, and selecting the unique physical solution as the only one for which $g(r)$ vanishes inside the hard-core overlap region $r < \sigma$.

APPENDIX

B

MPB-RMSA algorithm

Here, we describe the algorithm of our MPB-RMSA code based on the analytic MSA solution for $S(q)$, and the contact value $g(\sigma^+)$ of the HSY model given in Appendix A.

- Step 1:
  Specify input parameters $[\sigma,\gamma,k,\phi]$ of the considered repulsive HSY system. For charged colloids one may use Eqs. (2.5a) and (2.5b) for γ and k. Select tolerance $1 \gg \mathrm{TOL} > 0$ in Gillan criterion $|g(x'=1^+)| < \mathrm{TOL}$.

- Step 2:
  Calculate:
  $k_{\mathrm{mod}} = k\sqrt{1-\phi}$,
  $\gamma_{\mathrm{mod}} = \gamma \ \exp(k_{\mathrm{mod}}-k)\left(\dfrac{1+k/2}{1+k_{\mathrm{mod}}/2}\right)^2$.

- Step 3:
  Assign:
  $k^* = k_{\mathrm{mod}} - 2\phi^{1/3}\log(1-\phi)$,
  $\gamma^* = \gamma_{\mathrm{mod}}(1-\phi)^{-2}$.
  Determine $g_{\mathrm{MSA}}(x=1^+)$, with $x = r/\sigma$, using parameters $[\sigma,\gamma^*,k^*,\phi]$.
  If $g_{\mathrm{MSA}}(x=1^+)<0$, select s from $(0,1)$ and continue with step 4.
  Otherwise assign $\sigma^*=\sigma$ and $\phi^*=\phi$, then go to step 6

- Step 4:
  Assign:
  $x' = xs$,
  $\sigma^* = \sigma' = \sigma s^{-1}$,
  $\phi^* = \phi' = \phi s^{-3}$,
  $\gamma^* = \gamma'(1-\phi')^{-2} = \gamma_{\mathrm{mod}} s(1-\phi')^{-2}$,

$k' = k_{\mathrm{mod}} s^{-1}$,
$k^* = k' - 2\phi'^{1/3}\log(1-\phi')$.

- `Step 5:`
  `Determine` $g_{\mathrm{MSA}}(x' = 1^+)$ `for input parameters` $[\sigma^*, \gamma^*, k^*, \phi^*]$.
  `If` $|g_{\mathrm{MSA}}(x' = 1^+)| <$`TOL, go to step 6.`
  `Otherwise select` s `from` $(0,1)$ `and go to step 4.`
  `The new selection for` s `is made by a Newton-Raphson type algorithm, on accounting for previously obtained MSA contact values.`

- `Step 6:`
  `Calculate` $S_{\mathrm{MSA}}(q)$ `in given range` $0 \le q \le q_{max}$ `using input parameters` $[\sigma^*, \gamma^*, k^*, \phi^*]$, *i.e.* $S_{\text{MPB-RMSA}}(q) = S_{\mathrm{MSA}}(q; \sigma^*, \gamma^*, k^*, \phi^*)$. `The rdf follows numerically by a fast Fourier transform.`

If step 2 is replaced by $k_{\mathrm{mod}} = k$ and $\gamma_{\mathrm{mod}} = \gamma$, the original PB-RMSA scheme by Snook and Hayter [97] is recovered. In summary, the modification of the PB-RMSA simply consists of replacing the HSY input parameters (γ, k, ϕ) by $(\gamma_{\mathrm{mod}}, k_{\mathrm{mod}}, \phi)$.

If the first two instructions in step 3 are replaced by $k^* = k_{\mathrm{mod}} = k$ and $\gamma^* = \gamma_{\mathrm{mod}} = \gamma$, the RMSA scheme by Hansen and Hayter [98] is recovered, which, in turn, reduces to the MSA if a very large value, TOL$\to \infty$, for the tolerance in the Gillan criterion is chosen.

To obtain the rdf in MPB-RMSA, do not use Eq. (3.4) since the integrand decays slowly in q, making the integral quite sensitive to the selected cutoff wavenumber q_{max}. Instead, we suggest to use

$$g(r) = 1 + c(r) + \frac{1}{2\pi^2 r}\int_0^\infty dq\, q \sin(qr)\, \frac{(S(q)-1)^2}{S(q)}, \tag{B.1}$$

which has a faster decaying integrand. On the right-hand-side of Eq. (B.1), $S(q) = S_{\text{MPB-RMSA}}(q)$ and $c(r > \sigma^*) = -\beta u^*(r)$, where $u^*(r) = u(r; \sigma^*, \gamma^*, k^*, \phi^*)$ and σ^* is the MPB-RMSA rescaled diameter. The MPB-RMSA code with TOL$= 10^{-4}$ requires in general less than 10 iterations to determine the rescaling parameter s. The execution time on a standard PC is less than 0.1 seconds, for both $S(q)$ and $g(r)$ determined on a grid with 10^4 points.

APPENDIX

C

PA-scheme mobility coefficients

For completeness, and to allow for a convenient implementation of the PA-scheme by an interested user, we list here the PA-scheme mobility coefficients used in our work. The tables given here provide only an excerpt of available two-sphere mobilities in Stokes flow. A comprehensive textbook with tables and recursion formulas for two-body mobility and friction coefficients is Ref. [160].

Far-field mobility expressions

The two-body mobility components $x^a_{ij}(x)$ and $y^a_{ij}(x)$ in Eq. (4.9) can be analytically expanded as

$$x^a_{ij}(x) = \delta_{ij} + \sum_{n=1}^{\infty} x^{a\,(n)}_{ij} x^{-n}, \qquad y^a_{ij}(x) = \delta_{ij} + \sum_{n=1}^{\infty} y^{a\,(n)}_{ij} x^{-n}, \qquad i,j \in \{1,2\}, \tag{C.1}$$

where $x = r/\sigma$ is the separation centers of two isolated particles in units of the sphere diameter σ. The expansion coefficients $x^{a\,(n)}_{ij}$ and $y^{a\,(n)}_{ij}$ can be calculated using recursion formulas and are tabulated in Ref. [159]. Note that in Ref. [159], the expansion was carried out in powers of $2/x = 2r/\sigma$ instead of $1/x$, and a normalization factor different from the present one was used. In Tab. C.1, we give the coefficients $x^{a\,(n)}_{ij}$ and $y^{a\,(n)}_{ij}$, in the normalization used throughout the present work. The coefficients in columns 1, 2, 3, and 4 of Tab. C.1 are equal to the respective coefficients, $c_{(n)}$, listed in the first column (denoted Model a) of Tabs. I, XII, II, and XIII in Ref. [159], multiplied by $3/2 \times (1/2)^n$.

A corresponding $1/x$ expansion is available also for the two-body shear-mobility function $J(x)$. The corresponding expansion coefficients x^m_1, y^m_1, and z^m_1, with $J(x) = 1/5(x^m_1 + 2y^m_1 + 2z^m_1) - 1$, can be extracted, *e.g.*, from Refs. [161–163]. The function $J(x)$ decays more quickly with increasing x than $x^a_{ij}(x)$ and $y^a_{ij}(x)$, so that the leading-order far-field form for $J(x)$ becomes a good approximation already for $x \gtrsim 1.2$ (*c.f.*, Fig. 4.3). In our implementation of the

Tab. C.1: *Translational mobility coefficients $x_{ij}^a(x)$ and $y_{ij}^a(x)$ in Eq. (C.1), up to $\mathcal{O}(x^{-20})$. Values are taken from Ref. [159], but the expansion is carried out in powers of $1/x = r/\sigma$, and a normalization different from the one in [159] is used.*

n	$x_{11}^{a\,(n)} \times 10^2$	$x_{12}^{a\,(n)} \times 10^2$	$y_{11}^{a\,(n)} \times 10^2$	$y_{12}^{a\,(n)} \times 10^2$
1	0	75	0	37.50
2	0	0	0	0
3	0	-12.51	0	6.249
4	-23.44	0	0	0
5	0	0	0	0
6	8.595	0	-1.660	0
7	0	14.65	0	0
8	4.102	0	-0.4883	0
9	0	-1.465	0	0
10	-8.155	0	-0.4211	0
11	0	-4.797	0	0.2163
12	-2.695	0	-0.3783	0
13	0	2.082	0	0.2745
14	1.758	0	-0.2628	0
15	0	2.094	0	0.2404
16	-0.2275	0	-0.1706	0
17	0	0.01674	0	0.1579
18	-0.6529	0	-0.1277	0
19	0	0.6128	0	0.09072
20	0.3340	0	-0.1150	0

PA scheme, we therefore use $J(x) \approx 15/128x^{-6}$ for $x > 3$, together with accurate numerical tables by Jeffrey for $x \leq 3$. The values from these numerical tables cross over continuously from the far-field expression to the near-field expression.

Near-contact mobility expressions

At near-contact distances $\chi = x - 1 \gtrsim 0$, where lubrication effects become influential in systems with hydrodynamic stick boundary conditions, the expansions in Eq. (C.1) are slowly convergent. Jeffrey [158, 273] has provided the analytic expressions

$$x_{ij}^a(\chi) = k_{ij}^{a\,(1)} + k_{ij}^{a\,(2)}\chi + k_{ij}^{a\,(3)}\chi^2 \ln(2\chi) + k_{ij}^{a\,(4)}\chi^2 + \mathcal{O}(\chi^3(\ln\chi)^2), \tag{C.2a}$$

$$y_{ij}^a(\chi) = \frac{l_{ij}^{a\,(1)}\{\ln[1/(2\chi)]\}^2 + l_{ij}^{a\,(2)}\ln[1/(2\chi)] + l_{ij}^{a\,(3)}}{\{\ln[1/(2\chi)]\}^2 + m^{(1)}\ln[1/(2\chi)] + m^{(2)}} + \mathcal{O}(\chi(\ln\chi)^3), \tag{C.2b}$$

Tab. C.2: *Coefficients of the near-contact two-body mobility components in Eqs.* (C.2)*, taken from Ref. [158], and of the near-contact two-body shear-mobility function components in Eqs.* (C.3)*, taken from Ref. [160]. Note that, different from Eqs.* (C.2) *and* (C.3)*, in Refs. [158] and [160], the near-contact mobilities are given as functions of* $\xi = 2r/\sigma - 1 = 2\chi$

n	$k_{11}^{a\,(n)}$	$k_{12}^{a\,(n)}$	$l_{11}^{a\,(n)}$	$l_{12}^{a\,(n)}$	$l_1^{m(n)}$	$n_1^{m(n)}$	$k_1^{m(n)}$	$m^{(n)}$
1	0.7750	0.7750	0.891	0.489	1.1456	0.9527	1.910	6.0425
2	1.86	-2.140	5.77	2.81	6.1694	0.1828	-7.7	6.3255
3	3.60	-3.60	7.07	1.98	3.7112	-0.324		
4	-8.0	8.0						

for the mobility coefficients, which are accurate for small values of χ. The coefficients $k_{ij}^{(n)}$, $l_{ij}^{(n)}$, and $m^{(n)}$ are given in Ref. [158] for various diameter ratios in the two-sphere problem. Note that in Ref. [158] the near-contact mobilities are given as functions of $\xi = 2r/\sigma - 2 = 2\chi$. In Tab. C.2, we list the $k_{ij}^{(n)}$, $l_{ij}^{(n)}$, and $m^{(n)}$, for spheres of equal diameters, in the normalization used throughout the present work.

Similar near-field expressions exist for the two-body shear-mobility function $J(\chi) = 1/5[x_1^m(\chi) + 2y_1^m(\chi) + 2z_1^m(\chi)] - 1$, with

$$x_1^m(\chi) = k_1^{m(1)} + k_1^{m(2)}\chi \tag{C.3a}$$

$$y_1^m(\chi) = \frac{l_1^{m(1)}\{\ln[1/(2\chi)]\}^2 + l_1^{m(2)}\ln[1/(2\chi)] + l_1^{m(3)}}{\{\ln[1/(2\chi)]\}^2 + m^{(1)}\ln[1/(2\chi)] + m^{(2)}} + \mathcal{O}(\chi(\ln\chi)^3), \tag{C.3b}$$

$$z_1^m(\chi) = n_1^{m(1)} + n_1^{m(2)}\chi + n_1^{m(3)}\chi^3, \tag{C.3c}$$

and coefficients according to [160] listed in Tab. C.2.

APPENDIX

D

$\delta\gamma$-scheme coefficients

We give here the explicit expression for the function S_{γ_0} needed in calculating the self-diffusion coefficient, the hydrodynamic function, and the high-frequency limiting viscosity in the $\delta\gamma$ scheme. The function S_{γ_0}, introduced by Beenakker and Mazur in their original papers on the $\delta\gamma$ scheme [28, 168], is given by the infinite series,

$$S_{\gamma_0}(q) = C(q) + \sum_{p=2}^{\infty} \frac{9}{4}\pi\varepsilon_p(\gamma_0^{(p)} - n)n^{-1}(2p-1)^2 q^{-3} J^2_{p-1/2}(q), \tag{D.1}$$

where J_n denotes the Bessel function of the first kind and order n, $\varepsilon_p = 5/9$ for $p = 2$, and $\varepsilon_p = 1$ for $p > 2$. The function $C(q)$ is given by

$$C(q) = \frac{9}{2}\left(\frac{\mathrm{Si}(2q)}{q} + \frac{\cos(2q)}{2q^2} + \frac{\sin(2q)}{4q^3} - \frac{\sin^2(q)}{q^4} - \frac{4[\sin(q) - q\cos(q)]^2}{q^6}\right), \tag{D.2}$$

with $\mathrm{Si}(x) = \int_0^x \sin(y)/y \, \mathrm{d}y$. The coefficients $\gamma_0^{(p)} = n + \mathcal{O}(\phi^2)$ are determined from the infinite set of recursive relations

$$\gamma_0^{(p)} - \gamma_0^{(p)}\phi(2p-1)\int_0^{\infty} \frac{dq}{q} J^2_{p-1/2}(q) \frac{S_{\gamma_0}(q)}{1 + \phi S_{\gamma_0}(q)} = n, \qquad p = 2, 3, \ldots. \tag{D.3}$$

When truncated at an upper index $p_{\max}$, Eqs. (D.1) and (D.3) can be iterated numerically until convergence is achieved for $\gamma_0^{(p)}$, and $p = 2 \ldots p_{\max}$. As a zeroth iteration seed, all coefficients $\gamma_0^{(p)}$ are set equal to the colloid number concentration n. Note that the volume fraction ϕ enters explicitly into Eq. (D.3). To achieve convergence of the truncated series iteration for larger values of ϕ, it helps to increase ϕ in small steps starting from a value close to zero, and to use the converged values of the coefficients $\gamma_0^{(p)}$ as zeroth iteration seeds for each next-

Tab. D.1: *Coefficients $\gamma_0^{(p)}/n$, obtained from Eqs. (D.1) and (D.3), truncated at $p_{max} = 10$, and numerically solved by iteration. In Tab. 1 of Ref. [28], slightly different results are listed, obtained for $p_{max} = 5$.*

ϕ	$\gamma_0^{(p)}/n$ p = 2	p = 3	p = 4	p = 5	p = 6	p = 7	p = 8	p = 9	p = 10
0.05	1.1059	1.0842	1.0653	1.0514	1.0420	1.0354	1.0306	1.0269	1.0239
0.10	1.2279	1.1781	1.1364	1.1066	1.0864	1.0725	1.0623	1.0545	1.0484
0.15	1.3670	1.2818	1.2133	1.1653	1.1333	1.1111	1.0952	1.0830	1.0733
0.20	1.5242	1.3957	1.2961	1.2276	1.1825	1.1516	1.1292	1.1122	1.0987
0.25	1.7003	1.5195	1.3845	1.2936	1.2342	1.1937	1.1644	1.1422	1.1246
0.30	1.8952	1.6530	1.4785	1.3629	1.2881	1.2373	1.2007	1.1730	1.1510
0.35	2.1083	1.7956	1.5776	1.4356	1.3443	1.2825	1.2381	1.2045	1.1778
0.40	2.3383	1.9464	1.6813	1.5113	1.4026	1.3292	1.2766	1.2368	1.2052
0.45	2.5835	2.1043	1.7892	1.5897	1.4629	1.3773	1.3161	1.2698	1.2330

higher volume fraction. In this way, we have calculated the coefficients $\gamma_0^{(p)}$ with truncations at $p_{\max} = 5$, 10, and 15. The results for $p_{\max} = 10$, listed in Tab. D.1 differ from the results for $p_{\max} = 5$ and $p_{\max} = 15$ by no more than 3% and 0.3%, respectively. In our implementation of the (self-part corrected) $\delta\gamma$ scheme, the software described in Appendix E interpolates the values of the coefficients $\gamma_0^{(p)}$ at arbitrary ϕ using Tab. D.1. We have checked that the values for each of the short-time properties $d_s/d_{t,0}$, $H(q)$, and η_∞, expressed in the $\delta\gamma$ scheme as integrals comprising the coefficients $\gamma_0^{(p)}$ and the static structure factor $S(q)$, show only very slight dependencies on the truncation index $p_{\max}$, provided that $p_{\max} > 5$. For all practical purposes, it is therefore sufficient to use Tab. D.1, or even Tab. 1 of Ref. [28], for $p_{\max} = 5$.

APPENDIX

E

An integrated software for structure and dynamics of colloidal suspensions

A very useful ingredient in the present thesis has been the development of a new software for computing the structure and dynamics of hard-sphere Yukawa-like colloids. Using the programming language C in combination with the GNU scientific library (GSL) and the Gimp Toolkit (GTK+), the software has been implemented with a graphical user interface (GUI), that allows quick and convenient operation. Two snapshots of the GUI are displayed in Fig. E.1. The GSL and the GTK+ are available for free download under the GNU Public License at the websites in Refs. [274, 275]. The source code of our software is kept in a modular structure, allowing for a rather straightforward extension. At the current stage of on-going development, the software includes modules for the computation of:

- PY, MSA, RMSA, PB-RMSA and MPB-RMSA structure factors $S(q)$ and rdf's $g(r)$ for colloidal spheres interacting by the HSY pair-potential in Eq. (2.6),
- Static scattered intensities $I(q)$, obtained from combining any of the above solutions for $S(q)$ with the form factor, $P(q)$, of monodisperse spheres, spheres with size-polydispersity, monodisperse or polydisperse ellipsoids of revolution, or core-shell particles. For non-spherical or polydisperse particles, $I(q)$ is calculated in the decoupling approximation described in Section 3.5,
- High-frequency viscosities η_∞, the short-time diffusion coefficients d_s and d_c, and the functions $H(q)$ and $D(q)$, in an adjustable q-range. These short-time properties can be calculated using the PA-, $\delta\gamma$-, or self-part corrected $\delta\gamma$-schemes. In the PA-solution for $H(q)$ and $D(q)$, one can select between the pair-mobility coefficients for impermeable spheres with hydrodynamic stick boundaries listed in Appendix C, and far-field pair mobilities, so far up to $\mathcal{O}(x^{-7})$ [261], for uniformly solvent-permeable spheres,

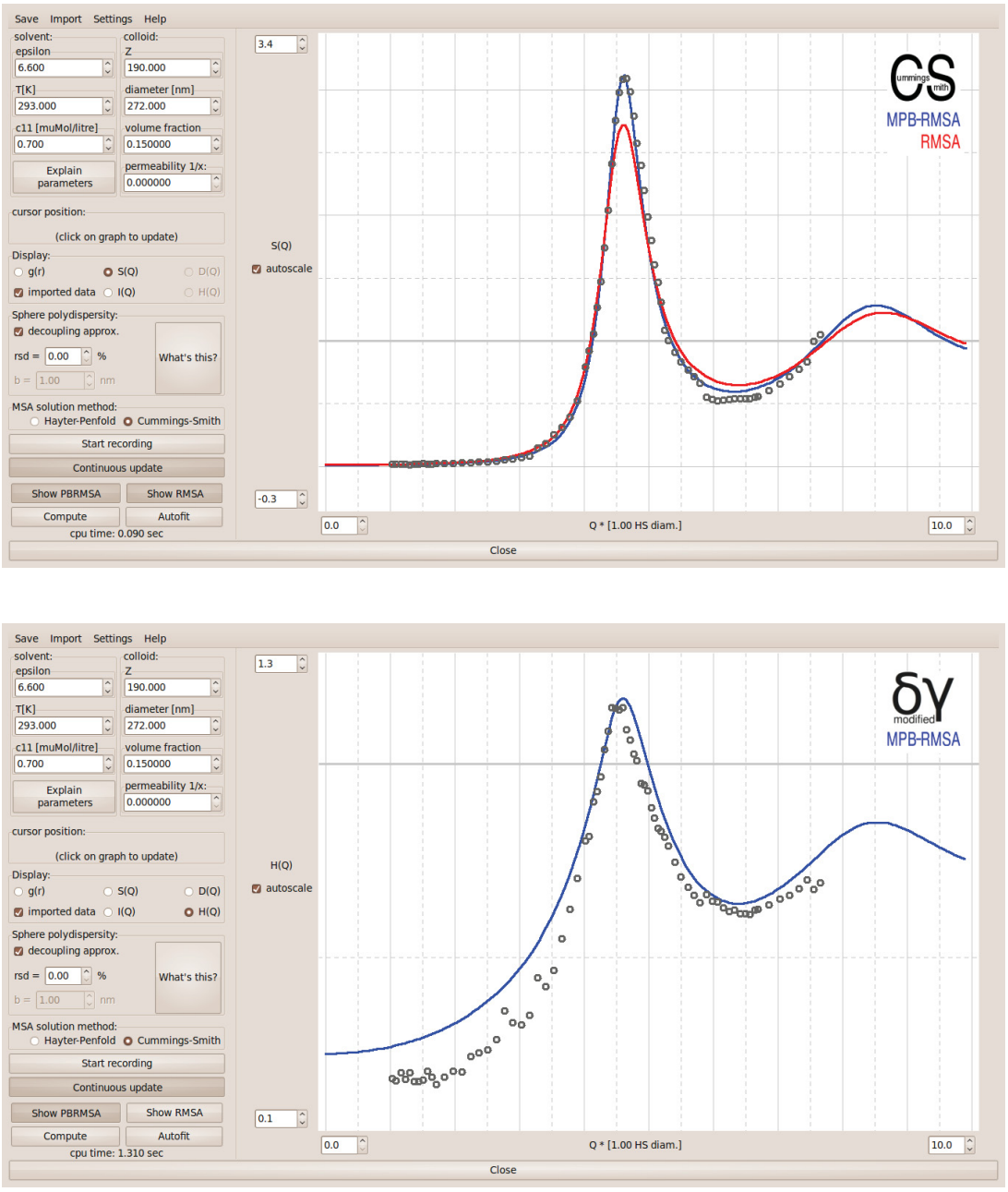

Fig. E.1: *Snapshots of the combined microstructure and dynamics solver. Top: Imported static light scattering data for $S(q)$ of charged silica spheres (Symbols) and fitted MPB-RMSA result (blue line). For comparison, $S(q)$ computed in RMSA for the same input parameters is displayed (red line). Bottom: Hydrodynamic function, $H(q)$, for the same system. Symbols: imported dynamic light scattering data. Blue line: $H(q)$ calculated by the self-part corrected $\delta\gamma$ scheme.*

- Long-time self-diffusion coefficients d_s^L, and the static viscosity η, using the simplified MCT expressions given in Section 4.5.

The functions $g(r)$, $S(q)$, $I(q)$, $H(q)$ and $D(q)$ are computed on user-defined meshes of r- and q-values. After entering the parameters of the HSY potential into the GUI, the computation times needed to generate $g(r)$, $S(q)$ and $I(q)$ is in the order of 0.1 sec. If $H(q)$ and $D(q)$ are additionally required, the computation time increases to about 1 sec. User-provided ASCII tables for each of the above functions can be imported and displayed in comparison with the computed functions, allowing for convenient real-time fitting of static and dynamic scattering data.

The software contains a weighted-least squares minimizer based on the Nelder-Mead downhill simplex method [276], which allows for an automatic fitting of $g(r)$, $S(q)$, and $I(q)$. An extension of the automatic fit to $H(q)$ and $D(q)$ could be easily implemented.

The static input $g(r)$ and $S(q)$ for the PA-, $\delta\gamma$-, and corrected $\delta\gamma$-schemes can be either computed in (M)(PB)-(R)MSA, or taken from user-provided tables. In this way, it is possible to compute short-time dynamic properties based on static microstructure input from different integral equation schemes like, *e.g*, the RY or HNC schemes, or from computer simulations. Since the imported microstructure functions need not necessarily correspond to systems of repulsive HSY-particles, the software can be applied to compute the short-time dynamics for particles with various types of pair-potentials, including, *e.g.*, attractive pair-interactions parts.

INDEX

Abbreviations .....

AFM ..... Atomic force microscopy, page 17

ASD ..... Accelerated Stokesian Dynamics simulations, Ref. [24], page 54

BSA ..... Bovine serum albumin (a globular protein), page 14

CCY ..... Circular cylinder-Yukawa model used for gibbsite platelets, page 90

CS-1 ..... A charged-sphere system with parameters $L_B = 5.617$ nm, $\sigma = 200$ nm, and $Z = 100$, page 105

CS-2 ..... A charged-sphere system with parameters $L_B = 0.71$ nm, $\sigma = 50$ nm, and $Z = 70$, page 105

DDLS ..... Depolarized dynamic light scattering, page 18

DLVO ..... Derjaguin-Landau-Verwey-Overbeek pair potential, Ref. [3], page 7

DMSO ..... Dimethyl sulfoxide, page 17

HIs ..... Hydrodynamic interactions, page 12

HNC ..... Hypernetted chain closure for the OZ equation, Ref. [99], page 23

HS ..... Neutral, non overlapping hard spheres with hydrodynamic stick boundaries, page 36

HSY ..... Hard-sphere Yukawa, page 10

I/LC ..... Isotropic-liquid crystal transition of gibbsite platelets, page 19

IACF ..... Intensity autocorrelation function, page 16

KWW ..... Kohlrausch-Williams-Watt stretched exponential, Refs. [249–251], page 133

lhs ..... Left hand side, page 130

MC ..... Monte Carlo, page 27

MCT ..... Mode-coupling theory of Brownian systems, Refs. [4, 177, 178], page 57

MPB-MSA ..... Special case of the MPB-RMSA when no hard-core rescaling is required, *i.e.* when $s = 1$, page 35

MPB-RMSA ..... Modified Penetrating Background corrected Rescaled Mean Spherical Approximation, Refs. [14, 15], page 27

MSA ..... Mean Spherical Approximation, Ref. [4], page 26

OCP ..... One component plasma, page 30

OMF ..... One-component macroion fluid, page 7

OZ ..... Ornstein-Zernike equation, Ref. [4], page 25

PB ..... Penetrating background of microions, assumed in the construction of the (M)PB-RMSA, page 30

PB-MSA ..... Special case of the PB-RMSA where no hard-core rescaling is required, *i.e.* when $s = 1$, page 33

PB-RMSA ..... Penetrating Background corrected Rescaled Mean Spherical Approximation, Ref. [97], page 27

PY ..... Percus-Yevick closure for the OZ equation, Ref. [121], page 30

rdf ..... Radial distribution function $g(r)$, Ref. [4], page 24

RMSA ..... Rescaled Mean Spherical Approximation, Ref. [98], page 27

RP ..... Rotne-Prager dipolar $\mathcal{O}(x^{-3})$ approximation of two-body HIs., page 53

RY ..... Rogers-Young closure for the OZ equation, Ref. [100], page 23

SAXS ..... Small angle X-ray scattering, page 12

SLS ..... Static light scattering, page 12

SY ..... Spheroid-Yukawa model used for BSA proteins, page 84

TEM ..... Transmission electron micrograph, page 11

TPM ..... Trimethoxysilylpropyl methacrylate, page 11

VH ..... Light scattering geometry with vertically aligned polarizer and horizontally aligned analyzer, page 18

VU ..... Light scattering geometry with vertically aligned polarizer, without analyzer, page 19

VV ..... Light scattering geometry with vertically aligned polarizer and vertically aligned analyzer, page 18

Greek Symbols .....

β ..... $\beta = 1/k_B T$ with absolute temperature T and Boltzmann constant k_B, page 8

χ ..... $\chi = x - 1$: dimensionless separation of sphere surfaces, page 48

Δ ..... Lower cutoff distance (in units of σ) for u_{vdW}, modeling Born repulsion, page 8

$\delta\gamma$ scheme ..... Renormalized concentration fluctuation expansion method of Beenakker and Mazur, Refs. [28, 29], page 51

ε ..... Solvent dielectric constant, page 8

η_0 ..... Shear viscosity of the suspending Newtonian solvent, page 43

γ ..... Coupling parameter of u_{HSY} and u_{el}, page 8

Ω ..... Solid angle, page 39

ϕ ..... Fraction of the suspension volume occupied by colloidal particles, page 8

ρ ..... Volume-averaged mass density of a colloidal sphere, page 44

ρ_S ..... Mass density of the suspending solvent, page 43

σ ..... Colloidal hard-core diameter, page 8

τ_B ..... $\tau_B = m/(3\pi\eta_0\sigma)$: momentum relaxation time of a Brownian particle, Refs. [21, 22], page 43

τ_H ..... $\tau_H = \sigma^2\rho_S/(4\eta_0)$: time scale of hydrodynamic vorticity diffusion across a diameter σ Refs. [21, 22], page 43

τ_I ..... $\tau_I = \sigma^2/(4d_{t,0})$: interaction time, during which a Brownian particle diffuses a distance comparable to its own diameter, Refs. [21, 22], page 43

$\tilde{\gamma}$ ..... $\tilde{\gamma} = \gamma\sigma/\tilde{d}$: reduced coupling parameter of u_{HSY} and u_{el}, used for systems with no direct hard-core contact, page 25

μ_0 ..... $\mu_0 = 1/(3\pi\eta_0\sigma)$: mobility of a single sphere with stick hydrodynamic boundary conditions, page 44

$\mu_{lj}^{dd}(\mathbf{r}^N)$ ..... Dipole-dipole mobility tensor, linearly relating the symmetric hydrodynamic force dipole moment tensor of sphere l to the rate of strain tensor related to sphere j, page 46

$\mu_{lj}^{tt}(\mathbf{r}^N)$ ..... Translational mobility tensor, linearly relating the hydrodynamic force on a sphere j to the translational velocity of a sphere l, page 44

Roman Symbols ...

$\lim_\infty$ ..... Thermodynamic limit $N \to \infty$ and $V \to \infty$, with $n = N/V$ fixed, page 24

$\mathbf{r}^N$ ..... $3 \times N$ center-of-mass coordinates of all colloidal particles in the system, page 23

$\mathbf{r}_l^\gamma$ ..... Center-of-mass position of the l-th particle of species γ, page 39

$\mathbf{r}_n(t)$ ..... The position vector pointing to the center of the n-th colloidal particle at time t, page 43

$\tilde{d}$ ..... $\tilde{d} = n^{-1/3}$: mean geometric distance of the colloid particle centers, page 25

$\tilde{f}_\gamma(\mathbf{q},\Omega)$ ..... $\tilde{f}_\gamma(\mathbf{q},\Omega) = v_\gamma^{-1} f_\gamma(\mathbf{q},\Omega)$: form amplitude for particles of species γ, page 39

$\tilde{k}$ ..... $\tilde{k} = k\tilde{d}/\sigma$: reduced screening parameter of u_{HSY} and u_{el}, used for systems with no direct hard-core contact, page 25

$\tilde{T}$ ..... $\tilde{T} = k_{\mathrm{B}}T/u(r = \tilde{d})$: a reduced temperature, in units of the pair-energy at mean geometric distance, page 71

$\tilde{x}$ ..... $\tilde{x} = r/\tilde{d}$: dimensionless separation of colloid centers in units of the mean geometric distance, page 25

$\tilde{y}$ ..... $\tilde{y} = q\tilde{d}$: dimensionless wavenumber in units of the inverse mean geometric distance, page 71

a ..... Semi-axis of revolution of the oblate BSA model spheroid, page 82

A_{H} ..... Hamaker constant in units of k_BT, entering linearly in u_{vdW}, page 8

b ..... Radius of the oblate BSA model spheroid, page 82

$c(r)$ ..... Direct correlation function, Ref. [4], page 25

c_p ..... Protein mass concentration, *i.e.* unit mass of dissolved protein per unit solution volume, page 15

$D(q)$ ..... Short-time diffusion function, Refs. [21, 22, 153], page 43

D_c ..... Experimental ϕ-dependent diffusion coefficient associated to the fast-mode in the decay of the IACF for gibbsite platelets, recorded in VU geometry. D_c is interpreted as a collective diffusion coefficient., page 136

d_c ..... $d_c = D(q \to 0)$: ϕ-dependent short-time collective diffusion coefficient, page 46

d_c^L ..... ϕ-dependent long-time collective diffusion coefficient, page 117

d_r ..... ϕ-dependent short-time rotational self-diffusion coefficient of spheres, page 139

$D_r^{\perp}$ ..... Experimental ϕ-dependent end-over-end tumbling rotational diffusion coefficient measured for gibbsite platelets at low scattering wavenumber q, page 135

d_s ..... ϕ-dependent short-time translational self-diffusion coefficient of spheres, page 44

D_t ..... Experimental ϕ-dependent translational diffusion coefficient measured for gibbsite platelets at low scattering wavenumber q. D_t is interpreted as a long-time self-diffusion coefficient, page 135

d_{cge} ..... $d_{\mathrm{cge}} = D(q_m)$: ϕ-dependent short-time cage diffusion coefficient, page 46

$d_{r,0}$ ..... $d_{r,0} = k_BT/(\pi\eta_0\sigma^3)$: rotational free diffusion coefficient of spheres with stick hydrodynamic boundary conditions, page 92

$d_{r,0}^{\parallel}$ ..... Rotational free diffusion coefficient for rotation around the particle's rotational symmetry axis, page 92

$d_{r,0}^{\perp}$ ..... End-over-end tumbling rotational free diffusion coefficient, page 92

$d_{t,0}$ ..... $d_{t,0} = k_BT/(3\pi\eta_0\sigma)$: translational free diffusion coefficient of spheres for stick hydrodynamic boundary conditions, page 43

e ..... Proton elementary charge, page 8

g ..... Gravitational acceleration, page 44

$g(r)$ ..... Radial distribution function, Ref. [4], page 25

$H(q)$ ..... $H(q) = D(q)S(q)$: hydrodynamic function, Ref. [22], page 44

$h(r)$ ..... $h(r) = g(r) - 1$: total correlation function, Ref. [4], page 25

$H^d(q)$ ..... Distinct part of the hydrodynamic function, page 44

K ..... $K = U_{\text{sed}}/U_0 = \lim_{q\to 0} H(q)$: sedimentation coefficient., page 44

k ..... Screening parameter of u_{HSY} and u_{el}, page 8

k_{c} ..... Surface-released counterion contribution to the screening parameter k, page 9

k_{s} ..... Contribution to the screening parameter k caused by all microions excluding the surface-released counterions, page 9

k_B ..... Boltzmann constant, page 8

L_{B} ..... $L_{\text{B}} = \beta e^2/\varepsilon$: solvent-characteristic Bjerrum length, page 8

m ..... Mass of a single colloidal sphere, page 43

N ..... $N = \sum_\gamma N_\gamma$: total number of particles in the scattering volume or an ensemble average, page 39

n ..... $n = N/V$: mean number concentration of colloids, page 8

N_γ ..... Number of particles of species γ in the scattering volume or an ensemble average, page 39

n_{s} ..... Number concentration of added monovalent coions such as salt, page 8

N_s ..... Number of particle species, differing in (pair) interaction potential or scattering amplitudes, page 39

p ..... Aspect ratio of a colloidal particle, *i.e.*, the ratio of the lengths of the shortest and longest principal axes, page 20

$P_m(q)$ ..... Measurable form factor in decoupling approximation, page 40

P_S ..... Unimodal Schulz-Zimm distribution, Refs. [95, 96], page 20

q ..... Scattering wavenumber, page 16

q^* ..... The first wavenumber larger than q_m, for which $S(q^*) = 1$, page 111

q_m ..... The wavenumber for which $S(q)$ (and practically also $H(q)$) attains its principal peak, page 27

r_m ..... The two-particle center-separation for which $g(r)$ attains its primary peak, page 61

s ..... Hard-core inflation parameter in (M)(PB)-RMSA, fulfilling $0 < s \leq 1$, page 29

$S(q)$ ..... Static structure factor, Ref. [4], page 25

$S(q,t)$ ..... Intermediate scattering function, fulfilling $S(q,0) = S(q)$, Ref. [4], page 43

$S_m(q)$ ..... Measurable structure factor in decoupling approximation, page 40

T ..... Absolute temperature, page 8

U_0 ..... $U_0 = \sigma^2 g(\rho - \rho_S)/(18\eta_0)$: sedimentation velocity of a slowly settling sphere at infinite dilution, page 44

u_{el} ..... Screened electrostatic pair potential, page 8

u_{HC} ..... Infinite potential step, inhibiting hard-core overlap, page 8

u_{HSY} ..... Hard-sphere Yukawa pair potential, page 10

u_{vdW} ..... Van der Waals attractive pair energy, page 8

U_{sed} ..... ϕ-dependent short time sedimentation velocity of a slowly settling, homogeneous suspension of spheres, page 44

V ..... Total system volume, page 24

v_γ ..... Volume of one particle of species γ, page 39

$W(t)$ ..... $W(t) = 1/6 < [\mathbf{r}(t) - \mathbf{r}(0)]^2 >$: 3-dimensional mean-squared displacement function of a colloidal particle, page 44

x ..... $x = r/\sigma$: dimensionless separation of colloid centers in units of the hard-core diameter, page 8

$X(q)$ ..... Decoupling amplitude, fulfilling $0 \leq X(q) \leq 1$, page 40

x_γ ..... $x_\gamma = N_\gamma/N$: Molar fraction of particle species γ, page 39

x_m ..... $x_m = r_m/\sigma$: dimensionless particle separation at which the principal peak in $g(r)$ occurs, page 63

y ..... $y = q\sigma$: dimensionless wavenumber in units of the inverse hard-core diameter, page 24

y_m ..... $y_m = q_m\sigma$: dimensionless wavenumber at which the principal peak in $S(q)$ occurs, page 69

Z ..... Colloidal effective charge in units of e, page 8

M ..... One mole (6.022×10^{23}) per liter, page 9

BIBLIOGRAPHY

[1] R. J. Hunter. *Foundations of Colloid Science*, chapter 14. Oxford University Press, Oxford, 2nd edition, 2001.

[2] W. B. Russel, D. A. Saville, and W. R. Schowalter. *Colloidal Dispersions*. Cambridge University Press, Cambridge, 1989.

[3] E. J. W. Verwey and J. T. G. Overbeek. *Theory of the Stability of Lyophobic Colloids*. Elsevier, New York, 1948.

[4] J.-P. Hansen and I. R. McDonald. *Theory of Simple Liquids*. Academic Press, London, 2nd edition, 1986.

[5] J. G. Kirkwood, E. K. Maun, and B. J. Alder. *J. Chem. Phys.*, 18:1040–1047, 1950.

[6] B. R. A. Nijboer and L. van Hove. *Phys. Rev.*, 85:777–783, 1952.

[7] N. F. Carnahan and K. E. Starling. *J. Chem. Phys.*, 51:635, 1969.

[8] M. S. Wertheim. *Phys. Rev. Lett.*, 10:321–323, 1963.

[9] P. N. Pusey and W. van Megen. *Nature*, 320:340–342, 1986.

[10] Z. Cheng, P. M. Chaikin, W. B. Russel, W. V. Meyer, J. Zhu, R. B. Rogers, and R. H. Ottewill. *Materials Design*, 22:529–534, 2001.

[11] M. N. Rosenbluth and A. W. Rosenbluth. *J. Chem. Phys.*, 22:881–884, 1954.

[12] W. W. Wood and J. D. Jacobson. *J. Chem. Phys.*, 27:1207–1208, 1957.

[13] B. J. Alder and T. E. Wainwright. *J. Chem. Phys.*, 27:1208–1209, 1957.

[14] M. Heinen, P. Holmqvist, A. J. Banchio, and G. Nägele. *J. Chem. Phys.*, 134:044532, 2011.

[15] M. Heinen, P. Holmqvist, A. J. Banchio, and G. Nägele. *J. Chem. Phys.*, 134:129901, 2011.

[16] M. Heinen, P. Holmqvist, A. J. Banchio, and G. Nägele. *J. Appl. Crystallogr.*, 43:970–980, 2010.

[17] M. Heinen, A. J. Banchio, and G. Nägele. *accepted for publication in J. Chem. Phys. preprint available at arXiv:1109.1163v1 [cond-mat.soft]*, 2011.

[18] M. Heinen, F. Zanini, F. Roosen-Runge, D. Fedunová, F. Zhang, M. Hennig, Seydel T., R. Schweins, M. Sztucki, M. Antalík, F. Schreiber, and G. Nägele. *submitted. preprint available at arXiv:1109.3101v1 [cond-mat.soft]*, 2011.

[19] D. Kleshchanok, M. Heinen, G. Nägele, and P. Holmqvist. *submitted. preprint available at arXiv:1109.3293v1 [cond-mat.soft]*, 2011.

[20] M. Heinen, P. Holmqvist, A. J. Banchio, and G. Nägele. Article in preparation.

[21] J. K. G. Dhont. *An Introduction to Dynamics of Colloids*. Elsevier, Amsterdam, 1996.

[22] G. Nägele. *Phys. Rep.*, 272:216–372, 1996.

[23] A. J. Banchio and G. Nägele. *J. Chem. Phys.*, 128:104903, 2008.

[24] A. J. Banchio and J. F. Brady. *J. Chem. Phys.*, 118:10323, 2003.

[25] G. C. Abade, B. Cichocki, M. L. Ekiel-Jeżewska, G. Nägele, and E. Wajnryb. *J. Chem. Phys.*, 133:084906, 2010.

[26] G. C. Abade, B. Cichocki, M. L. Ekiel-Jeżewska, G. Nägele, and E. Wajnryb. *J. Chem. Phys.*, 132:014503, 2010.

[27] C. W. J. Beenakker and P. Mazur. *Physica A*, 120:388–410, 1983.

[28] C. W. J. Beenakker and P. Mazur. *Physica A*, 126:349–370, 1984.

[29] C. W. J. Beenakker. *Physica A*, 128:48–81, 1984.

[30] A. L. Kholodenko and J. F. Douglas. *Phys. Rev. E*, 51:1081–1090, 1995.

[31] A. K. Gaigalas, V. Reipa, J. B. Hubbard, J. Edwards, and J. Douglas. *Chem. Eng. Sci.*, 50:1107–1114, 1995.

[32] D. E. Cohen, G. M. Thurston, R. A. Chamberlin, G. B. Benedek, and M. C. Carey. *Biochemistry*, 37:14798–14814, 1998.

[33] P. Boogerd, B. Scarlett, and R. Brouwer. *Irrig. Drain.*, 50:109–128, 2001.

[34] F. Nettesheim, M. W. Liberatore, T. K. Hodgdon, N. J. Wagner, E. W. Kaler, and M. Vethamuthu. *Langmuir*, 24:7718–7726, 2008.

[35] P. N. Pusey. North-Holland, Amsterdam, 1991.

[36] W. R. Bowen and A. Mongruel. *Colloids Surfaces A*, 138:161–172, 1998.

[37] P. Retailleau, M. Riès-Kautt, A. Ducruix, L. Belloni, S. J. Candau, and J. P. Munch. *Europhys. Lett.*, 46:154–159, 1999.

[38] W. R. Bowen, Y. C. Liang, and P. M. Williams. *Chem. Eng. Sci.*, 55:2359–2377, 2000.

[39] D. O. Riese, G. H. Wegdam, W. L. Vos, R. Sprik, D. Fenistein, J. H. H. Bongaerts, and G. Grübel. *Phys. Rev. Lett.*, 85:5460–5463, 2000.

[40] G. H. Koenderink, H. Y. Zhang, D. G. A. L. Aarts, M. P. Lettinga, A. P. Philipse, and G. Nägele. *Faraday Discuss.*, 123:335–354, 2003.

[41] J. Gapinski, A. Wilk, A. Patkowski, W. Häussler, A. J. Banchio, R. Pecora, and G. Nägele. *J. Chem. Phys.*, 123:054708, 2005.

[42] P. Prinsen and T. Odijk. *J. Chem. Phys.*, 127:115102, 2007.

[43] P. Holmqvist and G. Nägele. *Phys. Rev. Lett.*, 104:058301, 2010.

[44] G. Senatore and L. Blum. *J. Phys. Chem.*, 89:2676–2682, 1985.

[45] G. Nägele, R. Klein, and M. Medina-Noyola. *J. Chem. Phys.*, 83:2560–2568, 1985.

[46] F. Roosen-Runge, M. Hennig, F. Zhang, R. M. J. Jacobs, M. Sztucki, H. Schober, T. Seydel, and F. Schreiber. *PNAS*, 108:11815–11820, 2011.

[47] M. G. McPhie and G. Nägele. *Phys. Rev. E*, 78:060401(R), 2008.

[48] W. B. Russel and D. W. Benzing. *J. Colloid Interface Sci.*, 83:163–177, 1981.

[49] A. R. Denton. *Phys. Rev. E*, 62:3855–3864, 2000.

[50] J. A. Fornés. *Colloid Polym. Sci.*, 263:1004–1007, 1985.

[51] M. Medina-Noyola and D. A. McQuarrie. *J. Chem. Phys.*, 73:6279–6283, 1980.

[52] L. Belloni. *J. Chem. Phys.*, 85:519–526, 1986.

[53] H. Ruiz-Estrada, M. Medina-Noyola, and G. Nägele. *Physica A*, 168:919–941, 1990.

[54] E. Trizac, L. Bocquet, M. Aubouy, and H. H. von Grünberg. *Langmuir*, 19:4027–4033, 2003.

[55] A. Torres, G. Tellez, and R. van Roij. *J. Chem. Phys.*, 128:154906, 2008.

[56] S. Pianegonda, E. Trizac, and Y. Levin. *J. Chem. Phys.*, 126:014702, 2007.

[57] T. E. Colla, Y. Levin, and E. Trizac. *J. Chem. Phys.*, 131:074115, 2009.

[58] A. P. dos Santos, A. Diehl, and Y. Levin. *J. Chem. Phys.*, 132:104105, 2010.

[59] G. E. Morfill and A. V. Ivlev. *Rev. Mod. Phys.*, 81:1353–1404, 2009.

[60] S. Ichimuru, editor. *Strongly Coupled Plasma Physics*. North Holland/Yamada Foundation, Amsterdam, 1990.

[61] R. G. Palmer and J. D. Weeks. *J. Chem. Phys.*, 58:4171–4174, 1973.

[62] J. B. Hayter, R. Pynn, and J.-B. Suck. *J. Phys. F*, 13:L1–L6, 1983.

[63] J. N. Herrera, P. T. Cummings, and H. Ruiz-Estrada. *Mol. Phys.*, 96:835–847, 1999.

[64] E. M. Purcell. *Am. J. Phys.*, 45:3–11, 1977.

[65] A. P. Philipse and A. Vrij. *J. Chem. Phys.*, 88:6459–6470, 1988.

[66] P. Ball. *Chem. Rev.*, 108:74–108, 2008.

[67] R. J. Ellis. *Curr. Opin. Struct. Biol.*, 11:500, 2001.

[68] S. B. Zimmerman and A. P. Minton. *Annu. Rev. Biophys. Biomolec. Struct.*, 22:27–65, 1993.

[69] T. Ando and J. Skolnick. *Proc. Natl. Acad. Sci. U. S. A.*, 107:18457–18462, 2010.

[70] RCSB Protein Data Bank. http://www.rcsb.org/pdb/home/home.do.

[71] A. A. Bhattacharya, T. Grüne, and S. Curry. *J. Mol. Biol.*, 303:721–732, 2000.

[72] D. C. Carter and J. X. Ho. In *Advances In Protein Chemistry*, volume 45, pages 153–203. Academic Press Inc, San Diego, USA, 1994.

[73] C. Leggio, L. Galantini, and N. V. Pavel. *Phys. Chem. Chem. Phys.*, 10:6741–6750, 2008.

[74] M. L. Ferrer, R. Duchowicz, B. Carrasco, J. García de la Torre, and A. U. Acuna. *Biophys. J.*, 80:2422–2430, 2001.

[75] T. Peters. *Adv.Protein Chem.*, 37:161–245, 1985.

[76] U. Böhme and U. Scheler. *Chem. Phys. Lett.*, 435:342–345, 2007.

[77] J. Lee and S. Timasheff. *Biochemistry*, 13:257 – 265, 1974.

[78] M. Bano, I. Strharsky, and I. Hrmo. *Rev. Sci. Instrum.*, 74:4788–4793, 2003.

[79] F. Bergaya, B. K. G. Theng, and G. Lagaly, editors. *Handbook of clay science*. Elsevier, Amsterdam, 2006.

[80] A. Khaldoun, P. Moller, A. Fall, G. Wegdam, B. De Leeuw, Y. Meheust, J. O. Fossum, and D. Bonn. *Phys. Rev. Lett.*, 103:188301, 2009.

[81] G. C. Maitland. *Curr. Opin. Colloid Interface Sci.*, 5:301–311, 2000.

[82] H. H. Murray. *Appl. Clay Sci.*, 17:207–221, 2000.

[83] B. Ruzicka, L. Zulian, and G. Ruocco. *Phys. Rev. Lett.*, 93:258301, 2004.

[84] T. Nicolai and S. Cocard. *J. Colloid Interface Sci.*, 244:51–57, 2001.

[85] S. Mossa, C. De Michele, and F. Sciortino. *J. Chem. Phys.*, 126:014905, 2007.

[86] B. Abou, D. Bonn, and J. Meunier. *Phys. Rev. E*, 64:021510, 2001.

[87] R. Bandyopadhyay, D. Liang, H. Yardimci, D. A. Sessoms, M. A. Borthwick, S. G. J. Mochrie, J. L. Harden, and R. L. Leheny. *Phys. Rev. Lett.*, 93:228302, 2004.

[88] A. Ortega and J. García de la Torre. *J. Chem. Phys.*, 119:9914–9919, 2003.

[89] F. M. van der Kooij, A. P. Philipse, and J. K. G. Dhont. *Langmuir*, 16:5317–5323, 2000.

[90] D. Shah, G. Fytas, D. Vlassopoulos, J. Di, D. Sogah, and E. P. Giannelis. *Langmuir*, 21:19–25, 2005.

[91] R. Pecora. *J. Chem. Phys.*, 49:1036, 1968.

[92] W. Eimer, J. R. Williamson, S. G. Boxer, and R. Pecora. *Biochemistry*, 29:799–811, 1990.

[93] S. Fujime and K. Kubota. *Biophys. Chem.*, 23:1–13, 1985.

[94] B. J. Berne and R. Pecora. *Dynamic Light Scattering: With Applications to Chemistry, Biology, and Physics*. Wiley, New York, 1 edition, 1976.

[95] G. V. Schulz. *Z. Phys. Chem. B*, 43:25–46, 1939.

[96] B. H. Zimm. *J. Chem. Phys.*, 16:1099–1116, 1948.

[97] I. K. Snook and J. B. Hayter. *Langmuir*, 8:2880–2884, 1992.

[98] J.-P. Hansen and J. B. Hayter. *Mol. Phys.*, 46:651–656, 1982.

[99] T. Morita. *Prog. Theor. Phys.*, 20:920–938, 1958.

[100] F. J. Rogers and D. A. Young. *Phys. Rev. A*, 30:999–1007, 1984.

[101] L. S. Ornstein and F. Zernike. *Proc. Sect. Sci. K. ned. Akad. Wet.*, 17:793, 1914.

[102] E. J. Meijer and D. Frenkel. *J. Chem. Phys.*, 94:2269–2271, 1991.

[103] M. J. Stevens and M. O. Robbins. *J. Chem. Phys.*, 98:2319–2324, 1993.

[104] N. Pistoor and K. Kremer. *Physica A*, 201:171–177, 1993.

[105] S. Hamaguchi, R. T. Farouki, and D. H. E. Dubin. *J. Chem. Phys.*, 105:7641–7647, 1996.

[106] S. Hamaguchi, R. T. Farouki, and D. H. E. Dubin. *Phys. Rev. E*, 56:4671–4682, 1997.

[107] J. M. Brader. *Int. J. Thermophys.*, 27:394–412, 2006.

[108] F. El Azhar, M. Baus, J.-P. Ryckaert, and E. J. Meijer. *J. Chem. Phys.*, 112:5121–5126, 2000.

[109] A.-P. Hynninen and M. Dijkstra. *J. Phys.-Condes. Matter*, 15:S3557–S3567, 2003.

[110] M. J. Gillan. *J. Phys. C*, 7:L1–L4, 1974.

[111] E. Waisman. *Mol. Phys.*, 25:45–48, 1973.

[112] L. Blum and J. S. Hoye. *J. Stat. Phys.*, 19:317–324, 1978.

[113] P. T. Cummings and E. R. Smith. *Mol. Phys.*, 38:997–1001, 1979.

[114] P. T. Cummings and E. R. Smith. *Chem. Phys.*, 42:241–247, 1979.

[115] M. Ginoza. *J. Phys. Soc. Jpn.*, 55:95–101, 1986.

[116] S. K. Lai and G. F. Wang. *Phys. Rev. E*, 58:3072–3082, 1998.

[117] Sans Manuals and Data Reduction. Available online at http://www.ncnr.nist.gov/programs/sans/data/index.html.

[118] C. Beck, W. Härtl, and R. Hempelmann. *J. Chem. Phys.*, 111:8209–8213, 1999.

[119] A. J. Banchio, J. Bergenholtz, and G. Nägele. *Phys. Rev. Lett.*, 82:1792–1795, 1999.

[120] J. Gapinski, A. Patkowski, and G. Nägele. *J. Chem. Phys.*, 132:054510, 2010.

[121] J. K. Percus and G. J. Yevick. *Phys. Rev.*, 110:1–13, 1958.

[122] B. Svensson and B. Jönsson. *Mol. Phys.*, 50:489–495, 1983.

[123] B. Beresford-Smith, D. Y. C. Chan, and D. J. Mitchell. *J. Colloid Interface Sci.*, 105:216–234, 1985.

[124] S. Khan, T. L. Morton, and D. Ronis. *Phys. Rev. A*, 35:4295–4305, 1987.

[125] L. Belloni. *J. Phys.-Condes. Matter*, 12:R549–R587, 2000.

[126] A. A. Louis. *Philos. Trans. R. Soc. Lond. Ser. A-Math. Phys. Eng. Sci.*, 359:939–960, 2001.

[127] A. A. Louis. *J. Phys.-Condes. Matter*, 14:9187–9206, 2002.

[128] M. Dijkstra, R. van Roij, and R. Evans. *J. Chem. Phys.*, 113:4799–4807, 2000.

[129] J. Dobnikar, R. Castaneda-Priego, H. H. von Grünberg, and E. Trizac. *New J. Phys.*, 8:277, 2006.

[130] E. Trizac, Luc Belloni, J. Dobnikar, H. H. von Grünberg, and R. Castaneda-Priego. *Phys. Rev. E*, 75:011401, 2007.

[131] F. H. Stillinger, H. Sakai, and S. Torquato. *J. Chem. Phys.*, 117:288–296, 2002.

[132] C. F. Tejero and M. Baus. *J. Chem. Phys.*, 118:892–896, 2003.

[133] C. F. Tejero. *J. Phys.-Condes. Matter*, 15:S395–S400, 2003.

[134] H. C. Andersen and D. Chandler. *J. Chem. Phys.*, 53:547, 1970.

[135] K. S. Schweizer and J. G. Curro. *Adv. Chem. Phys.*, 98:1–142, 1997.

[136] L. Harnau and J.-P. Hansen. *J. Chem. Phys.*, 116:9051–9057, 2002.

[137] A. Yethiraj and C.-Y. Shew. *Phys. Rev. Lett.*, 77:3937–3940, 1996.

[138] C.-Y. Shew and A. Yethiraj. *J. Chem. Phys.*, 106:5706–5719, 1997.

[139] C.-Y. Shew and A. Yethiraj. *J. Chem. Phys.*, 109:5162–5163, 1998.

[140] L. Harnau and P. Reineker. *J. Chem. Phys.*, 112:437–441, 2000.

[141] L. Li, L. Harnau, S. Rosenfeldt, and M. Ballauff. *Phys. Rev. E*, 72:051504, 2005.

[142] L. Harnau, S. Rosenfeldt, and M. Ballauff. *J. Chem. Phys.*, 127:014901, 2007.

[143] L. Harnau. *Mol. Phys.*, 106:1975–2000, 2008.

[144] D. Laria, D. Wu, and D. Chandler. *J. Chem. Phys.*, 95:4444–4453, 1991.

[145] K. S. Schweizer and A. Yethiraj. *J. Chem. Phys.*, 98:9053–9079, 1993.

[146] B. J. Yoon. *J. Colloid Interface Sci.*, 142:575–581, 1991.

[147] E. Eggen and R. van Roij. *Phys. Rev. E*, 80:041402, 2009.

[148] N. Boon and R. van Roij. *J. Chem. Phys.*, 134:054706, 2011.

[149] C. Alvarez and G. Tellez. *J. Chem. Phys.*, 133:144908, 2010.

[150] R. Ramirez and R. Kjellander. *J. Chem. Phys.*, 119:11380–11395, 2003.

[151] N. Hoffmann, C. N. Likos, and J.-P. Hansen. *Mol. Phys.*, 102:857–867, 2004.

[152] N. W. Ashcroft and D. C. Langreth. *Phys. Rev.*, 156:685, 1967.

[153] R. B. Jones and P. N. Pusey. *Annu. Rev. Phys. Chem.*, 42:137–169, 1991.

[154] P. Szymczak and B. Cichocki. *J. Stat. Mech.-Theory Exp.*, page P01025, 2008.

[155] A. Einstein. *Annln. Phys.-Berlin*, 19:289–306, 1906.

[156] A. Einstein. *Annln. Phys.-Berlin*, 34:591–592, 1911.

[157] G. K. Batchelor and J. T. Green. *J. Fluid Mech.*, 56:401–427, 1972.

[158] D. J. Jeffrey and Y. Onishi. *J. Fluid Mech.*, 139:261–290, 1984.

[159] R. B. Jones and R. Schmitz. *Physica A*, 149:373–394, 1988.

[160] S. Kim and S. J. Karrila. *Microhydrodynamics: Principles and Selected Applications*. Butterworth-Heinemann, Boston, MA, 1991.

[161] D. J. Jeffrey. *Phys. Fluids A*, 4:16–29, 1992.

[162] S. Kim and R. T. Mifflin. *Phys. Fluids*, 28:2033, 1985.

[163] N. J. Wagner and A. T. J. M. Woutersen. *J. Fluid Mech.*, 278:267–287, 1994.

[164] W. B. Russel. *J. Chem. Soc., Faraday Trans.*, 80:31–41, 1984.

[165] B Cichocki, ML Ekiel-Jeżewska, and E Wajnryb. *J. Chem. Phys.*, 111:3265–3273, 1999.

[166] B. Cichocki, M. L. Ekiel-Jeżewska, P. Szymczak, and E. Wajnryb. *J. Chem. Phys.*, 117:1231–1241, 2002.

[167] B. Cichocki, M. L. Ekiel-Jeżewska, and E. Wajnryb. *J. Chem. Phys.*, 119:606–619, 2003.

[168] U. Genz and R. Klein. *Physica A*, 171:26–42, 1991.

[169] H. Löwen, T. Palberg, and R. Simon. *Phys. Rev. Lett.*, 70:1557–1560, 1993.

[170] A. J. Banchio, J. Gapinski, A. Patkowski, W. Häussler, A. Fluerasu, S. Sacanna, P. Holmqvist, G. Meier, M. P. Lettinga, and G. Nägele. *Phys. Rev. Lett.*, 96:138303, 2006.

[171] E. Overbeck, C. Sinn, and M. Watzlawek. *Phys. Rev. E*, 60:1936–1939, 1999.

[172] G. Nägele, B. Steininger, U. Genz, and R. Klein. *Phys. Scr.*, 55:119–126, 1994.

[173] G. Nägele, B. Mandl, and R. Klein. *Prog. Colloid Ploym. Sci.*, 98:117–123, 1995.

[174] M. Watzlawek and G. Nägele. *J. Colloid Interface Sci.*, 214:170–179, 1999.

[175] G. C. Abade, B. Cichocki, M. L. Ekiel-Jeżewska, G. Nägele, and E. Wajnryb. *J. Chem. Phys.*, 134:244903, 2011.

[176] F. M. Horn, W. Richtering, J. Bergenholtz, N. Willenbacher, and N. J. Wagner. *J. Coll. Interf. Sci.*, 225:166–178, 2000.

[177] W. Kob. *arXiv:cond-mat/0212344v1*, 2002.

[178] D. R. Reichman and P. Charbonneau. *J. Stat. Mech.-Theory Exp.*, page P05013, 2005.

[179] G. Nägele and P. Baur. *Physica A*, 245:297–336, 1997.

[180] G. Nägele and J. Bergenholtz. *J. Chem. Phys.*, 108:9893–9904, 1998.

[181] J.-P. Hansen and L. Verlet. *Phys. Rev.*, 184:151, 1969.

[182] K. Kremer, M. O. Robbins, and G. S. Grest. *Phys. Rev. Lett.*, 57:2694–2697, 1986.

[183] D. C. Wang and A. P. Gast. *J. Phys.-Condes. Matter*, 11:10133–10141, 1999.

[184] F. Bitzer, T. Palberg, H. Löwen, R. Simon, and P. Leiderer. *Phys. Rev. E*, 50:2821–2826, 1994.

[185] J. S. Pedersen. *Adv. Colloid Interface Sci.*, 70:171–210, 1997.

[186] P. Wette, I. Klassen, D. Holland-Moritz, D. M. Herlach, H. J. Schöpe, N. Lorenz, H. Reiber, T. Palberg, and S. V. Roth. *J. Chem. Phys.*, 132:131102, 2010.

[187] D. M. Herlach, I. Klassen, P. Wette, and D. Holland-Moritz. *J. Phys.-Condes. Matter*, 22:153101, 2010.

[188] J. García de la Torre, A. Ortega, D. Amoros, R. Rodriguez Schmidt, and J. G. Hernandez Cifre. *Macromol. Biosci.*, 10:721–730, 2010.

[189] M. Kotlarchyk and S.-H. Chen. *J. Chem. Phys.*, 79:2461–2469, 1983.

[190] W. R. Bowen and P. M. Williams. *J. Colloid Interface Sci.*, 184:241–250, 1996.

[191] C. M. Roth, B. L. Neal, and A. M. Lenhoff. *Biophys. J.*, 70:977–987, 1996.

[192] F. Zhang, M. W. A. Skoda, R. M. J. Jacobs, R. A. Martin, C. M. Martin, and F. Schreiber. *J. Phys. Chem. B*, 111:251–259, 2007.

[193] D. I. Svergun, S. Richard, M. H. J. Koch, Z. Sayers, S. Kuprin, and G. Zaccai. *PNAS*, 95:2267–2272, 1998.

[194] A. Isihara. *J. Chem. Phys.*, 18:1446–1449, 1950.

[195] B. R. Jennings and K. Parslow. *Proc. R. Soc. London Ser. A-Math. Phys. Eng. Sci.*, 419:137–149, 1988.

[196] F. Perrin. *J. Phys. Radium*, 7:1–11, 1936.

[197] G. B. Jeffery. *Proc. R. soc. Lond. Ser. A-Contain. Pap. Math. Phys. Character*, 102:161–179, 1922.

[198] F. M. van der Kooij, E. S. Boek, and A. P. Philipse. *J. Colloid Interface Sci.*, 235:344–349, 2001.

[199] J. M. Deutch. *Macromolecules*, 14:1826–1827, 1981.

[200] J. Happel and H. Brenner. *Low Reynolds Number Hydrodynamics*. Springer Netherlands, 1 edition, 1983.

[201] M. Tirado, M and J. García de la Torre. *J. Chem. Phys.*, 71:2581–2587, 1979.

[202] M. Tirado, M and J. García de la Torre. *J. Chem. Phys.*, 73:1986–1993, 1980.

[203] D. Frenkel and R. Eppenga. *Phy. Rev. Lett.*, 49:1089–1092, 1982.

[204] J. A. C. Veerman and D. Frenkel. *Phy. Rev. A.*, 45:5632–5648, 1992.

[205] Y. Gan and G. V. Franks. *Langmuir*, 22:6087–6092, 2006.

[206] A. J. C. Ladd. *J. Chem. Phys.*, 93:3484–3494, 1990.

[207] G. Mo and A. S. Sangani. *Phys. Fluids*, 6:1637–1652, 1994.

[208] P. N. Segrè, O. P. Behrend, and P. N. Pusey. *Phys. Rev. E*, 52:5070, 1995.

[209] A.J.C Ladd, H. Gang, Zhu J. X., and D. A. Weitz. *Phys. Rev. E*, 52:6550, 1995.

[210] A. J. Banchio, G. Nägele, and J. Bergenholtz. *J. Chem. Phys.*, 111:8721–8740, 1999.

[211] P. N. Pusey. *J. Phys. A*, 11:119–135, 1978.

[212] G. C. Abade, B. Cichocki, M. L. Ekiel-Jeżewska, G. Nägele, and E. Wajnryb. *Phys. Rev. E*, 81:020404, 2010.

[213] A. Robert. *J. Appl. Crystallogr.*, 40:S34–S37, 2007.

[214] L. Rojas-Ochoa. *Structure, dynamics and photon diffusion in charge-stabilized colloidal suspensions. PhD thesis*. Université de Fribourg, Switzerland, 2004.

[215] A. Robert, J. Wagner, W. Härtl, T. Autenrieth, and G. Grübel. *Eur. Phys. J. E*, 25:77–81, 2008.

[216] J. K. Phalakornkul, A. P. Gast, R. Pecora, G. Nägele, A. Ferrante, B. Mandl-Steininger, and R. Klein. *Phys. Rev. E*, 54:661–675, 1996.

[217] W. Härtl, C. Beck, and R. Hempelmann. *J. Chem. Phys.*, 110:7070–7072, 1999.

[218] L. F. Rojas-Ochoa, R. Vavrin, C. Urban, J. Kohlbrecher, A. Stradner, F. Scheffold, and P. Schurtenberger. *Faraday Discuss.*, 123:385–400, 2003.

[219] J. Gapinski, A. Patkowski, A. J. Banchio, J. Buitenhuis, P. Holmqvist, M. P. Lettinga, G. Meier, and G. Nägele. *J. Chem. Phys.*, 130, 2009.

[220] A. J. Banchio, J. Gapinski, A. Patkowski, W. Häussler, A. Fluerasu, S. Sacanna, P. Holmqvist, G. Meier, M. P. Lettinga, and G. Nägele. *Phys. Rev. Lett.*, 96:138303, 2006.

[221] G. Grübel, A. Madsen, and A. Robert. *X-ray Photon Correlation Spectroscopy (XPCS) in Soft-Matter Characterization*. Springer, Berlin, 2008.

[222] A. Robert. *PhD thesis*. Université Joseph Fourier, Grenoble, France, 2001.

[223] H. Diamant. *Isr. J. Chem.*, 47:225–231, 2007.

[224] J. Bergenholtz, F. M. Horn, W. Richtering, N. Willenbacher, and N. J. Wagner. *Phys. Rev. E*, 58:R4088–R4091, 1998.

[225] G. C. Abade, B. Cichocki, M. L. Ekiel-Jeżewska, G. Nägele, and E. Wajnryb. *J. Phys.-Condens. Matter*, 22:322101, 2010.

[226] A. Moncho-Jordá, A. A. Louis, and J. T. Padding. *Phys. Rev. Lett.*, 104:068301, 2010.

[227] C. van den Broeck, F. Lostak, and H. N. W. Lekkerkerker. *J. Chem. Phys.*, 74:2006–2010, 1981.

[228] B. Cichocki and B. U. Felderhof. *J. Chem. Phys.*, 93:4427–4432, 1990.

[229] K. F. Seefeldt and M. J. Solomon. *Phys. Rev. E*, 67:050402, 2003.

[230] S. D. Bembenek and G. Szamel. *J. Phys. Chem. B*, 104:10647–10652, 2000.

[231] M. G. McPhie and G. Nägele. *J. Chem. Phys.*, 127:034906, 2007.

[232] C. Tanford and J. G. Buzzell. *J. Phys. Chem.*, 60:225–231, 1956.

[233] D. W. Kupke, M. G. Hodgins, and J. W. Beams. *Proc. Natl. Acad. Sci. U. S. A.*, 69:2258, 1972.

[234] M. Placidi and S. Cannistraro. *Europhys. Lett.*, 43:476–481, 1998.

[235] R. Curvale, M. Masuelli, and A. P. Padilla. *Int. J. Biol. Macromol.*, 42:133–137, 2008.

[236] S. Förster and M. Schmidt. In *Physical properties of polymers*, volume 120 of *Adv. in Poly. Sci.*, pages 51–133. Springer, Berlin, 1995.

[237] M. Antonietti, A. Briel, and S. Förster. *J. Chem. Phys.*, 105:7795–7807, 1996.

[238] H. Eisenberg. *Biophys. Chem.*, 7:3–13, 1977.

[239] T. Okubo. *J. Chem. Phys.*, 87:6733–6739, 1987.

[240] Y. Dziechciarek, J. J. G. van Soest, and A. P. Philipse. *J. Colloid Interface Sci.*, 246:48–59, 2002.

[241] Y. Rabin. *Phys. Rev. A*, 35:3579–3581, 1987.

[242] S. A. Rice and J. G. Kirkwood. *J. Chem. Phys.*, 31:901–908, 1959.

[243] K. Nishida, K. Kiriyama, T. Kanaya, K. Kaji, and T. Okubo. *J. Polym. Sci. Pt. B-Polym. Phys.*, 42:1068–1074, 2004.

[244] K. Miyazaki, B. Bagchi, and A. Yethiraj. *J. Chem. Phys.*, 121:8120–8127, 2004.

[245] H. Ohshima. *Langmuir*, 23:12061–12066, 2007.

[246] J. D. Sherwood. *J. Phys. Chem. B*, 111:3370–3378, 2007.

[247] B. Cichocki and B. U. Felderhof. *J. Chem. Phys.*, 101:7850–7855, 1994.

[248] C. Gögelein, G. Nägele, R. Tuinier, T. Gibaud, A. Stradner, and P. Schurtenberger. *J. Chem. Phys.*, 129:085102, 2008.

[249] R. Kohlrausch. *Annalen der Physik und Chemie*, 91:56–82, 179–214, 1854.

[250] G. Williams and D. C. Watts. *Trans. Faraday Soc.*, 66:80, 1970.

[251] C. P. Lindsey and G. D. Patterson. *J. Chem. Phys.*, 73:3348–3357, 1980.

[252] V. Degiorgio, R. Piazza, and R. B. Jones. *Phys. Rev. E*, 52:2707–2717, 1995.

[253] M. Adam and M. Delsanti. *Macromolecules*, 10:1229–1237, 1977.

[254] U. Zettl, S. T. Hoffmann, F. Koberling, G. Krausch, J. Enderlein, L. Harnau, and M. Ballauff. *Macromolecules*, 42:9537–9547, 2009.

[255] E. Wajnryb, P. Szymczak, and B. Cichocki. *Physica A*, 335:339–358, 2004.

[256] P. Holmqvist, S. Pispas, N. Hadjichristidis, G. Fytas, and R. Sigel. *Macromolecules*, 36:830–838, 2003.

[257] H. Y. Zhang and G. Nägele. *J. Chem. Phys.*, 117:5908–5920, 2002.

[258] S. Jabbari-Farouji, E. Eiser, G. H. Wegdam, and D. Bonn. *J. Phys. Cond.-Mat.*, 16:L471–L477, 2004.

[259] H. C. Brinkmann. *Appl. Sci. Res.*, A1:27, 1947.

[260] P. Debye and A. M. Bueche. *J. Chem. Phys.*, 16:573, 1948.

[261] P. Reuland, B. U. Felderhof, and R. B. Jones. *Physica A*, 93:465–475, 1978.

[262] A. Pich and W. Richtering. Microgels by precipitation polymerization: Synthesis, characterization, and functionalization. In *Chemical Design of Responsive Microgels*, volume 234 of *Advances in Polymer Science*, pages 1–37. Springer Berlin / Heidelberg, 2011.

[263] H. Senff and W. Richtering. *J. Chem. Phys.*, 111:1705–1711, 1999.

[264] H. Senff, W. Richtering, C. Norhausen, A. Weiss, and M. Ballauff. *Langmuir*, 15:102–106, 1999.

[265] B. Cichocki, B. U. Felderhof, K. Hinsen, E. Wajnryb, and J. Bławzdziewicz. *J. Chem. Phys.*, 100:3780–3790, 1994.

[266] M. L. Ekiel-Jeżewska and E. Wajnryb. *Theoretical Methods for Micro Scale Viscous Flows*, chapter 6. Transworld Research Network.

[267] Y Liu, W.-R. Chen, and S.-H. Chen. *J. Chem. Phys.*, 122:044507, 2005.

[268] J. M. Kim, R. Castaneda-Priego, Y. Liu, and N. J. Wagner. *J. Chem. Phys.*, 134:064904, 2011.

[269] J. B. Hayter and J. Penfold. *Mol. Phys.*, 42:109–118, 1981.

[270] P. T. Cummings and G. Stell. *J. Chem. Phys.*, 78:1917–1923, 1983.

[271] G. Kahl. *Mol. Phys.*, 67:879–889, 1989.

[272] R. J. Baxter. *Aust. J. Phys.*, 21:563, 1968.

[273] D. J. Jeffrey. *Mathematika*, 29:58–66, 1982.

[274] GSL - GNU Scientific Library. Available online at http://www.gnu.org/software/gsl/.

[275] GTK+, the GIMP Toolkit. Available online at http://www.gtk.org/.

[276] J. A. Nelder and R. Mead. *Comput. J.*, 7:308–313, 1965.

Acknowledgements

First of all, I would like to express my gratitude to Gerhard Nägele, who has spent great efforts during the last 3½ years in introducing me to the physics of soft matter systems. He has provided me with a highly interesting research project that was well-outlined from its beginning. Also, he readily found the time for countless in-depth discussions that helped to drastically speed up my advancement. For his restless impetus and benign attitude, I will keep Gerhard in mind as a superb advisor.

I thank Jan Dhont for the great time I had in his group, and for suggesting me as an IHRS BioSoft fellow student. Also, I thank Jan for giving me the opportunity to attend various educational workshops, and to present my research at international conferences already at early stages. Most of all, however, I will remember Jan for his brilliant way of lecturing.

I would like to thank Prof. Löwen for having accepted to review my thesis, and for organizing the SFB TR-6 summer school in Cargèse, which was a great time for all attending students.

I greatly appreciate the work done by Adolfo Banchio in generating the many computer simulation results needed in our collaboration. I thank Adolfo also for the constructive criticism and suggestions during his visit to Jülich.

Peter Holmqvist and Dzina Kleshchanok are acknowledged for an enjoyable collaboration, and for their painstakingly conducted experiments. I thank Peter for his many critical comments, and his ability to put the finger on points that needed revision. In addition, I will remember Peter as a formidable chef de cuisine, sharing with me his fine fish recipes.

Maria Ekiel-Jeżewska, Bogdan Cichocki, Eligiusz Wajnryb, Karol Makuch, and Gustavo Abade are thanked for their kind hospitality and for our enjoyable conversations in Jülich, Warsaw and at the excellent school of statistical physics in Kazimierz.

I am grateful to Prof. Schreiber and the members of his soft matter group in Tübingen for the fruitful collaboration on BSA protein solutions. In particular, I would like to thank Felix Roosen-Runge and Fabio Zanini for many useful discussions and for sharing with me their knowledge on protein solutions.

All lecturers and students of IHRS BioSoft are gratefully acknowledged for the educating seminars and lectures combining physics with chemistry and biology. I thank the organizers of

BioSoft, in particular Thorsten Auth, for the thoughtfully prepared semester schedules, and for the financial support that has allowed me to attend several conferences. I would like to thank Prof. Egelhaaf for joining my advisory committee. Thank you Aggeliki, Karolina, Kyriakos, Richard, Martin, Sudipta, Michael, Helge, and Donald, for the great times we had in and out of Jülich.

I thank all members of ICS-3 (formerly IFF-7) for the superb working atmosphere. My special thanks go to our secretary Marie, who kept me from drowning in the bureaucratic chaos, to Johan Buitenhuis for our discussions about colloid synthesis, and for sharing with me his TEM pictures of silica, to Simon Rogers for proof-reading my manuscripts, to Cristoph July for his help with certain Linux configurations, to Christoph Gögelein for the short but enjoyable time we spent together at IFF-7 and at some conferences, to Kyong Kang for our refreshing conversations about science and the Korean peninsula, to Gerd Meier for introducing me to the fascinating cosmos of edible fungi, and to my officemate Claudio Contreras-Aburto, with whom I had many adventurous excursions far beyond the Jülich city limits.

Last but not least, I thank my mum and brother, and Jeannine for their enduring and loving support.

Die hier vorgelegte Dissertation habe ich eigenständig und ohne unerlaubte Hilfe angefertigt. Die Dissertation wurde in der vorgelegten oder in ähnlicher Form noch bei keiner anderen Institution eingereicht. Ich habe bisher keine erfolglosen Promotionsversuche unternommen.

Düsseldorf, den 20.09.2011

Marco Heinen